Alma Mater Studiorum - Università di Bologna

DOTTORATO DI RICERCA IN

ASTROFISICA

Ciclo XXXII

DYNAMICAL EVOLUTION OF DENSE STELLAR SYSTEMS FROM BLUE STRAGGLER STARS

Presentata da: Silvia Raso

Coordinatore Dottorato:

Chiar.mo Prof.
Francesco R. Ferraro

Supervisore:

Chiar.mo Prof.
Francesco R. Ferraro

Co-supervisori:

Chiar.ma Prof. Barbara Lanzoni
Dott.ssa Cristina Pallanca

Esame finale anno 2020

Settore Concorsuale: 02/C1 – Astronomia, Astrofisica, Fisica della Terra e dei Pianeti
Settore Scientifico Disciplinare: FIS/05 – Astronomia e Astrofisica

Abstract

The aim of this Thesis is to investigate the dynamical evolution of Globular Clusters (GCs) through a completely empirical approach, by exploiting the properties of a dynamically-sensitive stellar population: the so-called Blue Straggler Stars (BSSs). These objects are $\sim$3 times more massive than the average in GCs, and their presence cannot be explained in terms of the standard evolution of single stars. Hence, formation mechanisms involving two or more low-mass stars must be invoked, the most favorite ones being mass-transfer or coalescence in binary systems, and direct stellar collisions. The tight link between BSSs and GC internal dynamics is testified not only by their formation mechanisms, but also by the fact that, being more massive than the average, BSSs significantly suffer from the effects of dynamical friction, which makes them sink toward the cluster center, progressively modifying their radial distribution.

This Thesis, from one side, provides the first determination of the physical properties of BSSs along the entire extension of their sequence in the color-magnitude diagram, and from the other side it presents a comprehensive study of the BSS population in a sample of GCs, both in the Milky Way and in the Large Magellanic Cloud (LMC), to unveil the stage of dynamical evolution reached by the host systems.

The physical properties (mass, temperature, radius, surface gravity) of a large sample of BSSs have been derived in 47 Tucanae through the analysis of their spectral energy distributions from the far-ultraviolet to the near-infrared. This study confirmed the large mass of these objects and demonstrated that evolutionary tracks of individual stars can be used for first-order estimates of the mass of these exotica.

After having demonstrated that the selection of BSSs at ultraviolet wavelengths guarantees the highest achievable level of completeness, the "ultraviolet-driven approach" has been used to determine the BSS radial distribution in $\sim$ 30% of the entire Milky Way GC population. This allowed us to rank the host clusters in terms of the level of their internal dynamical evolution by using the so-called "A^+ parameter", which measures the central concentration of BSSs within the cluster. The same approach applied to five GCs in the LMC not only demonstrated that A^+ is a powerful dynamical indicator even in external galaxies, but also allowed us to solve a 30-yr old conundrum: we showed that the spread in core radius observed for the old GCs in the LMC is just the natural consequence of their internal dynamical evolution.

Following on previous discoveries, we pursued the search for double BSS sequences in post-core collapsed GCs, analyzing the case of M15. We found evidence for two distinct sequences of collisional BSSs that likely testify two major collisional events: the occurrence of core collapse $\sim$ 5.5 Gyr ago, and a core oscillation dating back to $\sim$ 2 Gyr ago. Instead, in NGC 1261 we found only a hint of a double BSS sequence, the detectability of which is not as solid as for the other reported cases. This is at odds with previous claims in the literature, but well consistent with the low level of dynamical evolution suggested by the value of A^+. In this GC we also determined the velocity dispersion profile of BSSs and main-sequence turnoff stars from the measurement of *Hubble Space Telescope* proper motions. This allowed us to obtain an independent confirmation that the system is poorly dynamically evolved.

Contents

List of Abbreviations

ACS	**A**dvanced **C**amera for **S**urveys
AGB	**A**symptotic **G**iant **B**ranch
BH	**B**lack **H**ole
BSS	**B**lue **S**traggler **S**tar
BSS-nRD	**B**lue **S**traggler **S**tar **n**ormalized **R**adial **D**istribution
CC	**C**ore **C**ollapse
CCD	**C**harge-**C**oupled **D**evice
CFHT	**C**anada-**F**rance-**H**awaii **T**elescope
CMD	**C**olor **M**agnitude **D**iagram
COL-BSS	**COL**lisional **B**lue **S**traggler **S**tar
CTE	**C**harge **T**ransfer **E**fficiency
CV	**C**ataclysmic **V**ariable
EBSS	**E**volved **B**lue **S**traggler **S**tar
ESO	**E**uropean **S**outhern **O**bservatory
FOV	**F**ield **O**f **V**iew
FUV	**F**ar **U**ltra**V**iolet
GC	**G**lobular **C**luster
GGC	**G**alactic **G**lobular **C**luster
GMM	**G**aussian **M**ixture **M**odeling
HB	**H**orizontal **B**ranch
HR	**H**ertzsprung-**R**ussel
HRC	**H**igh **R**esolution **C**hannel
HST	***H**ubble **S**pace **T**elescope*
IRAF	**I**mage **R**eduction and **A**nalysis **F**acility
LBC	**L**arge **B**inocular **C**ameras
LBT	**L**arge **B**inocular **T**elescope
LMC	**L**arge **M**agellanic **C**loud
LOS	**L**ine **O**f **S**ight
MCMC	**M**arkov **C**hain **M**onte **C**arlo
MMAS	**M**ake **M**e **A** **S**tar code
MOCCA	**MO**nte **C**arlo **C**luster Simul**A**tor
MS	**M**ain **S**equence
MT-BSS	**M**ass **T**ransfer **B**lue **S**traggler **S**tar
n-CMD	**n**ormalized **C**olor **M**agnitude **D**iagram
NGC	**N**ew **G**eneral **C**atalogue
PAM	**P**ixel **A**rea **M**ap
PDF	**P**robability **D**istribution **F**unction
PM	**P**roper **M**otion
PSF	**P**oint-**S**pread **F**unction
REF	**REF**erence
RGB	**R**ed **G**iant **B**ranch
SED	**S**pectral **E**nergy **D**istribution
SGB	**S**ub **G**iant **B**ranch

SSP	**S**imple **S**tellar **P**opulation
STIS	**S**pace **T**elescope **I**maging **S**pectrograph
TO	**T**urn **O**ff
UV	**U**ltra**V**iolet
UVIS	**U**ltraviolet and **VIS**ual
VPD	**V**ector **P**oint **D**iagram
WD	**W**hite **D**warf
WFC	**W**ide **F**ield **C**hannel
WFC3	**W**ide **F**ield **C**amera **3**
WFI	**W**ide **F**ield **I**mager
WFPC2	**W**ide **F**ield and **P**lanetary **C**amera **2**
YREC	**Y**ale **R**otational **E**volutionary **C**ode
ZAMS	**Z**ero **A**ge **M**ain **S**equence

Chapter 1

Introduction

1.1 Globular Clusters

Globular clusters (hereafter, GCs), are stellar systems typically composed of $10^5 - 10^6$ gravitationally bound stars, generally distributed with a spherical symmetry. About 150 GCs have been identified in our Galaxy (Harris 1996, 2010 edition), typically distributed in the Galactic halo and bulge, and they are usually referred to as Galactic GCs (GGCs). GGCs are old stellar systems, with ages between $\sim$ 10 and $\sim$ 13 Gyr (see, e.g., Gratton et al. 1997; Chaboyer et al. 1998; Marín-Franch et al. 2009), therefore they can be considered fossil remnants of the formation epoch of our Galaxy.

GCs have been considered for a long time as the best known realization of the concept of simple stellar population (SSP), i.e., stellar systems made of stars with the same age and chemical composition. In the last two decades, different subpopulations, with different chemical abundances of light elements (e.g., Na, O, C, N, He) have been discovered (e.g., Kraft 1994; Gratton, Sneden, and Carretta 2004; Carretta et al. 2009a,b; Gratton, Carretta, and Bragaglia 2012; Milone et al. 2017). This discovery challenges the paradigm of GCs as SSPs, however, given the absence of large iron spreads (Carretta et al. 2009b), GCs still represent the best approximation of SSP and continue to be used as ideal observational laboratories to test stellar evolution models.

1.2 Internal dynamics and structure

GCs are fundamental stellar laboratories to test stellar dynamics. GC internal dynamical evolution is mainly led by two-body encounters, during which stars exchange energy and, therefore, progressively lose memory of their initial conditions (e.g., Binney and Tremaine 1987; Meylan and Heggie 1997). The two-body relaxation timescale t_{2b} can be written as:

$$t_{2b} = n_{2b} t_{cross} \tag{1.1}$$

where t_{cross} is the crossing time, i.e., the time it takes a particle, with velocity v, to cross a system of characteristic length scale R ($t_{cross} = R/v$), and n_{2b} is the number of crossing necessary for a star to change its velocity of a quantity that is equal to its velocity itself. It can be demonstrated (Binney and Tremaine 1987) that:

$$t_{2b} = \frac{\sigma(r)^3}{8\pi G^2 \langle m \rangle \rho(r) \ln \Lambda} \tag{1.2}$$

where $\sigma(r)$ is the velocity dispersion at a distance r from the center, G is the gravitational constant, $\langle m \rangle$ is the mean stellar mass, $\rho(r)$ is the local density and $\ln \Lambda$ is the

Coulomb logarithm. Clearly, the relaxation timescale depends on the local velocity dispersion, and inversely on the local density and the stellar mass.

From Equation 1.2 the following approximated relation can be obtained:

$$t_{2b} \simeq \frac{0.1N}{\ln N} t_{cross} \tag{1.3}$$

where N is the number of object of the system. For a system like a GC, with N$\sim 10^5 - 10^6$, the relaxation timescale is less than 1 Gyr, significantly shorter than the typical GGC age. Therefore, the encounters between stars play a fundamental role in the dynamics and structure of GCs, and must be taken into account in modeling these systems and comparing them with observations. In general, a system that has a relaxation time shorter than its age is called collisional, while a system with a relaxation timescale longer than its age is called collisionless (e.g., galaxies, which have a much larger number of particles, N$\sim 10^{11}$, and therefore a longer relaxation timescale from Equation 1.3).

Since GCs are collisional systems, the velocity distribution tends to be Maxwellian. Formally, this distribution does not have an upper limit for the velocities, but, clearly, in a real GC, the Maxwellian must be truncated at the escape velocity of the cluster. Realistic dynamical models that well represent the GC structure are the King models (King 1966), which distribution function can be written as:

$$f(E) = \begin{cases} C(e^{-\frac{E}{\sigma^2}} - 1) & \text{if } E < 0; \\ 0 & \text{if } E \geq 0. \end{cases} \tag{1.4}$$

where σ is the velocity dispersion and E is the energy per unit mass:

$$E = \frac{v^2}{2} + \Psi(r) \tag{1.5}$$

where $\Psi(r)$ is the mean potential. GCs move in the gravitational potential of our Galaxy, therefore, at a certain radius from the center of the cluster, the Milky Way gravitational potential becomes predominant with respect to the one of the GC itself. Therefore, a truncation (or tidal) radius (r_t) is defined as the radius beyond which stars are not bound anymore to the cluster. The potential Ψ is defined so that $\Psi(r_t) = 0$. In Figure 1.1, for representation purposes, we show some King models with different r_t.

The King model family has a characteristic scale length, usually called King radius and defined as:

$$r_K = \sqrt{\frac{9\sigma^2}{4\pi G \rho_0}} \tag{1.6}$$

The concentration parameter, defined as:

$$c = \log\left(\frac{r_t}{r_c}\right) \tag{1.7}$$

univocally determines the shape of the profile. This is shown in Figure 1.1, where each curve is labelled with its own value of c, ranging from 0.5 to 2.5.

Other characteristic quantities of GCs are: the core radius, r_c, i.e., the distance from the center at which the surface brightness is equal to half of its central value[1];

[1]Note that the core radius and the King radius have similar values (especially for the most concentrated systems), but they should not be confused because they represent different quantities.

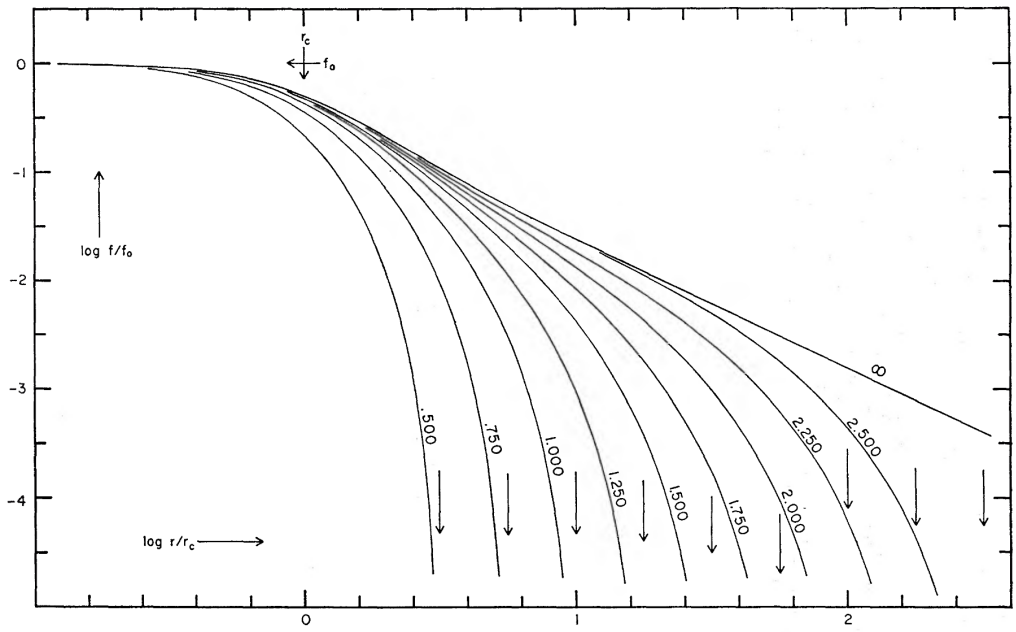

FIGURE 1.1: Some examples of King models. The distance from the center, normalized to the King radius and in logarithmic units, is on the x-axis, while the surface brightness, normalized to its central value and in logarithmic units, is on the y-axis. The vertical arrows at the bottom right show the positions of the truncation radius for each of the represented model. Taken from King (1966).

the half-mass radius $r_{\rm hm}$, i.e., the distance from the center that includes half the total mass; the half-light radius $r_{\rm hl}$, i.e., the distance from the center that includes half the total luminosity. A parameter that quantifies how closely packed stars are in a GC is the central luminosity density ρ_0, expressed in $L_\odot/pc^3$.

1.2.1 Phases of GC dynamical evolution

GC dynamical evolution can be divided into three main phases, which we describe in this Section.

GCs first experience a phase of early evolution that lasts a few Myr, mainly dominated by the effect of stellar evolution. This phase is characterized by the expulsion of the residual primordial gas, from which the cluster itself was born, due to the winds from massive stars and Type II supernovae explosions, leading in some cases to the disruption of the system (see, e.g., Applegate 1986; Chernoff and Shapiro 1987; Chernoff and Weinberg 1990; Fukushige and Heggie 1995; Portegies Zwart et al. 1998). Due to the significant and irregular mass loss, the gravitational potential of the system can change with a timescale shorter than the crossing time. This induces the so-called violent relaxation, first studied by Lynden-Bell (1962, 1967), Hénon (1964) and King (1966). During this phase, energy is redistributed without encounters between stars, because the variations of the potential directly change the orbits of the stars.

After this early, stellar evolution driven phase, GCs can be modeled, e.g., with King profiles (see Equation 1.4) and their dynamical evolution is dominated by two-body encounters. During this phase, the cluster can still lose mass: due to the energy exchanges between stars, which lead the system towards a state of energy equipartition, lighter stars can gain a velocity high enough to escape the potential of the

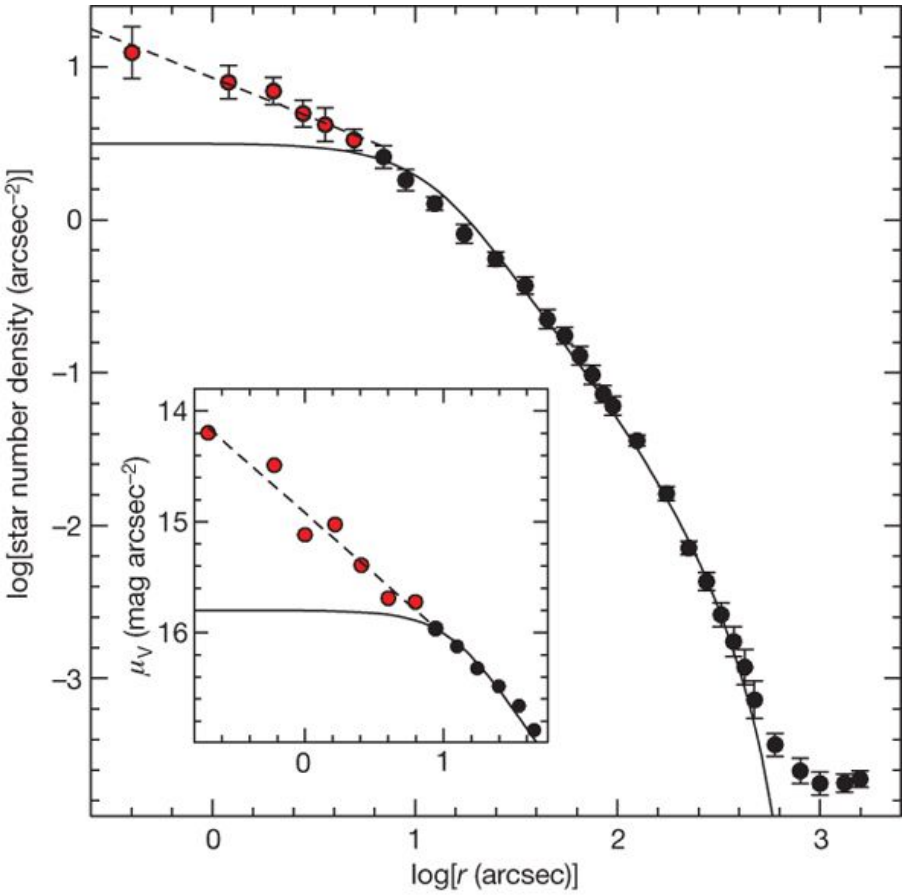

FIGURE 1.2: Black and red circles: density profile of M30, a post-CC GC. The solid black line is the best-fit King profile (excluding the most central points, $r < 5''$), and the dashed black line is a power-law with slope -0.5, which well fits the central region of the density profile that clearly deviates from a King profile. Taken from Ferraro et al. (2009).

cluster. This phenomenon is usually called evaporation. Evaporation is stronger if an external tidal field is present, rather than for isolated clusters (e.g., Giersz and Heggie 1994; Meylan and Heggie 1997; Vesperini and Heggie 1997; Aarseth and Heggie 1998; Takahashi and Portegies Zwart 2000; Gieles, Heggie, and Zhao 2011; Madrid et al. 2017).

At the same time, heavier stars slow down due to dynamical friction, moving toward more internal orbits. This process is called mass segregation. The overall result of this energy redistribution is a stratification of stars with different masses, with heavier stars placed preferentially in the central regions and progressively lighter stars at larger and larger distances from the center. The level of dynamical evolution of the system can therefore be traced observationally by the radial distribution of heavy objects, like Blue Straggler Stars (see Section 1.3 for an extended explanation), which is the main goal of this Thesis.

As the transfer of kinetic energy from more massive to less massive stars proceeds, the cluster core as a whole (where massive stars progressively sink) loses kinetic energy. Therefore, for the Virial Theorem, the core contracts. This phenomenon is called core-collapse (CC) and it is self-sustained, because, as the system contracts, stellar encounters become more frequent and the "flow" of kinetic energy from the core to the envelope increases (see, e.g., Hénon 1961; Lynden-Bell and Wood 1968, and also the reviews by Meylan and Heggie 1997; Heggie and Hut 2003). Therefore,

in absence of energy sources in the core, this process would lead in a finite time to a diverging central density. However, the presence of binary systems (both primordial and dynamically formed) provide the energy needed to arrest the CC. When a star interacts with a tight binary system, the binary system shrinks and releases energy to the cluster, contrasting the collapse. From the observational point of view, CC substantially modifies the density profile of a GC, because the central density significantly increases. Differently from the "King model" clusters, which have a flat density profile in the central region, core collapsed cluster show a power-law shaped cusp in the center, typically observable in the innermost $5'' - 10''$ (e.g., Meylan and Heggie 1997; see Figure 1.2 for an example). According to the Harris catalog (Harris 1996), more than 15% of the GCs known in our galaxy are classified as post-CC clusters.

1.3 Blue Straggler Stars

The intense dynamical activity and the repeated interactions between stars in GCs allow the formation of numerous exotic objects, i.e., objects that can not be explained by considering only the standard stellar evolution of a single star. The main exotica that can be found in GCs are millisecond pulsars, cataclysmic variables (CVs), low mass X-ray binaries, and Blue Straggler Stars (BSSs). The formation of exotica is strongly influenced by the formation and evolution of binary systems, and their interaction with other stars in the cluster. Therefore, the study of exotica is a powerful tool to probe the internal dynamics of GCs and their influence on stellar evolution.

In this Thesis, we focus our attention on BSSs. They are a peculiar group of stars that lies along an extrapolation of the main sequence (MS) in the color-magnitude diagram (CMD) of a stellar population, placed at brighter magnitudes and bluer colours with respect to the turn-off (TO) point of the population (see Figure 1.3). BSSs were discovered by Alan Sandage in 1953 in the GC M3 (Sandage 1953) and have been studied in numerous works thereafter (e.g., Ferraro, Fusi Pecci, and Buonanno 1992; Ferraro et al. 1993, 1997, 2004, 2018b; Piotto et al. 2004; Lanzoni et al. 2007a,b; Leigh, Sills, and Knigge 2007; Dalessandro et al. 2008; Moretti, de Angeli, and Piotto 2008; Beccari et al. 2011, 2012; Simunovic and Puzia 2016).

BSSs are easy to distinguish from the other cluster populations, given their distinctive position in the CMD; however, some caution must be used when constructing complete samples of BSSs. At optical wavelengths, cool, giant stars are significantly brighter than BSSs and can thus hamper the proper detection of BSSs. However, we can solve this problem by shifting our observation to the ultraviolet (UV) band, where BSSs are brighter because of their higher temperature. This point will be largely discussed in Chapter 3.

The position of BSSs in the CMD is anomalous, if we consider only standard, single star evolution, and it suggests that BSSs are more massive than TO stars. Their higher mass, with respect to the TO, has been confirmed by some mass measurements (see Chapter 2 in this Thesis, and Shara, Saffer, and Livio 1997; Gilliland et al. 1998; Ferraro et al. 2006; Fiorentino et al. 2014; Baldwin et al. 2016), using methods based on spectral energy distribution (SED) or spectra fitting with theoretical models, pulsational properties, or kinematics.

BSSs essentially mimic a younger population, but any recent star formation event can be safely excluded in GCs. Therefore, in order to explain the presence of BSSs in GCs, we need to take into account formation mechanisms that are able to increase the stellar mass of a "normal" star.

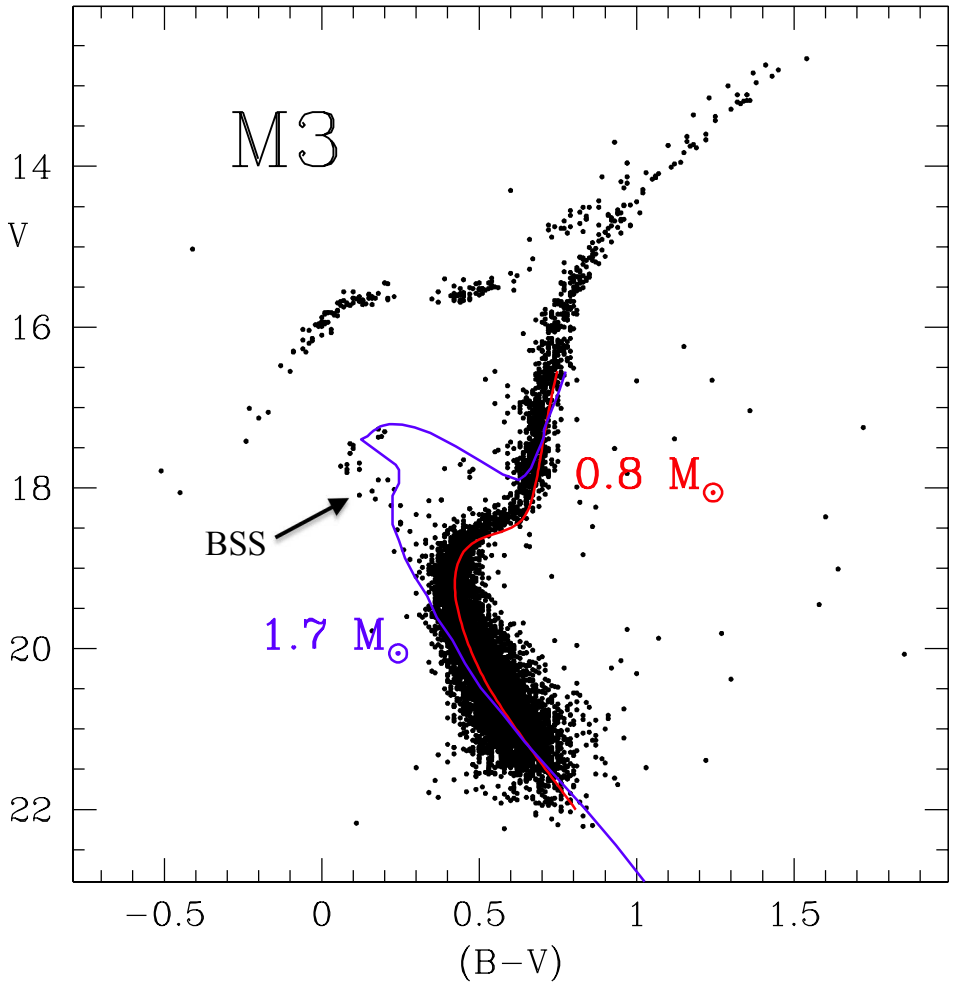

FIGURE 1.3: CMD of M3, taken from Ferraro et al. (2015). The region where BSSs lie is marked by the arrow. As a reference, the authors plotted two evolutionary tracks, corresponding to a 0.8 $M_\odot$ and a 1.7 $M_\odot$ star (red and blue line, respectively). As can be seen, the red line reproduces quite well the "normal" evolutionary sequence of the cluster, while the blue line crosses the BSS region of the CMD.

1.3.1 BSS formation mechanisms

Two main mechanisms have been proposed to explain the formation of BSSs, both involving two stars as progenitors. They are: mass transfer in binary systems, generating mass transfer BSSs (MT-BSSs, McCrea 1964), and direct collisions between stars, generating collisional BSSs (COL-BSSs, Hills and Day 1976).

The MT mechanism involves stars in binary systems, in which one of the stars gains mass from the companion. The MT in binary systems starts when one of the two stars fills its Roche lobe[2]. This can happen with a higher probability during the Sub-Giant Branch (SGB), Red Giant Branch (RGB) and Asymptotic Giant Branch (AGB) phases, when the star naturally expands. Moreover, the frequent interactions between stars in GCs can modify the binding energy between the components of the binary system, modifying the distance between them. When the distance between

[2]In a binary system, the Roche lobe is the surface that delimits the region where the material is gravitationally bound to each component.

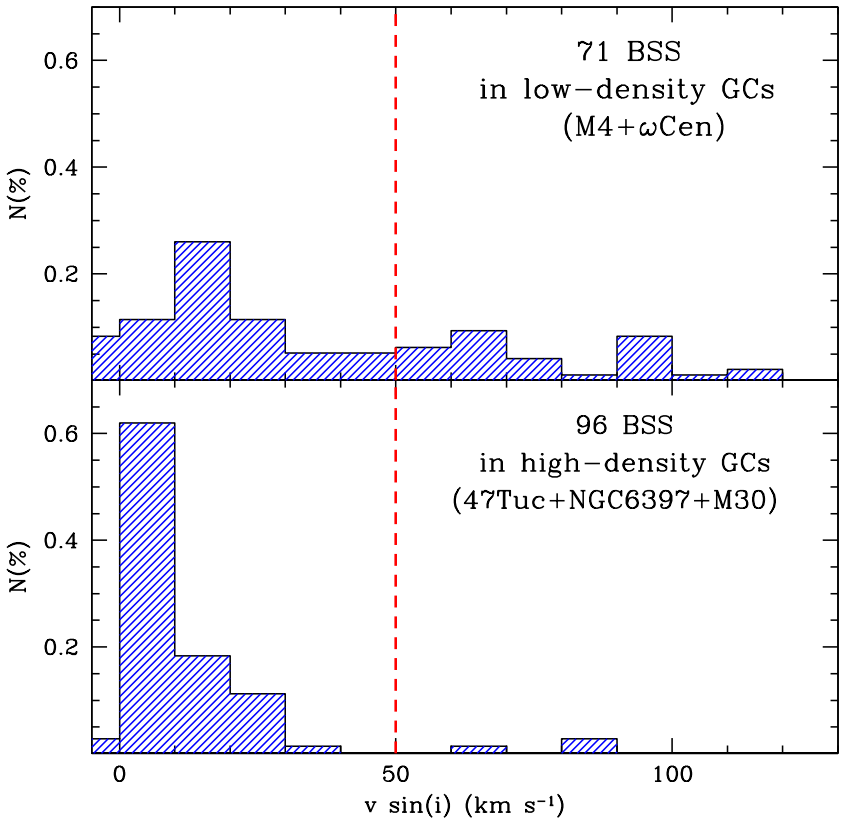

FIGURE 1.4: Number of BSSs with a given rotational velocity, in low density GCs (upper panel) and in high density GCs (lower panel). Taken from Ferraro et al. (2015).

the two components is reduced, the Roche lobe becomes smaller, therefore, sometimes the MT process can start also when a star is along the MS. The shrinking of the system can also lead to the coalescence of the two components: the two stars merge, both the envelopes and the nuclei, becoming essentially a new, single star. Also the loss of angular momentum, in some cases enhanced by stellar winds (Vilhu 1982), can lead to a progressive shrinking of the system until the the coalescence of the two components. Therefore, the formation of MT-BSSs depends mainly on the fraction and evolution of binary systems, and on stellar evolution.

COL-BSSs form directly from collisions between single stars. In dense environments like GCs, collisions between stars are favored, with respect to the galactic environment, where the probability of a collision is roughly equal to zero. In GCs, about 10% of the stars have experienced or will experience a collision during its lifetime (Davies 2015). The formation of COL-BSSs therefore depends on the rate of collision in GCs, which in turn depends on the cluster density.

In general, we expect to find both MT-BSSs and COL-BSSs in the core of GCs, while in the external regions, where the density is lower, we expect to find mainly MT-BSSs, due to the lower probability of collisions. We also expect to find COL-BSSs more likely in denser clusters, where collisions are favored, while low density environments should preferentially host MT-BSSs. However, it is very difficult to distinguish a MT-BSS from a COL-BSS. We expect, in general, MT-BSSs to be fast rotators. Indeed, Lovisi et al. (2010, 2012) observed that the fraction of fast rotating BSSs is higher in low density systems, where we expect a higher fraction of MT-BSSs (see Figure 1.4). On the contrary, COL-BSSs might not show high rotational

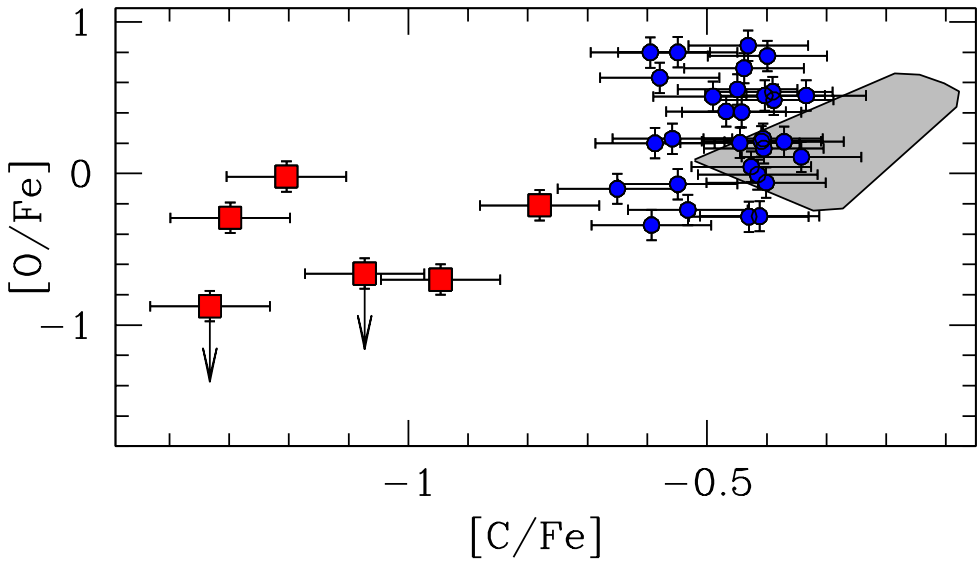

FIGURE 1.5: O and C abundances of a sample of BSSs in 47 Tuc. The C and O depleted BSSs are in the low left corner. Taken from Ferraro et al. (2015).

velocities, because of the effect of magnetic braking or disk locking (Benz and Hills 1987; Leonard and Livio 1995; Sills, Adams, and Davies 2005).

From the point of view of chemical abundances, we expect to find anomalies on the surface of MT-BSSs of elements that are processed in the donor star during the CNO cycle (Sarna and De Greve 1996). On the contrary, simulations have shown that COL-BSSs should not have significant chemical anomalies on their surface, because the mixing between the nuclei and envelopes of the colliding stars should be small (Lombardi, Rasio, and Shapiro 1995). A few BSSs in the globular cluster 47 Tucanae show a depletion of C and O, with respect to similar stars in the sample (Ferraro et al. 2006, see Figure 1.5). This characteristic could be a result of the CNO processed material transferred from the inner regions of the donor star, identifying these BSSs as MT-BSSs.

1.4 BSSs as tracers of the dynamical evolution of GCs

As already mentioned, GGCs have roughly the same chronological age. However, the dynamical evolution can be significantly different in different GCs, since it depends on the structural parameters of the cluster itself. Therefore, GCs with the same chronological age, can have very different "dynamical ages". In particular, as the dynamical evolution proceeds, the most massive stars progressively sink toward the cluster center, due to the effect of dynamical friction (see Section 1.2).

BSSs are the ideal test particles to probe the internal dynamical evolution, because, as already mentioned, they are more massive than the other luminous stellar populations, and they are quite bright; with the appropriate observational setup, they are rather easy to observe (see Chapter 3 for details).

1.4.1 BSS radial distribution and the "dynamical clock"

The radial distribution of BSSs is a very powerful tool to trace the dynamical evolution of GCs. Ferraro et al. (2012) analyzed the BSS radial distribution in 21 GGCs,

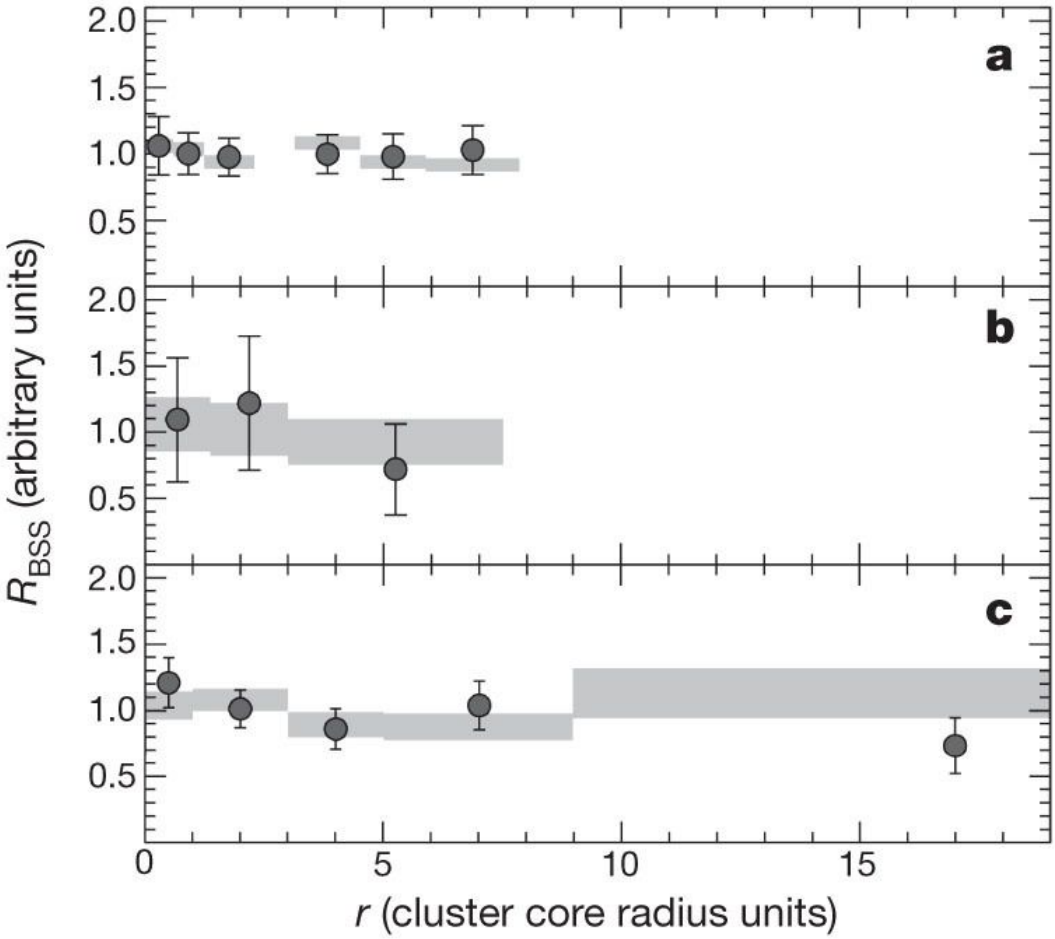

FIGURE 1.6: Radial distribution of the double normalized ratio of BSSs (grey circles) and of a reference population (grey bands), for Family I clusters. Panel (a): ω Centauri; panel (b): Palomar 14; panel (c): NGC 2419. Taken from Ferraro et al. (2012).

using the *double-normalized ratio* $R_{\rm BSS}(r)$, defined in Ferraro et al. (1993), as:

$$R_{\rm BSS}(r) = \frac{N_{\rm BSS}(r)/N_{\rm BSS,tot}}{L_{\rm sampl}(r)/L_{\rm sampl,tot}} \tag{1.8}$$

where $N_{\rm BSS}(r)$ is the number of BSSs in a given radial bin, $N_{\rm BSS,tot}$ is the total number of BSSs, $L_{\rm sampl}(r)$ is the sampled luminosity in the same radial bin, and $L_{\rm sampl,tot}$ is the total sampled luminosity. Hereafter, we will refer to the BSS radial distribution measured with the double normalized ratio as "BSS normalized radial distribution" (BSS-nRD). They compared the BSS-nRD thus obtained with the same quantity measured for a reference, post-MS population of lighter stars. Such a reference population is expected to have $R_{\rm pop} = 1$ (Renzini and Buzzoni 1986), because post-MS population are distributed as the cluster light. They expressed the distance from the center in units of core radii, in order to directly compare different clusters.

All the clusters studied in Ferraro et al. (2012) have an age of $\sim 12 - 13$ Gyr, with the only exception of Palomar 14, which is ~ 10.5 Gyr old, but they have different structural properties, therefore they are expected to be in different stages of dynamical evolution.

Indeed, the authors found that the 21 GGCs can be grouped in three families,

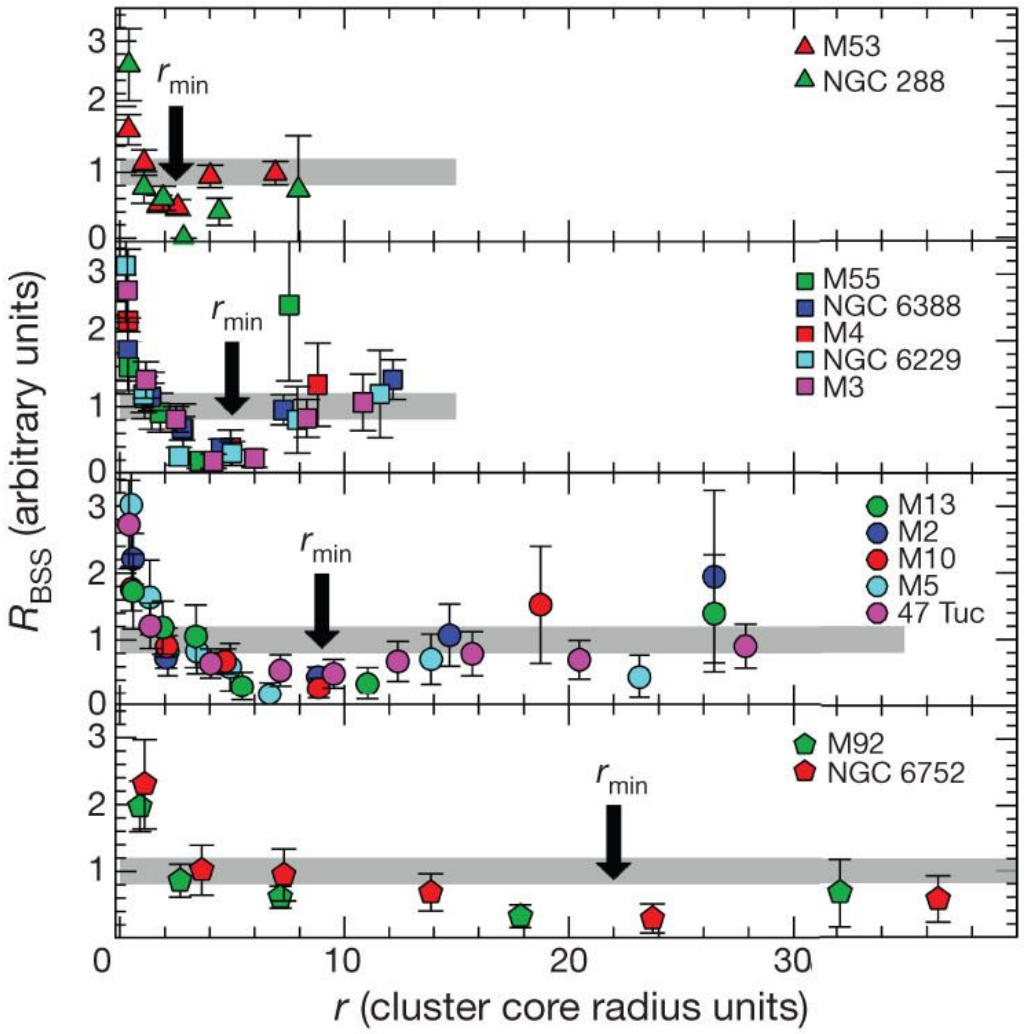

FIGURE 1.7: BSS-nRD (colored triangles, squares, circles and pentagons; see legend), compared to that of a reference population (grey bands), for Family II clusters. The four panels represents four sub-families, grouped on the basis of the position of the minimum of the BSS-nRD, at increasing distance from the cluster center (from top to bottom). Taken from Ferraro et al. (2012).

based on the shape of their BSS-nRDs. In the first family (Family I), BSSs and the reference population have the same normalized radial distribution, and both R_{BSS} and R_{pop} are thus constant and equal to 1 (see Figure 1.6). In the second family (Family II), the BSS-nRD is clearly different from the one of the reference population. The BSS-nRD has a bimodal behaviour, with a central maximum, then a minimum followed by a rising branch. Family II clusters are shown in Figure 1.7, where they are grouped in four sub-families, ordered on the basis of the position of the minimum of the distribution, at progressively larger distances from the center (from the top to the bottom panel). In the third and last family (Family III, see Figure 1.8), they grouped again clusters with a BSS-nRD significantly different from the one of the reference population. In this family, however, differently from Family II, the BSS-nRD is unimodal, showing only the central peak and no sign of an external rising branch, not even in the outermost region of the cluster.

Ferraro et al. (2012) conclude that the main responsible for the changes in the

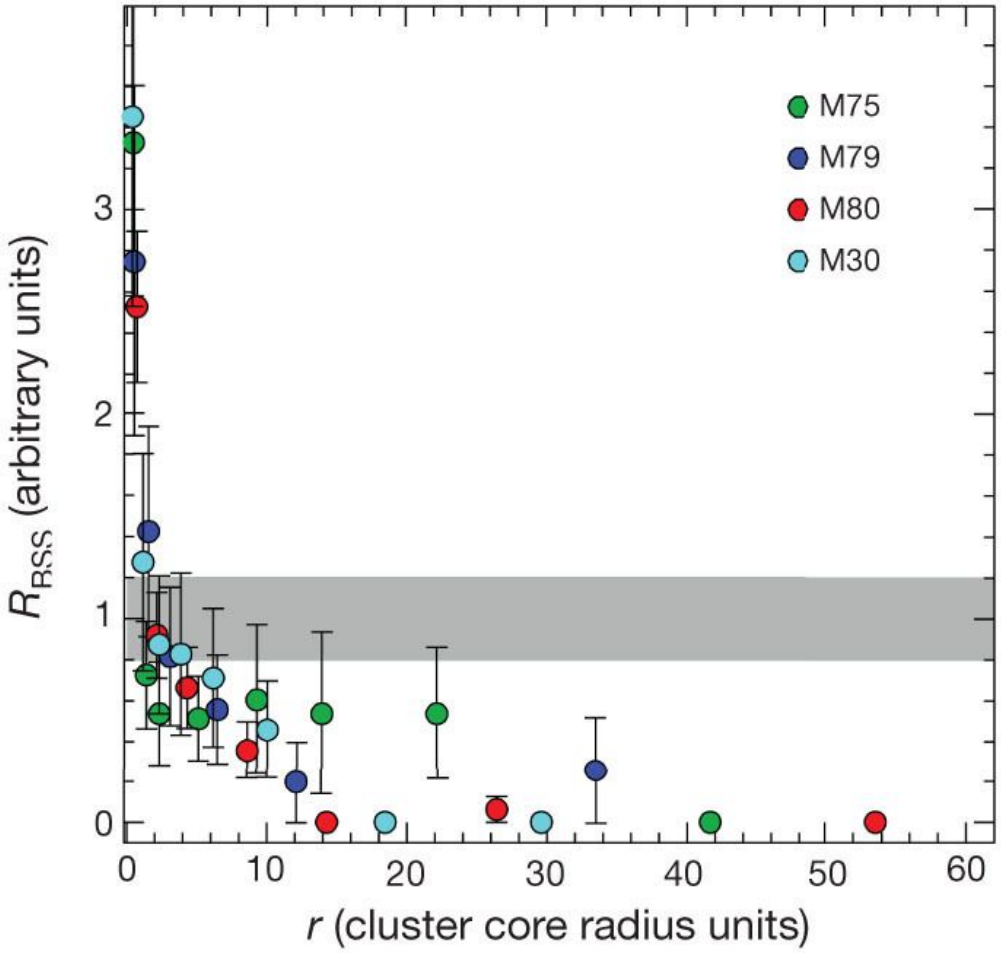

FIGURE 1.8: BSS-nRD (colored circles), compared to that of a reference population (grey bands), for Family III clusters. Taken from Ferraro et al. (2012).

BSS-nRD is dynamical friction (see also Mapelli et al. 2004; Mapelli et al. 2006). Dynamical friction primarily depends on the reciprocal of the local density (rather than the BSS mass and the velocity dispersion; Alessandrini et al. 2014), therefore its efficiency decreases for increasing distance from the center. As a function of time, massive objects at progressively larger distances from the center move toward the innermost region. As a consequence, a central peak in the BSS-nRD and a BSS-depleted region (hence a minimum in the radial distribution) appear. The position of the minimum corresponds to the most external regions in which dynamical friction has been efficient, and it moves outwards as a function of the dynamical evolution of the system.

Consequently, in this scenario the three families described above (Figures 1.6, 1.7, and 1.8) are ordered by increasing dynamical age. Family I GCs are dynamically unevolved systems, in which dynamical friction has not shaped yet the BSS-nRD, at any distance from the center. Family II GCs are in an intermediate state of dynamical evolution, in which dynamical friction has been efficient within a given distance from the center, which corresponds to the minimum of the BSS-nRD. Indeed, beyond the minimum position, the BSS distribution is not different from the one of the reference population, meaning that in those regions dynamical friction has not yet affected the BSS-nRD. The four panels of Figure 1.7 are therefore ordered by increasing dynamical age, because the position of the minimum is at progressively

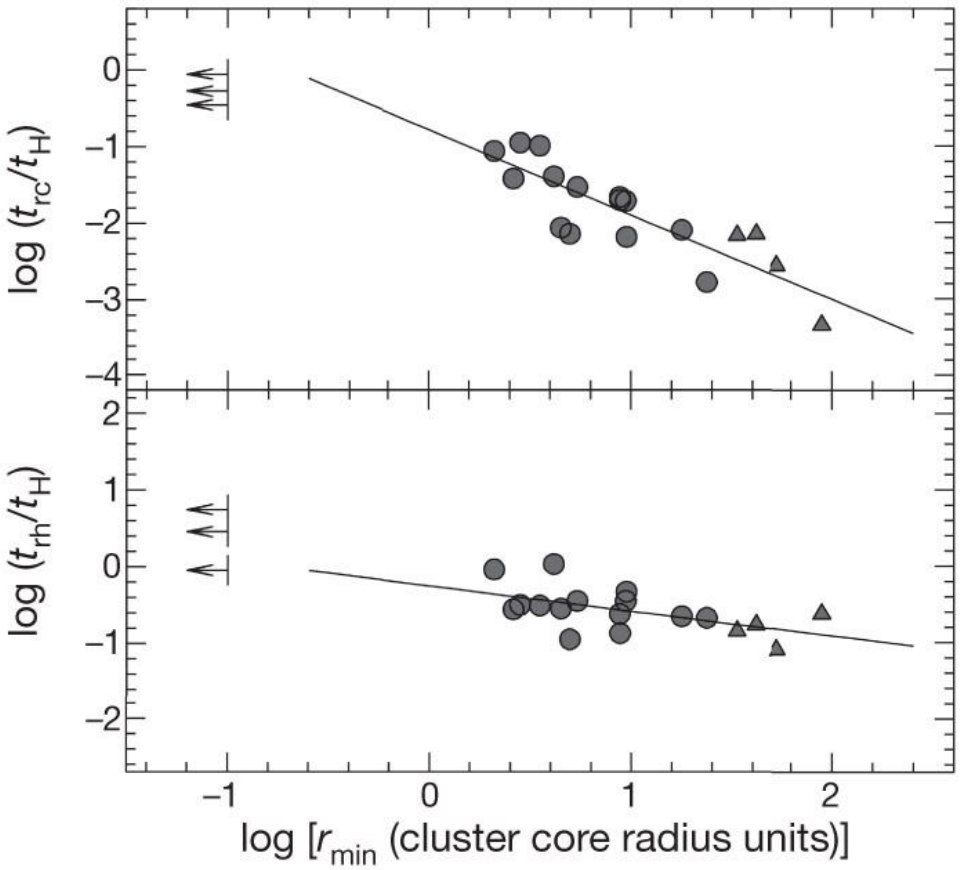

FIGURE 1.9: Upper panel: t_{rc} as a function of r_{min}. Lower panel: t_{rh} as a function of r_{min}. The relaxation times are normalized to the Hubble time, while r_{min} is expressed in core radius units. Family I clusters, in which no minimum can be detected, are shown as lower limit arrows. Family II clusters are represented as grey circles, and Family III clusters as grey triangles. For Family III clusters, r_{min} is the distance of the furthermost bin where no BSSs were found. Taken from Ferraro et al. (2012).

larger distances from the center. Family III GCs represent the most advanced phase of dynamical evolution. Dynamical friction has affected the whole extension of the cluster, hence BSSs at all distances from the center have moved toward the center. For this reason, the BSS-nRD has a monotonic behavior, constantly decreasing from the center to the external regions.

Hence, the shape of the BSS-nRD, and particularly the position of the minimum, works like a clock hand able to measure the dynamical age of GCs, which Ferraro et al. (2012) defined "dynamical clock". The reliability of this dynamical clock has been confirmed by the presence of a tight anti-correlation between the position of the minimum and both the central relaxation time and the half-mass relaxation time (t_{rc} and t_{rh}), shown in Figure 1.9. The presence of this anti-correlation shows that GCs with a larger r_{min} have lower relaxation times.

1.4.2 Refining the dynamical clock

The dynamical clock described in the previous section has been fundamental in showing the importance of BSSs and their radial distribution as tracers of GC internal dynamics. However, the position of the minimum (r_{min}) of the BSS-nRD, measured with the double normalized ratio (see Equation 1.8), is precisely defined only

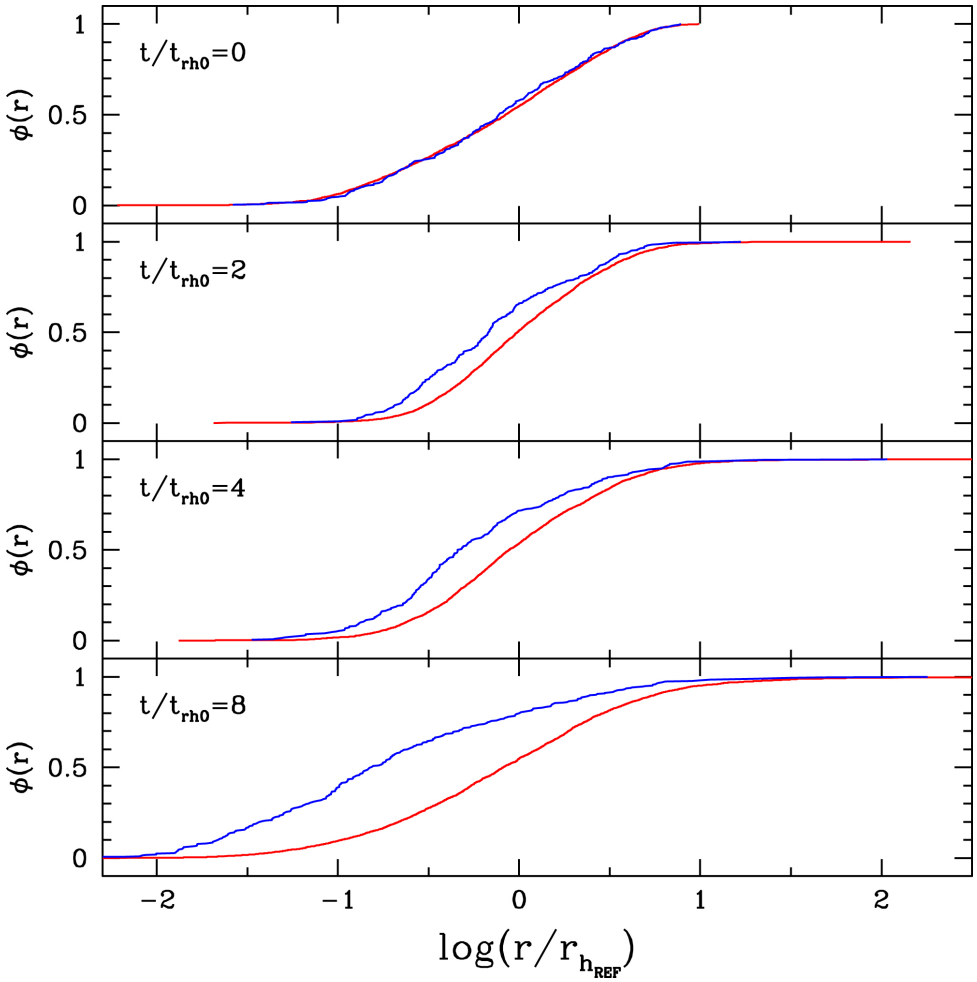

FIGURE 1.10: Evolution of the cumulative radial distributions of BSSs (blue line) and REF population (red line), as a function of time (from top to bottom). Taken from Alessandrini et al. (2016).

for Family II clusters. Instead, in Family I GCs, $r_{\rm min}$ has not yet developed, because dynamical friction has not affected yet even the most central BSSs, while in Family III clusters dynamical friction has completely shaped the BSS-nRD, and the position of the minimum corresponds to the outermost bin where no BSSs can be found. Also, the determination of $r_{\rm min}$ requires some assumptions on the radial binning of the observational sample. These assumptions are somehow arbitrary and can erase the feature, if the bins assumed are too wide, or can critically increase the noise of the distribution if the bins are too narrow. From the point of view of simulations, both N-body and Monte Carlo, it is difficult to reproduce the observed shape of the BSS-nRD. While a central peak develops, the bimodal distribution with the presence of $r_{\rm min}$ does not develop or appears to be unstable (see, e.g., Miocchi et al. 2015; Hypki and Giersz 2017; Sollima and Ferraro 2019).

For these reasons, it is necessary to define a new indicator that does not suffer from these drawbacks. Alessandrini et al. (2016) used a set of 10^5 particle N-body simulations to study the evolution of the BSS cumulative radial distribution, which by definition does not depend on binning. Their results are shown in Figure 1.10. They compared the BSS cumulative radial distribution (blue line) with the one of a reference (REF) population of lighter stars (red line), as a function of the evolutionary time. In their simulations, they assume no initial mass segregation, therefore

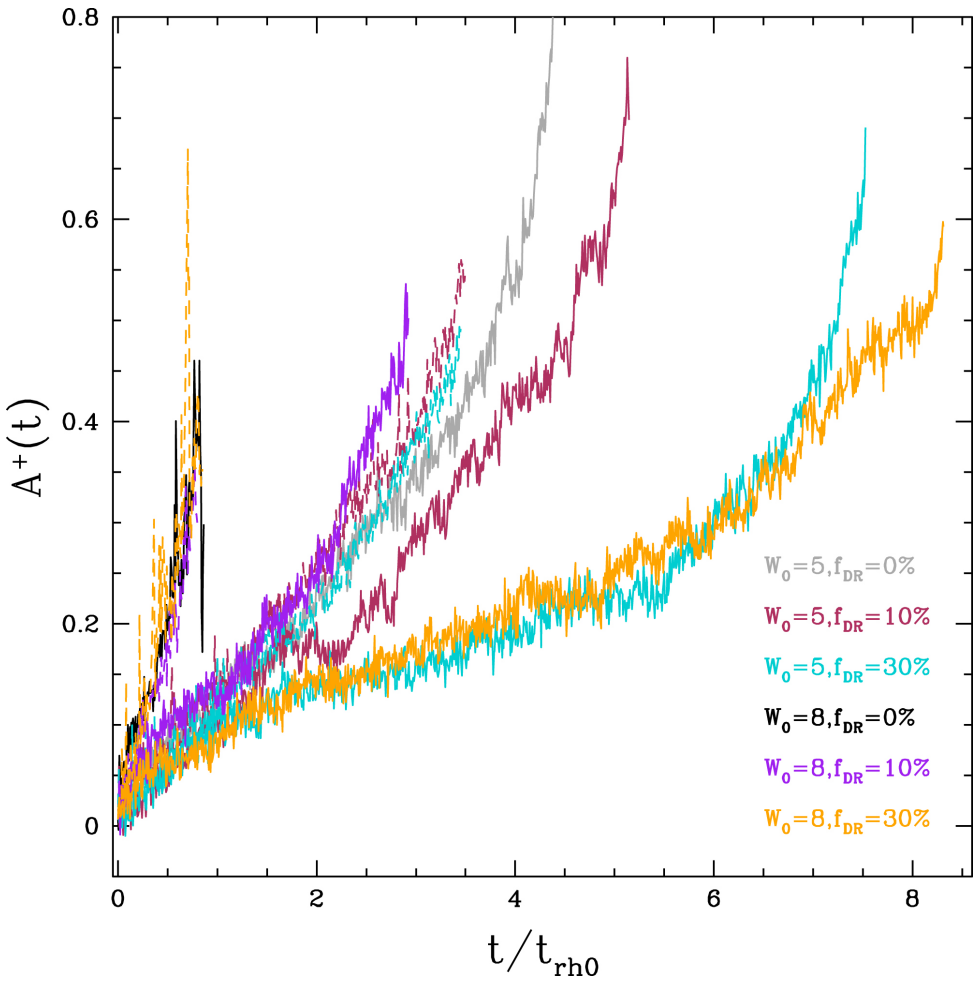

FIGURE 1.11: Evolution of the A^+ parameter as a function of time. Different colors corresponds to different parameters of the simulation (see legend within the Figure). Clearly, regardless of the initial conditions of the simulation, A^+ increases with time. Taken from Alessandrini et al. (2016).

the two populations are perfectly mixed at the beginning (see the upper panel of Figure 1.10). Afterwards, BSSs start to accumulate toward the central region of the cluster, due to the effect of dynamical friction, therefore the two cumulative distributions progressively separate, as it can be seen in the lower panels of Figure 1.10.

Therefore, the separation between the BSS and REF cumulative radial distribution (i.e., the area enclosed between the two curves) appears to be a reliable indicator of dynamical evolution. Hence, they defined a new parameter, called A^+, corresponding to the area between the two curves, as follows:

$$A^+(x) = \int_0^x \Big[\Phi_{\rm BSS}(x') - \Phi_{\rm REF}(x')\Big] dx' \tag{1.9}$$

where $\Phi_{\rm BSS}$ and $\Phi_{\rm REF}$ are the cumulative radial distribution of BSSs and of the REF population, respectively. The clustercentric distance, normalized to the half-mass radius $x = \log(r/r_{\rm h})$ is defined in logarithmic units, in order to maximize the sensitivity to the central regions, where most BSSs accumulates due to dynamical friction.

When the two population are perfectly mixed, $A^+ = 0$, then A^+ is expected to increase as the BSS segregation proceeds. Indeed, Alessandrini et al. (2016) show that A^+ increases with time, regardless of the particular initial conditions of the

simulations (see Figure 1.11), qualifying it as a good and sensitive indicator of BSS segregation.

In Chapter 3, we will study A^+ from the observational point of view, comparing it to the previous dynamical "clock-hand" ($r_{\rm min}$) and testing its reliability as dynamical age indicator. We will also show that a high completeness of the BSS sample is fundamental to obtain a reliable A^+ measurement, and this can be achieved by adopting an "UV-driven" approach in the data reduction process.

Chapter 2

Physical properties of BSSs in the core of 47 Tucanae from SEDs

Mainly based on:
Raso et al. (2019), ApJ, 879, 56

2.1 Introduction

As already explained in Section 1.3, BSSs are powerful indicators of GC internal dynamics (see also Chapter 3; Ferraro et al. 2012, 2018b; Lanzoni et al. 2016). This is because they are significantly more massive ($M_{BSS} \sim$ 1.2-1.3$M_{\odot}$) than the average stellar mass in GCs ($\langle m \rangle \sim 0.4M_{\odot}$), and they are therefore subject to dynamical friction, which makes them sink toward the cluster center (e.g., Mapelli et al. 2004, 2006). A detailed analysis of the BSS sedimentation process as dynamical probe, the tools that we use to measure it and its importance is carried out in Chapter 3. In this respect, however, an accurate knowledge of the BSS mass distribution is of paramount importance for a precise estimate of the BSS sedimentation timescale, thus allowing an accurate calibration of these empirical tools.

However, in spite of their importance, BSS masses have been determined only for a few BSSs per clusters (e.g., Shara, Saffer, and Livio 1997; Gilliland et al. 1998; De Marco et al. 2005; Fiorentino et al. 2014). These sparse measurements have helped to confirm that BSSs are indeed more massive than MS stars. However, systematic studies aimed at obtaining direct mass estimates for large samples of BSSs, covering the entire extension of the sequence, have been still unavailable due to observational difficulties.

BSS mass measurements can be obtained spectroscopically (e.g., Shara, Saffer, and Livio 1997; De Marco et al. 2005; see also the recent estimate of the mass of an evolved BSS in 47 Tucanae by Ferraro et al. 2016), from pulsational properties (e.g., Gilliland et al. 1998; Fiorentino et al. 2014), or through SED fitting (e.g., Knigge et al. 2006, 2008; in the latter case, also combined with far-ultraviolet, hereafter FUV, spectroscopy). All these methods require specifically designed observations and techniques: spectroscopic observations must deal with serious crowding issues in the dense environment of GCs, especially in their cores; variability and SED-based studies require *ad hoc* datasets (time-series photometry for the former, and photometry in a large number of filters for the latter), both of which are rarely available in the archives.

The GC 47 Tucanae (47 Tuc, NGC 104) is a notable exception, since it has been intensively studied over the years and has also been used as a calibration field for different *Hubble Space Telescope* (*HST*) instruments. Therefore, a large and multi-band

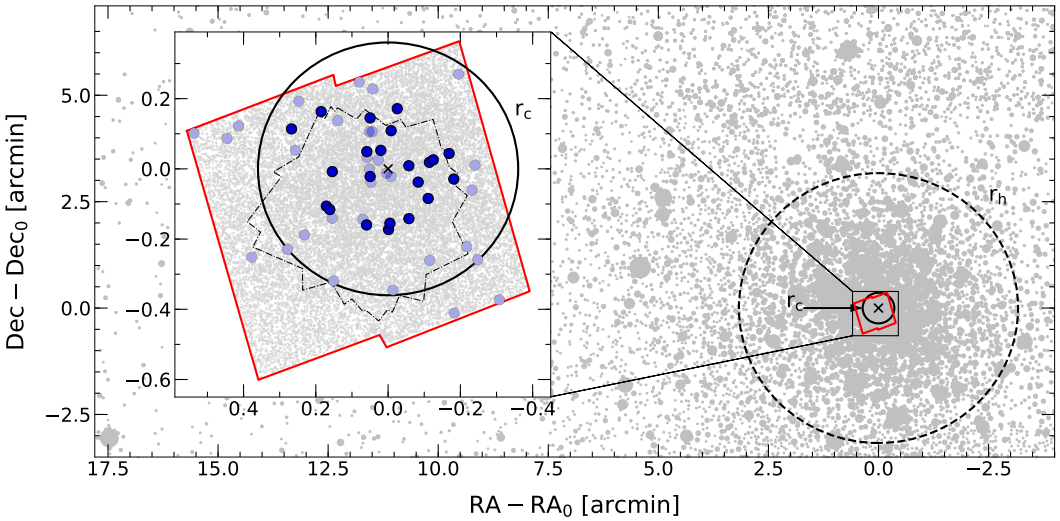

FIGURE 2.1: Map of the 47 Tuc region analyzed in this work. Positions are in arcmin, with respect to the cluster center (small black cross). The solid and dashed circles represent the core and half-light radius of the cluster, respectively, from Harris (1996). The red contour marks the FOV of the ACS/HRC dataset used in this work. In the inset on the left, we zoom in the ACS/HRC FOV. The dotted-dashed contour marks the FOV where the time baseline is long enough to measure PMs. The dark blue circles represent the BSSs that survived our selections (as described in Section 2.3.1), while the light-blue circles are all the remaining BSSs detected within the FOV.

set of images of the core of 47 Tuc is publicly available (see Section 2.2 for a detailed description of the dataset). In this Chapter, we use the Advanced Camera for Surveys (ACS) High Resolution Channel (HRC) images in this dataset to construct broad (extending from 2000 to 8000 Å) SEDs for a sample of 22 BSSs, distributed along the entire extent of the BSS sequence in 47 Tuc. We used these SEDs to derive BSS physical properties (such as luminosities, masses, radii, etc.).

2.2 Dataset and data reduction

The innermost region of 47 Tuc was used as calibration field for the ACS/HRC, e.g., to study flat-field stability and geometric distortion. For this reason, a large photometric dataset is available in the *HST* archive for this region of the sky, which has been repeatedly observed throughout the years of operation of the ACS/HRC (2002-2007). From the archive, we selected all images obtained through broadband filters, which range from the near UV to the near infrared (approximately, from 2000 Å to 8000 Å), thus covering the whole spectral extension of a typical BSS. The total field of view (FOV) covered by this dataset is shown in Figure 2.1 (red contour), compared to the core and half-light radii of the cluster (0.36′ and 3.17′, respectively; Harris 1996). In Table 2.1 we list the images used for this study; our final dataset consists of 285 images. Nearly the same data were used by Knigge et al. (2006, 2008) to study exotic objects such as CVs, white dwarfs (WDs) and BSSs. In particular, physical parameters of three BSSs were obtained from spectra and SED fitting. We compare their results with ours in Section 2.4.3.

The photometric reduction was performed on the `_flt` exposures, because the un-resampled pixel data for stellar profile fitting is preserved. We followed the procedures described in Bellini et al. (2017b, 2018), which we briefly summarize in the

TABLE 2.1: List of *HST* ACS/HRC observations of 47 Tuc used in this work.

Program ID	PI	Epoch (yyyy/mm)	Filter	Exposures N × t_{exp}
9019	R. Bohlin	2002/04	F220W	21 × 170 s
			F330W	18 × 66 s
			F435W	2 × 5 s, 2 × 20 s, 17 × 60 s, 2 × 300 s
			F475W	10 × 60 s
			F555W	14 × 60 s
			F606W	10 × 60 s
			F625W	10 × 60 s
			F775W	13 × 60 s
			F814W	2 × 5 s, 2 × 20 s, 14 × 60 s
9028	G. Meurer	2002/04	F475W	40 × 60 s
9443	I. King	2002/07	F250W	1 × 230 s, 1 × 460 s
			F330W	1 × 350 s
			F435W	1 × 350 s
			F475W	20 × 60 s
9662	R. Gilliland	2002/09	F606W	2 × 1 s
10055	J. Biretta	2004/02	F250W	2 × 50 s
			F330W	2 × 40 s
			F435W	2 × 20 s
			F606W	2 × 10 s
			F775W	2 × 10 s
10375	J. Mack	2004/12	F435W	4 × 60 s
		2005/03	F475W	4 × 60 s
		2005/06	F555W	4 × 60 s
		2005/10	F606W	4 × 60 s
			F625W	4 × 60 s
			F775W	4 × 60 s
			F814W	4 × 60 s
10737	J. Mack	2006/03	F330W	2 × 66 s
		2006/05	F435W	6 × 60 s
		2006/07	F475W	6 × 60 s
			F555W	6 × 60 s
			F606W	6 × 60 s
			F625W	6 × 60 s
			F775W	6 × 60 s
			F814W	6 × 60 s

following.

First, we performed one-pass photometry on the images. This consisted of a single finding procedure without neighbour subtraction. For this step, we determined a spatially variable point-spread function (PSF) model from each individual exposure by examining the residuals from the fit of an empirical library PSF (see Anderson and King 2004) to the bright, relatively isolated, unsaturated stars in that exposure. We then used this tailor-made PSF to measure stellar positions and fluxes in each exposure. We corrected stellar positions for geometric distortion using the distortion solutions provided by Anderson and King (2004).

Since we are focusing on the central, most crowded regions of the cluster, we secondly used a multi-pass photometric procedure, which is able to perform neighbour subtraction. We used the stellar positions in the early release catalog from the *HST* UV Legacy Survey of Galactic Globular Clusters (Piotto et al. 2015; Soto et al. 2017) as an absolute astrometric reference system. Based on these RA and Dec positions, we defined a common, pixel-based reference system, with the X and Y axes

increasing, respectively, toward West and North, and with the center of the cluster arbitrarily placed at position (5000,5000). We set the pixel scale to be 25 mas pixel^{-1}, consistent with that of ACS/HRC. We transformed each stellar position from the single-exposure, one-pass photometry catalogs into the reference frame by means of six-parameter linear transformations, using a subset of bright, unsaturated and well-measured stars in common between the two catalogs. We rescaled the instrumental magnitudes of each exposure to match those of the longest available exposures taken with that filter.

The multi-pass photometry was performed with the code KS2 (see Bellini et al. 2017b for details). KS2 combines the results of the one-pass photometry, transformed into the common reference frame, and it is able to simultaneously analyze multiple images of a given stellar field obtained with different filters. For this study, differently from the UV-driven approach adopted in Raso et al. (2017), here described in Chapter 3, we performed the finding procedure simultaneously on all the available exposures. This different approach is motivated by the necessity of detecting and subtracting all the potential contaminators (even faint red stars) that can potentially affect the SED of each selected BSS. Note that in the case of the data analyzed here, crowding is reduced because of the very high angular resolution of the ACS/HRC and the relative proximity of the cluster ($D = 4.5$ kpc, Harris 1996).

KS2 also provides a set of photometric quality parameters that can be used to select well-measured stars (see Bellini et al. 2017b for a complete description). Briefly, these parameters are: the QFIT parameter, which indicates the quality of the PSF fit; the o parameter, which measures the neighbour flux (normalized to the star flux) that had to be subtracted within the fitting radius; and the RADXS parameter, which measures the source flux beyond the fitting radius, with respect to the flux predicted by the PSF. The RADXS parameter is useful to distinguish between extended sources, like galaxies or blends, which have a substantial excess of flux outside the fitting radius with respect to the PSF, and cosmic rays or hot pixels, which have less flux in the outskirts of their profile with respect to the PSF predictions.

Our dataset covers a time baseline of about 4 years, long enough to measure proper motions (PMs), in order to separate cluster stars from field stars. We measured PMs using the technique developed in Bellini et al. (2014) and recently improved in Bellini et al. (2018). The region where PMs can be measured is smaller than the FOV of the whole dataset (see the dashed-dotted contour in the inset of Figure 2.1), since the external regions were only observed in one epoch (as part of the observing programs 9019 and 9028 performed in 2002).

2.2.1 Photometric calibration

Since the main goal of this work is to obtain broadband SEDs for a sample of BSSs and use them to estimate their physical parameters, a careful photometric calibration is required. Following the prescriptions given in Bellini et al. (2017b), we obtained VEGAMAG calibrated magnitudes from our instrumental magnitudes as follows:

$$m_{f,\mathrm{CAL}} = m_{f,\mathrm{INSTR}} + \Delta\mathrm{mag} + \mathrm{ZP}_f \tag{2.1}$$

where $m_{f,\mathrm{CAL}}$ is the calibrated magnitude in the VEGAMAG system in the considered filter f; $m_{f,\mathrm{INSTR}}$ is the instrumental magnitude resulting from the multi-pass photometry; Δmag is the 2.5σ-clipped median difference between the aperture photometry $m_{\mathrm{AP}}(\lambda)$ and the instrumental magnitudes; ZP_f is the photometric zero point of

TABLE 2.2: List of photometric calibration values.

Filter	Δmag	$\epsilon_{\Delta\text{mag}}$	ZP_f
F220W	5.336	0.029	21.883
F250W	5.782	0.042	22.261
F330W	4.407	0.025	22.913
F435W	4.342	0.030	25.188
F475W	4.398	0.074	25.635
F555W	4.391	0.054	25.261
F606W	4.433	0.056	25.906
F625W	4.394	0.062	25.210
F775W	4.305	0.051	24.568
F814W	4.297	0.078	24.856

the filter considered[1]. The value $m_{\text{AP}}(\lambda)$ is measured on the `_drz` images using aperture photometry with a 6-pixel radius and corrected for the finite aperture using the encircled energy values listed in Bohlin (2016). We chose to use a 6-pixel aperture since it represents the best compromise between the need to minimize the contribution of nearby stars and the need for a large aperture. In Table 2.2 we list the values of Δmag, with their errors $\epsilon_{\Delta\text{mag}}$, and ZP_f used in this work.

In order to compute the global photometric error for each star, we combined (in quadrature) the rms of the stellar mean magnitude with the uncertainties of the calibration process. The dominant component in the calibration error budget comes from the Δmag rms, which is of the order of $10^{-2} - 10^{-1}$ mag, while we neglected a minor possible contribution (of the order of 10^{-3} mag) due to the variation of the ZP_f as a function of time.

2.3 BSS selection and SED-fitting procedure

2.3.1 BSS Selection

Various studies have shown that BSSs in 47 Tuc are concentrated towards the cluster center, as expected for a population of stars heavier than the average (e.g., Paresce et al. 1991; Guhathakurta et al. 1992; de Marchi, Paresce, and Ferraro 1993; Ferraro et al. 2001, 2004, 2012; Parada et al. 2016). Hence, a significant sample of BSSs is expected to fall in the studied FOV, which probes the innermost $50'' \times 50''$ of the cluster (see Figure 2.1).

We used an ultraviolet CMD (m_{F220W} vs. $m_{\text{F220W}} - m_{\text{F330W}}$) to select BSSs (similar to the approach used in Ferraro et al. 2001; Raso et al. 2017, see also Chapter 3). In these UV filters, BSSs are among the brightest objects in the cluster, and they define a clear, almost vertical sequence, easily distinguishable from other stellar populations. We selected as BSSs all the 53 stars that fall within the dashed box reported in Figure 2.2.

Only a sub-sample of the selected BSSs, represented as dark blue circles in Figure 2.2, has been used to study the SEDs. First of all, we rejected stars that were detected in less than 8 out of the 10 available bandpasses, in order to have a significant number of spectral points for the SED-fitting procedure (see Section 2.3.3). We

[1]The photometric zero-points were obtained using the ACS zeropoints calculator available at https://acszeropoints.stsci.edu/

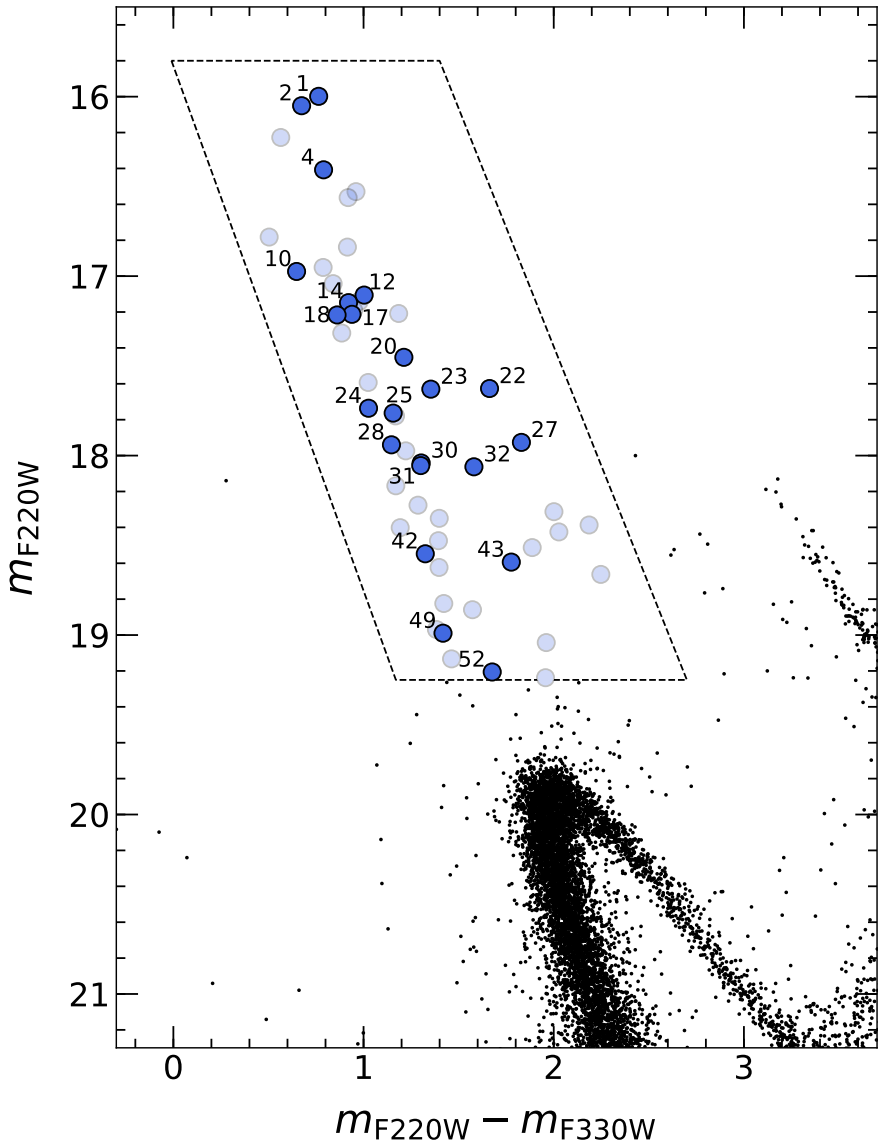

FIGURE 2.2: UV CMD (m_{F220W} vs. $m_{F220W} - m_{F330W}$) of the central region of 47 Tuc. The dashed box define the region where we selected BSSs. The blue circles (both light and dark) are the complete sample of BSSs in our dataset (53 objects), while the dark blue circles represent the cleaned BSS sample (22 objects, see text for details on the selection). The dark blue circles are labeled as in Table 2.3.

also excluded from our sample stars that were measured in less than 2 single exposures per filter, in an effort to include in the final sample only BSSs with robustly measured magnitudes. A further selection was performed by using the quality parameters obtained from the reduction software (described in Section 2.2). For each BSS, we computed the median value, over all the filters available, of the photometric error, `QFIT` and `RADXS` parameters. These median values do not have a real physical meaning, since they are averaged over different filters, but still they provide an overall photometric quality assessment. For example, an extended source should have a large `RADXS` value regardless of the filter. We thus computed the median and the relative error of the three parameters for all the 53 BSSs in our sample, and we assumed these values in order to select well-measured BSSs by rejecting any star having at least one parameter exceeding 5σ the mean value. We arbitrarily assumed $o = 0.2$

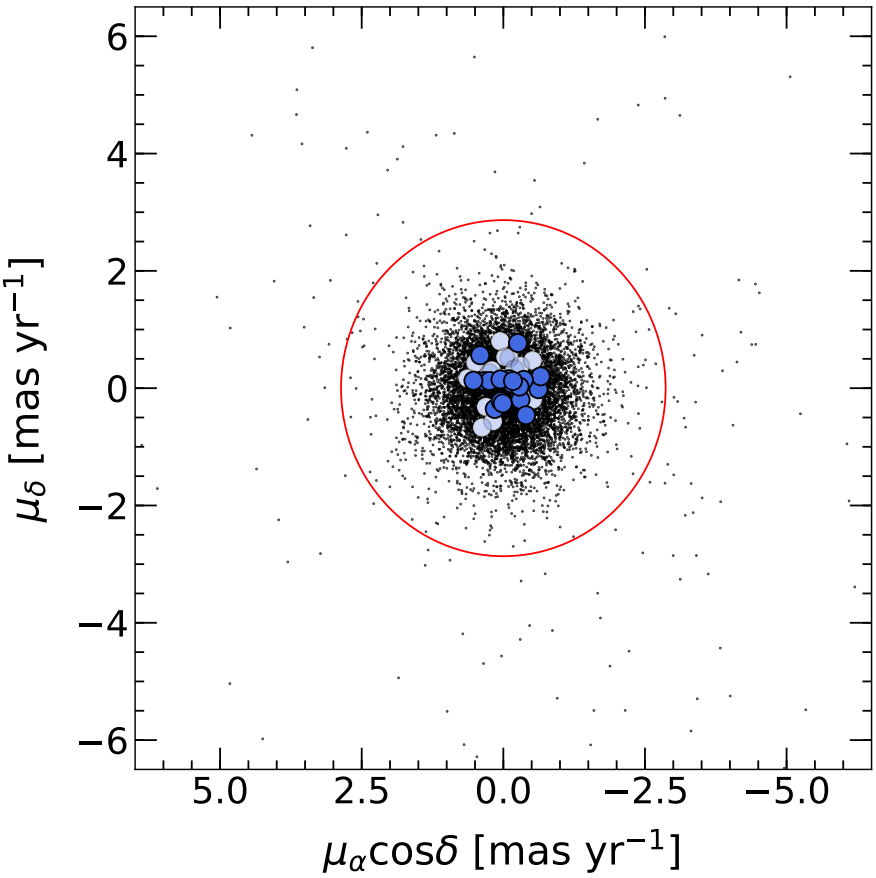

FIGURE 2.3: Vector-point diagram for all the stars with a PM measurement in our dataset (black points). The blue circles (color coded as in Figure 2.2) correspond to the 34 BSSs for which PMs could be measured. The red circle corresponds to 5 times the central velocity dispersion of bright stars in 47 Tuc, plotted as a reference.

(i.e., the median neighbour flux subtracted before measuring the star was equal to the 20% of the star flux itself) as our fixed rejection threshold, to safely exclude stars with bright neighbours.

We also checked the cluster membership of the selected BSSs. We show in Figure 2.3 the vector-point diagram (VPD) for all the stars with a valid PM measurement (black points). As expected, the figure shows a well-defined clump of stars (indicating the cluster members) with essentially no evidence of field contamination: this was somehow expected, since the observations sampled the innermost regions of the cluster. For reference, the red circle in Figure 2.3 corresponds to 5 times the central velocity dispersion of bright stars in 47 Tuc (0.573 mas yr^{-1}, or 12.2 km s^{-1}; Watkins et al. 2015a; Baumgardt and Hilker 2018). Since the FOV where PMs can be measured is smaller than the FOV of the whole dataset (see Figure 2.1), we can provide PM information for only 34 (out of 53) BSSs in our sample (both the light and dark blue circles in Figure 2.3; the dark blue circles represent BSSs that also survived the quality and variability selection). All these 34 BSSs are cluster members, as can be seen from Figure 2.3. Given the negligible level of field contamination, also the remaining 19 BSSs, for which we do not have a PM measurement, have a high probability of being cluster members.

2.3.2 Variability

Variable stars should be excluded from the final BSS sample to avoid the construction of SEDs using magnitudes measured at different phases of variability. The BSS sequence crosses the classical instability strip, so we expect that a few BSSs in our sample could be pulsating variables (e.g., SX Phoenicis). Moreover, some of them are known or suspected eclipsing variables or contact binaries (e.g., W Uma variables). Hence, to perform a meaningful comparison with theoretical SEDs, we excluded all variable BSSs by cross-correlating the BSS positions in our catalog with the positions of variable objects listed in the catalog of Variable Stars in Galactic Globular Clusters (Clement et al. 2001, last update for 47 Tuc: January 2017[2]), to identify the already known or suspected variables (both eclipsing and pulsating). We focused our attention on variables from Edmonds et al. (1996) and Gilliland et al. (1998), who studied variability in the central $66'' \times 66''$ of 47 Tuc with adequate *HST* photometry, and we finally identified 9 objects.

Summarizing, 9 BSSs have been excluded due to variability, 16 because they have been measured in too few bandpasses (or because only a few exposures were available per filter), and 6 because of the photometric quality selection. Therefore, the final, quality-selected and variable-cleaned BSS sample consists of 22 stars (the dark blue dots in Figures 2.1, 2.2 and 2.3), which still covers the whole magnitude and color ranges of the observed BSS sequence, thus allowing us to study this population in its entirety. 18 of the 22 BSSs from the clean sample have a PM measurement, that allowed us to definitely confirm that they are cluster members.

2.3.3 Spectral Energy Distribution fitting

We first corrected the observed magnitudes for reddening, adopting the following relation:

$$m_{f,\mathrm{corr}} = m_{f,\mathrm{obs}} - c_f \, \mathrm{R}_V \, \mathrm{E}(B-V) \tag{2.2}$$

where, for each bandpass f, $m_{f,\mathrm{corr}}$ is the reddening-corrected magnitude; $m_{f,\mathrm{obs}}$ is the original observed magnitude; $c_f = A_\lambda / A_V$ is the extinction law (Cardelli, Clayton, and Mathis 1989); $\mathrm{R}_V = 3.12$ is the extinction coefficient; $\mathrm{E}(B-V) = 0.04$ is the reddening value for 47 Tuc (Harris 1996).

We then constructed model SEDs as follows. We produced a grid of synthetic spectra with temperature and surface gravity ranges appropriate for BSSs: 5000 K $< T_{\mathrm{eff}} <$ 10000 K with a step of 100 K; $3 < \log(g) < 5$ with a step of 0.1. All the synthetic spectra were calculated with the software `SYNTHE` (Sbordone et al. 2004; Kurucz 2005). For each point of the grid, a one-dimensional, plane-parallel, LTE model atmosphere has been calculated with the code `ATLAS9` (Kurucz, 2005), adopting [Fe/H]=–0.70 dex and an α-enhanced chemical mixture[3] (Dotter et al., 2010). The spectral synthesis was performed in the wavelength range between 1000 and 10000 Å, including all the atomic and molecular lines available in the Kurucz/Castelli database[4], with the exclusion of TiO lines that are negligible for the investigated range of stellar parameters. Finally, each spectrum has been convolved with a Gaussian profile in order to obtain a spectral resolution of 1000. The flux of synthetic

[2] The catalog is available at http://www.astro.utoronto.ca/~cclement/cat/C0021m723.

[3] We tested if a small [Fe/H] variation ($\sim$ 0.1 dex) or a solar-scaled (instead of α-enhanced) chemical mixture could significantly affect our results, and we found that the impact on the derived synthetic magnitudes is negligible.

[4] http://wwwuser.oats.inaf.it/castelli/linelists.html

spectra $F(\nu)$ is in units of erg cm^{-2} s^{-1} Hz^{-1} sr^{-1}. We converted it into apparent flux $f(\lambda)$ (in `flam` units, i.e.: erg cm^{-2} s^{-1} Å^{-1}) as follows:

$$f_\lambda = \frac{4\pi c}{\lambda^2}\left(\frac{R}{D}\right)^2 F(\nu) \tag{2.3}$$

where $c = 3 \times 10^{10}$ cm s^{-1} is the speed of light; R is the star radius (defined by a grid in the range: $0.1R_\odot < R < 4.5R_\odot$, with a step of $0.01R_\odot$); D is the cluster distance. We converted the apparent fluxes to synthetic, apparent magnitudes $m_{f,\mathrm{syn}}$ (in the `VEGAMAG` system, to match our observed, calibrated magnitudes), by convolution with the filter throughputs, using the `pysynphot` package (STScI Development Team 2013).

We then directly compared observed and model SEDs. It is important to note that our model grid consists only of single star models, so we assume that all the BSSs in our sample are single stars. This assumption should be reasonably safe, since we have already excluded from the considered sample all the BSSs known or suspected to be eclipsing variables (see Section 2.3.2). Moreover, the presence of BSSs with a degenerate companion (i.e., a WD) should not affect our results, since the WD emission is expected to be too hot and faint to significantly affect even the flux measured with the bluest filter.

We performed the fit using a Markov chain Monte Carlo (MCMC) approach, based on the `emcee` algorithm (Foreman-Mackey et al. 2013). We thus obtained the posterior probability distribution function (PDF) for each parameter of the fit (T_{eff}, $\log(g)$, R) and subsequently derived the posterior PDF also for mass (M) and luminosity (L) through the following equations:

$$g = \frac{GM}{R^2}; \quad L = 4\pi R^2 \sigma T_{\mathrm{eff}}^4 \tag{2.4}$$

where $G = 6.67 \times 10^{-8}$ g^{-1} cm^3 s^{-2} is the gravitational constant, and $\sigma = 5.7 \times 10^{-5}$ erg cm^{-2} s^{-1} K^{-4} is the Stefan-Boltzmann constant. Since the priors we assumed are uniform, the posterior PDFs are proportional to the likelihood: $\mathcal{L} = \exp(-\chi^2/2)$. We computed χ^2 as:

$$\chi^2 = \sum_f \left(\frac{\Delta m}{\sigma_{f,\mathrm{obs}}}\right)^2 + \left(\frac{\Delta m_{UB,\mathrm{corr}} - \Delta m_{UB,\mathrm{syn}}}{\sigma_{UB,\mathrm{obs}}}\right)^2 \tag{2.5}$$

where the sum is performed over the 10 bandpasses used to construct the SEDs; $\Delta m = m_{f,\mathrm{corr}} - m_{f,\mathrm{syn}}$ is the difference between the observed, dereddened magnitudes and the synthetic ones; $\sigma_{f,\mathrm{obs}}$ is the error associated with the observed magnitudes (see Section 2.2.1). $\Delta m_{UB,\mathrm{corr}} = m_{\mathrm{F330W,corr}} - m_{\mathrm{F435W,corr}}$ is the observed magnitude difference (i.e., color) between the observed, dereddened magnitudes in the F330W and F435W bandpasses (roughly corresponding to Johnson U and B filters), $\Delta m_{UB,\mathrm{syn}} = m_{\mathrm{F330W,syn}} - m_{\mathrm{F435W,syn}}$ is the equivalent quantity for synthetic magnitudes, while $\sigma_{UB,\mathrm{obs}}$ is the error associated to $\Delta m_{UB,\mathrm{corr}}$, obtained by adding in quadrature $\sigma_{\mathrm{F330W,obs}}$ and $\sigma_{\mathrm{F435W,obs}}$, i.e., the errors associated to the observed magnitudes in these two bandpasses. The aim of this last term of the χ^2 is to increase the sensitivity of the fit to surface gravity. As can be seen in Figure 2.4, surface gravity has quite a weak impact on the SEDs. However, the spectral region sampled by the F330W and F435W filters (i.e., around the Balmer jump region; circled squares in Figure 2.4) seems instead to be sensitive to the adopted gravity. Increasing the fit sensitivity to surface gravity is particularly important for two reasons: first, the surface gravity grid is defined in logarithmic units; therefore, small uncertainties in

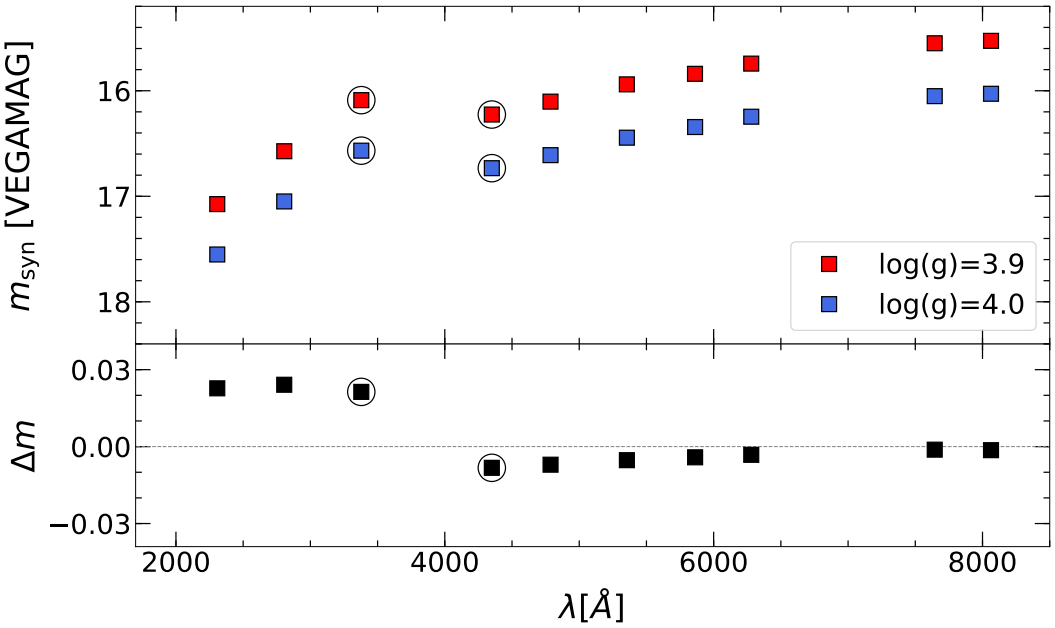

FIGURE 2.4: Top panel: Synthetic magnitudes for two values of $\log(g)$, differing only by 0.1 dex (see legend), while temperature and radius are fixed ($T_{\rm eff} = 7000$ K, $R = 2.5$ R$_\odot$, respectively). The $\log(g) = 4.0$ model is shifted by 0.5 mag fainter for clarity. Bottom panel: the black squares corresponds to the difference between the two models plotted in the top panel. As it can be seen, although the difference between the two models is quite small (of the order of a few hundredths of magnitude), it is positive at wavelengths shorter than $\simeq$ 4000 Å, and negative redwards, changing sign abruptly. The quantity $\Delta m_{UB,\rm syn} = m_{\rm F330W,syn} - m_{\rm F435W,syn}$, defined in Section 2.3.3, has been introduced to maximize the sensitivity of the fit to this spectral region, where the dependence of the models on surface gravity is higher. $m_{\rm F330W,syn}$ and $m_{\rm F435W,syn}$ are, respectively, the third and fourth squares from the left, circled for clarity.

$\log(g)$ translate into significant variations of the surface gravity. Second, mass is directly proportional to surface gravity, therefore the goodness of the fit on surface gravity directly influences the accuracy of the mass determination.

The results of the fitting procedure are listed in Table 2.3. The best fit values for each parameter correspond to the PDF median, while the reported uncertainties correspond to the 68% confidence interval. In Figure 2.5 we show the SEDs of a bright, an intermediate-magnitude and a faint BSSs, namely BSS4, BSS18, BSS52, overplotted to the corresponding best-fit model. In the lower panels we show the residuals between the observed SED and the best-fit model. It can be seen that, in any case, the residuals are small and that observed SEDs and models are in good agreement within the errors.

2.4 Results and Discussion

In Figure 2.6 we plot the luminosity and temperature of the selected BSSs in the ($\log L - \log T_{\rm eff}$) Hertzsprung-Russel (HR) diagram. As a reference, we also plot a 12 Gyr BaSTI isochrone[5] (Pietrinferni et al. 2004; Hidalgo et al. 2018, solid black

[5] http://basti-iac.oa-abruzzo.inaf.it/index.html

TABLE 2.3: Best fit parameters for the clean BSS sample.

BSS ID	T [K]	$\log(g)$	R [$R_\odot$]	L [$L_\odot$]	M [$M_\odot$]
BSS1	7600^{+80}_{-90}	$3.70^{+0.11}_{-0.13}$	$3.51^{+0.11}_{-0.09}$	$35.9^{+0.8}_{-0.8}$	$2.31^{+0.64}_{-0.59}$
BSS2	7900^{+90}_{-90}	$3.63^{+0.09}_{-0.07}$	$2.99^{+0.08}_{-0.08}$	$30.7^{+0.7}_{-0.7}$	$1.39^{+0.35}_{-0.22}$
BSS4	7600^{+110}_{-110}	$3.79^{+0.12}_{-0.11}$	$2.92^{+0.09}_{-0.09}$	$24.7^{+0.6}_{-0.6}$	$1.93^{+0.57}_{-0.45}$
BSS10	7800^{+130}_{-130}	$4.08^{+0.11}_{-0.11}$	$1.95^{+0.06}_{-0.07}$	$12.5^{+0.3}_{-0.3}$	$1.68^{+0.56}_{-0.40}$
BSS12	7100^{+90}_{-50}	$3.72^{+0.10}_{-0.10}$	$2.67^{+0.04}_{-0.08}$	$15.9^{+0.4}_{-0.3}$	$1.36^{+0.33}_{-0.31}$
BSS14	7200^{+90}_{-90}	$3.90^{+0.11}_{-0.13}$	$2.39^{+0.07}_{-0.06}$	$13.8^{+0.4}_{-0.4}$	$1.66^{+0.54}_{-0.43}$
BSS17	7200^{+50}_{-80}	$3.74^{+0.09}_{-0.08}$	$2.43^{+0.08}_{-0.03}$	$13.9^{+0.3}_{-0.3}$	$1.19^{+0.27}_{-0.22}$
BSS18	7400^{+70}_{-80}	$3.90^{+0.10}_{-0.09}$	$2.17^{+0.06}_{-0.03}$	$12.3^{+0.3}_{-0.3}$	$1.39^{+0.37}_{-0.25}$
BSS20	6800^{+70}_{-60}	$3.82^{+0.11}_{-0.10}$	$2.71^{+0.03}_{-0.09}$	$13.8^{+0.4}_{-0.3}$	$1.75^{+0.53}_{-0.38}$
BSS22	6400^{+50}_{-60}	$3.41^{+0.11}_{-0.10}$	$3.72^{+0.13}_{-0.04}$	$20.4^{+0.6}_{-0.5}$	$1.29^{+0.38}_{-0.28}$
BSS23	6700^{+50}_{-70}	$3.75^{+0.12}_{-0.12}$	$2.75^{+0.10}_{-0.04}$	$13.4^{+0.3}_{-0.3}$	$1.57^{+0.60}_{-0.37}$
BSS24	7100^{+50}_{-100}	$4.18^{+0.12}_{-0.10}$	$1.92^{+0.06}_{-0.03}$	$8.2^{+0.2}_{-0.2}$	$2.10^{+0.66}_{-0.45}$
BSS25	6900^{+70}_{-50}	$4.00^{+0.12}_{-0.11}$	$2.20^{+0.04}_{-0.06}$	$9.6^{+0.2}_{-0.2}$	$1.76^{+0.56}_{-0.42}$
BSS27	6200^{+60}_{-50}	$3.15^{+0.15}_{-0.11}$	$3.82^{+0.06}_{-0.13}$	$18.9^{+0.6}_{-0.5}$	$0.76^{+0.31}_{-0.16}$
BSS28	6900^{+60}_{-60}	$4.02^{+0.10}_{-0.11}$	$2.00^{+0.06}_{-0.03}$	$7.9^{+0.2}_{-0.2}$	$1.56^{+0.42}_{-0.35}$
BSS30	6700^{+90}_{-40}	$3.83^{+0.11}_{-0.10}$	$2.24^{+0.03}_{-0.06}$	$8.8^{+0.2}_{-0.2}$	$1.22^{+0.34}_{-0.25}$
BSS31	6700^{+80}_{-60}	$3.72^{+0.14}_{-0.14}$	$2.21^{+0.03}_{-0.07}$	$8.7^{+0.2}_{-0.2}$	$0.92^{+0.37}_{-0.27}$
BSS32	6400^{+60}_{-50}	$3.72^{+0.18}_{-0.19}$	$2.79^{+0.06}_{-0.06}$	$11.4^{+0.4}_{-0.3}$	$1.49^{+0.77}_{-0.54}$
BSS42	6600^{+70}_{-50}	$3.93^{+0.11}_{-0.11}$	$1.83^{+0.02}_{-0.06}$	$5.6^{+0.2}_{-0.2}$	$1.03^{+0.30}_{-0.25}$
BSS43	6200^{+90}_{-50}	$3.39^{+0.20}_{-0.20}$	$2.65^{+0.05}_{-0.09}$	$9.1^{+0.3}_{-0.3}$	$0.63^{+0.33}_{-0.26}$
BSS49	6600^{+60}_{-80}	$3.87^{+0.17}_{-0.16}$	$1.53^{+0.05}_{-0.02}$	$3.9^{+0.1}_{-0.1}$	$0.64^{+0.33}_{-0.20}$
BSS52	6300^{+80}_{-60}	$3.84^{+0.18}_{-0.15}$	$1.78^{+0.03}_{-0.06}$	$4.4^{+0.1}_{-0.1}$	$0.79^{+0.45}_{-0.24}$

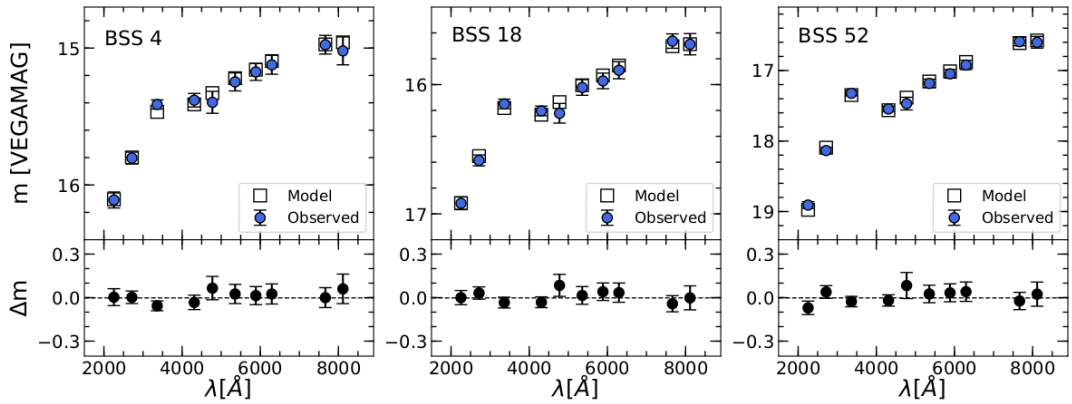

FIGURE 2.5: Top panels: observed SEDs of three BSSs from our sample, namely BSS4, BSS18, BSS52 (blue circles), overplotted to the corresponding best fit model (empty squares; see Table 2.3). Bottom panels: residuals between the observed SED and the best-fit model.

line) to highlight the TO, SGB, RGB and horizontal branch (HB) loci of "normal" stars of the cluster. As expected, the values of temperature and luminosity derived from the SED fitting make BSSs standing clearly outside the standard evolutionary loci, defining a sequence along the extrapolation of the cluster MS, with luminosities ranging from ~ 3 to ~ 30 $L_\odot$ and temperatures between ~ 6000 to ~ 8000 K.

In Figure 2.7 we show the distribution of the analyzed BSSs in the UV CMD, in which each BSS is marked with a color code that quantifies the value of the parameters derived from the SED analysis (see labels). As can be seen, the resulting

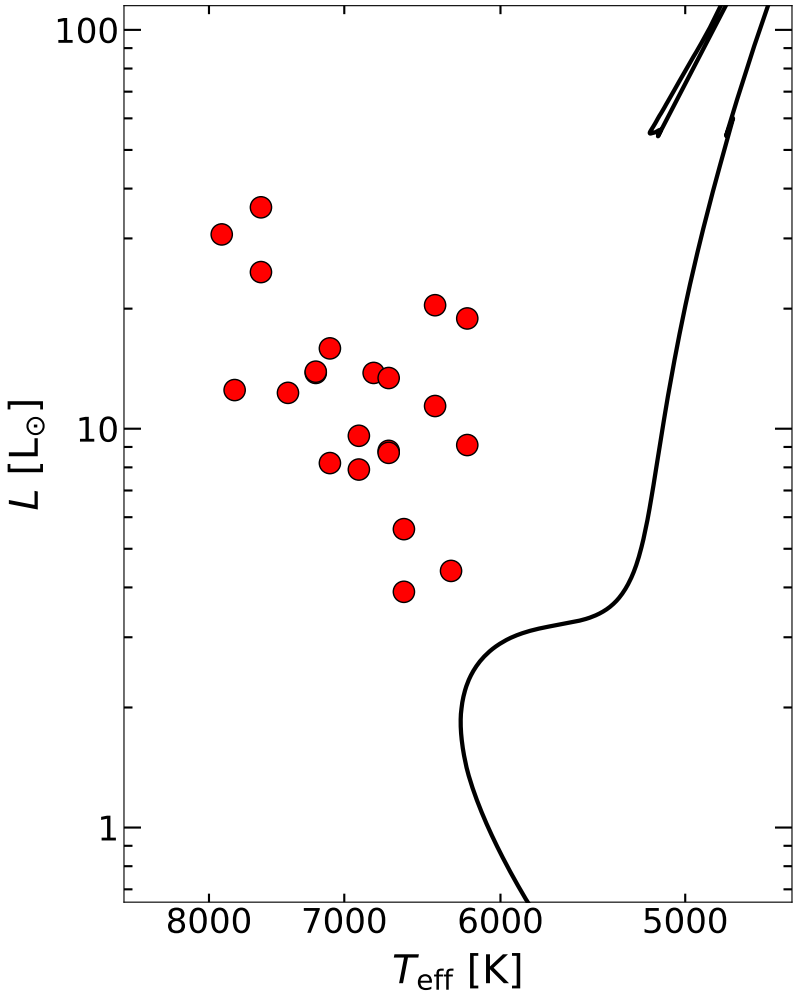

FIGURE 2.6: Position of the studied BSSs (red circles) in the HR diagram. The black solid line is a 12 Gyr BaSTI isochrone (Pietrinferni et al. 2004; Hidalgo et al. 2018), plotted as a reference to trace the normal TO, SGB and RGB sequences of the cluster.

parameters vary according to theoretical predictions. In the first panel, temperature decreases as BSS color increases. In the second and third panels respectively, surface gravity decreases and radius increases moving away from the zero age main sequence (ZAMS). In the fourth panel, bolometric luminosity increases as a function of the magnitude, but there is also an expected dependence on the color, since at fixed UV magnitudes, the reddest stars have lower temperatures, thus they are brighter at longer wavelengths (i.e., they have larger bolometric corrections): hence their bolometric luminosity is larger.

2.4.1 BSS mass distribution

Regarding BSS masses, the distribution shown in the rightmost panel of Figure 2.7 suggests the presence of a mass succession along the BSS sequence, with lower masses at the faint end and higher masses at the bright end of the sequence. We reiterate, however, that mass errors are quite large (see column 5 of Table 2.3, and Figure 2.8) due to the lack of very strong surface gravity tracers in the SEDs, as explained in the previous section. In spite of this, a mass sequence is also confirmed by the plot in Figure 2.8, where the BSS masses are plotted as a function of the F220W

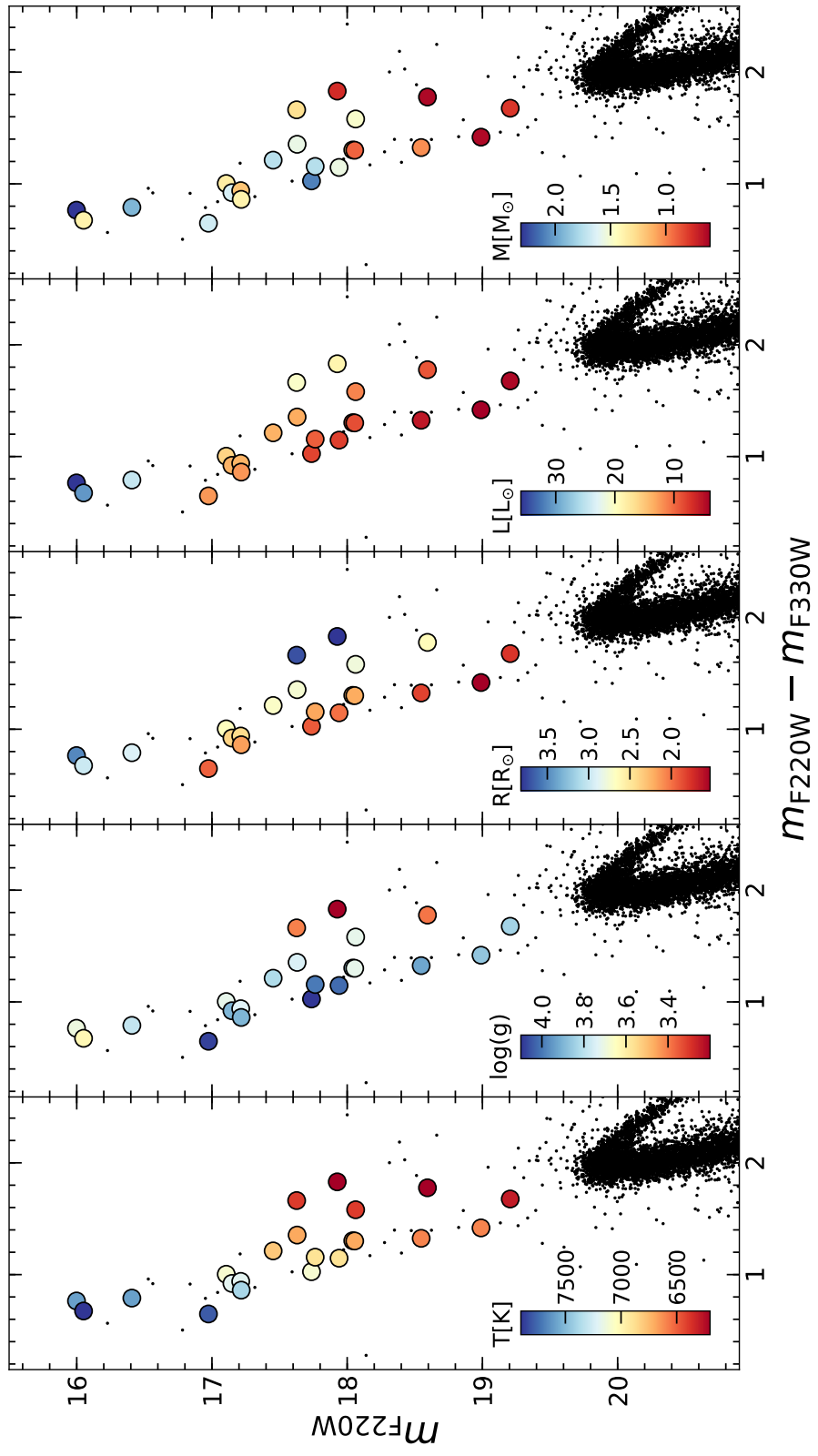

FIGURE 2.7: Distributions of the best-fit parameters obtained for the clean BSS sample, shown in the CMD. From left to right: temperature, surface gravity (logarithmic units), radius, bolometric luminosity, mass. Units and colorbars are marked inside each panel.

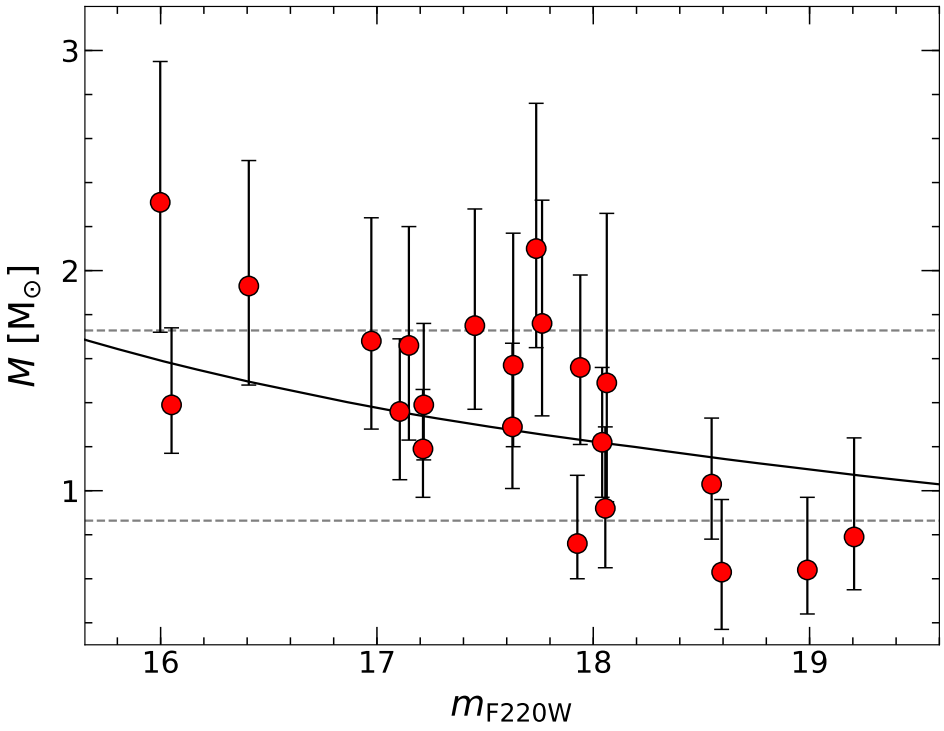

FIGURE 2.8: Resulting masses, with uncertainties corresponding to the 68% confidence interval, as a function of F220W magnitude (red points). The black solid line is a 100 Myr BaSTI isochrone (Pietrinferni et al. 2004; Hidalgo et al. 2018) with [Fe/H]=-0.70, plotted as a reference. The two horizontal, dashed lines corresponds to $M_{\rm TO}$ and $2M_{\rm TO}$ ($M_{\rm TO} \sim 0.86$ M$_\odot$, from the 12 Gyr BaSTI isochrone reported in Figure 2.6).

magnitude. Moreover, the mass distribution seems qualitatively in agreement with that predicted by theoretical ZAMS models: the black line in Figure 2.8 is a 100 Myr BaSTI isochrone (Pietrinferni et al. 2004; Hidalgo et al. 2018) with [Fe/H]$= -0.70$, plotted as a reference for the ZAMS of the cluster. In order to test the statistical significance of the detected BSS mass-magnitude relation, we measured the Spearman and Pearson correlation coefficients. We obtained $\rho = -0.64$ and $r = -0.70$ respectively, supporting the presence of an anti-correlation between mass and magnitude. Note that the mass-magnitude relation is also visible by using different bandpasses, but the adoption of UV filters tends to maximize the magnitude extension of the BSS sequence.

As shown in Figure 2.8, a few BSSs (specifically BSS1, BSS4, BSS20, BSS24, BSS25) in our sample have masses larger than $2M_{\rm TO}$ (we assumed $M_{\rm TO} \sim 0.86$ M$_\odot$, from the same 12 Gyr BaSTI isochrone reported in Figure 2.6). The presence of BSSs with twice the MS-TO mass would imply a formation mechanism that involves at least three stars (e.g., Knigge et al. 2006, 2008). However, within the uncertainties, these stars are still compatible with a mass lower than this threshold value, therefore they are just candidate supermassive-BSSs. It would be interesting to measure the masses of these stars with other direct methods, e.g., spectroscopically (see Ferraro et al. 2016), in order to confirm or reject this hypothesis. The masses derived for 4 BSSs (specifically BSS27, BSS43, BSS49, BSS52), turn out to be lower than $M_{\rm TO}$. These values are, however, still compatible with a mass larger than the TO mass within the errors. Most of them are (with the possible exception of BSS27) low-mass faint BSSs: they are clearly distinguishable from the MS only in an UV-CMD, as the one used in

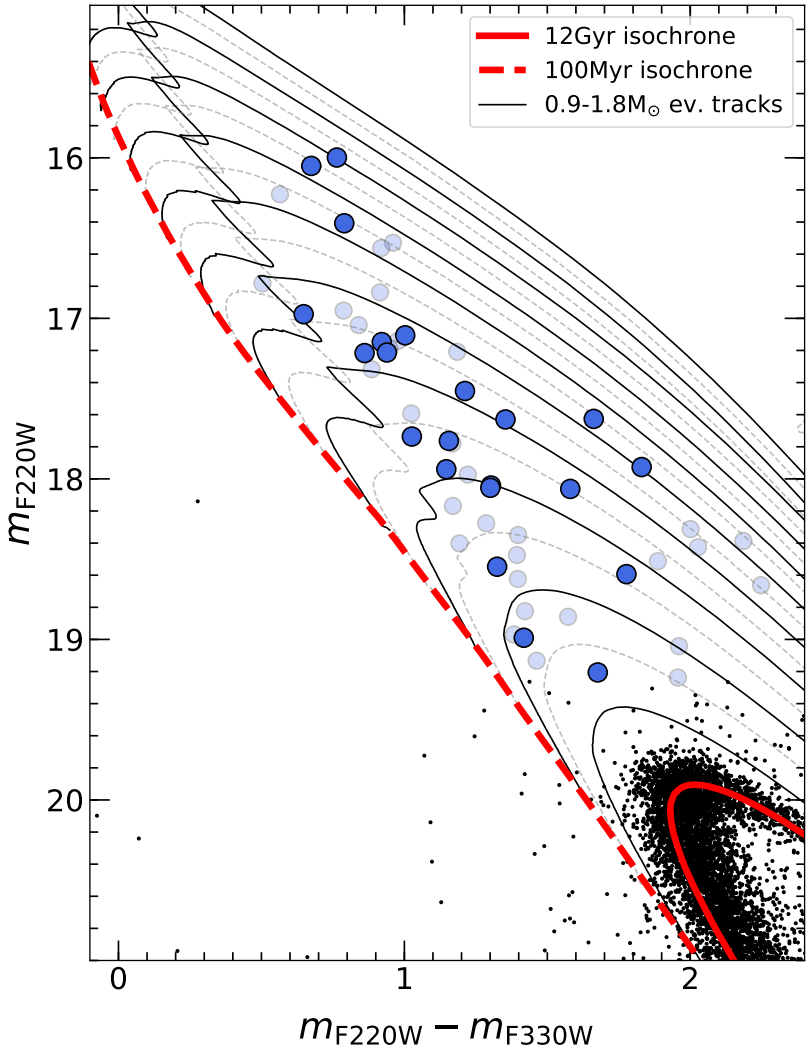

FIGURE 2.9: UV CMD with the BSS sample highlighted (blue circles; the dark blue ones represent the clean sample). The evolutionary tracks used to estimate the BSS mass (M_{TR}, see text for details) are also plotted. They span the range $0.9 - 1.8$ M$_\odot$, with a step of 0.05 M$_\odot$ (alternatively plotted as solid black lines and grey dashed lines for clarity). Two isochrones, of 12 Gyr and 100 Myr, are superposed for reference, respectively as solid and dashed red lines.

this work, while in a classical, optical diagram they do not appear to be significantly different from MS-TO stars (see Chapter 3).

2.4.2 BSS masses from evolutionary tracks

In general, a comparison with evolutionary tracks can provide a rough estimate of the BSS mass. Here we used a set of isochrones and evolutionary tracks (in the range $0.9 - 1.8$M$_\odot$) from the BaSTI model library. The theoretical models have been colored by convolving a grid of suitable Kurucz (1993) stellar spectra of appropriate metallicity with the transmission curves of the used ACS/HRC filters. Thus, for each given stellar temperature and gravity, both the color and the bolometric corrections in the VEGAMAG system have been computed. The set of evolutionary tracks (at [Fe/H]=-0.7) in the range $0.9 - 1.8$M$_\odot$ are shown in Figure 2.9, over-plotted to the (m_{F220W} vs. $m_{F220W} - m_{F330W}$) CMD: a distance modulus of $(m - M)_0 = 13.3$ and a

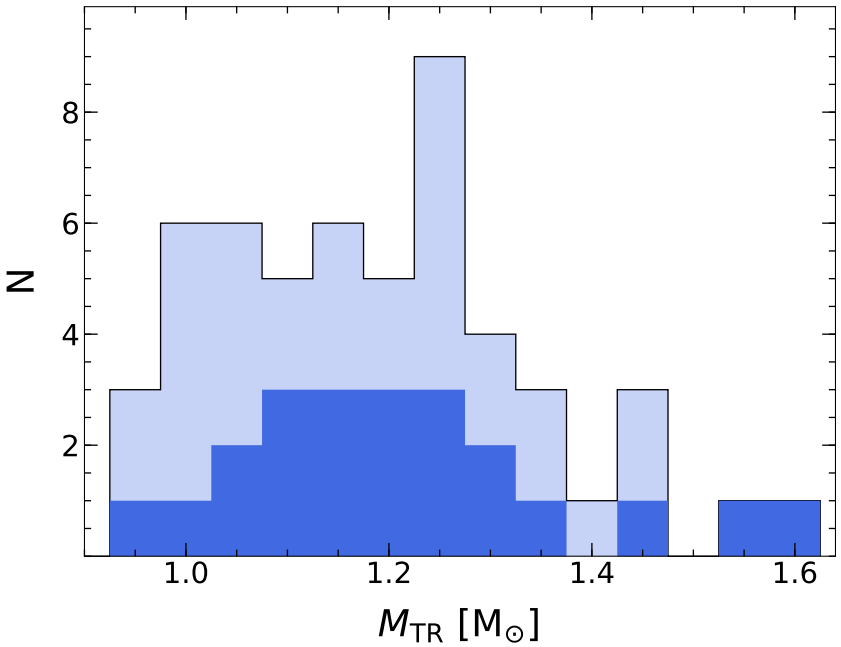

FIGURE 2.10: Light blue histogram: mass distribution, obtained from the evolutionary tracks, for the entire sample of 53 BSSs. Dark blue histogram: mass distribution, obtained from the evolutionary tracks, for the clean sample of 22 BSSs.

color excess E($B-V$)=0.04 have been adopted. Small offsets (of the order of a few 0.01) in color and magnitude have been applied to the evolutionary models in order to allow the 12 Gyr isochrone to perfectly match the MS-TO. The evolutionary tracks at steps of 0.05 $M_\odot$ shown in Figure 2.9 represent the reference "pillars" for the interpolation procedure that allowed us to estimate the mass of each BSS. The derived mass distribution for the entire sample of 53 BSSs is plotted in Figure 2.10. An average mass of 1.2 $M_\odot$, in agreement with other mass determination in the literature (see Ferraro et al. 2006; Lanzoni et al. 2007a; Fiorentino et al. 2014), is obtained from this sample.

Note that here we have the possibility of directly comparing the BSS masses obtained from the SED-fitting ($M_{\rm FIT}$) with those obtained from evolutionary tracks ($M_{\rm TR}$), for the sub-sample of 22 well-measured BSSs. We report the result of the comparison between $M_{\rm FIT}$ and $M_{\rm TR}$ in Figure 2.11. We fitted the points with a straight line using a maximum likelihood approach, equivalent to the one described in Section 2.3.3, considering both the y- and x-axis uncertainties. We obtained a slope $a = 1.46^{+0.53}_{-0.52}$ and an intercept $b = -0.55^{+0.60}_{-0.63}$ (the blue solid line in Figure 2.11). In the figure we also plotted, as a reference, the bisector line (black dashed line) i.e., a straight line with slope $a = 1$ and intercept $b = 0$, which represents the full correspondence between the $M_{\rm FIT}$ and $M_{\rm TR}$ values. As can be seen, the best fit relation turns out to be in reasonable agreement with the bisector. Therefore, we can conclude that, when a direct BSS mass estimate cannot be made, the evolutionary track method can be used to provide a reasonable first-guess estimate of the BSS mass.

2.4.3 Comparison with previous mass estimates

A few direct mass measurements of BSSs in the core of 47 Tuc are already available in the literature. In this section, we compare our results with previous estimates. The results of this comparison are summarized in Figure 2.12.

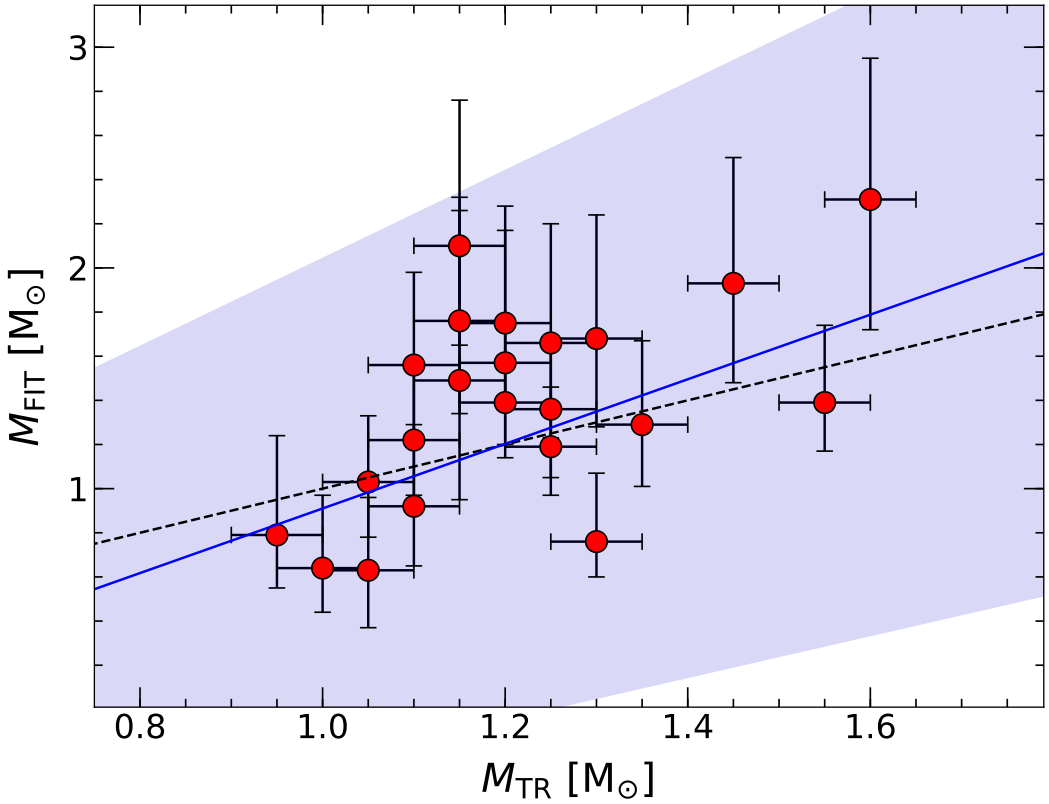

FIGURE 2.11: Red points: masses resulting from the SED-fitting method, with uncertainties corresponding to the 68% confidence interval, as a function of the masses estimated from evolutionary tracks (see text for details; the M_{TR} uncertainties are equal to 0.05 $M_\odot$, i.e., the step of the evolutionary grid used to measure M_{TR} itself). The black, dashed line is the bisector. The blue solid line is the best-fit straight line obtained with a maximum likelihood approach, considering both the y- and x-axis uncertainties (with slope $a = 1.46^{+0.53}_{-0.52}$ and intercept $b = -0.55^{+0.60}_{-0.63}$). The blue shaded area represents the 68% interval around the best-fit relation.

The first direct BSS mass measurement was indeed obtained on a 47 Tuc BSS by Shara, Saffer, and Livio (1997), comparing an *HST* spectrum (obtained with the Faint Object Spectrograph) with model spectra, and finding $M = 1.7 \pm 0.4$ $M_\odot$ (light blue triangle in Figure 2.12). The BSS they studied corresponds to our BSS4. The mass we obtain for this object is $M = 1.93^{+0.57}_{-0.45}$ $M_\odot$ (see Table 2.3), which is fully compatible, within the errors, with the value obtained spectroscopically by Shara, Saffer, and Livio (1997).

Gilliland et al. (1998) measured the masses of four variable BSSs in 47 Tuc on the basis of their pulsations (specifically V2, V14, V15, V16). They found masses equal to: 1.6 ± 0.2 $M_\odot$, 1.35 ± 0.1 $M_\odot$, 1.6 ± 0.15 $M_\odot$, 1.6 ± 0.15 $M_\odot$, respectively (light blue diamonds in Figure 2.12). We indeed detected in our FOV the four BSSs studied in Gilliland et al. (1998), which correspond to BSS6, BSS26, BSS3 and BSS9, respectively. We did not estimate their mass through SED fitting, since we excluded from this study all the known or suspected variables (see Section 2.3.2). However, we can compare the values reported in Gilliland et al. (1998) with the masses we obtained from evolutionary tracks. Specifically, our M_{TR} values for these four objects are: 1.40 $M_\odot$, 1.15 $M_\odot$, 1.45 $M_\odot$ and 1.25 $M_\odot$. As can be seen, the values for BSS3 and BSS6 are compatible with the values from Gilliland et al. (1998), while for

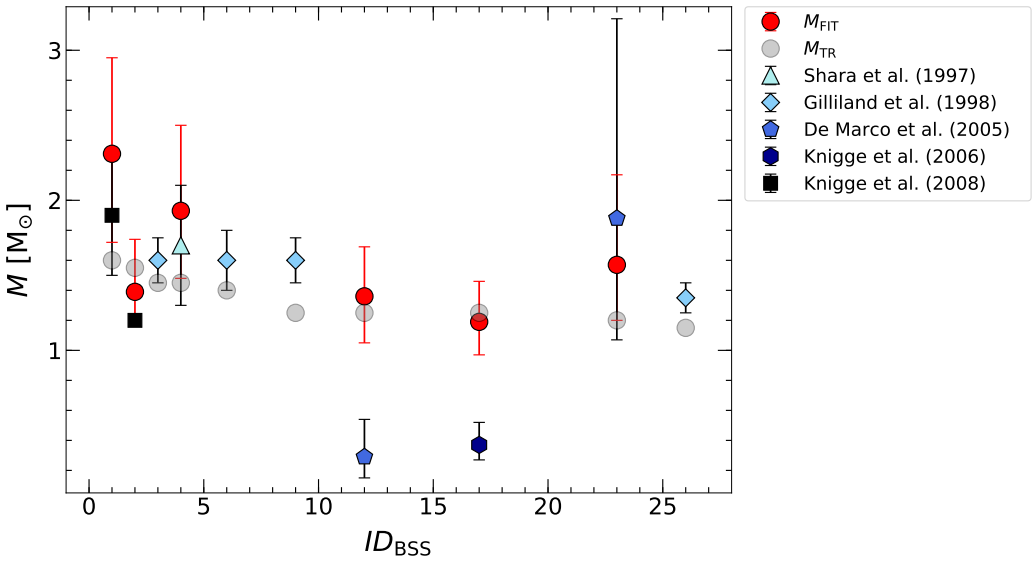

FIGURE 2.12: BSS masses obtained from our SED fitting method (red circles) and from the comparison with evolutionary tracks (grey circles), plotted against the BSS ID, compared to the values quoted in the literature for the same objects (points with different shades of blue, see legend).

BSS9 and BSS26 the masses from their work are slightly larger. However, estimating masses from evolutionary tracks could be less efficient for variable stars, since this kind of objects slightly changes position in the CMD depending on the phase of the variability.

De Marco et al. (2005) spectroscopically obtained masses and rotation rates of 55 stars (including 24 BSSs) in four GCs, including 47 Tuc. In particular, they analyzed 5 BSSs in 47 Tuc (see their Table 4). We detected all 5 of these objects in our sample, but only two of them pass our quality/variability conditions and therefore they have been analyzed in this work. Namely, their star NGC104-5 corresponds to our BSS12 and their NGC104-7 corresponds to our BSS23. They obtain masses equal to $0.29^{+0.25}_{-0.14}$ $M_\odot$ and $1.88^{+1.33}_{-0.81}$ $M_\odot$, respectively (blue pentagons in Figure 2.12), while we obtain $1.36^{+0.33}_{-0.31}$ $M_\odot$ and $1.57^{+0.60}_{-0.37}$ $M_\odot$, respectively. The two mass values for BSS23 are fully compatible within the errors, while those of BSS12 are not, with their mass estimate being significantly smaller than ours. The spectrum of this star has a high S/N ratio but is affected by blending (see Section 7.2 in De Marco et al., 2005). The authors also discuss a temperature inconsistency between the low- and the intermediate-resolution spectra (see their Section 11). These can be two possible explanations for the discrepancy between the two mass measurements.

Knigge et al. (2006, 2008) obtained physical parameter estimates for a few BSSs in the core of 47 Tuc using almost the same dataset as ours (excluding the ACS/HRC F220W images and including the ACS/HRC F850LP and Space Telescope Imaging Spectrograph (STIS) F25QTZ images, and also FUV spectroscopy in the latter work) and the same technique, i.e., SED fitting, albeit using a least squares approach.

In Knigge et al. (2006), they identify the star BSS7 (dark blue hexagon in Figure 2.12; nomenclature from Paresce et al. 1991; hereafter, to avoid confusion with our nomenclature, we will name this star K-BSS7) as the optical counterpart to the *Chandra* X-ray source W31 (Grindlay et al. 2001). They found K-BSS7 to be variable, but with a very small amplitude ($A_I = 0.0037$ mag). K-BSS7 corresponds to BSS17 in this work. Given its very small variability amplitude, BSS17 survived the selection

criteria discussed in Section 2.3.2 and has been kept in our final sample. Knigge et al. (2006) fit the SED with both a single and a binary model, finding comparable results for the physical parameters of the BSS, although the presence of a MS secondary improved the quality of their fit. Irrespective of the presence of a companion, the physical parameters they found from the fits point towards quite low mass values ($M = 0.34^{+0.15}_{-0.08}$ $M_\odot$ and $M = 0.37^{+0.15}_{-0.10}$ $M_\odot$ for the single and binary models, respectively). They argue that such low mass values can be due to systematic uncertainties in the $\log(g)$ estimates due to uncertainties on, e.g., the cluster distance, reddening and metallicity, or that the low $\log(g)$ values can be due to the rapid rotation of the star. Unfortunately, without spectroscopy it is not possible to disentangle between the two scenarios. On the contrary, our mass estimate for BSS17 is $M = 1.19^{+0.27}_{-0.22}$ $M_\odot$, larger than the TO mass and compatible with the value found for other BSSs of comparable magnitude. It is important to note that the cluster distance, reddening and metallicity we adopted are slightly different from theirs (0.01 kpc in distance, -0.13 dex in metallicity and 0.008 in reddening), but these small differences can hardly explain the large discrepancy in the derived mass. The significant difference between these two mass values for BSS17 might be explained by the fact that we use a MCMC approach to the SED fitting procedure, and we explicitly add a term in the χ^2 computation (see Equation 2.5) to increase the sensitivity of the fit to the surface gravity.

Knigge et al. (2008) used FUV spectroscopy (obtained with the Space Telescope Imaging Spectrograph onboard *HST*) to study 48 FUV-excess sources in the same FOV as this work, classifying them on the basis of their FUV-optical CMD and combining the FUV spectroscopy with UV-optical SEDs (constructed using the same photometric dataset used in Knigge et al., 2006, almost coincident with ours; see previous paragraph) to further study these sources and constrain their physical parameters. They found 8 BSSs in their sample, but they analyzed in detail, i.e., obtained physical parameter estimates, only for two of them (star 2 and star 999 using their nomenclature; shown as black squares in Figure 2.12). These two stars correspond to our BSS2 and BSS1, respectively. Regarding star 2 (BSS2), Knigge et al. (2008) detected a significant FUV excess from spectroscopy, which they associate to a WD companion. However, the photometric data can still be described by a single component since the WD emission is too blue to have a significant impact at those wavelengths. Therefore, regarding the BSS physical parameters, we can safely compare our result, obtained under the assumption of single stars (see Section 2.3.3), with theirs. They obtain a mass of 1.2 $M_\odot$ (no uncertainties reported), consistent, within the errors, with our result for BSS2 ($M = 1.39^{+0.35}_{-0.22}$ $M_\odot$). Regarding star 999 (BSS1), they obtain $M = 1.9 \pm 0.4$ $M_\odot$, fitting the broadband SED only, excluding the FUV spectrometry (see their Section 4.12 for a detailed explanation). This is also comparable to our measurement: $M = 2.31^{+0.64}_{-0.59}$ $M_\odot$. Our BSS1 mass measurement seems to further confirm that this star, as already discussed in Knigge et al. (2008), has a mass larger than $2M_{\rm TO}$. Unfortunately, both in Knigge et al. (2008) and in this work, the mass uncertainties are too large to definitively conclude that BSS1 must have had more than two progenitors.

Chapter 3

The new dynamical clock

Mainly based on:
Lanzoni, Ferraro, [...], Raso (2016), ApJL, 833, L29
Raso et al. (2017), ApJ, 839, 64
Ferraro, Lanzoni, Raso, et al. (2018), ApJ, 860, 36

3.1 Introduction

As already shown in Chapter 2, BSSs are significantly more massive ($M_{BSS} \sim$ 1.2-1.3$M_\odot$) than the average stellar mass in GCs ($\langle m \rangle \sim 0.4 M_\odot$; see also, e.g., Shara, Saffer, and Livio 1997; Gilliland et al. 1998; De Marco et al. 2005; Fiorentino et al. 2014). For this reason, they are subject to dynamical friction, which makes them sink toward the cluster center (e.g., Mapelli et al. 2004, 2006). BSS radial distribution is therefore shaped by dynamical friction, starting from the central regions where the relaxation time is shorter (see Equation 1.2) and at progressively larger distance from the center, as a function of time. BSSs are therefore powerful indicators of GC internal dynamics (see Section 1.3).

We have already discussed the so-called "dynamical clock" (Section 1.4.1), where the BSS-nRD was used as a clock hand to measure the dynamical age of the system (Ferraro et al. 2012). Although powerful, the BSS-nRD has a few disadvantages (e.g., it requires binning; it is difficult to reproduce its behaviour with simulations; for a more detailed discussion see Section 1.4.2), therefore we defined a new dynamical age indicator, A^+ (see Section 1.4.2 and Alessandrini et al. 2016), that does not suffer from this drawbacks. In this Chapter we describe the first observational results about the parameter A^+. Then, we show how to properly select complete samples of BSSs, by means of an "UV-driven" approach, and we show its advantages with respect to the classical, optical approach. We also show that completeness is a crucial requirement for an unbiased measurement of A^+. Finally, we expand the determination of A^+ to 27 GCs from the *HST* UV Legacy Survey of GGCs (Piotto et al. 2015), which, added to previously analyzed clusters, take the total number of GGCs where A^+ has been measured to 48, corresponding to $\sim$ 30% of the population of our Galaxy.

3.2 First observational determination of A^+

In this Section we study the parameter A^+ from the observational point of view. To empirically determine the value of A^+ in a significant number of GCs, we used the same photometric database from which the original dynamical clock was defined (Ferraro et al. 2012, here described in Section 1.4.1), plus four additional clusters discussed in subsequent papers (Beccari et al. 2013; Dalessandro et al. 2013a; Sanna

et al. 2014; Dalessandro et al. 2015). The details about the observations, data quality, and data analysis for each specific cluster can be found in those papers.

Here, we just provide a schematic summary of the data set characteristics and the general approach followed for the sample selection. The central regions of each cluster have been typically observed in the ultraviolet band with the Wide Field Planetary Camera 2 (WFPC2) on board the *HST*, and, where possible, with complementary optical observations secured with the *HST* ACS. The most external regions have been sampled by means of optical, ground-based observations performed with wide-field imagers, as the WFI@ESO and MegaCam@CFHT. Since BSSs are most reliably distinguishable from other cluster populations in the UV color–magnitude diagram (see Ferraro et al. 2015 and Section 3.3 in this Chapter)[1], we generally used this diagram to define the BSS selection box. The latter is then transformed into the optical planes by using sub-samples of BSSs observed in both the UV and the optical bands. As reference populations, we generally considered the RGB, SGB and/or HB stars, depending on the cluster properties and the available photometric data. In order to allow unbiased comparisons, their selection was performed using the same photometric catalogs adopted for the BSSs. However, depending on the surface temperature of each stellar population, we used the UV color–magnitude diagrams to select (hot) HB stars, and the optical diagrams for the (cool) RGB/SGB reference samples, so as to avoid any completeness bias. In the case of more than one reference population, we have verified that the corresponding radial distributions are in mutual agreement. This guarantees that any adopted reference population can be equivalently used for the determination of A^+.

By definition (see Section 1.4.2), A^+ depends on the considered cluster-centric distance. Hence, a meaningful cluster-to-cluster comparison requires that the parameter is measured over equivalent radial portions in every system and that the adopted region is large enough to be sensitive to the phenomenon that A^+ is describing (the effect of dynamical friction on BSSs). By using the set of N-body simulations discussed in Alessandrini et al. (2016), we verified that the value of the parameter computed at one half-mass radius is always representative of the cluster global value (i.e., the value attained if the entire radial extension is considered), corresponding to 70%–80% of it in all our runs. We also note that in the analysis of Ferraro et al. (2012), the level of BSS sedimentation is parameterized by the value of $R_{\rm BSS}$ (see Equation 1.8): a central peak in the BSS-nRD corresponds to $R_{\rm BSS} > 1$, indicating that the observed number of BSSs is in excess with respect to what expected from the sampled luminosity. Interestingly, values of $R_{\rm BSS} > 1$ are observed at $r < r_{\rm h}$ in all clusters belonging to Family II and Family III. This confirms that the region included within one half-mass radius is the most sensitive to the BSS sedimentation process. Thus, for a meaningful cluster-to-cluster comparison, in each system we determined the value of A^+ within one half-mass radius from the center[2] (hereafter $A^+_{\rm rh}$). As expected, in the cases where two reference populations (HB and RGB/SGB) are available, the two resulting values of $A^+_{\rm rh}$ are very similar. We therefore adopted their mean value as the best estimate, and the standard deviation as their error. Since these latter range between 0.01 and 0.03, we attributed an error of 0.02 to all the cases

[1] For M10 here we adopt the quantities obtained in Dalessandro et al. (2013b).

[2] The available *HST* data are sufficient to cover such a region in almost all the selected clusters. Exceptions are M3, M4, and M55, for which complementary wide-field catalogs are also needed, and the clusters NGC 5466 and Palomar 14, which, by virtue of their low density, have been entirely sampled with ground-based observations (with LBC@LBT and MegaCam@CFHT, respectively; see Beccari et al. 2011, 2013). In the case of 47 Tucanae, only the WFPC2 data discussed in Ferraro et al. (2004) have been used.

TABLE 3.1: Structural/Dynamical Parameters and Values of A^+_{rh} for the Program Clusters: Core Radius and Half-mass Radii in Arcseconds (Columns 2 and 3), Logarithm of the Central Relaxation Time in Gyr (Column 4), Value of r_{min} in Arcseconds (Column 5), Value of A^+_{rh} and Its Error (Columns 6 and 7)

Name	r_c	r_h	$\log(t_{rc})$	r_{min}	A^+_{rh}	ϵ
ω Centauri	153.0	443.7	9.86	0.0	-0.010	0.010
Palomar 14	41.0	69.7	9.68	0.0	-0.010	0.010
NGC 6101	61.3	128.2	9.38	0.0	0.030	0.018
NGC 2419	20.0	54.0	10.08	0.0	0.035	0.007
NGC 5466	72.0	213.8	9.42	180.0	0.100	0.020
M55	99.0	215.8	9.00	405.0	0.100	0.020
M4	70.0	308.0	8.00	350.0	0.120	0.014
NGC 288	88.0	167.2	9.19	250.0	0.130	0.014
M53	26.0	98.8	9.08	55.0	0.150	0.014
M5	27.0	124.2	8.43	255.0	0.150	0.020
M10	41.0	139.8	8.26	425.0	0.160	0.000
M13	49.5	148.5	9.03	185.0	0.165	0.007
M2	17.0	57.8	8.48	150.0	0.170	0.028
NGC 6388	7.2	45.4	8.08	32.5	0.190	0.020
NGC 362	13.0	73.8	8.08	515.0	0.200	0.020
M79	9.7	47.5	7.98	325.0	0.250	0.020
M92	14.0	84.0	8.05	250.0	0.255	0.007
M3	30.0	186.0	8.75	125.0	0.260	0.020
NGC 5824	4.4	29.0	8.28	20.0	0.280	0.028
47 Tucanae	21.0	201.6	7.96	200.0	0.290	0.020
NGC 6229	9.5	30.4	8.72	25.0	0.290	0.000
M80	7.0	40.6	7.57	375.0	0.290	0.014
NGC 6752	13.7	194.5	7.37	325.0	0.325	0.021
M75	5.4	29.2	8.00	225.0	0.380	0.020
M30	4.3	109.2	6.79	385.0	0.520	0.000

Note. The values of the structural/dynamical parameters come from Ferraro et al. (2012); Beccari et al. (2013); Dalessandro et al. (2013a); Dalessandro et al. (2013b); Sanna et al. (2014); Dalessandro et al. (2015). For NGC 6101 the value of $\log(t_{rc})$ has been recomputed by following Equation (10) in Djorgovski (1993) for homogeneity with the other clusters.

where only one reference population is available. The values thus obtained are listed in Table 3.1, together with a few key parameters of the program clusters.

3.2.1 Comparison with r_{min} and relaxation time

Figure 3.1 (left panels) shows the cumulative radial distributions of BSSs and REF stars for four GCs in our sample. The labeled values of A^+_{rh} (see also Table 3.1) correspond to the size of the shaded areas: formally zero for ω Cen, which has a non-segregated BSS population (Family I cluster), and up to 0.52 for M30, which is one of the dynamically oldest system (Family III) in the sample, with BSSs much more centrally concentrated than the reference population. As listed in Table 3.1, the parameter is smaller than 0.05 also for the other three GCs with non-segregated BSS populations known so far, namely, Palomar 14, NGC 2419, and NGC 6101. In all the other cases, it assumes larger values, depending on the separation between the BSS and the reference star cumulative distributions. Qualitatively, this is exactly the behavior expected from a reliable indicator of BSS segregation. In the right panels of the figure we plot the radial distributions of the BSS double normalized ratio R_{BSS}

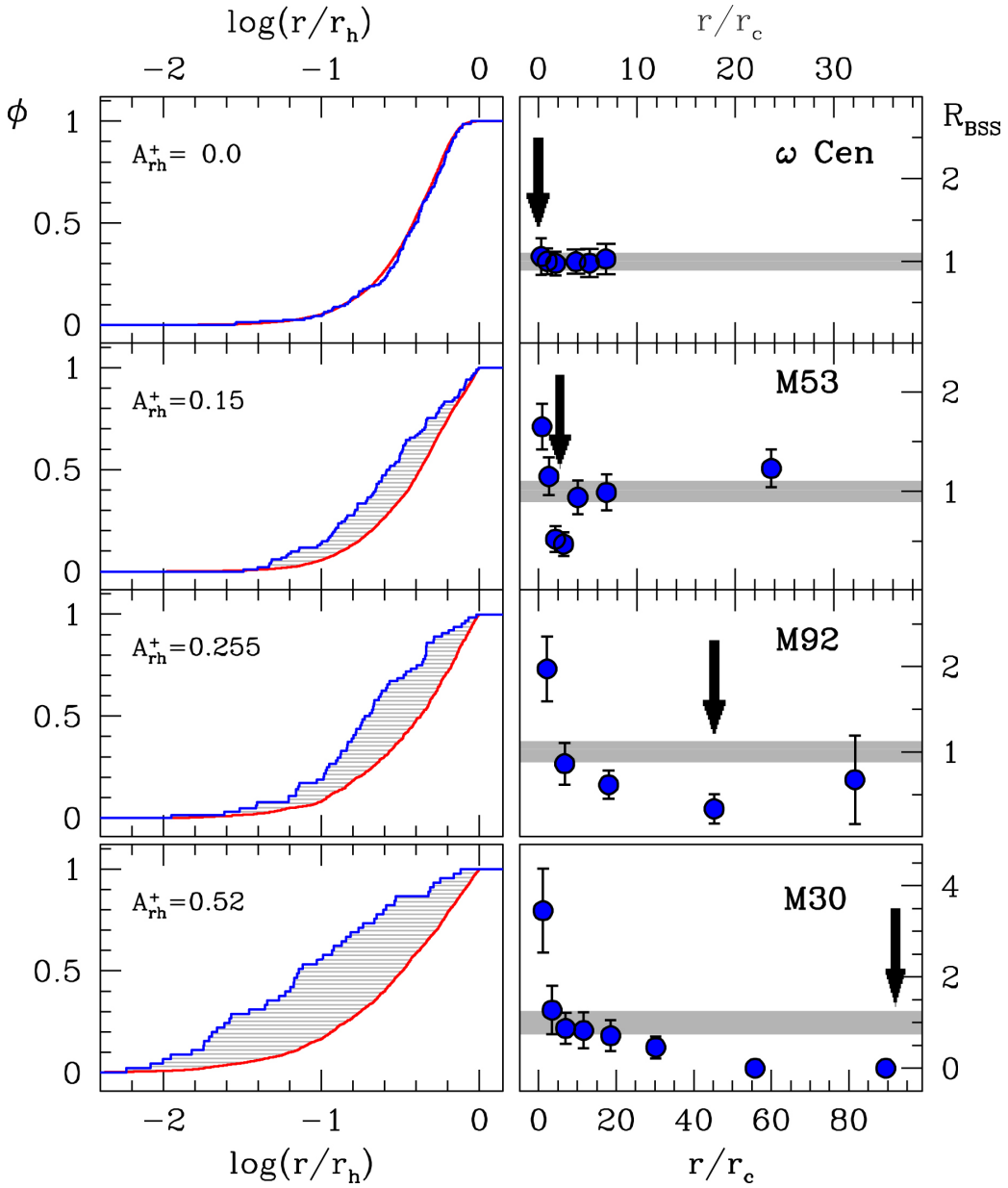

FIGURE 3.1: Left panels: cumulative radial distributions of BSSs (blue line) and REF stars (red line) observed within one half-mass radius (r_h) in four GCs of the considered sample (from top to bottom: ω Centauri, M53, M92, and M30). The size of the area between the two curves (shaded in gray) corresponds to the labeled value of A^+_{rh} (see also Table 3.1). Right panels: BSS-nRD (R_{BSS}, blue circles) for the same clusters shown in the left panels. The black arrows mark the position of the BSS-nRD minimum (r_{min}/r_c). The gray strips schematically show the distribution measured for the REF population.

for the same four clusters, with the black arrows indicating the position of the minimum r_{min}/r_c. The figure clearly shows that the increases of A^+_{rh} seen from top to bottom in the left panels is accompanied by a systematic increase of r_{min}/r_c in the corresponding right panels, thus indicating that these two parameters are mutually linked, as expected if they describe the same phenomenon.

For a closer comparison with results of Ferraro et al. (2012), we investigate the relation between A^+_{rh} and the parameter $\log(r_{min}/r_c)$ for the entire sample of 25 GCs. We point out that, although both these quantities describe the progressive central

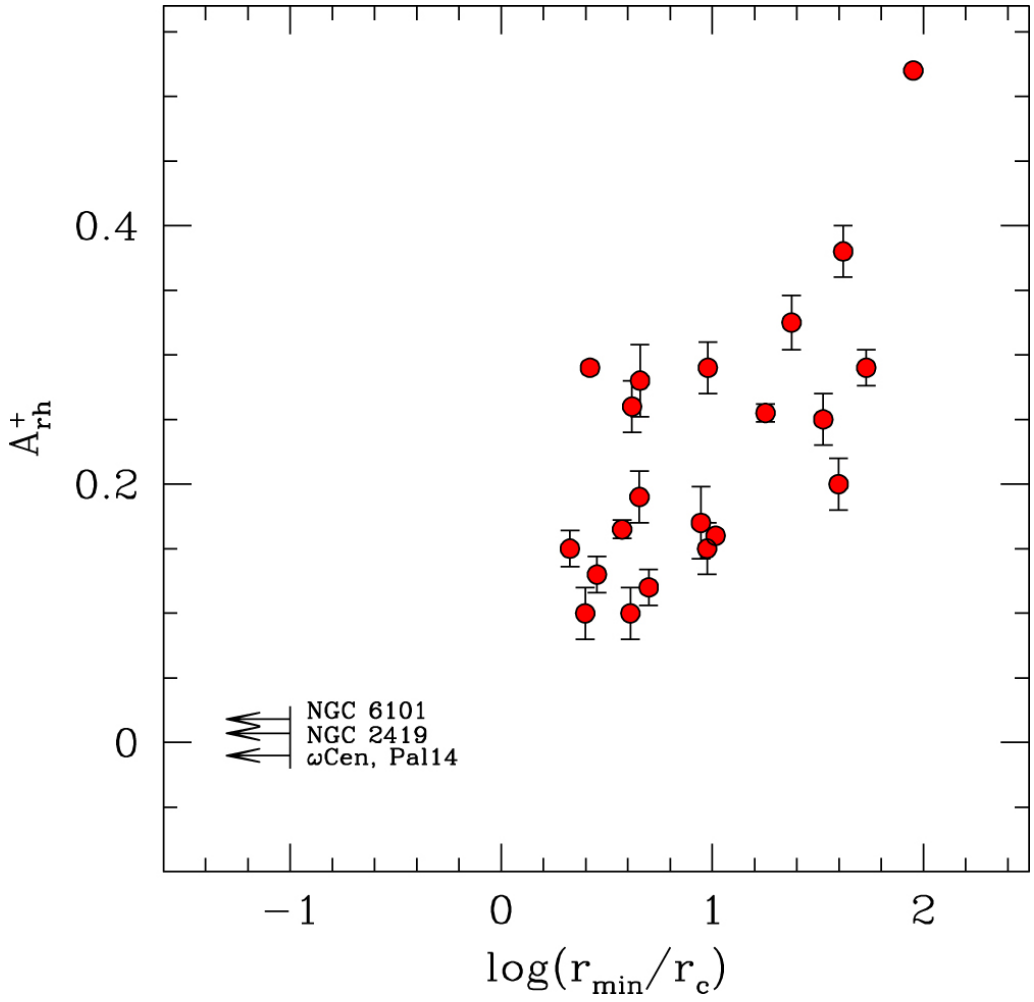

FIGURE 3.2: Parameter A^+_{rh} as a function of the observed position of the BSS-nRD minimum (r_{min}/r_c) expressed in logarithmic units. For Family I clusters, with an everywhere flat BSS-nRD, a value $r_{min}/r_c = 0.1$ has been arbitrarily assumed as an upper limit (see the arrows).

segregation of BSSs, their definitions are completely independent and, in principle, they could be completely uncorrelated. Figure 3.2 shows, instead, that the two parameters are linked through a quite tight and direct correlation. Indeed, the Spearman rank correlation coefficient between A^+_{rh} and r_{min}/r_c is $\rho = 0.77$, corresponding to a probability $P > 99.99\%$ that the two parameters are correlated. The significance remains very high ($P > 99.7\%$) even if one (arbitrarily) excludes from the sample the most extreme points (namely, M30 and the four Family I GCs), or if limiting the analysis to the 13 clusters with the smallest errors on A^+_{rh} ($\epsilon < 0.02$). This confirms that A^+_{rh} and r_{min}/r_c are actually different ways of measuring the same physical mechanism: as discussed in Ferraro et al. (2012), the underlying process is dynamical friction, which, as clusters get dynamically older, progressively removes BSSs at increasingly larger distances from the center (thus generating a minimum at increasingly larger values of r_{min}/r_c) and accumulates them toward the cluster center (thus increasing A^+_{rh}). As discussed in Alessandrini et al. (2016), the process of BSS segregation can be delayed by the presence of dark remnants and, in particular, by a population of stellar mass black holes. This adds another important element to the information contained in the BSS segregation level and the parameters introduced to measure it.

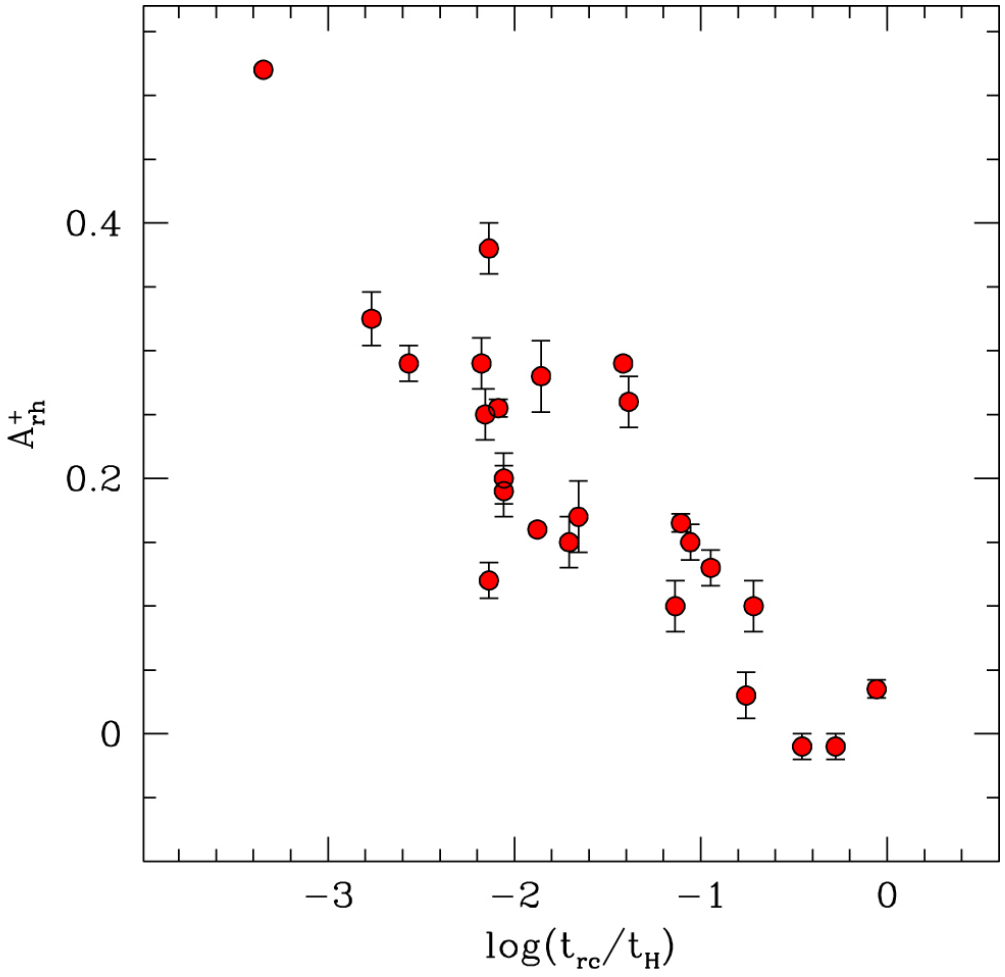

FIGURE 3.3: Relation between the new parameter A^+_{rh} and the logarithm of the cluster central relaxation time (t_{rc}) normalized to the Hubble time ($t_H = 13.7$ Gyr).

The results obtained suggest that A^+_{rh} could be used as an alternative indicator of the level of dynamical evolution experienced by star clusters since their formation, and we should expect that is related to other parameters measuring the dynamical evolution timescale. Indeed, Ferraro et al. (2012) found a nice correlation between the cluster-centric distance of the minimum of the BSS-nRD (r_{min}/r_c) and the central relaxation time of the cluster (t_{rc}). Figure 3.3 shows that the latter is also tightly related to A^+_{rh}, in the sense that the proposed new parameter systematically decreases for increasing values of the relaxation time. The Spearman rank correlation coefficient between A^+_{rh} and t_{rc}/t_H (with $t_H = 13.7$ Gyr being the Hubble time) is $\rho = -0.81$, corresponding to $P > 99.99\%$, and it decreases only to $\rho = -0.63$ ($P = 99.7\%$) if Family I clusters and M30 are (arbitrarily) excluded from the sample. Also the Pearson correlation coefficient is very high ($r = -0.85$), indicating a strong linear correlation between A^+_{rh} and $\log(t_{rc}/t_H)$. As apparent from Figure 3.3, the relation between these two variables shows some scatter. This may indicate that further refinements should be used to measure A^+_{rh}, or, more likely, that the values of t_{rc} empirically estimated by following Djorgovski (1993) are rough approximations of the true relaxation times of GGCs (as discussed, e.g., by Chatterjee et al. 2013 from dedicated Monte Carlo simulations). Besides the scatter, however, our analysis fully

confirms that A^+_{rh} is a powerful indicator of cluster dynamical evolution and, once properly calibrated, it promises to be usable as an alternative, and hopefully more precise, measure of the central relaxation time of GCs.

Summarizing, in the framework of the dynamical clock described Section 1.4.1, originally defined by Ferraro et al. (2012) in terms of the position of the minimum in the BSS-nRD (r_{min}/r_c), the new parameter A^+ corresponds to a new clock-hand, while the engine of the clock remains the same (the dynamical friction process). From the observational point of view, the advantage of this new clock-hand is that it is easier to measure and somewhat less "fragile" than the position of the BSS-nRD minimum. In fact, for determining r_{min} it is necessary to sample the entire cluster radial extension (typically by means of a combination of *HST* and wide-field, ground-based observations), while only the central regions ($r < r_h$), possibly probed just by *HST*, are sufficient to measure A^+_{rh}. Moreover, it does not require any (somehow arbitrary) assumption on the radial binning (which is instead needed to build the BSS-nRD). Finally, from its own definition, r_{min} is located in a region of "low signal", where dynamical friction is removing heavy stars and the number of BSSs reaches its minimum (the so-called "zone of avoidance"; Mapelli et al. 2004, 2006); instead, A^+_{rh} is measured in a "high signal" region, where dynamical friction is accumulating heavy stars and the number of BSSs reaches its maximum. Thus, the proposed change of clock-hand makes the reading of the dynamical clock easier and less prone to low statistics uncertainties.

3.3 The "UV-route" to search for BSSs in GCs

In the previous Section of this Chapter, we showed how to observationally measure A^+_{rh} in a sample of GCs originally used by Ferraro et al. (2012) to define the dynamical clock (see Section 1.4.1). The completeness of the BSS sample used to measure A^+_{rh} is fundamental in order to obtain reliable values of this parameter. In this Section, we show how to properly select BSSs, by means of an "UV-driven" approach, and we quantify the impact of an incomplete sample of BSSs in the determination of A^+_{rh}.

Because of their anomalous position in the CMD, BSSs are, at least in principle, clearly distinguishable from the other cluster stars. However, the construction of complete samples of BSSs can be critical in old star clusters, since the optical emission in these systems is primarily dominated by a large population of much brighter (several $10^2 \times L_\odot$) and cool ($3500 - 5000$ K) giants. Clearly, this task is particularly difficult (even with the *HST*) in very crowded enviroments, as those observed in the central regions of high-density GCs (several 10^{5-6} stars per cubic parsec). However, because of their hot surface temperatures, BSSs appear among the brightest objects at UV wavelengths, where red giants are, instead, particularly faint. Hence the combination of high angular resolution and UV imaging capabilities (as offered by the *HST*) is the only solution to significantly reduce the level of crowding and acquire complete samples of BSSs even in the core of highly concentrated GCs. Our research group promoted the so-called *"UV route" to the study of BSSs in GCs* starting from approximately 20 years ago (see Ferraro et al. 1997, 1999a, 2001, 2003a). This approach allowed our group to derive complete samples of BSSs in several GGCs, including systems of very high central density (see Lanzoni et al. 2007a,b,c; Dalessandro et al. 2008, 2009; Contreras Ramos et al. 2012; Sanna et al. 2012, 2014).

The dataset recently acquired within the *HST* UV Legacy Survey of GGCs (Piotto et al., 2015; see also Section 3.3.1) allows the extension of this approach to a significantly larger number of clusters. The complete study of the BSS population

in most of the surveyed GCs will be discussed later in this Chapter (see also Ferraro et al. 2018b), while in this Section we present the first results obtained for four intermediate/high density systems. The specific aim of this Section is to illustrate the advantages of the *"UV-guided"* search, with respect to the *"optical-driven"* selection (e.g. Soto et al. 2017), for the identification of complete samples of BSSs.

3.3.1 The *HST* UV Legacy Survey of GGCs

The data used in this Section have been secured as part of the *HST* UV Legacy Survey of GGCs (GO-13297; PI: Piotto) and in two pilot companion projects (GO-12311 and GO-12605; see Piotto et al. 2015). This survey includes 57 GGCs, which have been observed using the F275W, F336W and F438W filters of the Ultraviolet and Visual (UVIS) channel of the Wide Field Camera 3 (WFC3) onboard the *HST*. The selected targets have already been observed in the optical bands (F606W and F814W) in the previous ACS Survey of GGCs (GO-10775, PI: Sarajedini; Sarajedini et al. 2007) and all have a color excess $E(B-V) < 0.1$[3]. The selected targets are a representative sample of the GGCs for what concerns mass, metallicity and structural parameters.

The main aim of this survey is the study and characterization of multiple populations (Piotto et al. 2015). Indeed, this filter combination provides the ideal set to generate pseudo-colors able to maximize the sequence splitting in the CMD, typical of multiple stellar populations (see e.g., Milone et al. 2013). However, the survey also offers the possibility to construct diagrams where an appropriate selection of hot populations (like BSSs) can be performed. In particular, to optimally study BSSs we adopted a "pure" UV diagram: the $(m_{\rm F275W}, m_{\rm F275W} - m_{\rm F336W})$ CMD.

3.3.2 The photometric database and data reduction

The four clusters studied in this Section (namely, NGC 2808, NGC 6388, NGC 6541 and NGC 7078) are massive ($M_V < -8.5$, $M > 5 \times 10^5 M_\odot$), with high central density ($\log \rho_0 > 4.6$ in units of $L_\odot$ pc^{-3})[4] and moderately extended core radius ($7'' < r_c < 15''$), and they span a large range in metallicity ($-2.4 <$[Fe/H]< -0.55; all parameters are from Harris, 1996). Hence, the four selected clusters represent the ideal systems to test the advantages of BSS searches in the UV domain over those carried out using the optical band.

The WFC3/UVIS camera consists of two twin chips, each of 4096×2051 pixels and with a pixel scale of $0.0395''$, resulting in a total field of view of $\sim 162'' \times 162''$. For each cluster several images were obtained in the F275W and F336W bands (see Table 3.2 for details). To allow a better subtraction of Charge-Coupled Device (CCD) defects, artifacts and false detections, different pointings dithered by several pixels, and in some cases also rotated by $\sim 90°$ (NGC 6541) or $\sim 70°$ (NGC 6388), have been acquired in each band.

For the photometric analysis we used the set of images processed, flat-fielded, bias subtracted and corrected for charge transfer efficiency (CTE) by standard *HST* pipelines (`_flc` images). Pixel-area effects have been accounted for by applying the

[3]Reddening has a stronger effect at shorter wavelengths. Therefore, it is extremely expensive to observe reddened clusters at UV wavelengths, in terms of exposure time. Hence, this reddening selection is justified by the need of observing a large number of clusters while keeping the observing time for each cluster as low as possible.

[4]Two of them (namely NGC 7078 and NGC 6541) are cataloged as core collapsed clusters.

TABLE 3.2: Number of exposures (n) and exposure times in seconds (t_{exp}) of the data used to study the BSS population in the four program clusters.

Filter	F275W	F336W
Name	$n \times t_{exp}$	$n \times t_{exp}$
NGC 2808	12×985	6×650
NGC 6388	2×888	4×350
	2×889	
	2×961	
	2×999	
NGC 6541	2×708	4×300
	2×758	
NGC 7078	3×615	6×350
	3×700	

most updated pixel-area-maps (PAM images) to each image by means of IRAF tasks.[5] The analysis has been performed independently on each chip by using DAOPHOT IV (Stetson, 1987). For each image we selected several ($\sim$ 200) bright, unsaturated and relatively isolated stars to model the PSF, for which we used a spatially variable Moffat function. A first star list has been obtained for each frame by independently fitting all the star-like sources at 3σ above the local background. To take advantage of the reduced crowding conditions at UV wavelengths, we created a *master list* composed of stars detected in a sub-sample of at least half of the total number of F275W images available for any given cluster (see Table 3.2). Then, at the corresponding positions of the stars present in the *master list*, a fit was forced with DAOPHOT/ALLFRAME (Stetson, 1994) in each single frame obtained through each filter. For each star, multiple magnitude estimates obtained in each filter were homogenized by using DAOMASTER and DAOMATCH, and their weighted mean and standard deviation were finally adopted as the star magnitude and photometric error. The final catalog of each cluster has been finally cross-correlated with those published in the Survey intermediate release (Piotto et al., 2015)[6]. In all cases, we found thousand stars in common, that allowed us to: *(i)* report the final instrumental magnitudes in each filter to the VEGAMAG photometric system, and *(ii)* convert the instrumental coordinates into the absolute astrometric system. For NGC 2808, NGC 7078 and NGC 6388 we used the stellar PMs of Bellini et al. (2014), while for NGC 6541 the PM measures available in the on-line catalogs at the Survey web page were adopted.

3.3.3 The BSS selection

To define selection criteria for the BSS population that can be consistently adopted in all clusters (see, e.g., Leigh, Sills, and Knigge 2007, 2011) we followed a fully empirical approach. We defined a sort of "normalized" CMD, with the magnitudes and the colors arbitrarily shifted to locate the MS-TO at approximately $m^*_{F275W} = 0$ and $(m_{F275W} - m_{F336W})^* = 0$. This allows us to locate the BSS sequence in the same portion of the diagram independently of the cluster distance and metallicity.

[5] IRAF (Image Reduction and Analysis Facility) is distributed by the National Optical Astronomy Observatory, which is operated by the Association of Universities for Research in Astronomy, Inc., under cooperative agreement with the National Science Foundation.

[6] The intermediate release was available upon request at the web page http://groups.dfa.unipd.it/ESPG/treasury.php at the time this work was carried out. At present, the final release is available at the same web page.

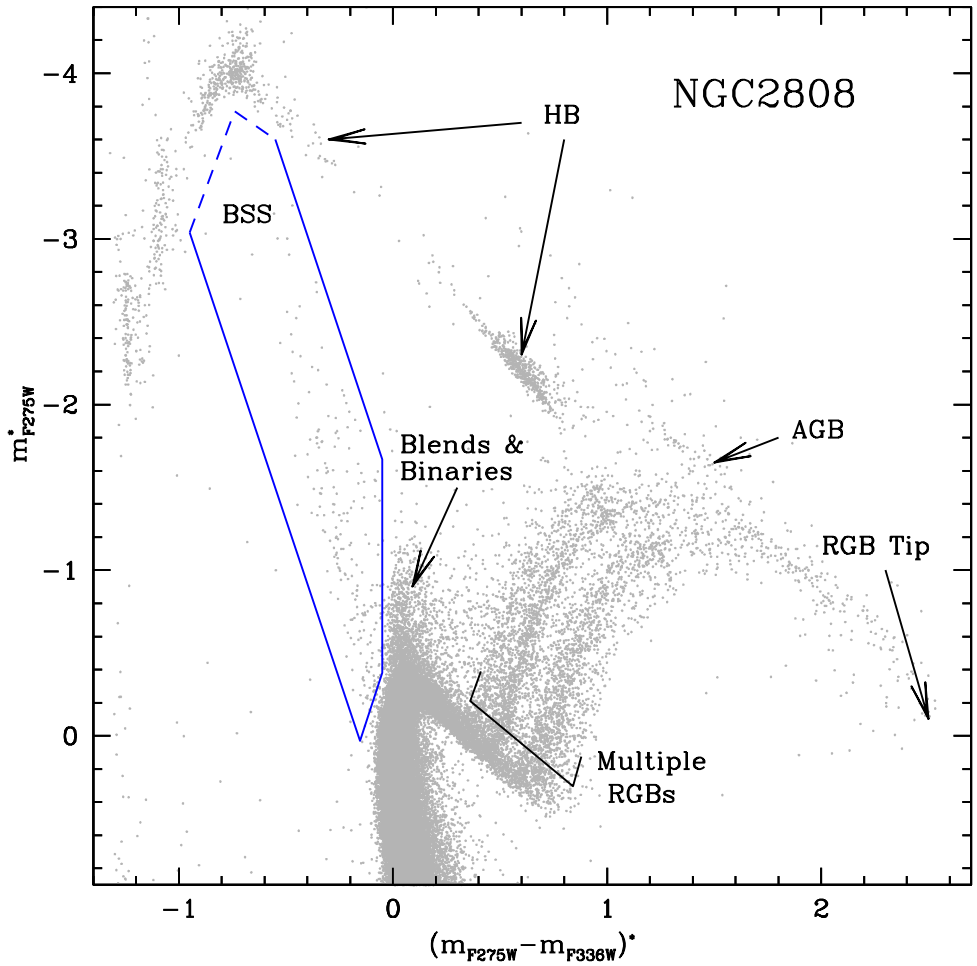

FIGURE 3.4: "Normalized" UV CMD of NGC 2808: magnitudes and colors have been arbitrarily shifted to locate the MS-TO at $m^*_{F275W} = 0$ and $(m_{F275W} - m_{F336W})^* = 0$. The location of the main evolutionary sequences is labelled. Clearly, the brightest objects in this diagram are hot HB stars and BSSs, while cool giants, as RGB and AGB stars, are significantly less luminous. The box adopted for the BSS population selection is drawn in blue. The brightest boundary of the box is plotted as dashed line, since it can vary for cluster-to-cluster depending on the HB morphology (see Section 3.3.3). The locus expected to be populated by photometric blends is also shown.

Figure 3.4 shows the "normalized" UV CMD of NGC 2808 (adopted as template). For the sake of reference, the position of the main evolutionary sequences in the diagram is also labeled. As can be seen, the hot stars belonging to the blue tail of the HB dominate the UV emission, while RGB and AGB stars are significantly fainter. As apparent, this diagram allows an efficient and reliable selection of BSS samples. Also the region where optical blends (and possibly binaries) are expected to be located is easily recognizable in the selected CMD (see the well visible plume just above the MS-TO), and their contamination to the BSS sample is therefore minimized.

The selection box has been defined in order to be virtually applicable to all the clusters observed in the *HST* UV Legacy Survey of GGCs. In this diagram, BSSs define a clean sequence populating a $\sim$ 2 mag-wide strip spanning approximately 3 magnitudes, diagonally crossing the diagram from the cluster MS-TO, toward the blue extension of the HB. Hence the selection box is defined along two parallel lines including the bulk of the BSS population. The equations of the two lines are:

TABLE 3.3: Parameters of the program clusters: total number of BSSs detected in the WFC3 field of view (column 1); half-mass radius in arcseconds (column 2), logarithm of the central relaxation time in Gyr (column 3), value of A^+_{rh} and its error (columns 5 and 6).

Name	$N_{\rm BSS}$	r_h	$\log(t_{\rm rc})$	A^+_{rh}	ϵ
NGC 2808	215	48.0	8.24	0.23	0.01
NGC 6388	288	45.4	8.08	0.19	0.02
NGC 6541	94	63.6	7.80	0.25	0.01
NGC 7078	167	60.0	7.84	0.34	0.02

$$m^*_{\rm F275W} = 3.86 \times (m_{\rm F275W} - m_{\rm F336W})^* - 1.48 \quad (3.1)$$

$$m^*_{\rm F275W} = 3.86 \times (m_{\rm F275W} - m_{\rm F336W})^* + 0.56 \quad (3.2)$$

We also define a red boundary to separate BSSs from the supra-MS plume. A vertical line at $(m_{\rm F275W} - m_{\rm F336W})^* = -0.05$ has been found to efficiently exclude the bulk of the supra-MS plume, which can be more or less populated, depending on the crowding conditions of each system. The faint edge, needed to separate BSSs from the MS-TO stars, has been conservatively set at more than 5σ from the mean color of the brightest portion of the MS-TO stars. The equation defining this edge is:

$$m^*_{\rm F275W} = -4 \times (m_{\rm F275W} - m_{\rm F336W})^* - 0.58 \quad (3.3)$$

In principle a bright/blue edge of the box is needed to distinguish very bright BSSs from stars populating the blue portion of the HB (when present). However, in order to study the frequency, distribution and luminosity extension of the BSS population at its bright end, we preferred not to set any formal boundary on this side of the box. In fact, a precise boundary set on the basis of the CMD of GCs with blue HB would cause an artificial cut-off of the brightest portion of the BSS sequence in clusters with red HB morphology. Moreover, we emphasize that only a few objects are expected in this (very bright) portion of the BSS sequence and different assumptions on the bright/blue boundary of the selection box therefore make very little difference. Hence, in clusters with extended HB morphology, the boundary (see the dashed lines in Figure 3.4) has been set by considering the mean colors and the distribution of the HB stars, while no formal boundary has been adopted for red HB systems. Once the entire sample of GCs is analyzed, this approach will allow us to estimate the fraction of very bright BSSs that can potentially contaminate the blue portion of the HB in clusters with an extended HB.

The BSS selection box defined according to the above relations is shown in Figure 3.4. We emphasize that slightly different assumptions about its boundaries do not alter the main results presented here. Figure 3.5 highlights the BSS populations thus selected in the four program clusters, shown in the "normalized" UV CMDs. Note that in the case of NGC 6388, only BSSs more luminous than $m^*_{\rm F275W} = -4 \times (m_{\rm F275W} - m_{\rm F336W})^* - 1.71$ have been considered because of the large photometric errors affecting the MS-TO region, which prevented a safe BSS selection at fainter magnitudes. The total number of BSSs selected in each cluster is listed in Table 3.3.

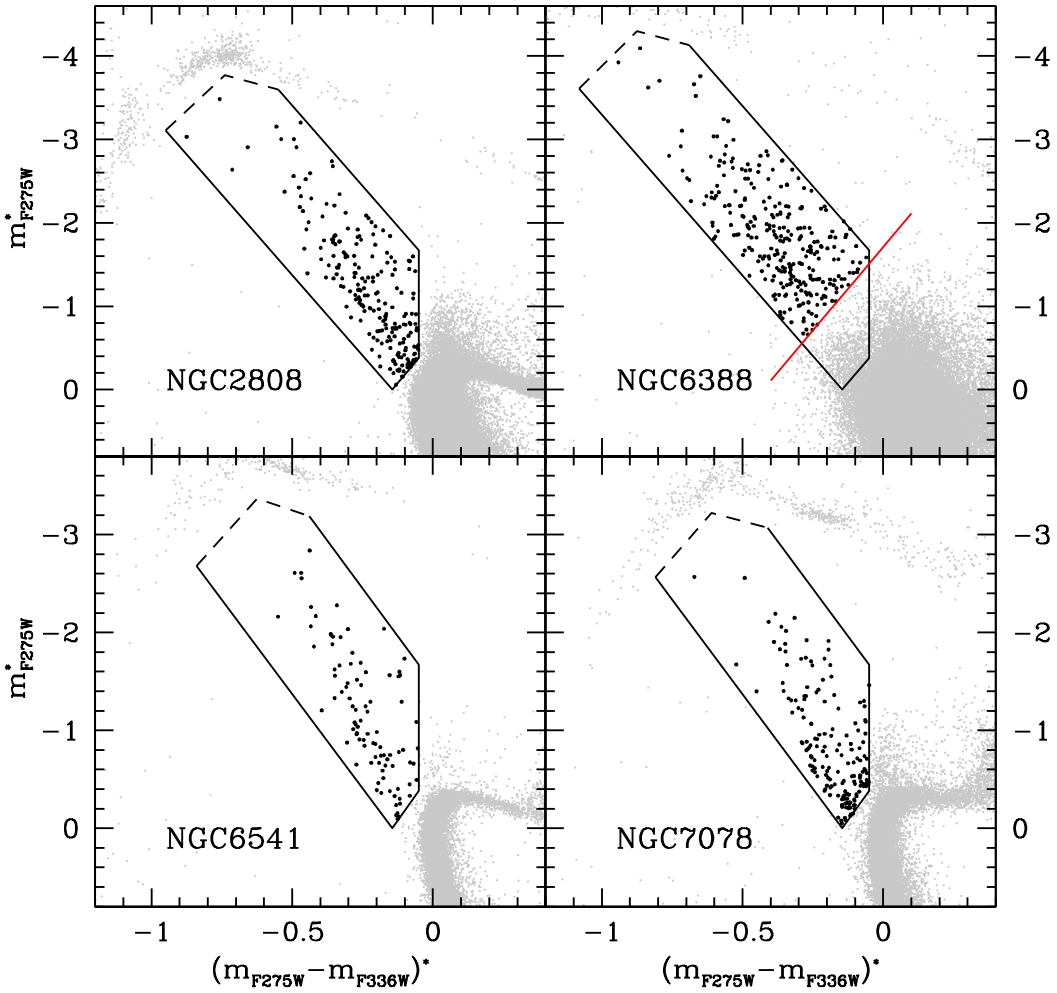

FIGURE 3.5: Normalized UV CMDs (as in Figure 3.4) of the four program clusters zoomed in the BSS region, with the selected BSS populations highlighted with black dots. The selection box defined in Figure 3.4 is also plotted in each panel. In the case of NGC 6388 only stars brighter than the red line have been considered because of the large photometric errors affecting the MS-TO region.

3.3.4 Comparison to previous BSS selections and online catalogs

In the recent years, several works aimed at characterizing the properties of BSSs in GGCs have been published (see, e.g., Leigh, Sills, and Knigge, 2007; Knigge, Leigh, and Sills 2009; Leigh et al. 2013). Most of them are based on online catalogs obtained from the ACS GC Survey (Sarajedini et al., 2007). Unfortunately, those catalogs turn out to be (sometimes severely) incomplete in the inner regions of high-density clusters. This is because the ACS GC Survey was designed to secure a series of dithered and deep images in the optical band (F606W and F814W filters), with the aim of properly sampling the entire extension of the MS. Hence, the bright giant stars are heavily saturated in those images and their combined blooming effect strongly prevent the proper measuring of fainter stars in relevant portions of the central regions of high-density GCs. In some cases the short exposure (only one per filter) concurrently acquired in each *HST* visit alleviates, but does not completely solve, the problem, since the gap between the ACS chips remains not sampled at all (and it

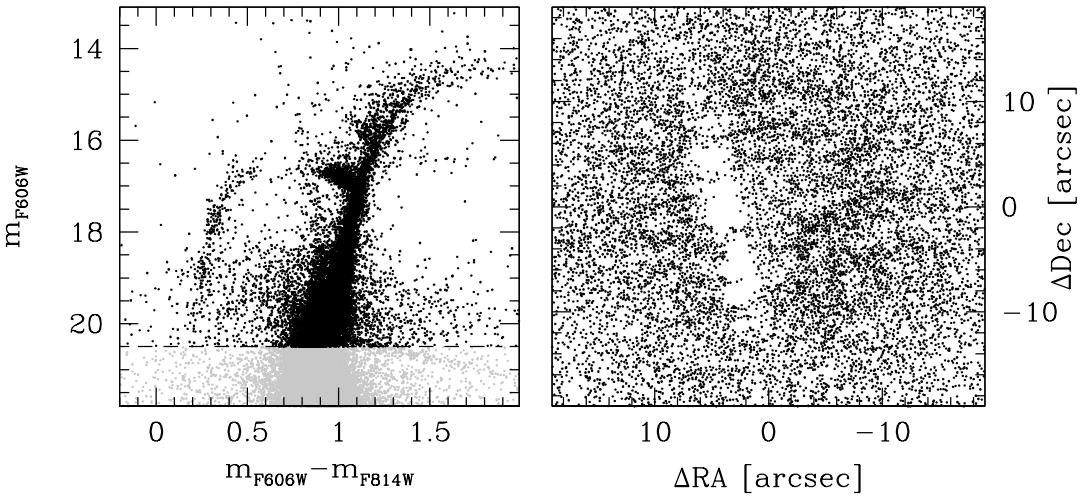

FIGURE 3.6: Left panel: optical CMD of NGC 6388 obtained from the online ACS GC Survey catalog. Right panel: map of the central $40'' \times 40''$ of NGC 6388 obtained from all the stars brighter than $m_{F606W} = 20.5$ in the online ACS GC Survey catalog (see black dots above the dashed line in the left panel). The empty region is due to the ACS inter-chip gap.

crosses the central regions of most of the clusters). The combination of these effects produces large incompleteness in the samples of stars measurable above the MS-TO (including most of the BSSs), and this is well visible even without specific completeness estimates. In fact, while faint stars are detected in any cluster region thanks to the dithering pattern adopted during the observations, the ACS inter-chip gap clearly appears in the cluster map built by using only stars brighter than the MS-TO in the ACS GC Survey catalogs of any high-density cluster. Figure 3.6 dramatically demonstrates the problem for the case of NGC 6388. Of course any other catalog that has been constructed starting from the (*optical-driven*) ACS GC Survey samples suffers from the same bias. In the following we discuss a few recent cases.

3.3.4.1 Comparing BSS selection boxes

Based on the ACS GC Survey catalogs, Leigh, Sills, and Knigge (2011) presented a thoughtful definition of the BSS selection box in the optical CMD. Unfortunately no direct cluster-to-cluster comparison can be performed with that work, since no one of the four clusters discussed here is in common with the sample of Leigh, Sills, and Knigge (2011). However the detailed description of how they defined the BSS selection box allows us to compare our (UV-selected) BSS samples with what would be obtained by using their criteria.

Figure 3.7 and Table 3.4 illustrate the case of NGC 2808. In the upper-left panel of Figure 3.7 we show the BSS selection in the UV diagram, made by using the box discussed in Section 3.3.3. A total number of 215 BSSs is found. Of these, 18 are completely missed in the optical catalog (see the red dots in the upper-left panel of Figure 3.7), i.e. no optical counterpart to these sources can be found in the optical data set. The bottom-left panel of Figure 3.7 shows the optical CMD of NGC 2808 from the Sarajedini et al. (2007) catalog, with the UV-selected BSSs highlighted as black circles and the Leigh, Sills, and Knigge (2011) selection box drawn. As apparent, this box includes the bulk of the UV-selected BSSs (113 out of 215), indicating that our selection criteria agree with those of Leigh, Sills, and Knigge (2011). However the comparison also highlights that using the optical CMD (instead of the UV diagram) can have two opposite consequences: (1) a loss of genuine BSSs, and (2)

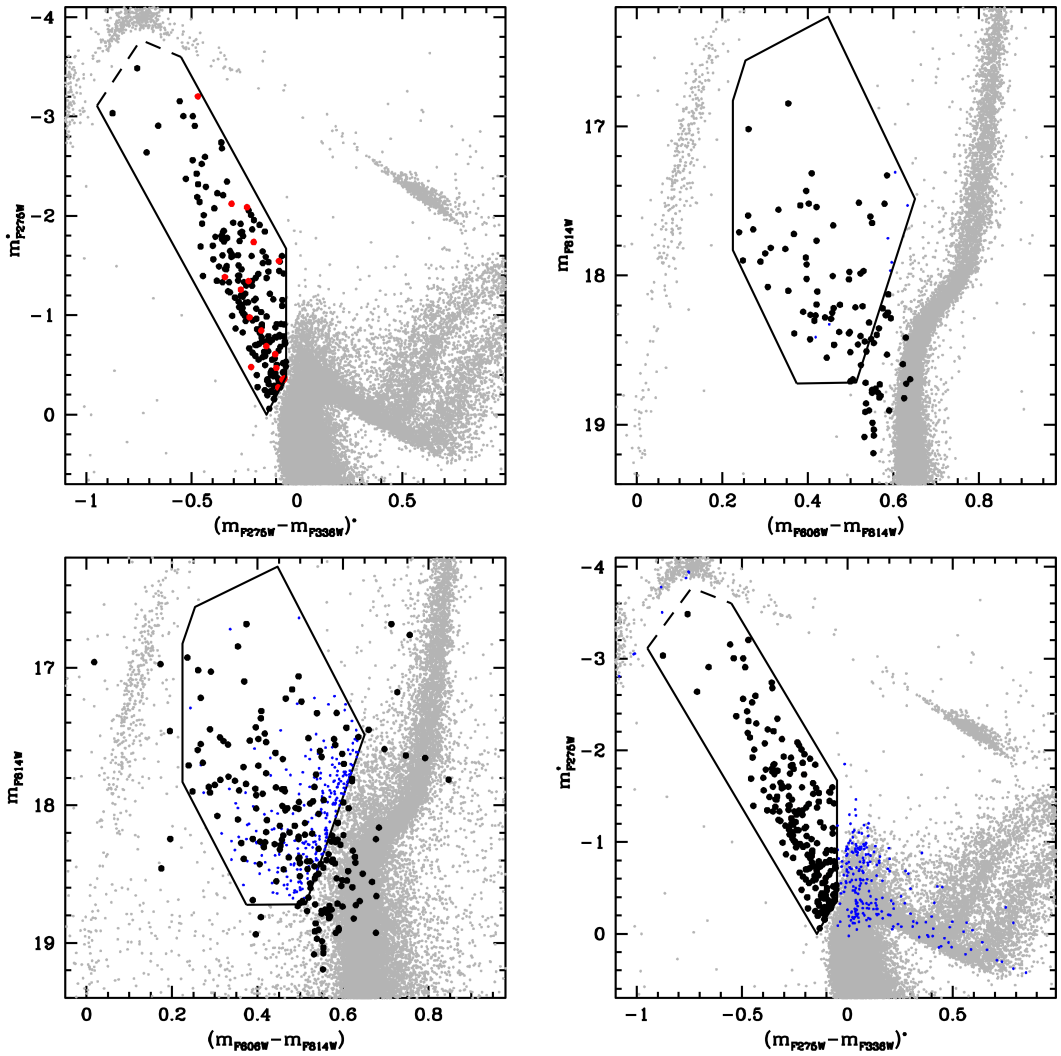

FIGURE 3.7: Comparison between UV-based and optical-based BSS selections in the case of NGC 2808 (see also Table 3.4). Upper left panel: The 215 BSSs selected in the UV CMD are shown as large dots. The 18 sources for which no counterpart has been found in the optical catalog are highlighted in red. Bottom left panel: Optical CMD obtained from the ACS GC Survey catalog (Sarajedini et al. 2007), with the BSS selection box built by following the prescriptions of Leigh, Sills, and Knigge (2011) drawn. The 197 UV-selected BSSs having an optical counterpart are plotted as large black dots. As it can be seen, a significant number of them (84) lie outside the BSS optical selection box, while a large number (235) of "intruders" (small blue dots) is found within the BSS optical box. Bottom-right panel: UV CMD and UV-selected BSSs (as in the upper-left panel), with the position of the "intruders" marked with small blue dots (as in the bottom-left panel). As it can be seen, in the UV CMD these objects are MS/SGB/RGB stars and blends. Upper-right panel: Optical CMD (same as in the bottom-left panel) obtained by considering only stars with good photometry (see Milone et al. 2012). The 95 UV-selected BSSs with good optical photometry are shown as large black dots. The optical BSS selection box (following Leigh, Sills, and Knigge 2011) is also drawn: it includes 32 UV-selected BSSs.

the inclusion of several "intruders" (i.e., stars falling within the optical BSS selection box, that, however, are blends or MS/SGB/RGB stars in the UV CMD; they are plotted as small blue dots in the Figure). In fact, several (84) UV-selected BSSs lie outside the optical selection box. Most of them are located close to the MS-TO, in the region where the BSS sequence merges into the MS. This shows that the UV diagram allows

TABLE 3.4: Number of UV-selected BSSs with good optical photometry (first row, see Milone et al. 2012), poor optical photometry (second row), and no optical counterpart (third row), found within the UV selection box (N_{UV-BSS}, column 2), within the optical selection box ($N_{UV-BSS,IN}$, column 3), and outside the optical selection box ($N_{UV-BSS,OUT}$, column 4) for NGC 2808. The last column lists the number of "intruders", i.e., stars that are found within the optical selection box but are not selected as BSSs in the UV diagram. The optical selection box has been defined following the prescription of Leigh, Sills, and Knigge (2011). See Section 3.3.4.1 for a detailed discussion.

Sample	N_{UV-BSS}	$N_{UV-BSS,IN}$	$N_{UV-BSS,OUT}$	Intruders
Good opt. photometry	102	62	32	7
Poor opt. photometry	95	51	52	235
No opt. counterpart	18	-	-	-
Total	215	113	84	242

a safe exploration of a fainter portion of the BSS luminosity function, while a proper selection of BSSs in the optical CMD is limited to brighter objects. A few other stars lie outside the optical box probably because their optical photometry is perturbed by the presence of bright giants. In addition, a large number (235) of sources that are not UV-selected BSSs is found within the optical box (blue dots). The location of these "intruders" in the UV diagram is shown in the bottom-right panel of the Figure: clearly these are MS/SGB/RGB stars and blends, which erroneously fall within the BSS selection box in the optical CMD because of their poor photometry. The optical CMD obtained by using only stars with good photometry (see Milone et al. 2012) is plotted in the upper-right panel of Figure 3.7 and it shows that, in fact, essentially all the "intruders" (but 7) have disappeared. This high quality optical CMD confirms that most of the UV-selected BSSs fall within the Leigh, Sills, and Knigge (2011) box and the majority of those found beyond the box are located close to the MS-TO. However, only 62+7 stars would have been classified as BSSs based on this diagram, while a total of 215 BSSs is found in the UV. By considering the numbers listed in Table 3.4 we can conclude that, in the specific case of NGC 2808, an analysis carried out in the optical band would have safely sampled (by considering only stars with good optical photometry) about 35% of the UV-selected population (69 vs 215), while $\sim$ 15% of them would have been lost because these are too faint to be properly separated from the MS-TO in the optical. On the other hand, the entire optical sample (including objects of poor photometry) would be completely dominated by "intruders" (235), thus making the BSS selection meaningless.

This study clearly highlights the benefits of using UV-driven (instead of optical-driven) catalogs for the proper selection of BSS samples, independently of the precise boundaries adopted for the selection box. It demonstrates that the effect of crowding in the central regions of high density clusters can (1) prevent the identification of BSSs that are too close to bright giants (red dots in the upper left panel), (2) make inaccurate the photometry of genuine BSSs, thus "moving them out" of a reasonably drawn selection box (bottom-left and upper-right panels of Figure 3.7) and (3) "move within" the BSS selection box a large number of MS/SGB/RGB stars and blends (bottom-right panel of Figure 3.7).

3.3.4.2 Comparison to online catalogs

Simunovic and Puzia (2016, hereafter SP16) present PM-cleaned catalogs of BSSs in 35 GGCs. PMs have been measured from the comparison between the stellar

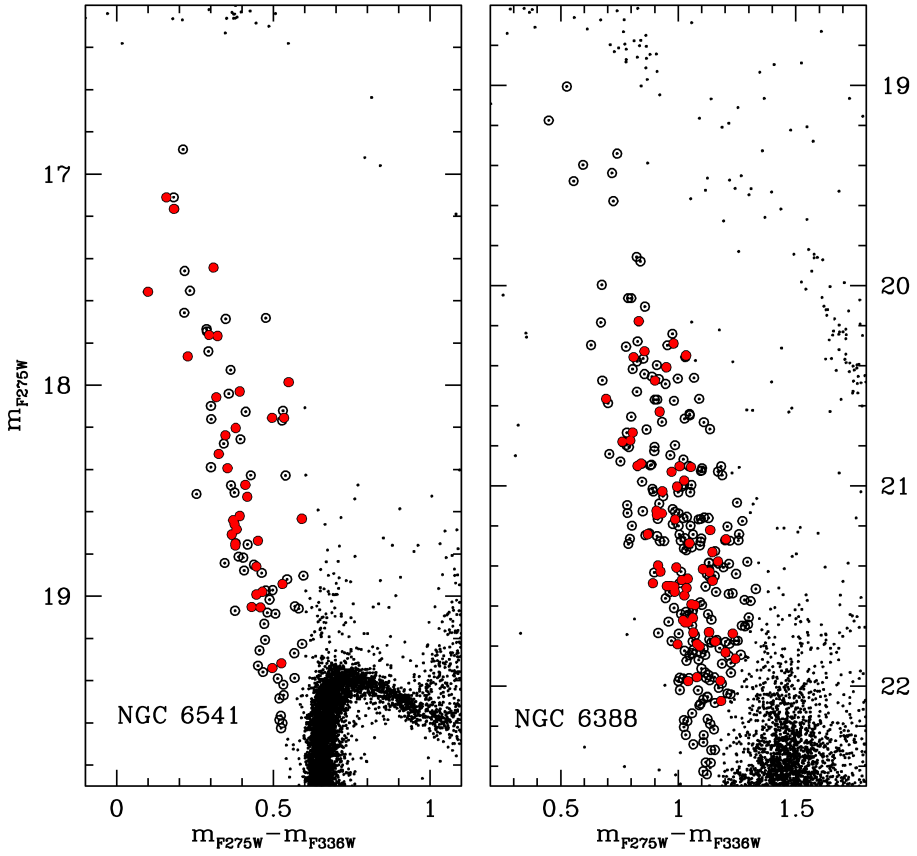

FIGURE 3.8: UV CMDs of NGC 6541 (left) and NGC 6388 (right), zoomed in the BSS region. The large empty circles mark the BSS population detected with the *UV-guided* approach in this work. The filled red circles mark the BSSs also present in the *optical-driven* and PM-cleaned catalogs of SP16. Clearly, a large fraction of BSSs is missed in the latter.

centroids listed in the ACS GC Survey catalogs and those measured in the F336W exposures of the UV Legacy Survey of GGCs. Hence, by construction, these catalogs include only stars that are present in the (*optical-driven*) ACS GC Survey sample, and therefore suffer from the bias described above. In addition, only stars with high-quality flags have been used, thus further reducing the number of stars listed in the online PM-cleaned BSS catalogs. In order to perform a quantitative comparison, we discuss the specific case of the two clusters in common with SP16, namely NGC 6541 and NGC 6388. SP16 list 41 BSSs in their catalog of NGC 6541, also including evolved BSSs (EBSSs), i.e., objects that already evolved off the MS phase. Our UV-driven selection identifies 94 BSSs in NGC 6541, and no objects have been excluded on the basis of the PM measurements. Our sample includes 35 BSSs in common with SP16, while their remaining 6 stars correspond, in the UV diagram, to a bright object too close to the HB to be safely classified as a BSS, and 5 EBSSs. Thus, a total of 59 BSSs (representing 63% of the entire sample) are missed in the SP16 catalog (see Figure 3.8, left panel), possibly because *these objects* did not match the quality-flag criteria adopted by SP16.

In NGC 6388, our UV-driven selection identifies 288 candidate BSSs. Instead, only 74 BSSs and EBSSs are listed in the SP16 online catalog. Out of these, 64 BSSs are in common with our sample (see Figure 3.8, right panel), while the remaining 10 are located, in the UV diagram, in the region of stellar blends or EBSSs. Hence, the optical-driven, PM-cleaned and quality fit-selected sample of BSSs discussed in

SP16 includes only a small fraction (22%) of the potential global population of NGC 6388. About 30 UV-selected BSSs are lacking in the optical sample just because they fall in the ACS gap (see Figure 3.6). On the other hand, the Galactic field contamination is known to be significant in this cluster and the PM measurements of Bellini et al. (2014) suggest that this is particularly relevant for the faintest portion of the BSS sequence (see also Figure 6 in SP16). Unfortunately, the high-precision PMs currently available for NGC 6388 (Bellini et al., 2014) do not include the very center of the cluster, since they are based on the ACS GC Survey master frame and therefore are also affected by the presence of the ACS gap (a more sophisticated approach able to include also the innermost regions of the cluster is planned as part of the *HST* UV Legacy Survey of GGCs). Hence, deeper analyses of the BSS population in NGC 6388 are unfeasible at the moment. These examples clearly demonstrate that, while the PM-cleaned BSS catalogs presented by SP16 allow a secure screening of cluster members useful for spectroscopic follow-ups, they include only a small fraction of the cluster BSS population, and thus cannot be used to derive global properties and perform quantitative studies aimed at exploring, for example, the BSS radial distribution, central segregation, and the number ratio of BSS with respect to the cluster "normal" stars.

Soto et al. (2017) present a preliminary public release of photometric catalogs for the 57 GGCs observed in the UV Legacy Survey of GGCs. These catalogs have been built by assigning the magnitudes measured in the F275W, F336W and F438W filters to all the stars listed in the (*optical-driven*) ACS GC Survey samples. Hence, by construction, also these catalogs suffer from the problems discussed above and are not suitable for quantitative studies of the evolved stellar populations (brighter than the MS-TO). The detailed comparison between the Soto online catalogs and the "UV-guided" samples discussed in this Section offers the opportunity to quantitatively study the distribution (both in space and in the CMD) of the stars missed in the *optical-driven* approach. For the four clusters under study, Figure 3.9 shows the UV CMD and the spatial distribution of all the stars detected in the *UV-guided* approach that are missed in the Soto online catalogs. As apparent, they are distributed along all the evolved sequences in the CMD (HB, RGB, BSS and WD sequences) and a significant number of stars is also missed in the MS-TO and upper MS regions. The number of missed stars depends on the cluster structure: by considering only the brightest portion of the CMD (approximately brighter than the cluster MS-TO), it varies from near 200 in NGC 6541, up to more than five thousand in NGC 6388. The right panels show the spatial distribution of the missed stars, revealing that they are mainly concentrated in the innermost regions, as it is expected in the case of incompleteness due to an effect of stellar crowding. To further illustrate the problem, in Figure 3.10 we plot the cumulative radial distribution of the stars lost in the optical-search for the four program clusters. As it can be seen, the vast majority ($\gtrsim 70\%$) of the missed stars is located within the innermost 20″-30″ from the cluster center, thus demonstrating the benefits of using UV-driven over optical-driven catalogs to study the radial distributions and population ratios of evolved stars.

This analysis shows also that the online *optical-driven* catalogs should be used with caution when quantitative studies of any evolved stellar population is attempted.

3.3.5 Measuring the level of radial segregation of BSSs

Here we measure $A^{+}_{\rm rh}$ for the four clusters from the *HST* UV Legacy Survey of GGCs that we studied to show the advantages of the "UV driven" approach.

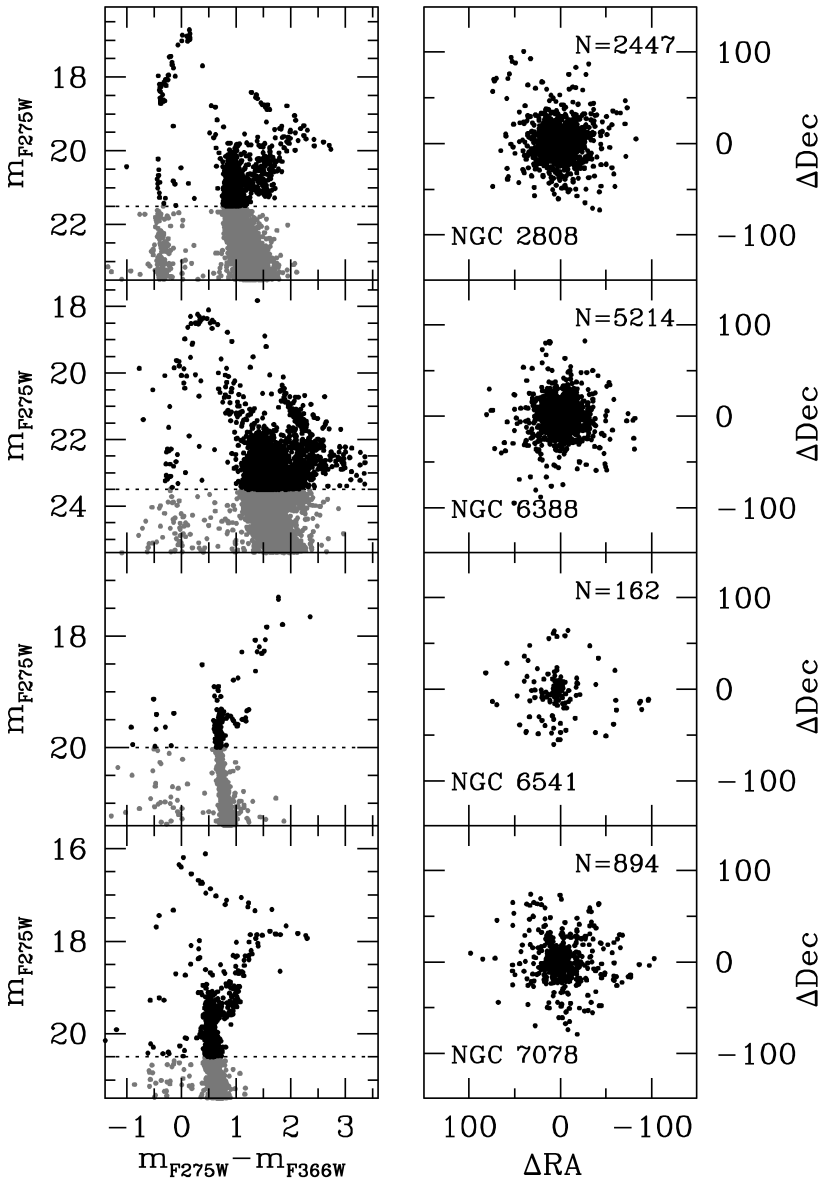

FIGURE 3.9: Left: UV CMDs of the stars missed in the optical-driven catalogs of Soto et al. (2017) for the four program clusters. Right: spatial distribution (in arcseconds and with respect to the cluster center) of the missed stars brighter than the limits marked by the dashed lines in the left panels. The number of the missed stars is labelled in each panel.

NGC 6388 is one of the clusters discussed in Section 3.2, where the BSS sample adopted was obtained from *HST*-WFPC2 observations by Dalessandro et al. (2008), which was complete but limited only to the brightest portion of the sequence (corresponding to $m_{F275W} < 21.5$).[7] Indeed, the value of A^+_{rh} that we measure here by considering only such a sub-sample turns out to be $A^+_{rh} = 0.19$, in perfect agreement

[7]Note that the sample of BSSs used in Section 3.2 to measure the parameter A^+_{rh} was the same adopted by Ferraro et al. (2012) to locate the position of the minimum of the BSS-nRD. This required to cover the entire cluster radial extension by complementing *HST* data with wide-field photometry obtained from the ground. In turn, the necessity of considering samples of BSSs homogeneous in magnitude over the whole cluster forced us to use only the brightest portion of the BSS sequence even in the regions observed with the *HST*, where much fainter magnitudes were reached.

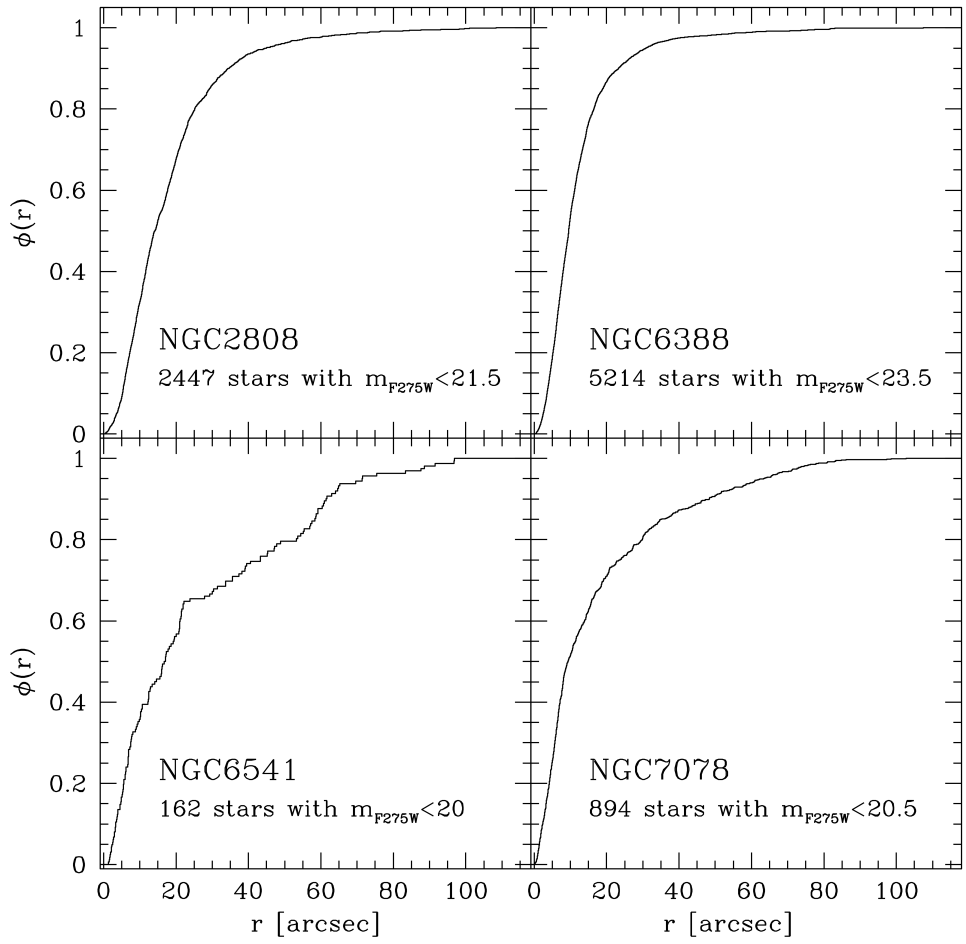

FIGURE 3.10: Cumulative radial distribution of the bright stars (brighter than the dashed lines in the left panels of Figure 3.9) missed in the optical-driven catalogs (Soto et al., 2017) of the four program clusters. The central segregation of the missed stars is evident: in all the cases a fraction larger than $\sim$ 70% of missed stars is located within the innermost 10″ from the cluster center.

with the value quoted in Section 3.2. On the other hand, the severe Galactic field contamination affecting the faintest portion of the BSS sequence (see also SP16) and the lack of accurate PMs especially in the innermost cluster regions (see Section 3.3.4.2), suggest that the investigation of the entire BSS sequence of NGC 6388 is unreliable at the moment. Hence for this cluster here we adopt the value $A^{+}_{\rm rh} = 0.19$.

For the other three clusters in our samples, we followed the prescriptions described in Section 3.2 to measure the value of $A^{+}_{\rm rh}$. As a first step, the cluster center needs to be determined. To this end, we adopted the iterative procedure proposed by Montegriffo et al. (1995), and used in Lanzoni et al. (2010) and Miocchi et al. (2013). We determined the center of gravity ($C_{\rm grav}$) by averaging the right ascension (α) and declination (δ) of all the stars detected within a circle of (first-guess) radius r, brighter than a given magnitude limit. Depending on the cluster characteristics, in each GC we selected the optimal range of stellar magnitudes to guarantee high enough statistics and to avoid spurious effects due to photometric incompleteness. In the specific cases presented here, we used all the stars down to the MS-TO region (approximately with $m^{*}_{\rm F275W} < 0.8$). Table 3.5 lists the adopted values of $C_{\rm grav}$ and reports the differences with respect to those quoted in Goldsbury et al. (2010). These are always smaller than 0.35″, both in α and in δ, with the exception of NGC 6541,

TABLE 3.5: Centers of gravity determined here (columns 2 and 3), compared to those published in Goldsbury et al. (2010, shortened in G10, columns 4 and 5). The differences (in arcsec) between the two determinations of α and δ are listed in columns 6 and 7.

Name	α (h:m:s)	δ (°:′:″)	α (G10) (h:m:s)	δ(G10) (°:′:″)	$\Delta\alpha$ (arcsec)	$\Delta\delta$ (arcsec)
NGC 2808	09:12:03.08	−64:51:48.80	09:12:03.10	−64:51:48.6	−0.34	−0.20
NGC 6388	17:36:17.21	−44:44:07.64	17:36:17.23	−44:44:07.8	−0.34	0.16
NGC 6541	18:08:02.48	−43:42:53.42	18:08:02.36	−43:42:53.6	1.80	0.18
NGC 7078	21:29:58.31	12:10:01.30	21:29:58.33	12:10:01.2	−0.31	0.09

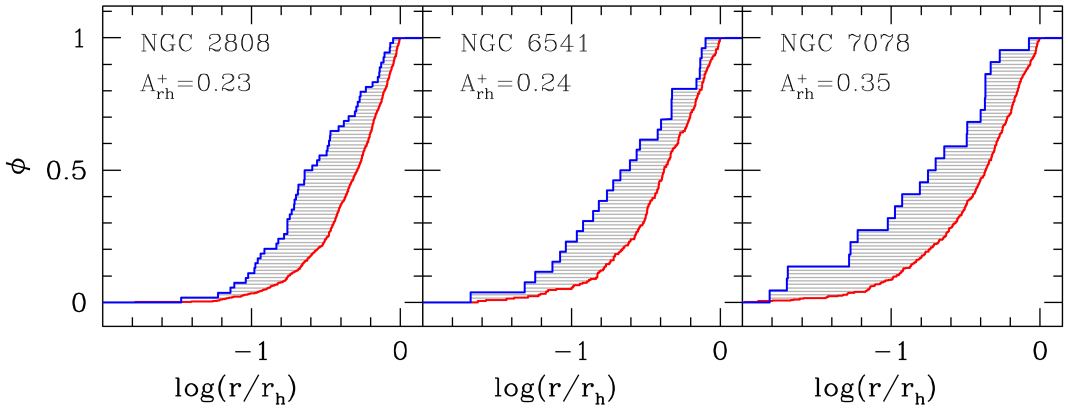

FIGURE 3.11: Cumulative radial distributions of BSSs (blue line) and reference stars (red line) observed within one half-mass radius (r_h) in NGC 2808, NGC 6541, NGC 7078. The area between the two curves (shaded in grey) corresponds to the labelled value of A^+_{rh} (see also Table 3.3).

for which a difference of $\sim 1.8''$ in α is found.

Once C_{grav} is located, to determine A^+_{rh} one needs to compare the cumulative radial distribution of BSSs out to r_h, with that of a reference population assumed to trace normal cluster stars. In all the selected GCs, the radial region extending from C_{grav} out to r_h is entirely covered by the WFC3/UVIS data. For a proper comparison with the results of Section 3.2, where only the bright portion of the BSS sequence has been used (see Footnote 7), here we computed A^+_{rh} by considering BSSs with $m^*_{F275W} < -1.5$ (see Figure 3.5). Moreover, we adopted both the HB and the RGB populations as reference, and we assumed the average of the two resulting values as the best estimate of A^+_{rh}, and the standard deviation as its error.

Figure 3.11 shows the cumulative radial distributions of BSSs and HB stars for the clusters in our sample. The adopted values of A^+_{rh} are labelled in the figure and listed in Table 3.3.[8] In the case of NGC 6541, the value of A^+_{rh} changes from 0.24 to 0.22 if the center determined by Goldsbury et al. (2010) is adopted. More in general, to explore the effect of an imprecise location of the cluster center, we have re-determined A^+_{rh} by applying an arbitrary shift of $0.5'' - 1''$ in all directions to the nominal value of C_{grav}. We found variations of 0.01-0.04, the largest effect being observed (as expected) for the most concentrated system (NGC 7078). Figure 3.12 shows the behaviour of the A^+_{rh} parameter as a function of t_{rc} (expressed in units of Hubble time t_H) for the four clusters presented here (red circles), compared to the 25 GGCs discussed in Section 3.2 (see Figure 3.3). As it can be seen, they nicely fit into

[8]The values of A^+_{rh} obtained from the catalogs of Soto et al. (2017) and Simunovic and Puzia (2016) for the clusters in common are always smaller than those found here, with average and maximum differences of 0.04 and 0.09, respectively.

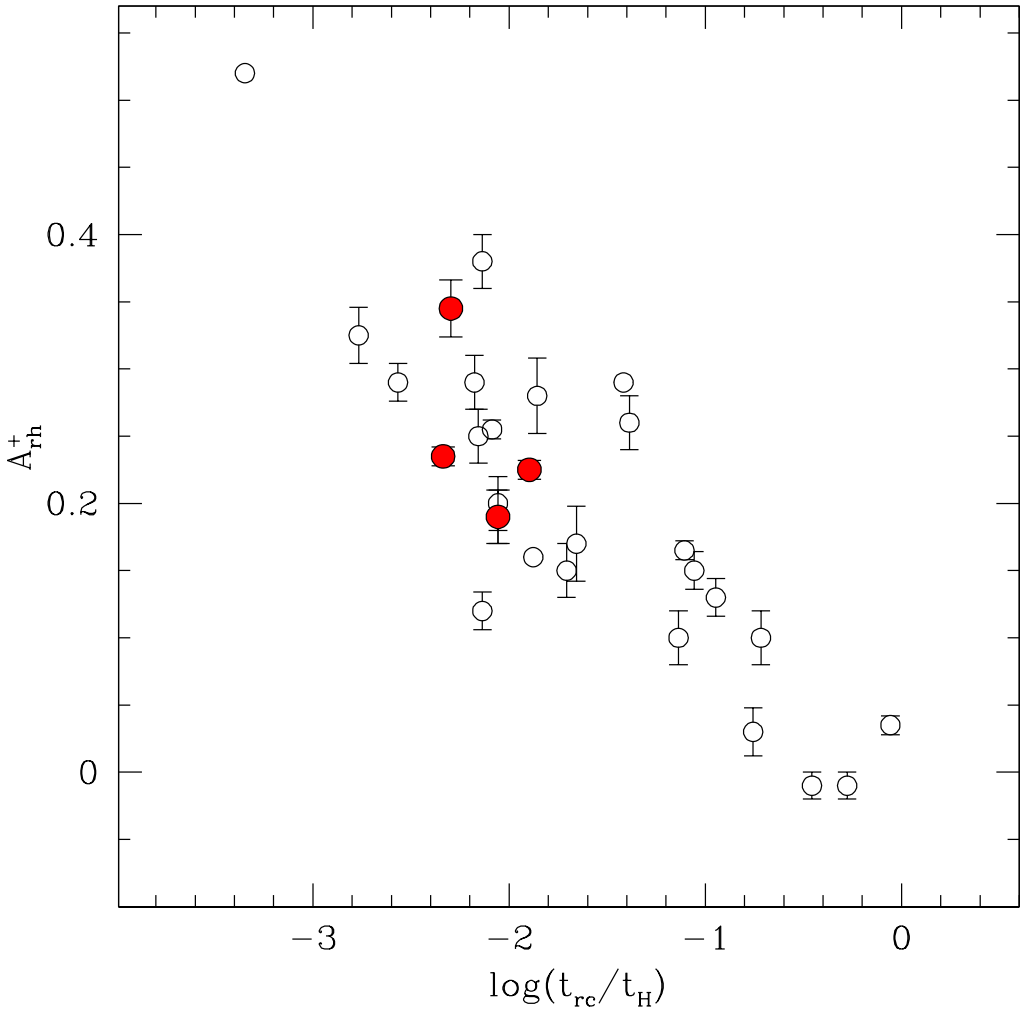

FIGURE 3.12: Relation between the parameter A^+_{rh} and the cluster central relaxation time (t_{rc}) normalized to the Hubble time ($t_H = 13.7$ Gyr). The open circles are the 25 clusters presented in Section 3.2 (Figure 3.3), while the clusters discussed in this Section are plotted as red circles.

the relation, thus providing new support to the fact that A^+_{rh} is a powerful indicator of the cluster dynamical evolution and, once properly calibrated, it promises to be usable as a direct measure of the central relaxation time of these systems.

3.4 BSSs in the *HST* UV Legacy Survey of GGCs

As part of the *HST* UV Legacy Survey of GGCs (Piotto et al., 2015), in this Section we present the determination of A^+ in 27 systems from the Survey that have been observed out to $\sim 1r_h$ (see Section 3.4.3 for the justification of this requirement). In combination with the sample presented previously in this Chapter, this provides us with a measure of A^+ in roughly 32% of the entire GC population in the Milky Way. For this sample we find a strong correlation between A^+ and the number of central relaxation times that have occurred in each cluster since formation. A correlation between the level of BSS central segregation (as quantified by A^+) and the degree of

energy equipartition experienced by BSSs in the cluster (as measured by the velocity-dispersion ratio of BSSs and MS-TO stars) is also found for the 14 GCs in common with Baldwin et al. (2016).

3.4.1 The photometric database and data analysis

An overview of the *HST* UV Legacy Survey of GGCs is presented in Section 3.3.1 and Piotto et al. (2015)[9]. Several images have been obtained for each cluster in the F275W, F336W and F438W bands with the UVIS channel of the WFC3. WFC3/UVIS consists of two chips, each of 4096×2051 pixels, with a pixel scale of $0.04''$, resulting in a total field of view of $\sim 162'' \times 162''$. In each band, different pointings were dithered by several pixels, and in some cases they were also rotated by $\sim 90^{\circ}$, to allow an optimal subtraction of CCD defects, artifacts, charge loss and false detections. All the images have been corrected for the effect of poor CTE following Anderson and Bedin (2010). We applied the *UV-guided* photometric approach described in Section 3.3, which, as already explained, is significantly convenient with respect to the early data releases based on an *optical-guided* reduction of the images (see, e.g., Soto et al. 2017).

The photometric catalogs were obtained using the software described by Anderson et al. (2008) and adapted to WFC3 images. Briefly, for each image we obtained an *ad hoc* array of PSFs by perturbing the tabulated static PSFs[10], to properly take into account both the spatial and the temporal PSF variations. To extract the photometric catalogs from each individual exposure by using the adopted arrays of PSFs we then ran the software `img2xym_wfc3uv`, which has been optimized for UVIS/WFC3 data by Jay Anderson and is similar to the `img2xym_WFC` program (Anderson et al., 2008). After correcting the stellar positions for geometric distortion (Bellini and Bedin 2009; Bellini, Anderson, and Bedin 2011), we determined the transformations between the single-exposure catalogs. Finally, to take full advantage of the reduced crowding conditions at UV wavelengths, we chose to perform the finding procedure on the F275W and F336W images (see Section 3.3 and Raso et al. 2017) and then measured stars in all the individual exposures. To this end, we used the `FORTRAN` program `kitchen_sync`, described by Anderson et al. (2008) and adapted to WFC3 images. The final product is an astro-photometric catalog containing the positions and the F275W, F336W, and F438W magnitudes of all the stars found. For a first-guess differential reddening correction and field decontamination, information about reddening and proper motions have been added to all the stars in common with the catalogs published in the intermediate release[11] (Piotto et al., 2015).

3.4.2 The BSS selection in UV-CMDs

In Section 3.3.3 we identified the purely UV ($m_{\rm F275W}, m_{\rm F275W} - m_{\rm F336W}$) CMD as the ideal diagram for BSS selection, since this population is clearly distinguishable from the other evolutionary sequences (see Figure 3.4).

To perform a homogeneous selection of BSSs in clusters with different values of distance, reddening and metallicity, as in Section 3.3.3 we adopted a "normalized" CMD (hereafter n-CMD) where the magnitudes and the colors of all the measured stars in a given cluster are arbitrarily shifted to locate the MS-TO at $m^*_{\rm F275W} = 0$

[9] See also: http://groups.dfa.unipd.it/ESPG/treasury.php

[10] Available at: http://www.stsci.edu/$\sim$jayander/STDPSFs/

[11] Since these latter are based on an *optical-guided* data reduction, reddening and proper motion measures are available only for a sub-sample of the stars in our final catalogs. The intermediate release catalogs were available upon request at http://groups.dfa.unipd.it/ESPG/treasury.php when this work was carried out; at present the final release catalogs are publicly available.

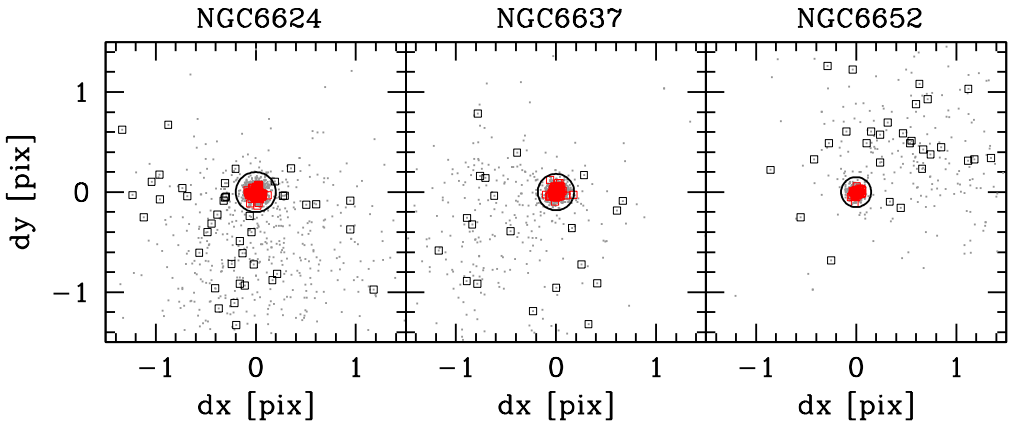

FIGURE 3.13: VPDs for three clusters in the survey (see labels), showing the measured displacements (in ACS/WFC pixels) of stars brighter than the MS-TO level (with $m^*_{\rm F275W} < 0.5$), over a ∼7-8 yr time-baseline. All stars within the circle (as well as stars with no displacement information) are assumed to be cluster members and have been included in the analysis, while those beyond the circle are considered as field contaminants. The red and black squares mark the cluster-member and the field-contaminant BSSs, respectively.

and $(m_{\rm F275W} - m_{\rm F336W})^* = 0$. Since the morphology of the MS-TO and the SGB region changes as a function of metallicity, and because the surveyed GCs have quite different iron abundances (ranging from [Fe/H]$= -0.4$ for NGC 6624, to [Fe/H]$= -2.4$ for NGC 7078), we adopted the following procedure to determine the necessary shifts for a proper normalization of the CMDs:

1. While the updated determination of precise proper motions for all the clusters in the survey is in progress, here we used the currently available measurements for a first-order identification of field stars in the most contaminated systems. Proper motions have been determined over a ∼7-8 yr time-baseline using the ACS Globular Cluster Survey data (GO-10775; Sarajedini et al., 2007) as first-epoch observations and the new WFC3 UV positions as the second epoch. To separate cluster members from field stars, we built the VPDs plotting all the available displacement measures in each cluster. We thus used an iterative σ-rejection procedure[12] to distinguish cluster members, which are well-grouped around the VPD center, from field contaminants, which generally exhibit a much more scattered distribution (see also King et al. 1998; Bedin et al. 2003; Bellini and Bedin 2009; Milone et al. 2012; Bellini et al. 2014; Massari et al. 2015; Cadelano et al. 2017; Soto et al. 2017). For illustration purposes we show in Figure 3.13 the VPDs of three clusters. All stars with no displacement information have been conservatively retained as members in the following analysis.

2. All the stars for which we have color-excess determinations available were then corrected for differential reddening following the approach described, e.g., in Milone et al. (2012, 2017).

[12]Starting from a first-guess circle of radius r_i in the VPD, we selected all the enclosed stars and determined their dispersion along the two axes (dx and dy). At the following step, the new selection radius is defined as $r = 4 \times \sigma_{xy}$, where $\sigma_{xy} = \sqrt{dx^2 + dy^2}$. The final selection radius is then obtained when convergence is reached (typically, after five iterations).

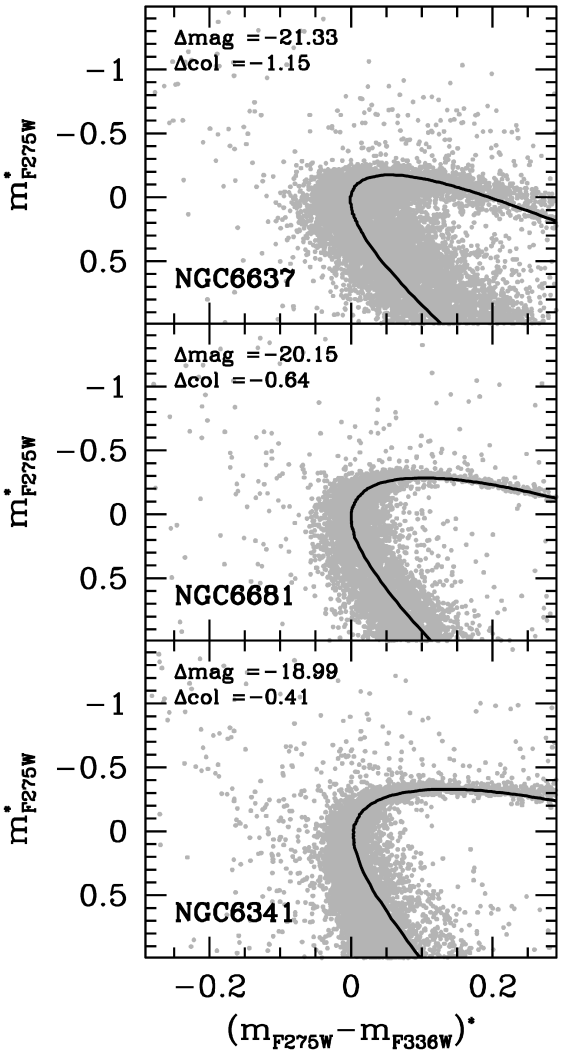

FIGURE 3.14: Normalized CMD zoomed in the MS-TO region for three clusters (namely NGC 6637, NGC 6681, NGC 6341) belonging to the three metallicity groups defined in the text (from top to bottom, metal rich, metal intermediate and metal poor). The adopted 12-Gyr isocrone (from the BaSTI database) is shown as a solid line, and shifts in color and magnitude have been adopted to locate the MS-TO at $m^*_{\rm F275W} = 0$ and $(m_{\rm F275W} - m_{\rm F336W})^* = 0$ are labelled in each panel.

3. The available clusters were divided into three groups according to their metallicity: metal-poor, with [Fe/H]< -2, metal-intermediate, with $-2 <$[Fe/H]< -1, and metal-rich, with [Fe/H]> -1.

4. For each group, a 12 Gyr-old isochrone of appropriate metallicity was adopted from the BASTI database (Pietrinferni et al., 2006) and was plotted for reference in the n-CMD, i.e., in the CMD with the MS-TO located at (0,0).

5. The stellar magnitudes and colors in each cluster were then shifted to match the appropriate reference isochrone.

For the sake of illustration, Figure 3.14 shows the n-CMD zoomed in the MS-TO region for three clusters representative of the three adopted metallicity groups (see labels). The observed sequences at the MS-TO/SGB level nicely agree with the shape of the appropriate isochrone.

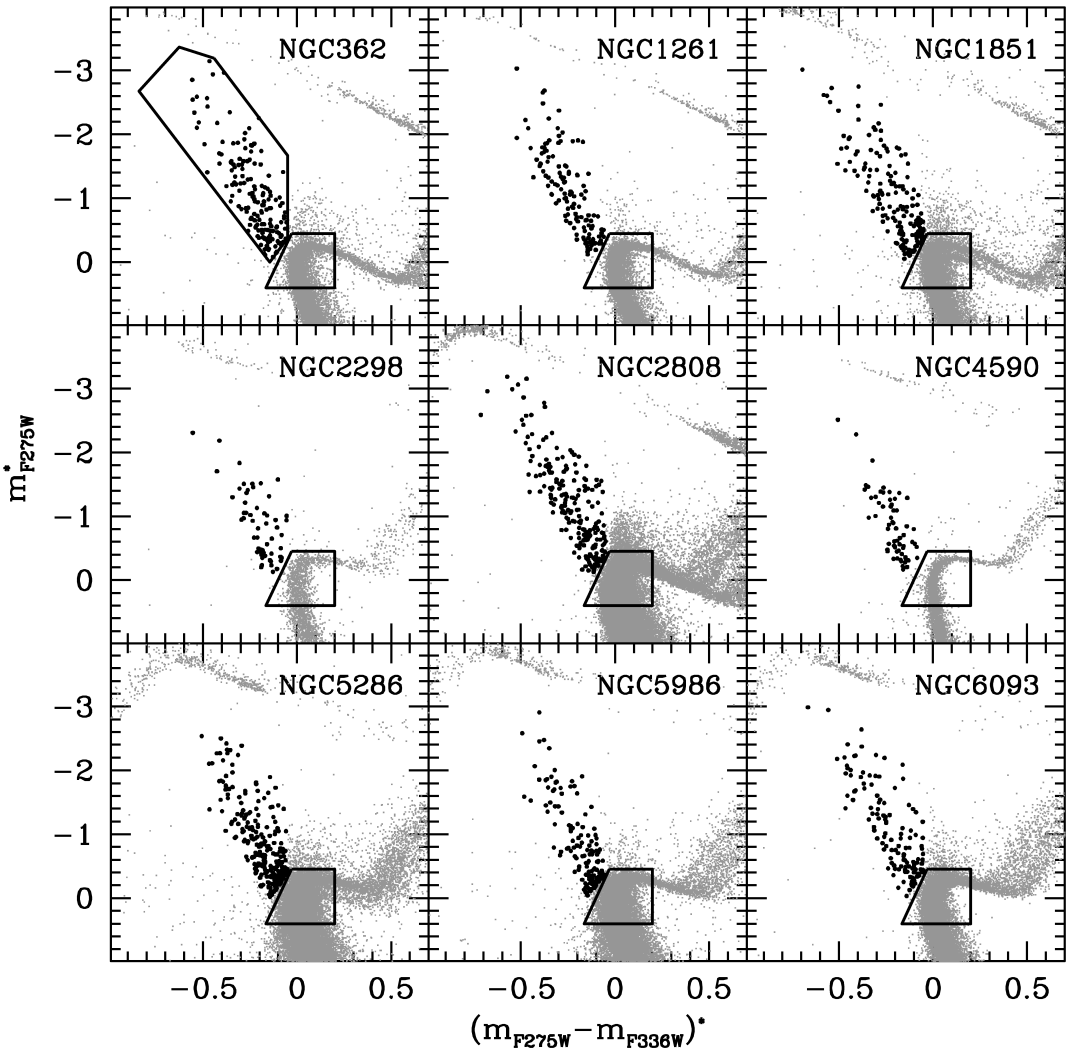

FIGURE 3.15: The sample of BSSs (black dots) identified in each cluster is shown in the n-CMD. The BSS selection box is drawn in the first panel, the one adopted for the MS-TO population is marked for all clusters.

By construction, BSSs are expected to populate the same region in the n-CMDs, Hence they can be selected in a homogeneous way by defining a unique selection box (see the upper-left panel in Figure 3.15). Here we adopt the same boundaries defined in Section 3.3.3 (see Equations 3.1-3.3), which have been designed to include the bulk of the BSS population in all the clusters, independent of their metallicity (note that the BSS sequence slightly moves from blue to red for increasing iron content).[13] As discussed in Section 3.3.3, the bright edge of the BSS selection box is needed to distinguish very luminous BSSs from stars populating the blue portion of the HB (when present). Since the HB morphology is expected to vary (primarily) as a function of the metallicity, different bright boundaries of the BSS selection boxes were adopted for the three metallicity groups. Figures 3.15-3.17 show the BSS sample selected in the 27 GCs discussed in this Section.

For meaningful conclusions, the radial distribution of BSSs needs to be compared with that of a population of normal cluster stars tracing the overall density

[13]Note that in some cases a few objects lying close to the selection box boundaries have been excluded to minimize the presence of contaminating stars. This has no impact on the discussed results.

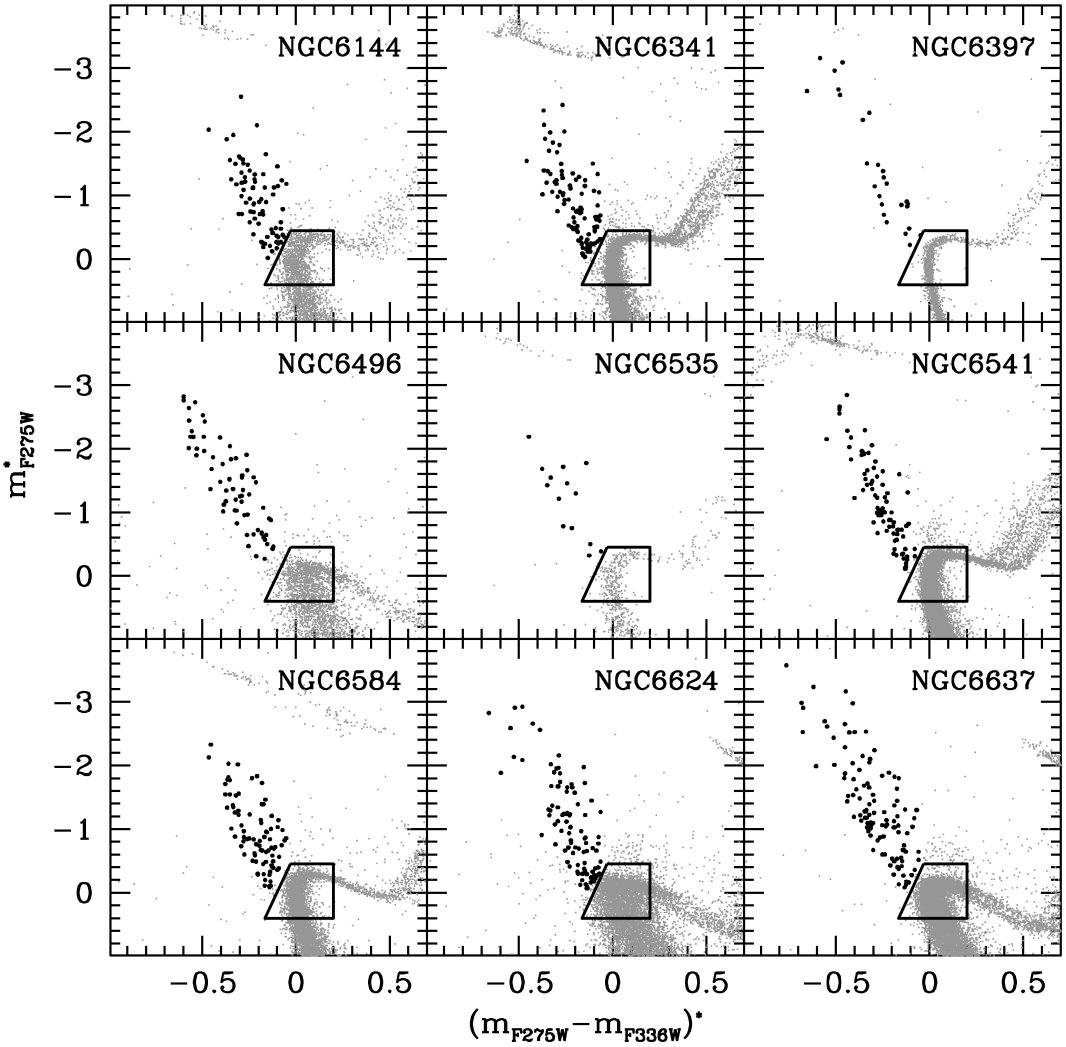

FIGURE 3.16: As in Figure 3.15.

profile of the system (the so called REF population). In order to measure the A^+ parameter as accurately as possible, we choose to use MS stars around the MS-TO level. The adopted REF population selection box (see Figures 3.15-3.17) is delimited in magnitude between $m^*_{\rm F275W} = -0.45$ and $m^*_{\rm F275W} = 0.4$ and in color between $(m_{\rm F275W} - m_{\rm F336W})^* = 0.2$ and the line $m^*_{\rm F275W} = -6.30 \times (m_{\rm F275W} - m_{\rm F336W})^* - 0.62$. This portion of the CMD turns out to provide the ideal REF population, since it includes several hundred stars and therefore is negligibly affected by statistical fluctuations. It is also expected to be poorly affected by the possible presence of binary systems, since the number of single MS-TO stars is largely dominant within the adopted box.

3.4.3 Results and Discussion

To measure the level of BSS segregation in the surveyed clusters we used again the parameter A^+, defined Section 1.4.2 (see Equation 1.9) and already described and discussed previously in this Chapter. In particular, we use $A^+_{\rm rh}$ to allow a meaningful cluster to cluster comparisons.

Our *HST*-WFC3 data covers approximately the innermost 80″-85″ in each surveyed cluster. This is large enough to sample the entire half-mass radius in 22 of the

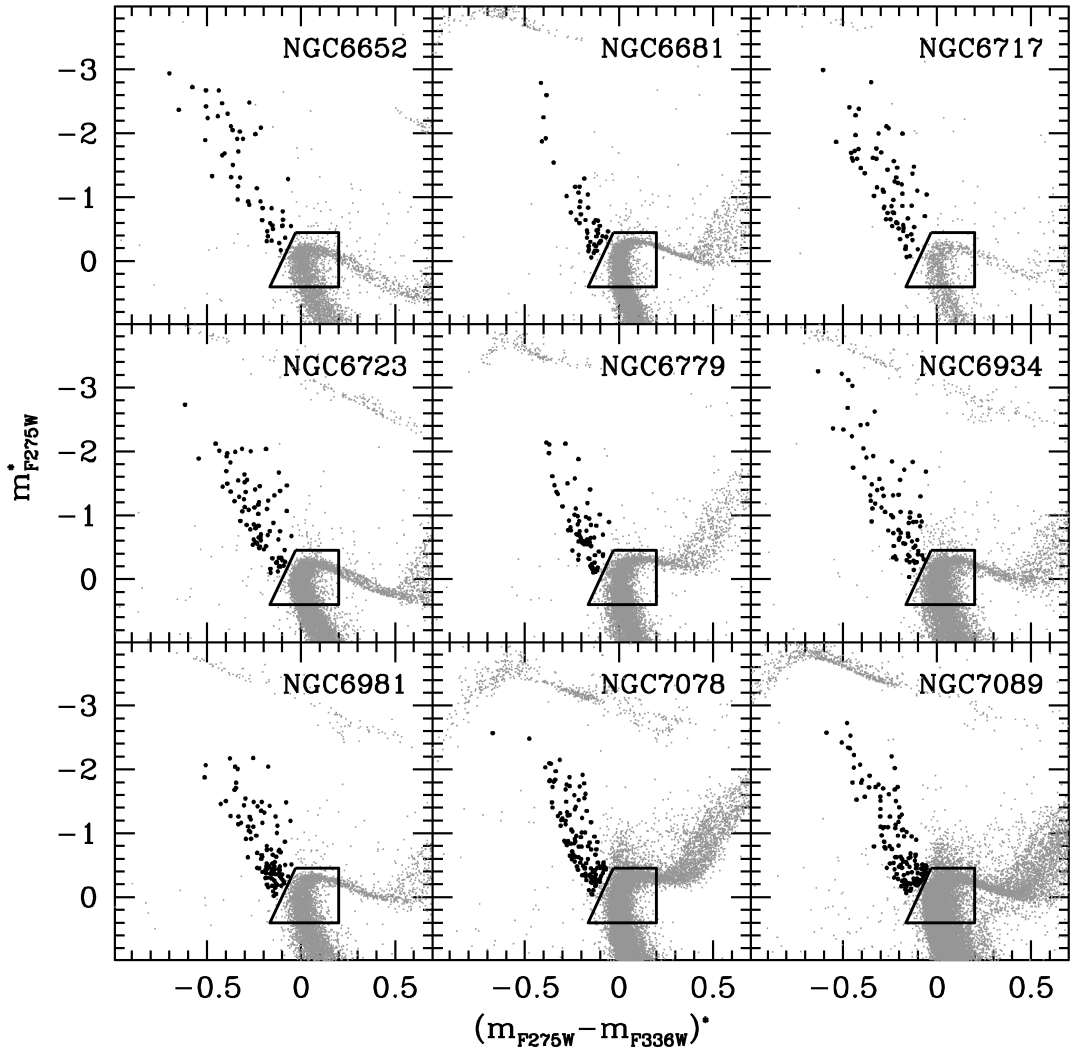

FIGURE 3.17: As in Figure 3.15.

clusters. We also added to the sample four clusters (namely, NGC 4590, NGC 6144, NGC 6496 and NGC 6723) for which the available data cover between $\sim$ 90% and 98% of r_h. We also added NGC 6397, which is known to be a post-core collapse cluster and therefore is expected to belong to the family of dynamically-old GCs (Family III as defined in Section 1.4.1; see also Ferraro et al. 2012) and which has a BSS population highly segregated in the central regions. Our data sample $\sim$ 30 core radii in this cluster, and based on the BSS-nRDs discussed in Ferraro et al. (2012), this is a large enough distance for a proper study of BSS segregation. In fact, Figures 1.7 and 1.8 clearly show that the region where the BSS-nRD shows a central peak (which is the signature of BSS sedimentation) is of the order of a few core radii in all clusters. Hence, the total sample extracted from the *HST* UV Legacy Survey of GGCs for the present analysis amounts to 27 objects. To increase the size of the sample, we also take into account 21 GCs from Section 3.2. The parameter A^+ in Section 3.2 has been determined from a combination of *HST* UV observations and complementary wide-field optical data from the ground able to sample the entire half-mass radius region of each system. To minimize the risk of stellar blends mimicking BSSs at optical wavelengths (see an example in Figures 5 and 6 in Lanzoni et al., 2007b), in

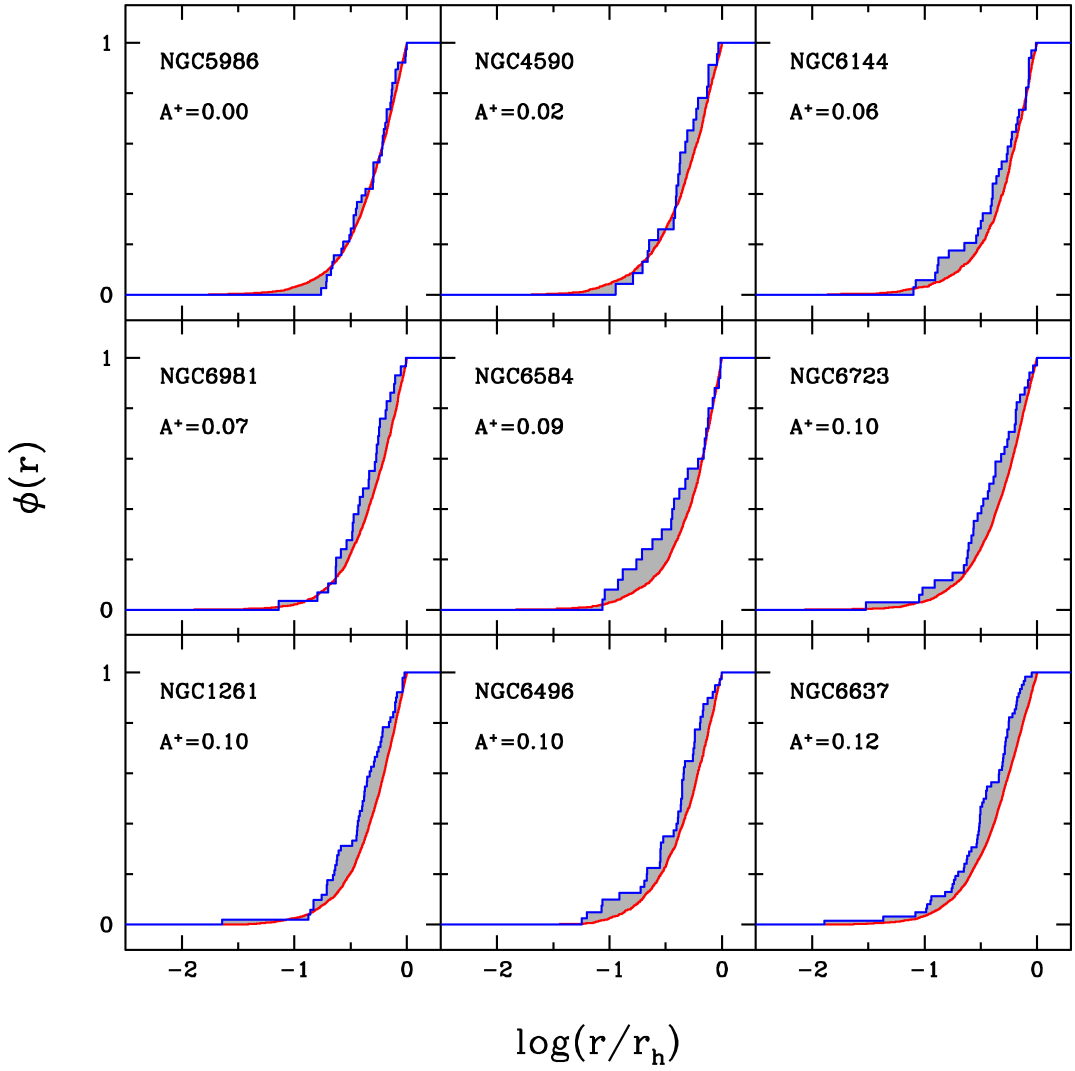

FIGURE 3.18: Cumulative radial distributions of BSSs (blue line) and REF stars (red line) in the nine GCs with the smallest values of $A^+_{\rm rh}$. By construction (see Section 3.4.2), the cumulative radial distributions are normalized to unity at $r_{\rm h}$. The size of the area between the two curves (shaded in grey) corresponds to the labelled value of $A^+_{\rm rh}$ (see also Table 1). Clusters are ranked in terms of increasing value of $A^+_{\rm rh}$.

Section 3.2 only the brightest portion of the BSS distribution has been taken into account. Hence, for consistency, in the present analysis we consider only BSSs with $m^*_{\rm F275W} < -1.0$. This selection corresponds to including only the most massive tail of the BSS population, thus maximizing the sensitivity of the A^+ parameter to the mass-segregation effect. Although caution is needed in deriving BSS masses from their luminosity distribution (see Geller and Mathieu 2012; but also Chapter 2 in this Thesis), the adopted magnitude cut roughly corresponds to selecting BSSs that are more massive than $\sim 1.2 M_\odot$. The cumulative radial distributions of BSS and REF populations here determined for the 27 investigated clusters are shown in Figures 3.18-3.20, and the corresponding values of $A^+_{\rm rh}$ are labeled in each panel and listed in Table 3.6. The primary source of uncertainty on A^+ is the relatively small-number statistics of the BSS sample in each system. To estimate the errors on A^+ (see Table

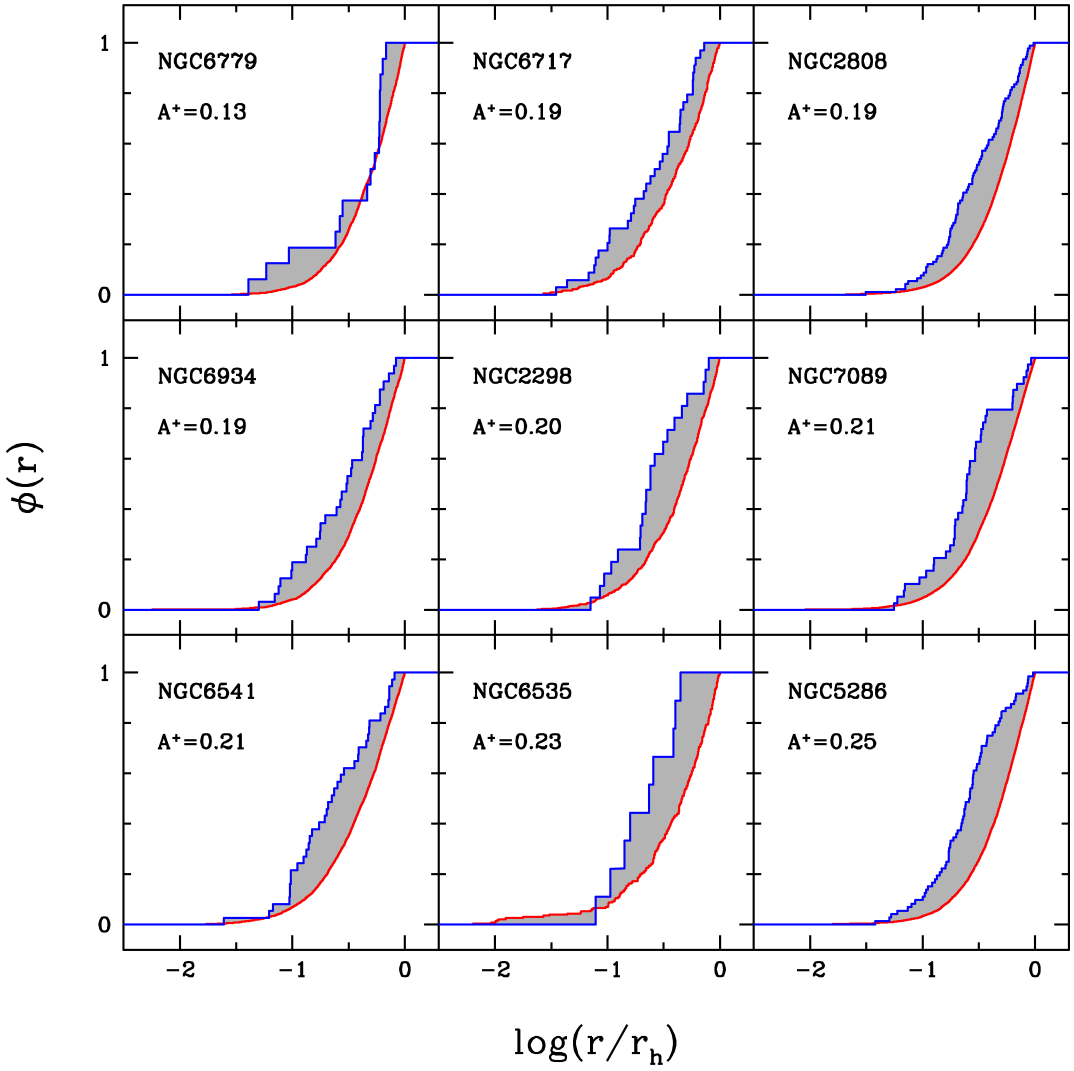

FIGURE 3.19: As in Figure 3.18, for the nine GCs with increasingly larger value of $A^+_{\rm rh}$.

3.6) we therefore used a jackknife bootstrapping technique (Lupton, 1993).[14]

Since the adopted BSS and REF populations have different magnitude limits, they could be characterized by different levels of completeness, which, in turn, could impact the value of $A^+_{\rm rh}$. Hence, we performed artificial star experiments to estimate the photometric completeness of the two populations in some of the most massive (hence most crowded) clusters with different central densities. In the worst cases of the intermediate density systems (as NGC 2808) the completeness of the BSS and REF populations is always larger than $\sim$ 90%, with the only exception being the faintest MS-TO stars at $r < 15''$, for which it decreases to $\sim$ 80%. In the most compact clusters (as M15) the selected populations are complete at more than 90% for $r > 30''$, while the completeness decreases to 80% and 70-75% at the faintest boundary of the MS-TO selection box for $15'' < r < 30''$ and $r < 15''$, respectively. We redetermined the value of $A^+_{\rm rh}$ from 1000 random realizations of the two population samples corrected for the estimated incompleteness levels. The mean value and dispersion of the resulting $A^+_{\rm rh}$ distributions are well within the uncertainties estimated

[14]For sake of consistency, we re-evaluated the errors on A^+ of the sample from Section 3.2 using the same technique.

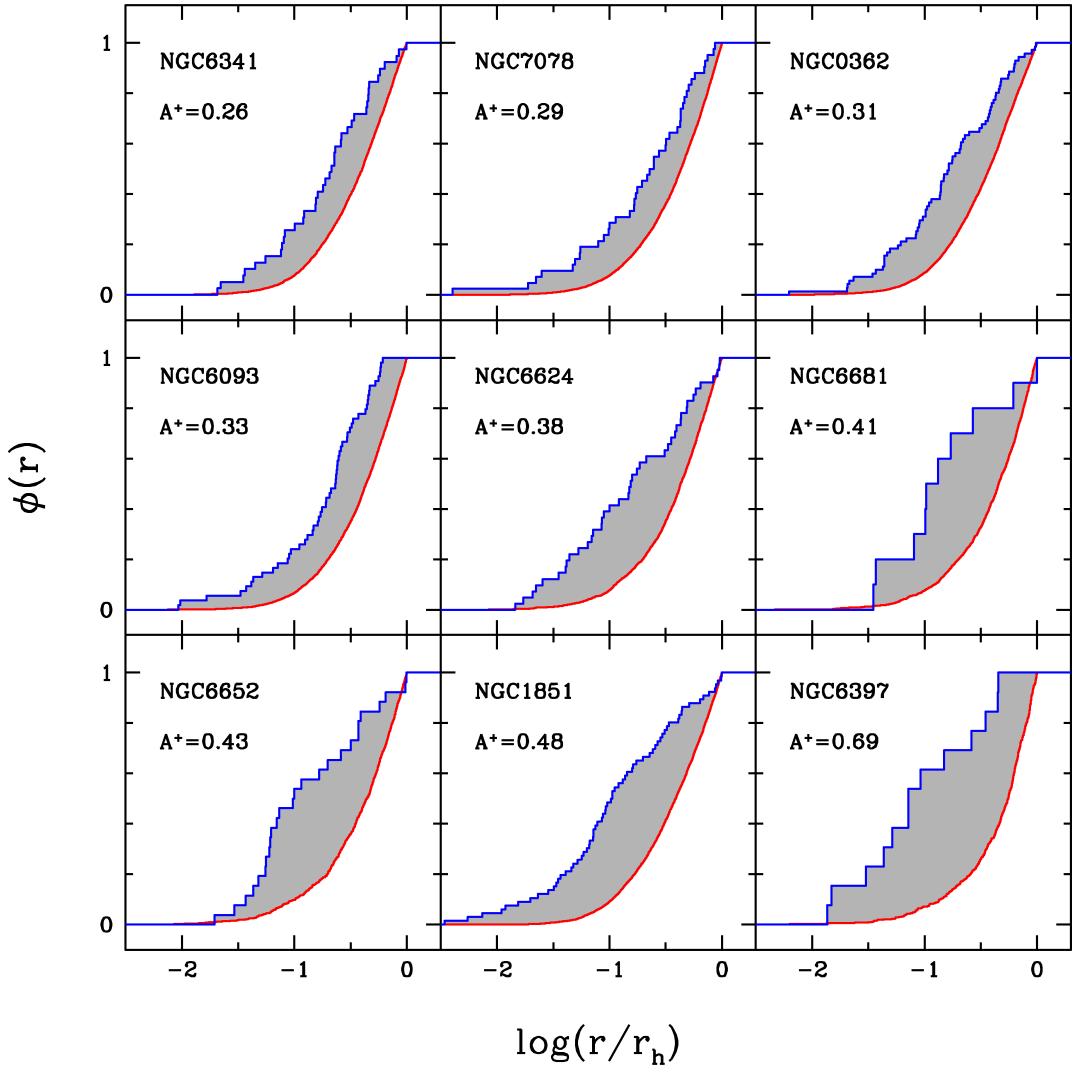

FIGURE 3.20: As in Figure 3.18, for the remaining nine GCs, those with the largest values of $A^+_{\rm rh}$.

with the jackknife bootstrapping technique, thus indicating that the photometric incompleteness of the adopted samples does not affect the present analysis.

To investigate the connection between the BSS segregation level and the dynamical status of the parent cluster, we studied the relation between the measured values of $A^+_{\rm rh}$ and the dynamical age of the system quantified by the number of current central relaxation times ($t_{\rm rc}$) that have occurred since the epoch of cluster formation ($t_{\rm GC}$): $N_{\rm relax} = t_{\rm GC}/t_{\rm rc}$. Because all Galactic GCs have approximately the same age, this is simply an alternative way of illustrating the connection between A^+ and the dynamical evolution experienced by a cluster, with respect to the direct comparison between A^+ and $t_{\rm rc}$ adopted previously (see Sections 3.2 and 3.3, and particularly Figures 3.3 and 3.12; see also Ferraro et al. 2012; Lanzoni et al. 2016; Raso et al. 2017). Indeed, to keep the sources of uncertainty at a minimum, for all the program clusters we assumed the same average age ($t_{\rm GC} = 12$ Gyr from the compilation of Forbes and Bridges 2010). Note however that adopting individual age estimates for each cluster does not change the result. The central relaxation times have been empirically estimated as in Equation (10) of Djorgovski (1993), adopting $0.3 M_\odot$ as average stellar mass, $M/L_V = 2$ as V-band mass-to-light ratio, the integrated V magnitudes listed

TABLE 3.6: Structural/dynamical parameters and values of A^+_{rh} for the 27 program clusters: concentration parameter (column 2), core and half-mass radii in arcseconds (columns 3 and 4, respectively), logarithm of the central relaxation time in Gyr (column 5), derived value of A^+_{rh} and its error (columns 6 and 7). The structural parameters are from Miocchi et al. (2013); Lanzoni et al. (2016); Cadelano et al. (2017), and Harris (1996) if not available in the previous studies, but for NGC 6717 and NGC 6535 and NGC 6496 for which we performed new determinations. Clusters are ordered in terms of increasing value of A^+_{rh}.

Name	c	r_c	r_h	$\log(t_{rc})$	A^+_{rh}	ϵ_{A^+}
NGC 5986	1.23	28.2	58.8	8.75	-0.00	0.02
NGC 4590	1.41	34.8	90.6	8.66	0.02	0.03
NGC 6144	1.55	56.4	97.8	8.73	0.06	0.03
NGC 6981	1.21	27.6	55.8	8.79	0.07	0.03
NGC 6584	1.47	15.6	43.8	8.33	0.09	0.04
NGC 6723	1.11	49.8	91.8	8.93	0.10	0.03
NGC 1261	1.16	21.0	40.8	8.74	0.10	0.02
NGC 6496	1.18	35.6	93.6	8.76	0.10	0.03
NGC 6637	1.38	19.8	50.4	8.17	0.12	0.02
NGC 6779	1.38	26.4	66.0	8.42	0.13	0.06
NGC 6717	1.71	8.0	45.0	7.13	0.19	0.04
NGC 2808	1.56	15.0	48.0	8.35	0.19	0.02
NGC 6934	1.53	13.2	41.4	8.29	0.19	0.03
NGC 2298	1.38	18.6	58.8	8.10	0.20	0.04
NGC 7089	1.57	15.4	66.3	8.42	0.21	0.03
NGC 6541	1.86	10.8	63.6	7.72	0.21	0.03
NGC 6535	1.56	17.5	73.4	7.50	0.23	0.05
NGC 5286	1.41	16.8	43.8	8.46	0.25	0.02
NGC 6341	1.74	14.6	85.0	8.06	0.26	0.04
NGC 7078	2.29	8.4	60.0	7.69	0.29	0.05
NGC 0362	1.73	13.0	73.8	7.96	0.31	0.03
NGC 6093	1.74	7.0	40.6	7.60	0.33	0.03
NGC 6624	2.50	3.6	49.2	6.54	0.38	0.05
NGC 6681	2.50	1.8	42.6	6.21	0.41	0.09
NGC 6652	1.80	6.0	28.8	7.26	0.43	0.06
NGC 1851	1.95	5.4	51.0	7.53	0.48	0.04
NGC 6397	2.50	3.0	174.0	5.52	0.69	0.09

in Harris (1996), and the structural parameters listed in Table 3.6.

The nice correlation in Figure 3.21 clearly shows that A^+ is a powerful indicator of cluster dynamical evolution. The most dynamically evolved cluster in the sample is NGC 6397, and the five objects with the next largest values of A^+_{rh} (namely, M30, NGC 1851, NGC 6652, NGC 6681, and NGC 6624) are all post-core collapse or high-density systems. The present study also increased the number of clusters showing a modest level of dynamical evolution. In fact we count at least 6-7 GCs with extremely low values of A^+_{rh} (< 0.05-0.06). Interestingly, we also find similarly small values for other objects not included in the present study (as NGC 5053 and NGC 6809) because the WFC3 field of view does not entirely sample their half-mass radius. This suggests that they may also belong to this class, although more radially extended observations are needed. Hence, a significant fraction (possibly $\sim 10\%$) of the Galactic GC population could still be relatively unevolved dynamically.

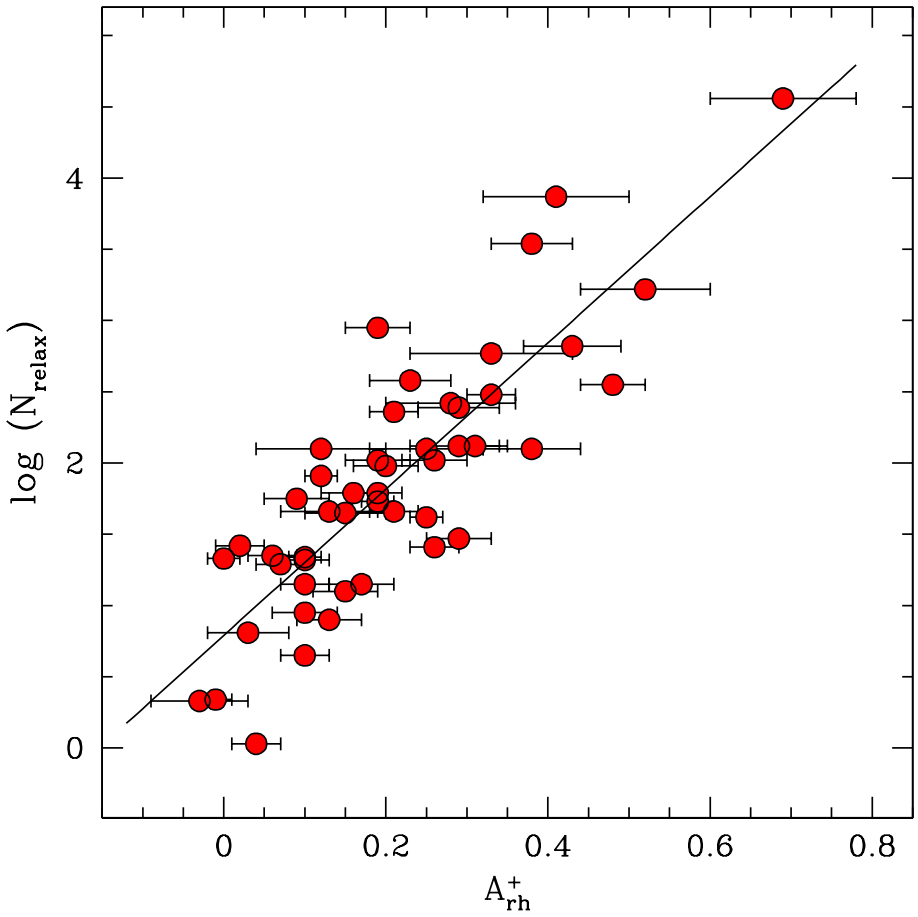

FIGURE 3.21: Relation between A^+_{rh} and $\log(N_{\rm relax})$ for the entire sample of 48 GCs. The parameter $N_{\rm relax} = t_{\rm GC}/t_{\rm rc}$ quantifies the number of current central relaxation times occurred since cluster formation. The tight relation between these two parameters demonstrates that the segregation level of BSSs measured by A^+ can be used to evaluate the level of dynamical evolution experienced by the parent cluster.

The best-fit relation to the observed points plotted in Figure 3.21 is:

$$\log N_{\rm relax} = 5.1(\pm0.5) \times A^+_{rh} + 0.79(\pm0.12) \tag{3.4}$$

with a scatter of 0.47 and a high statistical significance: the Spearman rank correlation coefficient is $\rho = 0.82$, and the Pearson correlation coefficient is $r = 0.85$, indicating a strong linear correlation between the two parameters. The relation remains the same even if NGC 6397, which has the largest value of $A^+_{\rm rh}$, and/or the four GCs that are not sampled all the way out to $r_{\rm h}$ are excluded from the analysis. On one hand, this new relation is obtained from $\sim 1/3$ of the total GC population of the Milky Way and thus definitely consolidates the idea that the segregation level of BSSs can be used to evaluate the dynamical evolution experienced by the parent cluster. On the other hand, the scatter of this relation may indicate that further refinements should be used to measure $A^+_{\rm rh}$, and, more likely, that the empirical values of $t_{\rm rc}$ are crude approximations of the true relaxation times of Galactic GCs (as discussed, e.g., by Chatterjee et al., 2013 from dedicated Monte Carlo simulations). It is also worth noticing that the current estimates of $t_{\rm rc}$ are still largely based on cluster parameters derived from surface brightness profiles, which could be biased by the

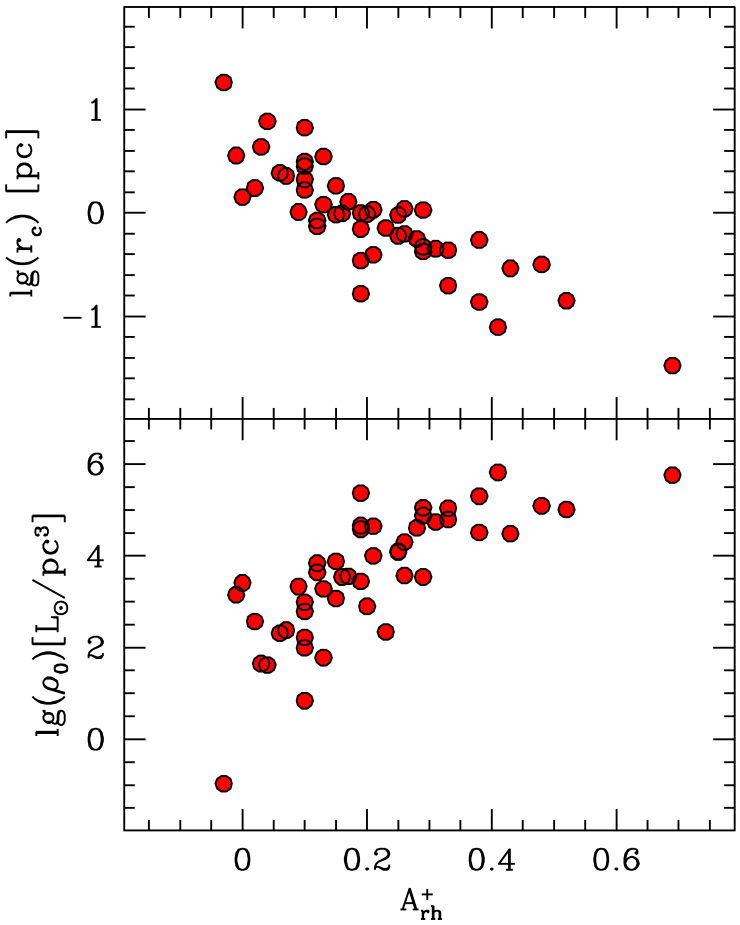

FIGURE 3.22: Relation between A^+_{rh} and two physical parameters that are expected to change with the long-term dynamical evolution of GCs: the core radius (upper panel) and the central luminosity density (lower panel), both taken from Harris (1996).

presence of few bright stars. A new determination of the central density, core and half-mass radii, and concentration parameter from star count profiles might possibly reduce the scatter and provide a refinement of the proposed relation. The scatter notwithstanding, our analysis fully confirms that this is the correct route for a proper description of the dynamical evolution of star clusters. The calibration of the relation via N-body or Monte Carlo simulations requires that all the (known) ingredients (such as dark remnants, primordial binaries, etc.) are taken into account. Indeed preliminary N-body simulations (Alessandrini et al., 2016) have shown how the inclusion of dark remnants can significantly change the BSS segregation timescale in simulated clusters, hence caution should be exercised when calibrating these observables via simulations of simplified models.

To further investigate the solidity of the A^+ parameter as dynamical aging indicator we also studied the dependence on A^+ of two physical parameters that are expected to change with the long-term dynamical evolution of the cluster. Figure 3.22 shows the behaviour of the core radius (r_c) and the central luminosity density (ρ_0, both from Harris 1996) as a function of A^+. The well-defined trends shown in the figure, with r_c decreasing and ρ_0 increasing with A^+_{rh} (i.e., with increasing dynamical age), nicely match the expectations. The tight and strong detected relations, although somehow predictable on the basis of the result shown in Figure 3.21, fully confirm the eligibility of the A^+ parameter as dynamical aging indicator.

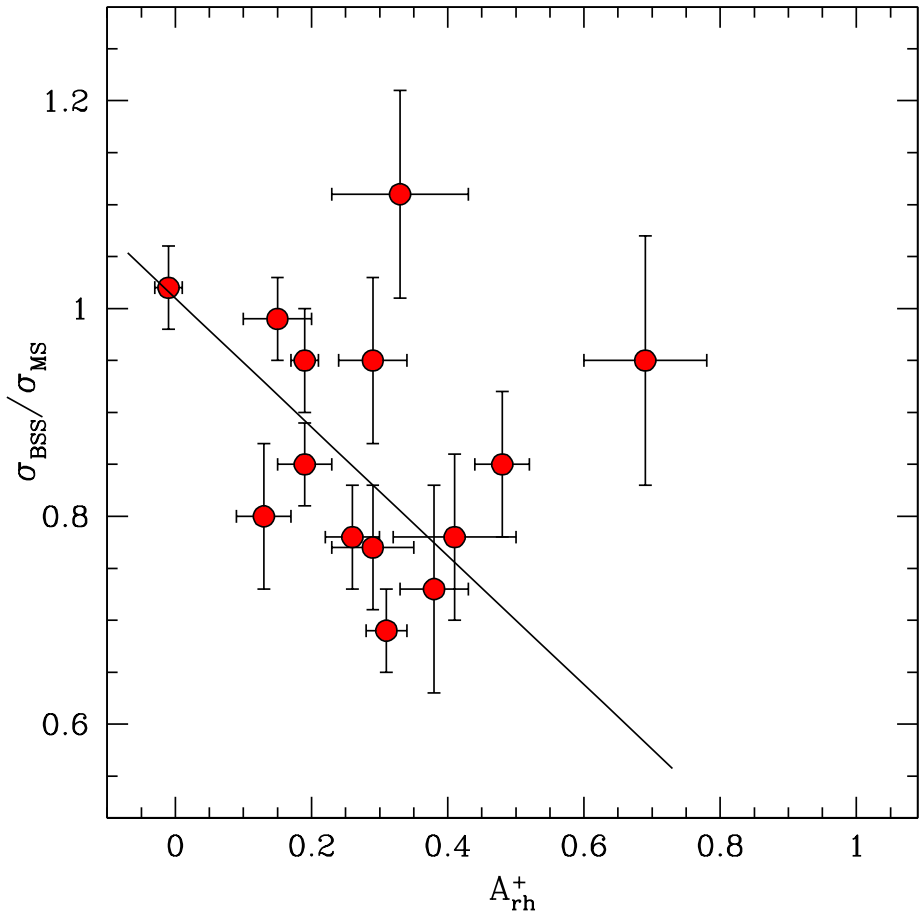

FIGURE 3.23: Relation between $A^+_{\rm rh}$ and the ratio $\alpha \equiv \sigma_{\rm BSS}/\sigma_{\rm MS-TO}$ between the BSS velocity dispersion and that of stars near the top of the MS for the 14 GCs in common with Baldwin et al. (2016). The best-fit relation quoted in Equation 3.5 is shown as a solid line.

Baldwin et al. (2016) measured the proper motions of 598 BSSs across 19 GCs, and inferred the ratio (α) of the velocity dispersion of BSSs ($\sigma_{\rm BSS}$) relative to that of stars near the top of the MS ($\sigma_{\rm MS-TO}$), which is a measure of BSS equipartition (see their Equation 3). Figure 3.23 compares this parameter with our measurement of BSS mass segregation for the 14 GCs in common between the two samples. The best-fit relation is

$$\alpha \equiv \frac{\sigma_{\rm BSS}}{\sigma_{\rm MS-TO}} = -0.62(\pm0.23) \times A^+_{rh} + 1.01(\pm0.06) \tag{3.5}$$

indicating a weak anti-correlation at $\sim 3\sigma$ confidence. The size and the significance of the correlation are strengthened upon omission of NGC 6397 (the cluster with the largest value of $A^+_{\rm rh}$ in Figure 3.23), which has the most uncertain velocity dispersion in Baldwin et al. (2016), on account of their measuring only 10 BSSs. The Spearman rank correlation coefficient is then $\rho = -0.39$, and the Pearson correlation coefficient is $r = -0.38$. The relation indicates that when $A^+_{\rm rh} = 0$, then $\alpha \sim 1$. So when there not yet been sufficient time for mass segregation to develop, no energy equipartition has developed yet either. These results imply, as expected, that as mass segregation develops, so does a certain level of energy equipartition ($\sigma \propto M^{-\eta}$, where M is the stellar mass and η trends over time from 0 to a maximum value of $\approx$ 0.1-0.2, with $\eta = 0.5$ corresponding to complete equipartition; Trenti and van der Marel, 2013).

These results further confirm our physical understanding of the dynamical evolution of GCs, as well as our earlier arguments that A^+ can be used as the "clock hand" of a dynamical chronometer.

Chapter 4

BSSs in the Large Magellanic Cloud

Mainly based on:
Ferraro, Lanzoni, [...], Raso, et al. (2019), Nature Astronomy, 3, 1149

4.1 Introduction

In this Chapter we extend the study on GC dynamical age, presented in Chapter 3 for $\sim$ 30% of the Milky Way GCs, to clusters in the Large Magellanic Cloud (LMC). Milky Way GCs are old stellar systems, with ages larger than $\sim$ 10 Gyr (see Chapter 1 and, e.g., Gratton et al. 1997; Chaboyer et al. 1998; Marín-Franch et al. 2009), while GCs in the LMC cover a wider age range, from a few 10^6 yr to $\sim 10^9 - 10^{10}$ yr. The LMC thus offers a unique opportunity to explore the evolutionary processes of stellar clusters over cosmic time. One of the most intriguing features emerging from these studies (Elson, Freeman, and Lauer 1989; Elson 1991, 1992; Mackey and Gilmore 2003) is the behaviour of the core radius (r_c, which characterizes the size of the innermost cluster region) as a function of age (as measured from the cluster stellar population): the youngest clusters are all compact (with $r_c < 2.5$ pc), while the oldest ones span the full range of observed r_c values, from a fraction of a parsec to almost 10 pc (Figure 4.1, panel a), similar to what is measured for the Milky Way (old) GCs. After ruling out any possible bias due to selection effects, the observed trend has been interpreted in terms of an evolutionary sequence (Mackey and Gilmore 2003). In this scenario, all clusters formed relatively compact ($r_c \sim 2-3$ pc), then most of them maintained small cores, while several others experienced core expansion and moved to the upper-right corner of the diagram. Such an expansion, however, needs to be powered by some *ad hoc* mechanism. Among the different possibilities discussed in the literature (de Grijs et al. 2002; Wilkinson et al. 2003), one often quoted scenario (Mackey et al. 2008) is that the core expansion is due to the heating action of a population of stellar-mass binary black holes (BHs) retained after the supernova explosions. Dynamical interactions among single and binary BHs led to multiple BH scatterings and ejections, thus driving the expansion of the central cluster regions.

4.1.1 An alternative reading of the cluster size-age distribution

Although intriguing, the proposed scenario implicitly requires an evolutionary link between the younger and the older GCs in the LMC, with the former being representative of the progenitors of the oldest ones. However, the two groups show different masses and positions within the LMC: all the young clusters are light stellar systems (with $M < 10^5 M_\odot$), while old clusters are all more massive than $10^5 M_\odot$ (panel b in

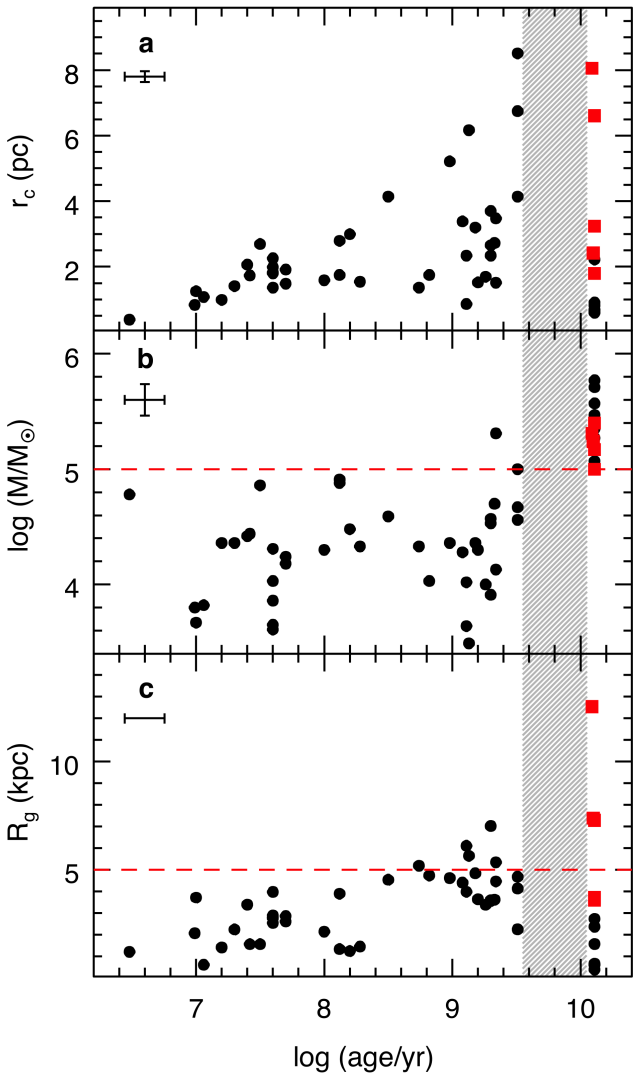

FIGURE 4.1: Observed distribution of core radius (r_c), total mass (M) and galactocentric distance (R_g) versus chronological age (values from McLaughlin and van der Marel 2005) for the LMC GCs (panels a, b, and c, respectively). The average 1σ errors are marked in each panel. The ∼10 Gyr long period of cluster formation quiescence (Da Costa 1991; Geisler et al. 1997; Rich, Shara, and Zurek 2001) is marked with a grey shaded region. The dashed red lines in panels b and c mark, respectively, the limits in mass and galactocentric distance characterizing the recent cluster formation process. The five clusters discussed in this Chapter are shown as red squares.

Figure 4.1); moreover, the young objects are observed in the innermost regions of the host galaxy (within ∼5 kpc from the centre), while the old ones are orbiting at any distance (panel c in Figure 4.1). These pieces of evidence strongly indicate that the progenitors of the old LMC clusters must have been more massive (up to a factor of 100) than the currently young systems, hence there does not appear to be a direct evolutionary connection between the two groups. In turn, this seriously challenges the reading of the LMC r_c-age distribution in terms of an "evolutionary sequence".

On the other hand, the observed distributions (Figure 4.1) show how the cluster parameters changed over the time in the LMC:

- during the early formation epoch of the LMC (∼ 13 Gyr ago), many star clusters more massive than $10^5 M_\odot$ formed over a quite short time scale. The old

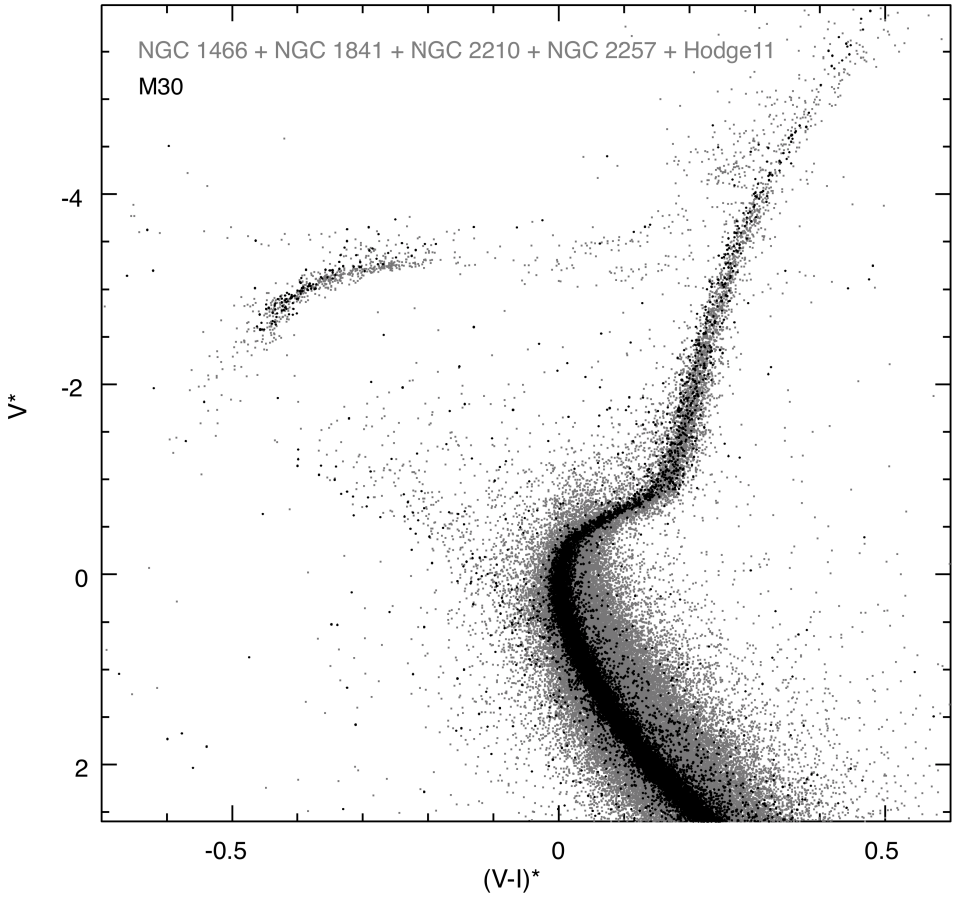

FIGURE 4.2: The co-added n-CMDs of the 5 LMC clusters (in grey) is compared with that of the Galactic GC M30 (Sarajedini et al. 2007; t=13 Gyr, Ferraro et al. 2009; Forbes and Bridges 2010). The comparison clearly demonstrates that the 5 clusters are all old and coeval, with an age of ∼13 Gyr.

clusters, in fact, all formed within a period of $\sim$ 1 Gyr: this can be appreciated in Figure 4.2 (grey dots), where the co-added n-CMDs of the 5 targets are plotted. Only stars within the half-mass radius of each system have been plotted to better highlight the cluster populations. As can be seen, the match among the main evolutionary sequences is impressive: the co-added n-CMD appears as a single population, thus demonstrating that the 5 clusters are indeed coeval within less than 1 Gyr. To quantify their age, we superimposed the n-CMD of M30 (Sarajedini et al. 2007), a Galactic GC with comparable metallicity ([Fe/H]=-1.9, Carretta and Gratton 1997) and very well constrained age (13 Gyr, Ferraro et al. 2009; Forbes and Bridges 2010). Another impressive match of the main evolutionary sequences is found, demonstrating that M30 is coeval to the 5 LMC clusters. Thus an age of 13 Gyr $\pm$ 1 Gyr (with a conservative estimate of the error) can be assumed for the 5 LMC clusters.

- after a long period of quiescence ($\Delta t \sim$ 10 Gyr, the so-called "age-gap", Da Costa 1991; Geisler et al. 1997; Rich, Shara, and Zurek 2001), about 3 Gyr ago cluster formation was reactivated (likely because of a strong tidal interaction with the Small Magellanic Cloud, Bekki et al. 2004) and only less massive structures have been generated since then (i.e., over a much more extended period, of several Gyr) essentially in the innermost region of the galaxy ($R_g < 4-5$

kpc) around the LMC bar (Bekki et al. 2004).

Within this scenario, the lack of young clusters with large r_c would be the natural consequence of the observed mass-age and distance-age distributions: since all recent clusters are light systems formed in the innermost region of the LMC, only the most compact ones can survive the tidal effects of the host galaxy, while any loose and light system that might have formed had been already disrupted. This directly explains why the upper-left portion of the r_c-age diagram is empty. According to the observed mass distribution of the old clusters, none of the young light systems currently observable in the LMC will probably survive over the next 10 Gyr.

Following these considerations, it remains to be understood why old GCs span a wide range of r_c values. Here we propose that this is primarily due to a combination of different properties at the moment of cluster formation and different stages of internal dynamical evolution (different dynamical ages) currently reached by each system, with the larger-core GCs being dynamically less evolved (younger) than those with small r_c. Indeed, as already largely discussed in this Thesis, it is well known that GCs are dynamically active stellar systems, where gravitational interactions among stars can significantly alter the overall energy budget and lead to a progressive internal dynamical evolution (Meylan and Heggie 1997) through processes like mass segregation, evaporation of light stars, core collapse, etc. Thus, star clusters formed at the same cosmic time (i.e., with the same chronological age) may have reached quite different stages of dynamical evolution, corresponding to different modifications of their internal structure with respect to the initial conditions. Following this line of reasoning, we propose that the r_c spread observed for old GCs in the LMC could be explained in terms of different levels of dynamical evolution reached by systems of fixed chronological age.

4.2 The dynamical ages of five old star clusters in the LMC

To provide arguments to support this scenario, we determined (through the A^+ parameter) the dynamical age of a sample of old LMC clusters, for which *HST* observations adequate enough to properly study the BSS population and reliably evaluate the LMC field star contamination are available.

4.2.1 The Data-set

We used a set of high-resolution images acquired with the ACS/Wide Field Channel (WFC) on board the *HST*, secured under proposal GO14164 (PI: Sarajedini). We used the images acquired through the filters F606W (V) and F814W (I) to sample the cluster population, and those (typically located 5′ from the cluster centre) obtained through the filters F606W and F435W (B) to sample the LMC field population. For both data-sets, an appropriate dither pattern of a few arcseconds has been adopted in each pointing in order to fill the inter-chip gaps and avoid spurious effects due to bad pixels. The photometric analysis was performed via the PSF fitting method, by using `DAOPHOT IV` (Stetson 1987), following the "standard" approach used in previous works (Dalessandro et al. 2018, 2019a). Briefly, PSF models were derived for each image and chip by using some dozens of stars, and then applied to all the sources with flux peaks at least 3σ above the local background. A master list including stars detected in at least four images was then created. At the position of each star in the master-list, a fit was forced with `DAOPHOT/ALLFRAME` (Stetson 1994) in each frame. For each star thus recovered, multiple magnitude estimates obtained in each chip

TABLE 4.1: Cluster parameters determined in this work.

Cluster	Gravitational centre	r.m.s.	offset from MG03	r_c	r_h	$\log(\frac{t_{rc}}{yr})$	A^+
NGC 1466	$03^h44^m32.72^s$ $-71°40'15.63''$	$0.3''$	$2.8''$	$(8.1^{+0.8}_{-0.7})''$ $(2.0^{+0.2}_{-0.2})$ pc	$(24.5^{+0.2}_{-0.2})''$ $(5.9^{+0.1}_{-0.1})$ pc	8.56	0.15 ± 0.05
NGC 1841	$04^h45^m22.49^s$ $-83°59'55.06''$	$0.4''$	$2.4''$	$(30.3^{+1.3}_{-1.3})''$ $(7.3^{+0.3}_{-0.3})$ pc	$(57.9^{+3.9}_{-3.9})''$ $(14.0^{+0.9}_{-0.9})$ pc	9.54	0.2 ± 0.07
NGC 2210	$06^h11^m31.69^s$ $-69°07'18.37''$	$0.1''$	$1.7''$	$(4.4^{+0.3}_{-0.5})''$ $(1.1^{+0.1}_{-0.1})$ pc	$(15.9^{+0.6}_{-0.2})''$ $(3.9^{+0.1}_{-0.1})$ pc	8.07	0.24 ± 0.05
NGC 2257	$06^h30^m12.59^s$ $-64°19'37.21''$	$0.4''$	$5.7''$	$(26.7^{+1.6}_{-1.4})''$ $(6.5^{+0.4}_{-0.3})$ pc	$(56.4^{+2.6}_{-1.6})''$ $(13.6^{+0.6}_{-0.4})$ pc	9.51	0.11 ± 0.05
Hodge 11	$06^h14^m22.99^s$ $-69°50'49.92''$	$0.2''$	$3.6''$	$(15.0^{+1.0}_{-0.8})''$ $(3.6^{+0.2}_{-0.2})$ pc	$(36.3^{+1.5}_{-0.6})''$ $(8.8^{+0.4}_{-0.1})$ pc	9.11	0.04 ± 0.05

with the same filter were homogenized by using `DAOMATCH` and `DAOMASTER`, and their weighted mean and standard deviation were finally adopted as star magnitude and photometric error. Instrumental magnitudes were calibrated onto the `VEGAMAG` photometric system (Bohlin 2016) by using the recipes and zero-points reported in the *HST* web-sites. Instrumental coordinates were first corrected for geometric distortions by using the most updated Distortion Correction Tables IDCTAB provided on the dedicated page of the Space Telescope Science Institute for the ACS/WFC images. Then, they were reported to the absolute coordinate system (α, δ) as defined by the World Coordinate System by using the stars in common with the publicly available *Gaia* DR2 catalog (Gaia Collaboration et al. 2018b). The resulting 1σ astrometric accuracy is typically ≤ 0.1 mas.

The 5 selected clusters (namely NGC 1466, NGC 1841, NGC 2210, NGC 2257 and Hodge 11) are old, massive ($\log(M/M_\odot) \sim 5.2 \pm 0.2$, McLaughlin and van der Marel 2005) and metal poor ([Fe/H] $\sim -1.9 \pm 0.2$, McLaughlin and van der Marel 2005): they are marked with red squares in Figure 4.1.

4.2.2 Cluster structural parameters

We determined new star density profiles and structural parameters (namely the core, half-mass and tidal radii, the concentration parameter, etc.; see Table 4.1) from resolved star counts and by properly taking into account the LMC field contamination (see Section 4.2.4).

Many papers in the literature (Lugger, Cohn, and Grindlay 1995; Montegriffo et al. 1995; Ferraro et al. 2003b) underline the advantages of using star counts, instead of surface brightness, profiles to derive the cluster structural parameters. In fact, surface brightness profiles are known to suffer from possible biases due to the presence of a few very bright stars, which instead do not affect the number density profiles. In spite of this, most of the morphological parameter estimates (including those for the 5 LMC clusters considered here) are still based on surface brightness profiles. We thus performed new determinations based on star count profiles. The full analysis, including artificial star experiments for the photometric completeness estimate, will be described and discussed in Lanzoni et al. (2019, submitted to ApJ). Here we just summarize its main steps and the structural parameters relevant for the present discussion. According to the procedure adopted in previous works (Lanzoni et al. 2010; Miocchi et al. 2013), we first determined the centre of gravity (C_{grav}) of each system. In fact, a correct location of the cluster centre is a key step, especially in such

distant stellar systems, since even small errors can significantly affect the derived radial behaviour of the observed stellar populations. Note that one arcsecond corresponds to 0.24 pc at the distance of the LMC (we assumed d=50 kpc, Pietrzyński et al. 2013). To determine C_{grav}, we averaged α and δ of all stars brighter than a given threshold magnitude (to avoid incompleteness biases) and lying within a circle of radius r. For the five clusters discussed here, the threshold magnitude is around the main sequence turnoff level, while the typical radius r varies from $6'' - 65''$ depending on the cluster morphology. The derived values of C_{grav} differ by $\sim 2'' - 3''$ from previous determinations, but for NGC 2257 where the difference amounts to almost $6''$ (see Table 4.1). To build the number density profile, we thus divided the photometric sample in (typically 15-20) concentric annuli centred on C_{grav}, each one split into an adequate number of sub-sectors. The number of stars lying within each sub-sector (and with magnitude above a threshold adopted to avoid incompleteness biases) was then counted, and the star surface density was obtained by dividing these values by the corresponding sub-sector area. The stellar density in each annulus was then obtained as the average of the sub-sector densities, and the standard deviation was adopted as the uncertainty. The LMC background level has been estimated from the parallel observations, typically located at $5'$ from each cluster (see Section 4.2.1 and 4.2.4). These have the F606W filter in common with the cluster observations, thus allowing a consistent estimate of the level of LMC field contamination at any fixed magnitude limit. Once estimated, the background level was subtracted to the stellar density measured in each annulus, thus to obtain the density profile of the cluster. Finally, this has been compared with the family of King models (King 1966) characterized by different values of the dimensionless parameter W_0, which is proportional to the gravitational potential at the center of the system. The best-fit solution has been determined through a procedure that minimizes the sum of the unweighted squares of the residuals and evaluates the corresponding reduced χ^2. The uncertainties on the derived structural parameters have been estimated in agreement with other studies in the literature (Montegriffo et al. 1995; McLaughlin and van der Marel 2005): they correspond to the maximum variations of the parameter within the subset of models that provide a $\chi^2_{min} \leq \chi^2_{best} + 1$, where χ^2_{best} is the best-fit χ^2, while χ^2_{min} is the minimum χ^2 obtained for every value of W_0 explored. The core and half-mass radii of the 5 clusters, which are relevant for the present discussion, are listed in Table 4.1.

4.2.3 BSS selection

As already discussed in Chapter 3 for what regards Galactic GCs (see also Raso et al. 2017; Ferraro et al. 2018b), the BSS population has been selected in the normalized CMD (see Section 3.3.3), where the magnitudes of all the measured stars are shifted to assign coordinates (0,0) to the colour and magnitude of the MS-TO point. As already mentioned, the co-added n-CMD of the 5 target clusters is plotted in Figure 4.2 (grey dots): as apparent, the main stellar evolutionary sequences of the five GCs are remarkably well superposed one on another, suggesting that these systems are all coeval. Moreover the perfect match with the CMD of M30, one of the oldest Milky Way GCs with comparable metallicity (Carretta and Gratton 1997), suggests a common age of $\sim$13 Gyr. Hence, the BSS population has been identified by adopting the same selection box in all the target clusters. The same holds for the selection of the reference population, i.e., a sample of normal cluster stars tracing the overall star density profile of the system. In particular, to be consistent with the selections

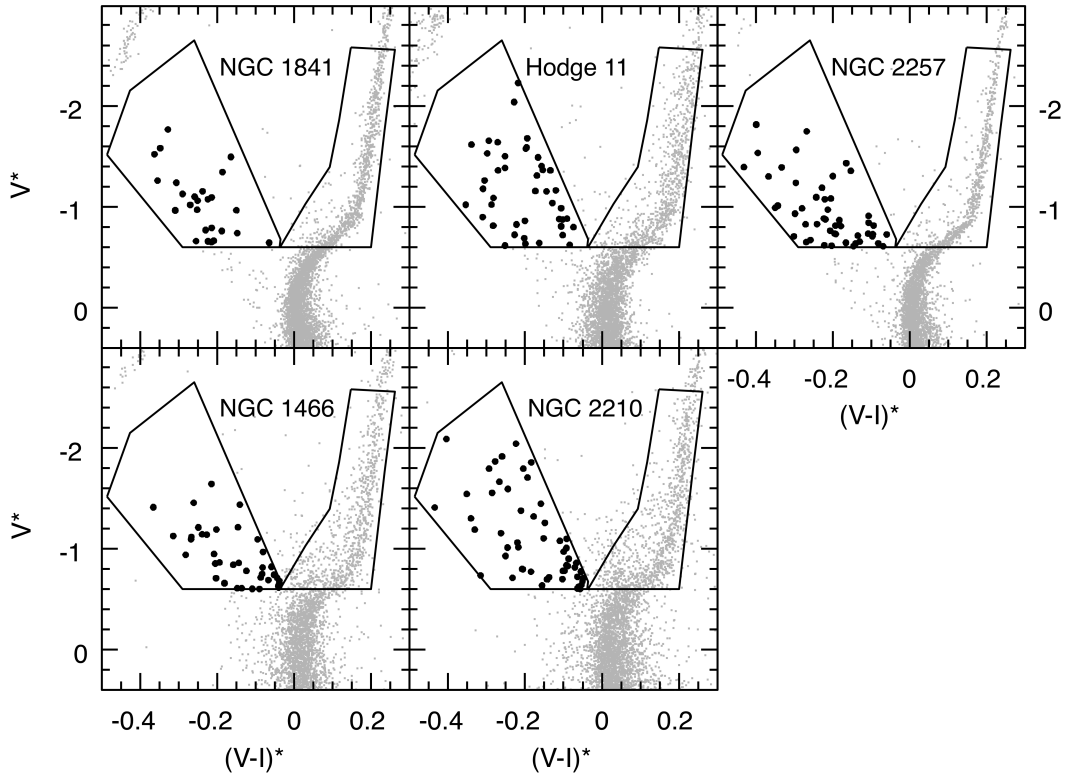

FIGURE 4.3: The selection boxes of BSSs and reference population are shown in the n-CMD of each cluster, where only stars measured within one half-mass radius are plotted. Only BSSs (black circles) and reference stars brighter than $V^{\star} = -0.6$ have been considered in the present analysis. For the two most contaminated clusters (Hodge 11 and NGC 2210) the selection box appears to be more populated on the red side, thus suggesting that this is the region where the field contamination is more severe (see Section 4.2.4 for more details).

performed in Chapter 3 for Galactic GCs (see also Raso et al. 2017; Ferraro et al. 2018b):

1. we only considered BSSs with normalized V magnitude $V^{*} < -0.6$. This selection includes only the most massive portion of the BSS population, thus maximizing the sensitivity of the A^{+} parameter to the dynamical friction effect. Moreover, it excludes the faintest portion where increasing photometric errors and blends can make the BSS selection more problematic;

2. as reference population we adopted the lower portion of the RGB and the SGB, in the same range of magnitudes of the selected BSSs. This indeed provides the ideal reference population, as it includes several hundred stars (thus making statistical fluctuations negligible), and it assures the same level of completeness of the BSS sample;

3. we measured the A^{+} parameter within one half-mass radius ($r_{\rm h}$). This assumption allows a direct comparison among the five different systems and with the large sample of Galactic GCs studied before (see Chapter 3, and also Lanzoni et al. 2016; Ferraro et al. 2018b).

The n-CMDs for all the stars measured within one $r_{\rm h}$ in the five programme clusters are shown in Figure 4.3, where the selection boxes of the BSS and REF populations are also drawn. The cumulative radial distributions of the two populations

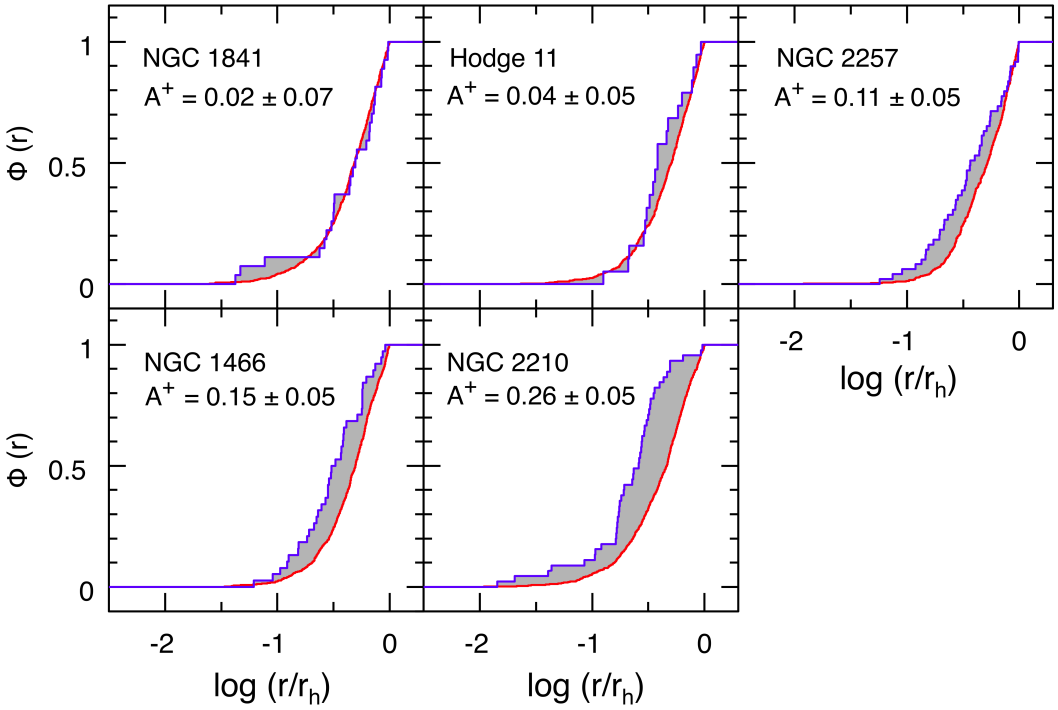

FIGURE 4.4: Cumulative radial distributions of BSSs (blue line) and reference stars (red line) in the five LMC GCs discussed in this Chapter. Only stars within one half-mass radius have been considered and the cumulative radial distributions are thus normalized to unity at r_h. The size of the area between the two curves (shaded in grey) corresponds to the labelled value of A^+. Clusters are ranked in terms of increasing value of A^+.

are plotted in Figure 4.4, where we also marked the measured values of A^+ and related errors. As discussed previously (Section 3.4, and Lanzoni et al. 2016; Ferraro et al. 2018b) the main source of errors in the determination of the parameter A^+ is due to the relative small statistics of the BSS sample detected in each cluster. Thus, the uncertainties in A^+ have been estimated by applying a jackknife bootstrapping technique (Lupton 1993). Following this approach, given a sample of N BSSs, A^+ is recomputed N times from samples of N-1 BSSs obtained by excluding, each time, one different star. Thus the procedure yields N estimates of A^+ and the final uncertainty on A^+ is obtained as $\sigma_{A^+} = \sqrt{N-1}\sigma_{\rm distr}$, where $\sigma_{\rm distr}$ is the standard deviation of the A^+ distribution derived from the N realizations. The uncertainties are listed in Table 4.1 and reported in each panel of Figure 4.4.

4.2.4 Field decontamination

It is well known that the CMD of the LMC clusters can be significantly contaminated by field star interlopers observed along the line of sight. Unfortunately, given the LMC distance, a detailed separation between field and cluster stars based on proper motions is possible only for a few cases. Moreover, accurate *Gaia* DR2 proper motions are available only for the brightest stars. As a consequence, to asses the impact of field contamination in the five cases discussed here we used a statistical approach based on the comparison between the CMD stellar distribution observed in the innermost regions of each cluster and that of a region representative of the surrounding LMC field.

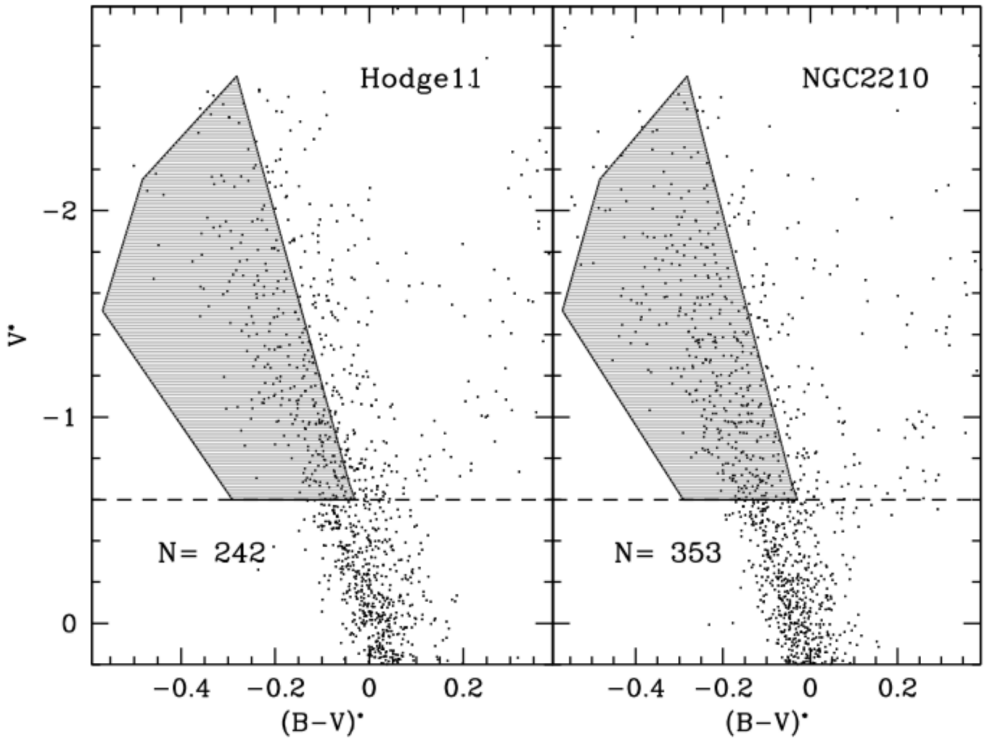

FIGURE 4.5: The n-CMDs of the LMC fields adjacent to Hodge 11 and NGC 2210, zoomed in the BSS region, are shown. The grey shaded area marks the BSS selection box converted in the $[V^*, (B-V)^*]$ n-CMD by using theoretical isochrones (Marigo et al. 2017) of appropriate metallicity. The total number of contaminating stars (which preferentially populate the redder portion of the BSS selection box) are marked. When the considered cluster area ($r < r_h$) is taken into account, they translate into 24 potential field interlopers for Hodge 11 and 6 for NGC 2210.

To this end, we accurately analyzed all the available observations in the vicinity of the program clusters. For three of them (namely NGC 1466, NGC 1841 and NGC 2257) the field contamination turns out to be negligible, with only a few stars measured over the entire field of view (11 square arcmin) of the ACS/WFC parallel observations sampling the nearby LMC field.

In the case of NGC 2210 and Hodge 11, the LMC field appears to be more pronounced and we thus performed a statistical decontamination procedure. This required us to transform the boxes used for the population selection (see Figure 4.3) into the (V, B-V) diagram, because the fields surrounding these two clusters have been observed in the F606W (V) and F435W (B) filters. The former is exactly the same filter used in the cluster pointings. Hence the magnitude range along the vertical axis is precisely anchored. To determine the (B-V) limits of the adopted selection boxes we made use of theoretical models (Marigo et al. 2017) of the appropriate metallicity, coloured in the ACS/WFC filter system. The BSS selection boxes transformed into the (V, B-V) CMD are shown in Figure 4.5. We then counted the number of stars in the parallel observations falling within the selection boxes and we determined the LMC field density dividing this number by the area of the ACS/WFC field of view. The number of field stars contaminating the BSS population is thus obtained as the product between the number of selected BSSs and the field density, and the same holds for the reference population. It is important to remember that

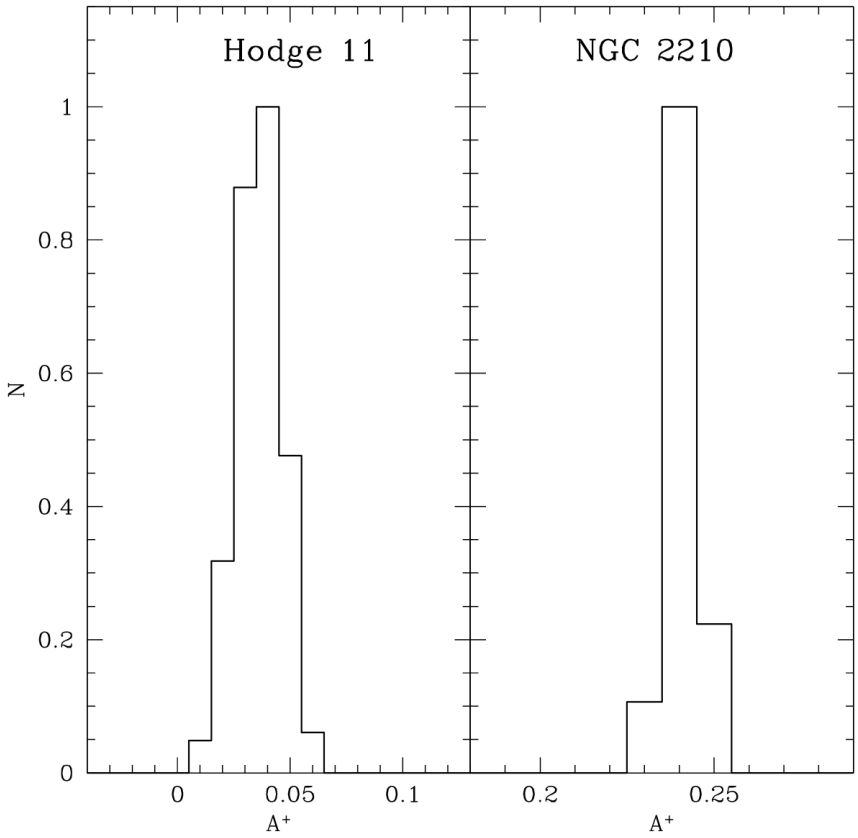

FIGURE 4.6: Normalized distribution of the values of A^+ obtained from 5000 independent decontamination procedures applied to the BSS region of Hodge 11 and NGC 2210. In each realization, 24 (in Hodge 11) and 6 stars (in NGC 2210) have been randomly removed from the BSS region of the two clusters and the A^+ parameter has been re-determined. As can be seen, in both cases the result is a peaked distribution with a well defined maximum ($A^+ = 0.04$ for Hodge 11, and $A^+ = 0.24$ for NGC 2210) and a small dispersion ($\sigma = 0.01$).

in our analysis we are considering only the stars observed within one half-mass radius of each cluster. This corresponds to an area of only $\sim$1 square arcmin (i.e., 1/10 of the ACS field of view) in the case of Hodge 11 (for which $r_h = 36.3''$), and just $\sim$0.2 square arcmin (i.e., 1/50 of the ACS area) in the case of NGC 2210 (having $r_h = 15.9''$). The results are that the LMC field contamination to the reference population is completely negligible in both clusters, while a few selected BSSs are likely field interlopers. Their exact number is listed in Table 4.2 for three radial bins ($r < r_c, r_c < r < r_h/2, r_h/2 < r < r_h$) adopted to preserve the radial information. To determine reliable (i.e., field-decontaminated) values of A^+ we thus randomly removed these numbers of stars from the BSS population sampled in each bin, and we repeated this random decontamination procedure 5000 times, each time registering the resulting value of A^+. Figure 4.6 shows the histogram of the obtained values. As can be seen, a peaked distribution with a small dispersion (smaller than 0.01) is obtained in both cases, thus testifying that the value of A^+ is solidly estimated also in these contaminated clusters.

TABLE 4.2: Field contamination

Cluster	N_{BSS} $r < r_h$	N_{field} $r < r_c$	N_{field} $r_c < r < r_h/2$	N_{field} $r_h/2 < r < r_h$
NGC 1466	38	0	0	0
NGC 1841	27	0	0	0
NGC 2210	52	0	1	5
NGC 2257	49	0	0	0
Hodge 11	45	4	1	19

4.3 Discussion

From our A^+ measurements (see Figure 4.4 and Table 4.1), we find that NGC 1841 and Hodge 11 show a low level of BSS segregation ($A^+ = 0.02 - 0.04$), suggesting that they both are dynamically young, while NGC 2257, NGC 1466 and NGC 2210 have increasing values of A^+ (up to 0.24), corresponding to a moderate/large dynamical evolution. Hence, in spite of their comparable chronological ages, these systems show different levels of BSS segregation and, thus, different levels of dynamical evolution. This is further confirmed by the left panel of Figure 4.7, showing the dynamical age of the investigated LMC GCs (large red squares) as a function of A^+. The dynamical age is expressed in terms of the ratio N_{relax} between the chronological age of the systems (t=13 Gyr) and their current central relaxation times (t_{rc}). Central relaxation times have been computed by adopting the newly determined structural parameters and following the well-known relation (Djorgovski 1993):

$$t_{rc} = 8.338 \times 10^6 \times \frac{\sqrt{\rho_c}}{\ln(0.4 \times M_{cl}/m_*)} \times \frac{r_c^3}{m_*} \text{ yr} \quad (4.1)$$

where ρ_c is the central mass density in $M_\odot/pc^3$, M_{cl} is the cluster mass in $M_\odot$; m_* is the average star mass (here we adopted 0.3 $M_\odot$) and r_c is the core radius in pc. The values of the central relaxation times for the five clusters are listed in Table 4.1.

The $N_{relax} = t_{age}/t_{rc}$ index quantifies the number of t_{rc} occurred since the epoch of cluster formation: a large value of N_{relax} means a dynamically evolved stellar system, while a small value means a dynamically unevolved cluster. As apparent from Figure 4.7, the BSS segregation level measured in NGC 2210 indicates that ∼100 central relaxation times have occurred since the formation epoch of this cluster, while this index drops to 20-30 for NGC 1466 and NGC 2257, and to just a few units for Hodge 11 and NGC 1841. The figure also shows an impressive match between the results shown in this Chapter for the five LMC clusters and those previously shown in Chapter 3 for a sample of 48 old and coeval GGCs (grey circles, see Ferraro et al. 2018b), demonstrating that the "dynamical clock" can be efficiently used in any stellar environment. The right panel of Figure 4.7 shows the effect of dynamical evolution on the core size for the entire sample of 48 Galactic GCs (grey dots) and the five LMC systems studied here (large red squares). As can be seen from the nice correlation, clusters with large core radius are dynamically younger (with lower values of the A^+ parameter) than compact systems. The former have possibly maintained unchanged or only slightly modified their initial structure (in terms of core size, concentration, central density), while all dynamically old clusters currently appear as quite compact objects, although they possibly formed with a larger core. Hence, the internal dynamical evolution tends to generate compact clusters, systematically moving large-core systems toward small-size compact objects over a timescale that

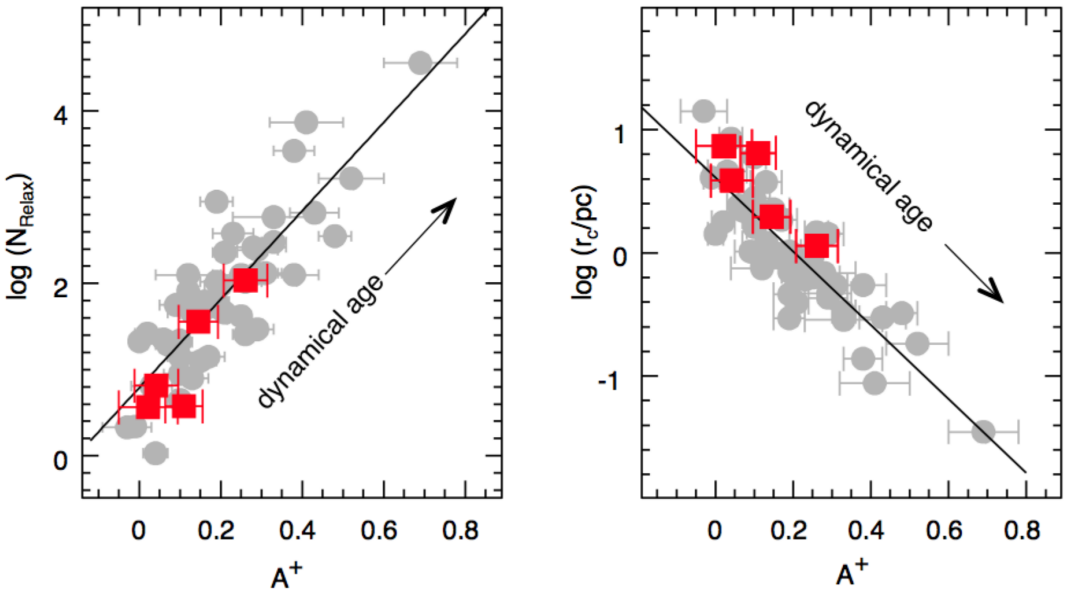

FIGURE 4.7: Left Panel: Relation between the segregation level of BSSs (measured by A^+) and the number of current central relaxation times occurred since cluster formation ($N_{\rm Relax}$) for the 5 LMC clusters studied here (large red squares) and 48 Galactic GCs (grey circles, see Chapter 3 and Ferraro et al. 2018b). The plotted 1σ errors have been computed as discussed in Section 4.2.3. Right Panel: Relation between A^+ and the core radius, illustrating that cluster sizes move toward smaller values with the long-term internal dynamical evolution of the system: compact clusters are dynamically more evolved than large-r_c GCs.

mainly depends on the cluster structure. Panels (a) and (c) in Figure 4.1 suggest that also the local environment might have had some impact on the cluster dynamical evolution: in fact, the old GCs with smallest core radii are located at the smallest galactocentric distances, indicating that their internal evolution has been accelerated by an increased evaporation/tidal stripping of low mass stars in the innermost region of the LMC. Of course also the fraction of dark remnants (as BHs and neutron stars) retained within each cluster and their ejection timescale has an impact on the dynamical evolution of the system (in the sense of slowing it down for increasing retention fraction, Alessandrini et al. 2016). However both these quantities are unknown at the moment, and only a few observational evidence of BH candidates in GCs has been found so far (Strader et al. 2012; Chomiuk et al. 2013). Hence, here we consider the action of dark remnants as a second-order effect on the dynamical cluster aging.

4.3.1 Conclusion and future perspectives

On the basis of these results, we conclude that the observed spread of r_c at a given chronological age can be interpreted as the "natural" consequence of GC internal dynamical evolution that brings systems with relaxation time significantly shorter than their age to populate the small core radius region of the diagram. It is also somehow "natural" that chronologically old GCs display the largest spread of core sizes, since in this case a variety of initial configurations (with intermediate/short relaxation times) could have evolved toward small r_c configuration. Of course the proposed scenario leaves completely unaffected the portion of the diagram corresponding to small chronological ages ($t = 10^7 - 10^8$ yr), because all young clusters have relaxation times comparable to (or larger than) their age and their internal dynamical

evolution processes had not enough time to move them toward the small r_c portion of the diagram. It will be interesting to extend this study to the intermediate-age clusters ($\log t > 8 - 9$), which could also show evidence of different levels of dynamical evolution. Indeed a first attempt (Li et al. 2019) to measure the dynamical age of 7 LMC clusters in this age range suggests quite modest levels of dynamical evolution. However, a detailed analysis of the oldest clusters in this age range (with ages larger than 2-3 Gyr, as NGC 2121, NGC 2155 and SL 663) is still lacking and it can certainly provide further hints on this topic.

The evidence presented in this Chapter provides a new interpretative scenario for the age-size distribution in the LMC clusters that does not require the action of BHs, but it is essentially driven by the cluster internal dynamical evolution. This scenario removes the necessity of an evolutionary path in which compact young clusters evolve into old globulars with a wide range of radii. Moreover, it provides further support to the other structural (see Figure 4.1) and chemical (Mucciarelli et al. 2008; Mucciarelli et al. 2014; Martocchia et al. 2018) pieces of evidence that already challenged such an evolutionary connection. Hence, this result redirects our attention to the cluster formation history in the LMC, its dramatic changes over the cosmic time and the environmental conditions at which this process is occurring.

Chapter 5

BSS Double Sequences

Mainly based on:
Beccari, Ferraro, [...], Raso, et al. (2019), ApJ, 876, 87

5.1 Introduction

As already explained in Chapter 1, BSSs are generated through two main formation channels: (1) MT phenomena and/or coalescence in primordial binary systems (McCrea, 1964), and (2) direct stellar collisions (Hills and Day, 1976). While the first process (which is driven by the secular evolution of binary systems) is common to any stellar environment (low and high-density stellar systems, as globular and open clusters, dwarf galaxies, the Galactic field), the second one requires a high-density environment, where the rate of stellar collisions is increased. Note that a collisional environment can affect also the efficiency of the MT formation channel, since dynamical interactions involve single and binary stars, thus favoring the tightening of binaries. The congested central regions of high density GCs are the ideal habitat where collisions can occur. Hence in such an environment both the BSS channels can be active (Ferraro et al. 1993; Ferraro, Fusi Pecci, and Bellazzini 1995), although the MT formation channel seems to be the most active one (see Davies, Piotto, and de Angeli 2004; Knigge, Leigh, and Sills 2009).

Although a few intriguing spectroscopic features have been interpreted as the fingerprints of the MT formation channels (see Ferraro et al. 2006), BSSs produced by different formation processes still appear photometrically indistinguishable. In this respect, a promising route of investigation was opened by the discovery of two distinct sequences of BSSs in the post core-collapse cluster M30 by Ferraro et al. (2009). After this discovery, a similar feature has been detected in NGC 362 (Dalessandro et al., 2013a) and NGC 1261 (Simunovic, Puzia, and Sills, 2014). In only one case a double BSS sequence has been detected in a young cluster in the Large Magellanic Cloud (Li et al., 2018a,b). However, it has been argued (Dalessandro et al., 2019a,b) that the observed bifurcation could be an artifact due to field star contamination.

The main characteristic ubiquitously detected in these clusters is the presence of a narrow BSS sequence on the blue side of the CMD, separated through a clear-cut gap from a more scattered population of BSSs on the red side. The narrowness of the blue sequence demonstrates that it is populated by a nearly coeval population of stars with different masses, generated over a relatively short period of time. Moreover, the perfect agreement of the blue sequence locus with collisional isochrones (Sills, Karakas, and Lattanzio, 2009) suggests that these objects have been formed through collisions. Instead, the red sequence is by far too red to be reproduced by collisional models of any age. All these facts support the hypothesis that the origin of the blue BSS sequence is related to a phenomenon able to enhance the probability

of collisions over a relatively short period of time, thus promoting the formation of collisional BSSs. Ferraro et al. (2009) proposed that this phenomenon is the cluster core collapse (see also Chapter 1). This hypothesis has been recently confirmed by numerical simulations (Portegies Zwart, 2019).

In this context, Ferraro et al. (2009) also suggested that the properties of the blue-BSS sequence (essentially its extension in luminosity) can be used to date the epoch of CC. In short, while the MS-TO luminosity is a sensitive indicator of the age of the cluster, the luminosity of TO point of the blue BSS sequence can be used to determine the epoch at which the collisional event has promoted the formation of this stellar population. In fact the comparison with collisional models allowed the dating of the epoch of the CC event: approximately 2 Gyr ago in M30 (Ferraro et al., 2009) and NGC 1261 (Simunovic, Puzia, and Sills, 2014), and 0.2 Gyr ago in NGC 362 (Dalessandro et al., 2013a).

Recent Monte-Carlo simulations of synthetic MT-BSSs (Jiang et al., 2017) showed that the blue-BSS sequence can be also populated by MT-BSSs. This finding by itself does not invalidate the possibility that the blue BSS sequence might be mainly populated by collisional BSSs, since the easiest way to reproduce the observed narrowness of the blue sequence and the adjacent gap is still the hypothesis that the vast majority of BSSs along this sequence formed almost simultaneously, instead than being the result of a continuous process extending over a long time interval. Conversely, the result of Jiang et al. (2017) might explain the presence of the few W Uma stars (which are close binaries) actually detected by Ferraro et al. (2009) and Dalessandro et al. (2013a) along the blue BSS sequence in M30 and in NGC 362. In this framework it is important to stress that, although the location in the CMD cannot be used to individually distinguish collisional from MT-BSSs, it mirrors the occurrence of the two formation mechanisms: when a narrow blue sequence is detected, this is mainly populated by collisional-BSSs, with some possible contamination from MT-BSSs (as the W Uma variables detected along the blue sequences); the red side, instead, cannot be reproduced by any of the available collisional models (Sills, Karakas, and Lattanzio, 2009) and is mainly populated by MT-BSSs with some contamination from evolved BSSs generated by collisions.

In this Chapter we present the discovery of a double BSS sequence in the post-core collapse cluster M15 (NGC 7078). Indeed, M15 is one of the most massive cluster of the Galaxy ($\log(M/M_\odot) = 6.3$, several $10^6 M_\odot$) and dense ($\log \rho_0 = 6.2$ in units of $M_\odot/pc^3$). As emphasized by Leigh et al. (2013), while binary evolution seems to be the dominant channel for BSS formation, the fact that M15 has one of the densest and most massive cores among Galactic GCs, makes it the ideal environment where to expect the collisional formation channel to be relevant. This fact has been recently confirmed by Leigh et al. (2019) where the authors foresee the collisions via 2+2 interactions to play a crucial role on the formation of BSSs in post-core collapse clusters. Since the very first detections of a central cusp in its surface brightness profile (Djorgovski and King 1986; Lauer et al. 1991; Stetson 1994) it has been considered as a sort of "prototype" of post-CC clusters, and it is still cataloged so in all the most recent GC compilations (see the updated version of the Harris Catalog, Harris 1996). The BSS sequence studied here shows a complex structure that might provide crucial information on the core-collapse phenomenon.

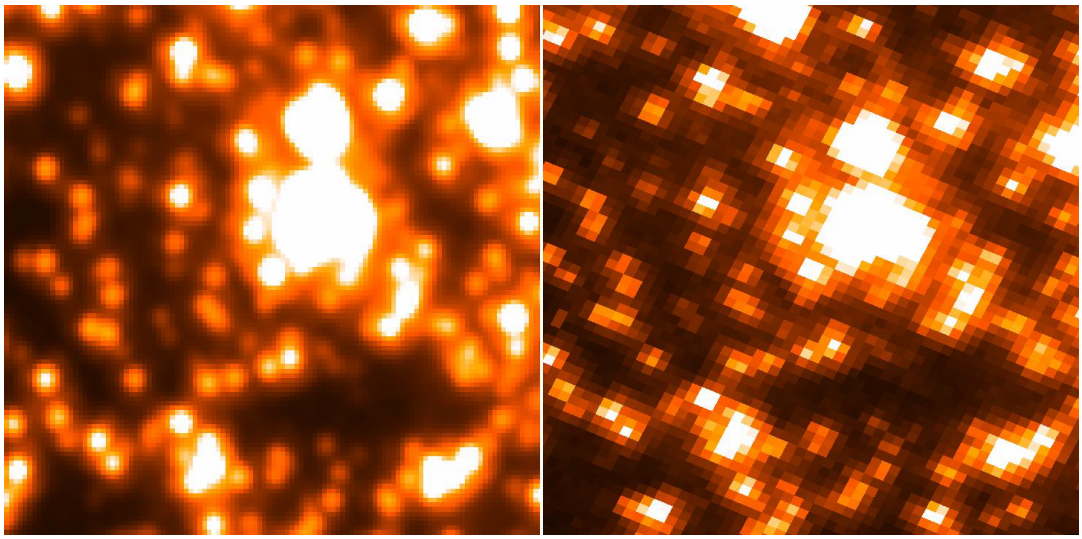

FIGURE 5.1: Comparison between the central $1.5'' \times 1.5''$ region of M15 as seen through the super sampled B_{435} image, and that observed through a single exposure in the same filter (left and right panels, respectively). North is up and East is to the left.

5.2 Data reduction

In this work we use a set of archival high resolution images obtained with the ACS on board the *HST*. The core of the cluster was observed with the HRC mode of the ACS in the F220W and F435W filters (hereafter, U_{220} and B_{435}, respectively). The HRC provides a supreme spatial resolution, with a pixel scale of $\sim 0.028''$/pixel $\times$ $0.025''$/pixel in a field of view of $29'' \times 26''$. A total of 13 images of 125s of exposure time each were acquired in the B_{435} filter under the program GO-10401 (PI: Chandar), while 8×290s exposures were taken with the U_{220} filter under the program GO-9792 (PI: Knigge). These images were already used in Dieball et al. (2007) and Haurberg et al. (2010) to probe the stellar population in the innermost regions of the cluster. As described in Haurberg et al. (2010), the HRC images were combined using a dedicated software developed by Jay Anderson and similar to DrizzlePack[1]. In short, the software combines single raw images of a given band to improve the sampling of the PSF. A $3'' \times 3''$ section of a super sampled frame thus obtained in the B_{435} band is shown in Figure 5.1 (left panel), where it is also compared to a single raw exposure (right panel). As immediately visible in the figure, the software allows to reduce the pixel size to $\sim 0.0125''$/pixel $\times$ $0.0125''$/pixel on the combined images, thus doubling the effective spatial resolution in both the U_{220} and the B_{435} filters. This image processing is crucial as it allows us to resolve the stars in the very central region of the cluster, where the stellar crowding is too severe even for the resolving power of the HRC (see also Figure 1 from Haurberg et al., 2010).

We first performed a standard PSF fitting photometry on the two super-sampled U_{220} and B_{435} frames using `DAOPHOT II` (Stetson, 1987). The catalog was calibrated into the `VEGAMAG` system using the recipe from Sirianni et al. (2005) and adopting the most recent zero points available through the ACS Zeropoint Calculator[2]. All the post-MS stellar evolutionary sequences typical of a GC are well distinguishable on the first version of the CMD shown on the left panel of Figure 5.2. Still, we notice

[1] http://www.stsci.edu/hst/HST_overview/drizzlepac

[2] https://acszeropoints.stsci.edu

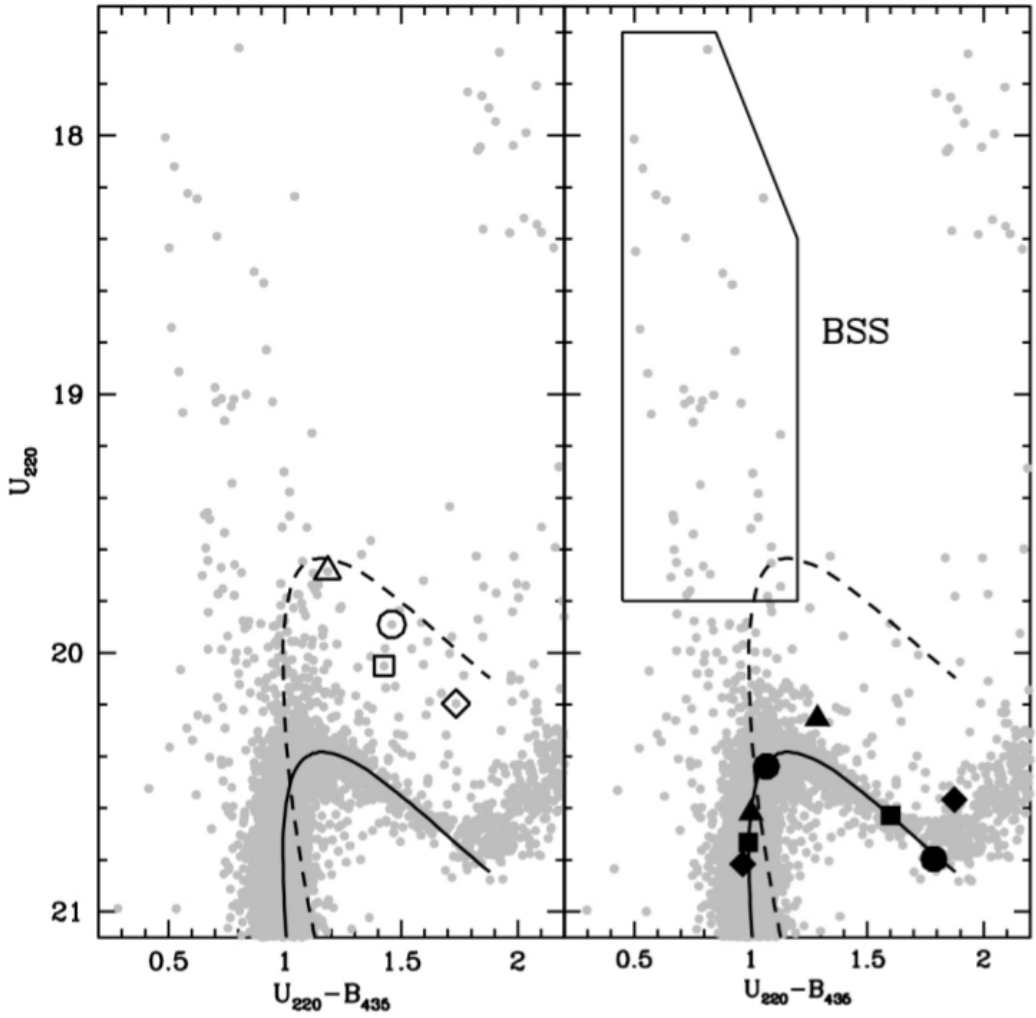

FIGURE 5.2: CMDs obtained with standard PSF fitting photometry (left panel) and our de-blending procedure with ROMAFOT (right panel). For reference, the best-fit isochrone and the equal-mass binary sequence are shown as solid and dashed lines, respectively. As apparent, many stars are located between these two lines in the left panel: the vast majority of these objects turned out to be blends due to poor PSF fitting. For illustration purposes, four blends are highlighted with open symbols in the left-hand panel and their corresponding de-blended components are marked with the same (solid) symbols in the right panel. Each of the four blends is the combination of a MS-TO and a SGB star. The box used to select the BSS population is also shown.

a number of objects falling in the region brighter than the SGB and bluer than the RGB.

The origin and the reliability of these stars (sometimes called "yellow stragglers") is a well known problem and it has been discussed in many papers in the literature. The vast majority of these objects have been demonstrated to be optical blends (see, e.g., Figure 8 in Ferraro, Fusi Pecci, and Buonanno 1992 and Figure 7 in Ferraro et al. 1991, where a few examples of de-blending are illustrated). Here, we used the package ROMAFOT (Buonanno et al., 1983) to manually inspect the quality of the residuals of the initial PSF fitting process, and to iteratively improve the quality of the PSF fitting for a selection of individual problematic stars. ROMAFOT is a software developed to perform accurate photometry in crowded fields. While the PSF

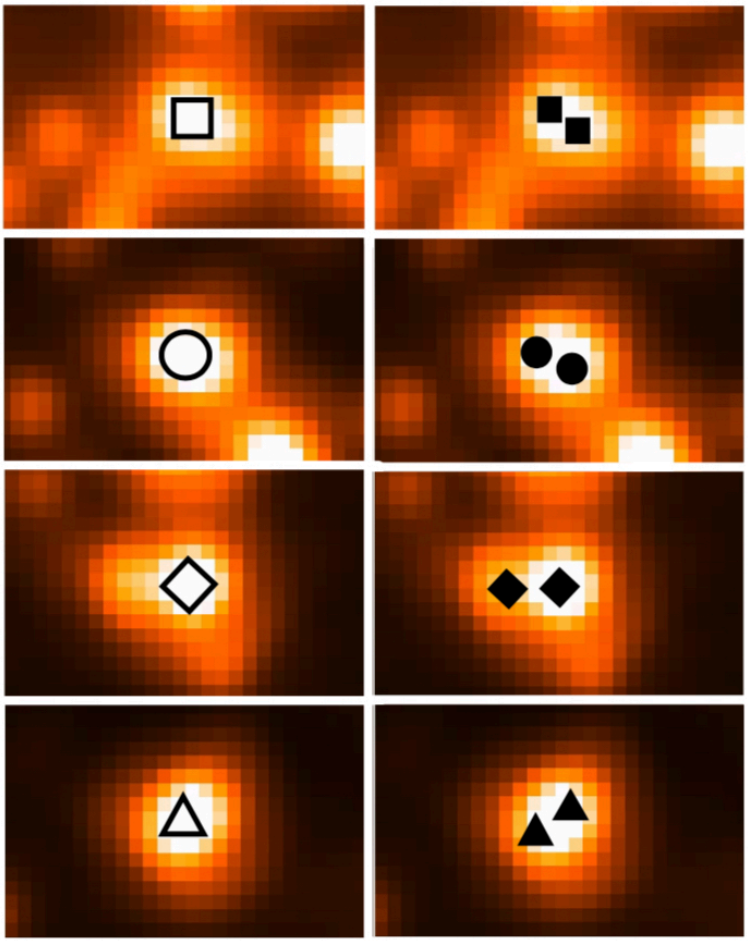

FIGURE 5.3: B_{435} images of the same sources discussed in Figure 5.2: the single (blended) objects in our starting photometry are marked with empty symbols in the left panels, while the corresponding resolved components, obtained after our de-blending procedure with ROMAFOT, are shown with the same (solid) symbols in the right panels.

fitting procedure with ROMAFOT requires a higher level of manual interaction by the user with respect to DAOPHOT II, it has the unique advantage of a graphical interface that allows the user to improve the local deconvolution of stellar profiles (see also Monelli et al., 2015). Indeed the results of the analysis with ROMAFOT fully confirm the findings by Ferraro et al. (1991) and Ferraro, Fusi Pecci, and Buonanno (1992): most of the objects lying in the yellow stragglers region turned out to be blends. For the sake of illustration, in the left panel of Figure 5.2 we highlight four spurious sources (open symbols) due to poor PSF fitting. As shown in the right-hand panel, each of these sources is indeed the blend of a MS-TO and a SGB star (solid symbols). These sources are also highlighted with the same symbols on the B_{435} images shown in Figure 5.3. In Figure 5.2 we also plot the equal-mass binary sequence (dashed line) and the adopted BSS selection box. It is evident that the conservative BSS selection discussed in Section 3 (considering only BSSs brighter than $U = 19.8$) prevents any significant contamination from unresolved binaries and blends.

The iterative de-blending process described above was used to optimize the PSF

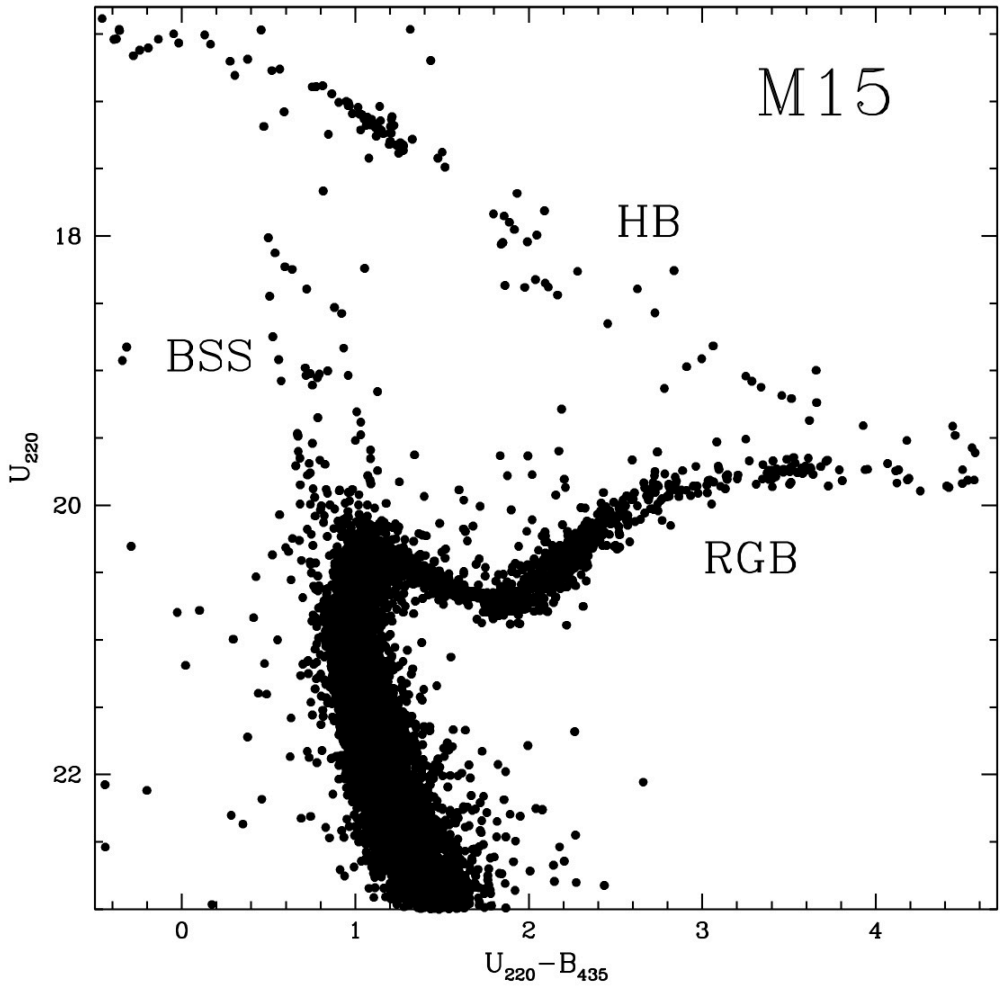

FIGURE 5.4: Final, de-blended UV-CMD of the core of M15. The position in the CMD of the BSS population, and of the RGB and HB evolutionary sequences is labeled.

modeling of all the objects lying outside the well recognizable canonical evolutionary sequences in the CMD, including all the BSSs. In Figure 5.4 we show the final CMD obtained at the end of the accurate de-blending procedure. It should be noted that the HRC data-set that we use in this Chapter allows us to resolve stars with a separation larger than $\sim 0.012''$, which translates into a separation of ~ 125 au at the distance of M15 (10.4 kpc). Hence, even after our de-blending procedure, it is still possible that a few unresolved binaries and blends with separation smaller that 125 au are still populating the "yellow straggler region". On the other hand, some of these objects could also be BSSs that are evolving from their main-sequence (core hydrogen burning) stage to a more evolved evolutionary phase (the SGB). Still, given the overall low number of BSSs, and taking into account that the SGB stage at the typical BSS mass ($\sim 1.2\ M_{\odot}$) is quite rapid, we expect just a few evolved BSSs in this part of the CMD.

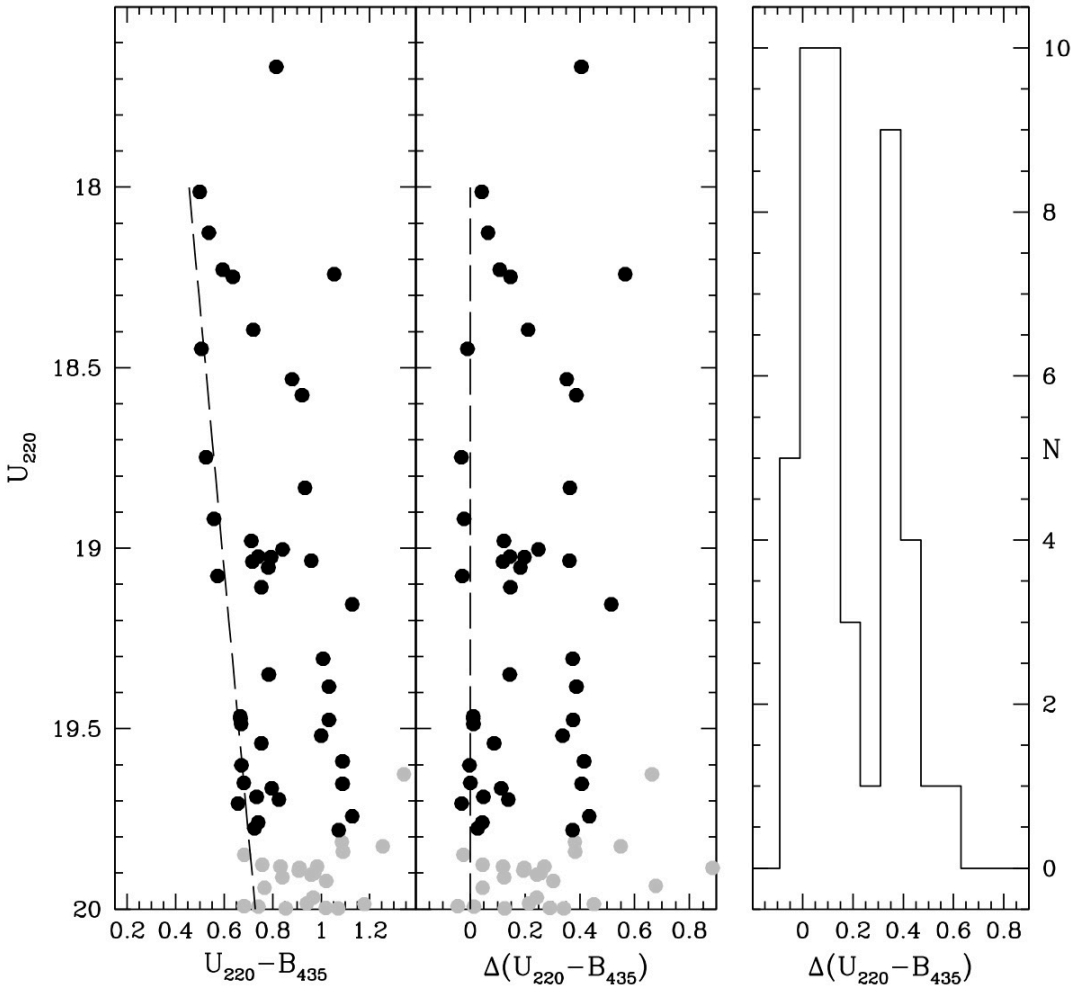

FIGURE 5.5: Left Panel: Portion of the CMD zoomed on the BSS region. All the BSSs used in this study (which are brighter than $U_{220} < 19.8$) are marked as black circles. The dashed line shows a fit to the bluest stars of the blue-BSS population. The line is used as reference to calculate the distribution in U_{220}-B_{435} color of the BSS population. Central Panel: Rectification of the CMD, showing the color distance $\Delta(U_{220}$-$B_{435})$ of the surveyed stars from the mean ridge line of the blue-BSS population (dashed line, the same as in the left panel). Right Panel: Histogram of the BSS color distances from the mean ridge line of the blue population.

5.3 The BSS population in the core of M15

The CMD shown in Figure 5.4 demonstrates the outstanding quality of the data, which allows us to properly sample the hot stellar population in the core of M15 and to detect MS stars well below the MS-TO. Thanks to the use of the U_{220} filter, the hot HB stars describe a very narrow and well defined sequence. This fact per se demonstrates already the excellent photometric quality of the data (see also Dieball et al., 2007). The same applies to the RGB stars whose sequence spans almost 2.5 mag in color on the CMD. As expected, and as already described in Chapter 3, the use of the UV filter clearly suppresses the contribution of the RGB stars to the total cluster light, making this diagram optimal for sampling the hottest stellar populations in the cluster (see also Ferraro et al. 1997, 2003a, 2018b; Raso et al. 2017).

5.3.1 A double sequence of BSSs

A surprising feature clearly visible in the CMD of Figure 5.4 is the presence of two distinct, parallel and well separated sequences of BSSs. The two sequences are almost vertical in the CMD, in a magnitude range 18 $<U_{220}<$ 20, and located at (U_{220}-B_{435}) $\sim$ 0.8 and $\sim$ 1.2. A similar feature was previously detected using optical bands in the GCs M30, NGC 362 and NGC 1261 (respectively, Ferraro et al. 2009; Dalessandro et al. 2013a; Simunovic, Puzia, and Sills 2014). This is the first time that such feature is detected in an UV-CMD.

We show in Figure 5.5 a portion of the CMD zoomed on the BSS region. Hereafter, we will consider as bona-fide BSSs those stars populating the region of the CMD in the colour ranges explicitly mentioned above and with $U \lesssim 19.8$. As discussed above, such a conservative magnitude threshold guarantees that the BSS sample is negligibly affected by residual blended sources and unresolved binaries (see right panel in Figure 5.2). On the left panel we show with a dashed line the fit to the bluest sequence of BSSs. We take this line as a reference and we then calculate the distance in ($U_{220}-B_{435}$) color of the BSSs observed at $U_{220} < 19.8$ (black dots). In the rightmost panel we show the histogram of the distribution of the colour's distances. This is clearly not unimodal: at least two peaks, with a clear gap in-between, are well distinguishable. To assess the statistical significance of such bi-modality, we used the Gaussian mixture modeling (GMM) algorithm presented by Muratov and Gnedin (2010), which works under the assumption that the multi-modes of a distribution are well modeled via Gaussian functions. We found that the separation of the means of the 2 peaks relative to their widths is $D = 4.71 \pm 0.78$. The parametric bootstrap probability of drawing such value of D randomly from a unimodal distribution is 3.6%. The probability of drawing the measured kurtosis is 0.4%. As such, all three statistics clearly indicate that the observed BSS color distribution in the UV-CMD is bi-modal. The GMM code also provides the user with the probability distribution of each element to belong to a given peak. We find that 27 and 15 stars have a probability $>$ 98% to belong to the bluest and reddest peak, respectively. Their location in the CMD is shown in Figure 5.6. The 2 stars shown as black dots in the figure have a probability of 96% (36%) and 69% (31%) to belong to the bluest (reddest) sequence. We also used the Dip test of uni-modality (Hartigan and Hartigan, 1985) to further investigate on the significance of the deviation from uni-modality of the BSS color distribution shown if Figure 5.5. The Dip test has the benefit of being insensitive to the assumption of Gaussianity. We found that the observed BSS color distribution has 98.5% probability to deviate from a unimodal distribution. The tests described above hence indicate that the bi-modality of the BSS sequence that we have found in the UV-CMD of M15 is a statistically solid result.

In order to further prove the presence of the observed bi-modality in the BSS colour distribution, we retrieved a number of high resolution images of the core of M15 obtained with the *HST*/WFC3 (GO-13297; PI: Piotto). These images, obtained using the F275W and F336W filters, were already used in Raso et al. (2017, , see Chapter 3) to investigate the dynamical age of the cluster through the study if the BSS radial distribution (see also Lanzoni et al., 2016). We stress here that the plate scale of $\sim 0.04''$ offered by the WFC3 did not allow us to firmly detect the double BSS sequence in the core of the cluster as reported in this Chapter. Interestingly enough, hints for the presence of a double BSS sequence are visible in the CMD of M15 shown in Figure 22 of Piotto et al. (2015).

We used the photometric catalog obtained by Raso et al. (2017) to resolve the BSS in a region outside the area covered by our HRC data out to a radius $r = 80''$.

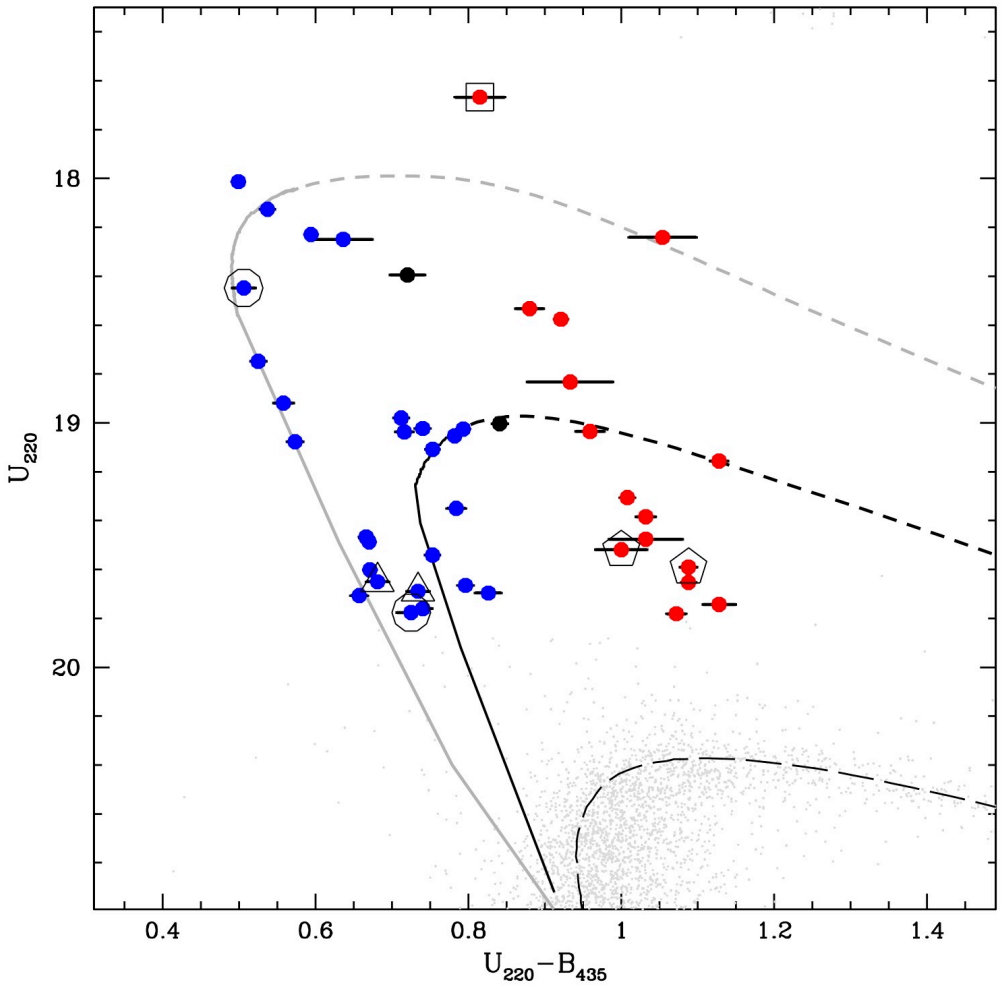

FIGURE 5.6: UV-CMD zoomed on the BSS population. The stars belonging to the blue-BSS and red-BSS sequences are shown as blue and red circles, respectively. Each BSS is assigned to a given sequence according to a statistical test based on the GMM algorithm presented in Muratov and Gnedin (2010). The two stars shown as black circles have a probability of 96% (36%) and 69% (31%) to belong to the blue (red) sequence. Variable BSSs are highlighted with open symbols (see text). Two collisional isochrones, of 2 Gyr (thick grey line) and 5.5 Gyr (thick black line), are superimposed to the observed CMD. The evolutionary tracks of a $0.6 + 0.6 M_{\odot}$ and a $0.6 + 0.4 M_{\odot}$ collision product are also plotted (grey and black dashed lines, respectively). For the sake of comparison, we also mark the 12 Gyr-old isochrone for normal (single) stars (black long-dashed line).

Moreover we used several hundreds stars in common between the WFC3 and our HRC catalog to accurately register the position of the stars in the HRC catalog to the WFC3 position. We then used `ALLFRAME` (Stetson, 1994) to obtain accurate PSF fitting photometry of the F275W and F336W images of the WFC3 using as input catalog of stellar centroids the coordinates of HRC stars registered on the WFC3 coordinate system.

We show on Figure 5.7 the CMDs obtained with the two data-sets. Clearly the separation of the BSS into a blue and red sequences according to the selection done in the HRC plane, holds also in the CMD obtained with the WFC3.

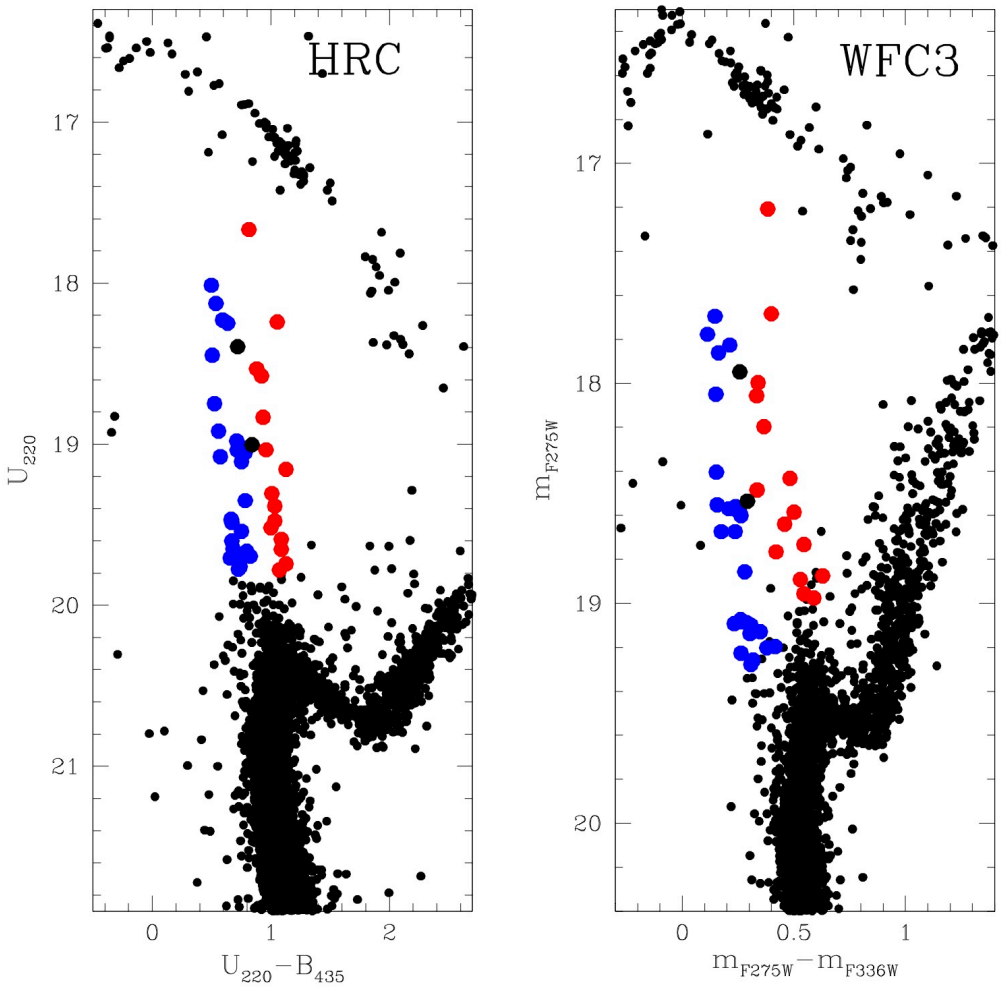

FIGURE 5.7: UV-CMD obtained in the same area with the HRC (left panel) and WFC3 (right panel; see text for details) zoomed on the BSS population. The stars belonging to the blue-BSS and red-BSS sequences are shown as blue and red circles, respectively.

5.3.2 Variable BSSs

Dieball et al. (2007) used the HRC data-set to identify the variable stars in the core of M15 (see their Table 2). We have used their catalog to identify possible variable among the BSS population. We have found 7 variables among our BSS populations, namely V20, V22, V33, V37, V39, V38, V41 (nomenclature from Table 2 of Dieball et al., 2007). The location of these variables in the CMD is shown with open symbols in Figure 5.6. Two variables (V22 and V33; open pentagons) are classified as SX-Ph, 2 as CV candidates (V39 and V41; open circles), 2 are unclassified variables observed in the CMD region of BSSs (V37 and V38; open triangles) and V20 is classified as candidate B-HB star (open square). The variables V37, V38, V39 and V41 show flickering, i.e. irregular and small (few tenths of a magnitude) variations on short timescales. For this reason Dieball et al. (2007) identify them as candidate CVs. While V37 and V38 are indeed located along the BSS sequence also in the CMD shown by Dieball et al. (2007), the authors speculate that V39 and V41 might be early CVs. Our UV-CMD convincingly shows that these stars are all BSSs. Additional observations are needed to firmly assess the nature of these variables, primarily to clarify if they are

binary systems or single stars. Indeed a few W Uma Variables (which are contact binaries) have been found along both the BSS sequences in M30 (Ferraro et al., 2009) and NGC 362 (Dalessandro et al., 2013a). Using dedicated theoretical models, Jiang et al. (2017) found that the contribution of the MT-BSSs to the blue or red sequence strongly depends on the contribution of the donor to the total luminosity of the unresolved binary system. Hence our observations further support the possibility that both collisional and MT-BSSs can populate the blue sequence.

5.3.3 A collisional sequence

We used a set of tracks and isochrones extracted from the collisional model library of Sills, Karakas, and Lattanzio (2009) to evaluate whether the location of the blue BSS sequence in M15 is in agreement with the locus predicted by BSS collisional models (as previously found in M30 and in NGC 362). While the details of the model are described in Sills, Karakas, and Lattanzio (2009), we list shortly here the main ingredients: (1) BSSs are formed by direct collisions between two unrelated main-sequence stars: a set of 16 cases are investigated and involving the collisions of 0.4, 0.6 and 0.8 $M_{\odot}$ stars. (2) Evolutionary tracks have been calculated by using the Yale Rotational Evolutionary Code (YREC, Guenther et al. 1992). (3) Collisional products are generated by using the code *"Make Me A Star"* (MMAS, Lombardi et al. 2002) that uses the YREC results to calculate (via the so-called *"sort by entropy"* method) the structure and chemical profile of the collision products. (4) Collisions are assumed to occur with a periastron separation of 0.5 times the sum of the radii of the two stars. (5) Any rotation of the collision product is neglected. (6) Finally, the recipe outlined in Sills et al. (1997) has been adopted to evolve the collision products from the end of the collision to the main sequence: in particular the evolution is stopped when the energy generation due to hydrogen burning was larger than that due to gravitational contraction, which corresponds to the zero age main sequence for a normal pre-main-sequence evolutionary track.

We have colored the tracks and isochrones in the U_{220} and B_{435} photometric bands by convolving a grid of suitable Kurucz (1993) stellar spectra of appropriate metallicity ([Fe/H]~ -2.4 Harris 1996) with the transmission curves of the used ACS/HRC filters. Thus, for each given stellar temperature and gravity, both the color and the bolometric corrections in the `VEGAMAG` system have been computed.

A 2 Gyr-old collisional isochrone thus obtained is shown in Figure 5.6 (grey thick line): a distance modulus $(m-M)_0 = 15.14$ and a color excess $E(B-V) = 0.08$ (Harris, 1996) have been adopted. As can be seen, the 2 Gyr isochrone well reproduces the brightest portion of the blue sequence (with $U_{220} < 19.2$). To better illustrate the expected post-MS evolutionary path of collisional BSS we also plotted the track (dashed line) of a $0.6 + 0.6 M_{\odot}$ collisional product whose TO point occurs at 2 Gyr. As sanity check we also plotted a canonical single star 12 Gyr-old isochrone of appropriate metallicity (black long-dashed line). As can be seen, it nicely reproduces the single star MS-TO of the cluster, thus demonstrating that the transformation and the adopted choice of distance modulus and reddening are appropriate. The impressive agreement of the 2 Gyr collisional isochrone with the brightest portion of the blue sequence strongly supports the hypothesis that these BSSs have been simultaneously formed by an event that, about 2 Gyr ago, led to a significant increase of the stellar interaction rate. On the other hand, the red-BSS sequence cannot be reproduced by any of the available collisional models, regardless of the age. All the features revealed by our analysis so far nicely resemble what was found in the study of the

BSS populations in M30 and NGC 362. Still, the BSSs in M15 show an additional intriguing feature.

5.3.4 An additional intriguing feature

As can be seen from Figure 5.6, a clump of 7 stars (approximately at $U_{220} = 19$) together with a few sparse stars at lower luminosity, can be distinguished in the region of the CMD between the blue and red BSS sequences. As explained in Section 5.2, we manually checked the accuracy of the PSF fitting solution for each of these stars. Moreover, the visual inspection of their location on the ACS/HRC images indicates that they are not contaminated by bright neighbors. We also carefully analyzed the shape of the brightness profile of each star and the corresponding parameters characterizing their PSF: indeed this analysis fully confirms that they are not blends, but well-measured single stars.

Although we are dealing with a small number of stars (and the statistical significance is therefore unavoidably low), such a clump of BSSs between the two sequences has never been observed before, neither in M30 nor in NGC 362, where the overall population numbers are similar, but this region of the CMD is essentially empty. Hence, the question raises: "what is the origin of these objects?". Following the scenario suggested by Ferraro et al. (2009), stars within the gap should be evolved (post-MS) BSSs that, because of the natural stellar evolution aging process, are leaving the MS stage. However, for being as clumped as observed, these stars should be all evolving at the same rate and have been caught in the same evolutionary stage. This seems to be quite implausible, especially because the post-MS evolutionary time-scale is rapid. Instead the comparison with a 5.5 Gyr-old collisional isochrone (black thick line in Figure 5.6) shows an impressive match: the CMD location of the clump is nicely reproduced by the TO point of this model. Such a nice correspondence suggests that the observed clump is made of collisional BSSs with an age of 5.5 Gyr that are currently reaching the main sequence TO evolutionary stage. By definition, the TO is the phase during which a star is leaving the MS and moves to the SGB stage, keeping roughly the same brightness (i.e. magnitude) while becoming colder (redder). Hence it is not surprising to have an over-density at this position in the CMD. In the same plot we also show the corresponding collisional track to illustrate the post-MS evolution of the collisional BSS currently located at the MS-TO point (in this case the BSS is originated by the collision of two stars of $0.4M_{\odot}$ and $0.6M_{\odot}$, respectively; black dashed line).

5.3.5 BSS radial distribution

We plot in Figure 5.8 the cumulative radial distribution of the BSSs belonging to the blue and the red sequences (blue/solid and red/dashed lines, respectively). As explained in Section 5.3, we used a photometric catalog obtained with the WFC3 to extend the BSS radial distribution out to a radius $r = 80''$. As expected the BSSs are significantly more segregated than normal MS stars (black dotted line), regardless of which population they belong to. As also found in the GCs M30 and NGC 362, the red sequence appears to be more segregated than the blue one. As discussed in Dalessandro et al. (2013a), this difference may offer further support for a difference formation history of the two populations. In short the blue-BSSs, born as a consequence of increase of collisions during the core-collapse, have been also kicked outward during collisional interactions while most of the red BSSs sank into

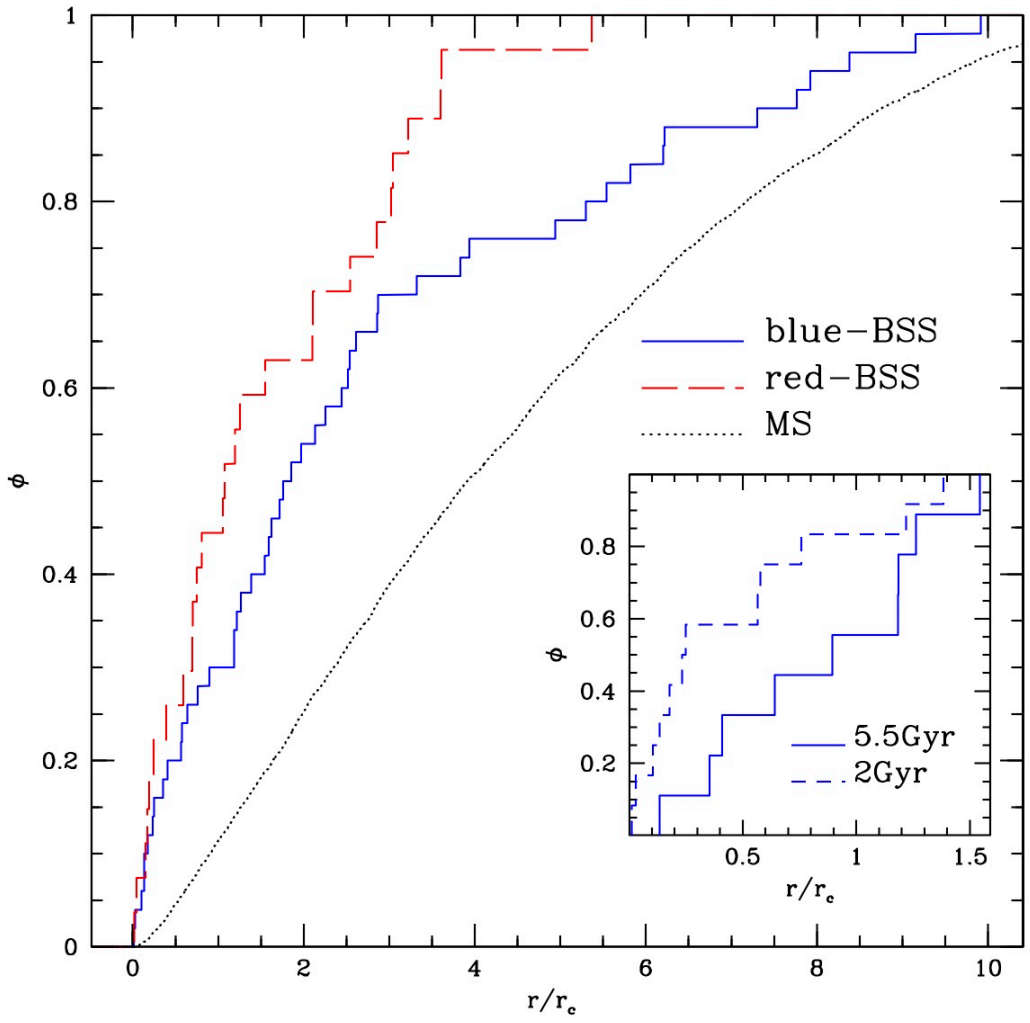

FIGURE 5.8: Cumulative radial distributions of the BSSs belonging to the blue and the red populations (blue/solid and red/dashed lines, respectively) as a function of the core radius $r_c = 0.14'$ Harris 1996). The cumulative radial distribution of MS stars is also shown for comparison (black dotted line). The inset shows the cumulative radial distributions of the BSSs observed along the two branches of the blue sequence: those with CMD position well reproduced by a 2 Gyr collisional isochrone (dashed line), and those corresponding to the 5.5 Gyr collisional isochrone (solid line).

the cluster center because of dynamical friction and did not suffer significant hardening during the core-collapse phase. The Kolmogorov-Smirnov test applied to the cumulative radial distributions suggests that the blue and the red sequences do not belong to the same parent population at only 1.5 σ level of significance. We stress here that this is likely due to the small number statistics of the two populations. The inset in the Figure shows the cumulative radial distributions of the BSS along the two branches of the blue sequence. The BSSs populating the youngest collisional sequence (dashed line) appear more centrally segregated than the oldest ones (solid line). Although the two sub-populations include only a few stars each, the statistical significance of such a difference turns out to be of the order of 1.5-2 σ.

5.4 Discussion

As previously discussed, the presence of a double sequence of BSSs is a feature that was already discovered using optical photometry in the core of the GCs M30, NGC 362 and NGC 1261.

Ferraro et al. (2009) first suggested that the presence of two parallel sequences of BSSs in the CMD can be explained by the coexistence of BSSs formed through two different formation mechanisms: the blue sequence would be originated mainly by collisions, while the red sequence derives from a continuous MT formation process (see also Dalessandro et al. 2013a and Xin et al. 2015). This scenario has been recently confirmed by a set of simulations that follow the evolution of a sample of BSSs generated by stellar collisions (Portegies Zwart, 2019). This work concludes the blue BSS chain detected in M30 can be indeed populated by collisional BSSs originated (over a short timescale) during the CC phase, thus finally proving that CC can be at the origin of a narrow sequence of nearly coeval Blue BSSs. Conversely, the photometric properties of BSSs generated by MT processes in binary systems are currently controversial, since different models seem to predict different MT-BSS distributions in the CMD (see the case of the models computed for M30 by Xin et al. 2015 and Jiang et al. 2017). In addition, even admitting that MT-BSSs may extend to the blue side of the BSS distribution in the CMD, it is unclear if and how MT processes alone could produce two split sequences, distinctly separated by gap. Since at the moment there are no consolidated and specific models of BSS formation through MT for M15, here we focus on the blue sequence that, in this cluster, shows the most intriguing features. The nice match between the blue-BSS locus in the CMD and the collisional isochrones of Sills, Karakas, and Lattanzio (2009) strongly suggests that this population could be produced during a dynamical phase characterized by a high rate of stellar collisions. Moreover, in striking similarity with previous cases, the fact that the blue BSSs in the CMD appear so nicely aligned along the collisional isochrone MS suggest that they were mostly generated over a relatively short timescale (within a few 10^8 yr), thus representing an essentially coeval population. The superb photometric quality of the data presented here allows us to make a significant step forward in our understanding of this phenomenon. It is particularly interesting that in M15 we are able to distinguish possible sub-structures along the collisional sequence. The two branches discovered here, in fact, can be interpreted as two generations of collisional BSSs, possibly formed during two distinct episodes of intense dynamical interactions. Since M15 is a core-collapsed cluster (see, e.g., Djorgovski and King 1986; Chernoff and Djorgovski 1989; Murphy, Cohn, and Lugger 2011), such episodes can quite possibly be associated to the cluster's structural properties at the time of core collapse and during the dynamical stages following this event. In particular, after reaching a phase of deep core collapse, clusters may undergo a series of core oscillations driven by gravothermal effects and binary activity (see, e.g., Bettwieser and Sugimoto 1984; Cohn, Hut, and Wise 1989; Heggie and Ramamani 1989; Takahashi and Inagaki 1991; Makino 1996; McMillan and Engle 1996; Heggie and Giersz 2009; Breen and Heggie 2012), characterized by several distinct phases of high central density followed by more extended stages during which a cluster rebounds toward a structure with lower density and a more extended core. Interestingly, Grabhorn et al. (1992) performed detailed numerical simulations, including post-collapse core oscillations, able to reproduce the contemporary presence of a large core radius (13 pc) and a cusp in the stellar density profile of M15 as revealed by early *HST* observations from Lauer et al. (1991).

The two branches of blue-BSS sequence might be the outcome of the increased

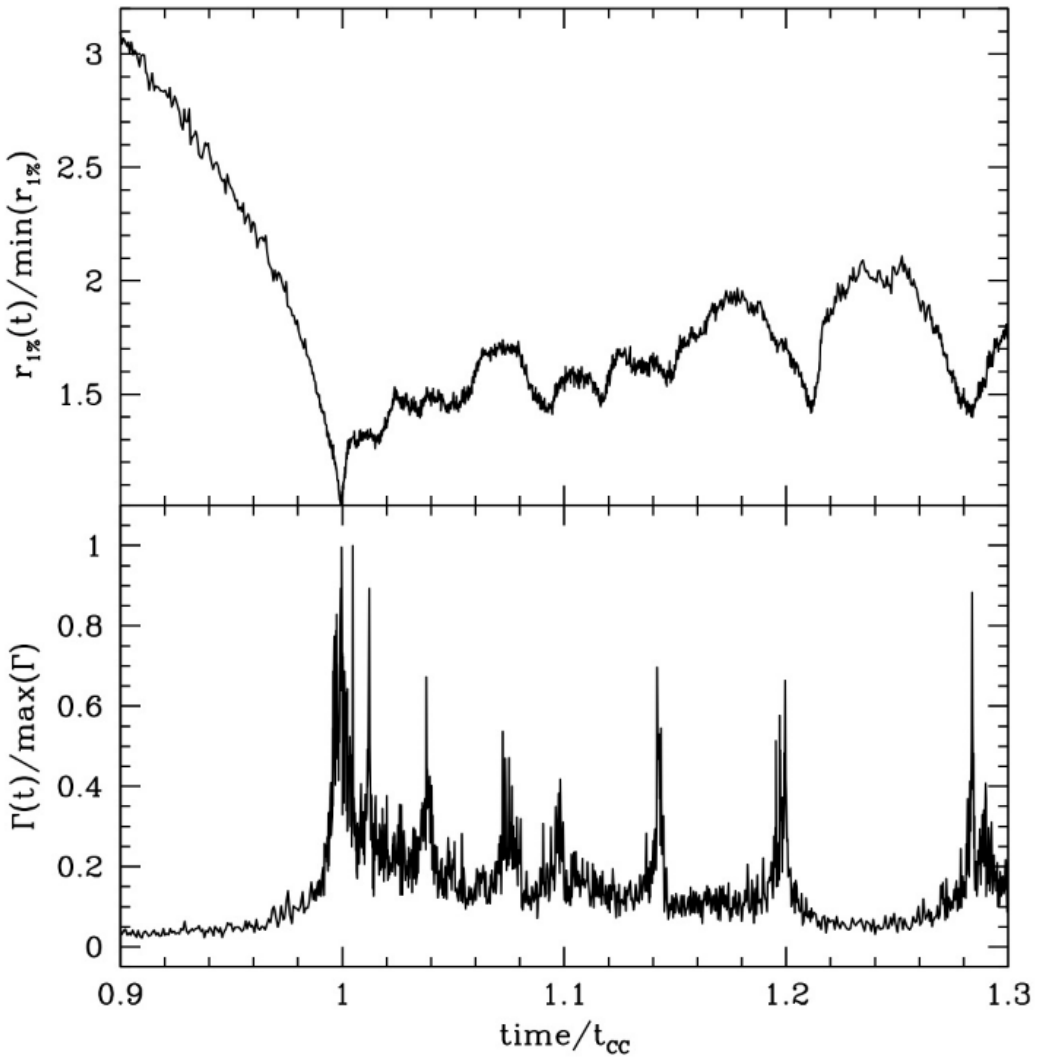

FIGURE 5.9: Time evolution of the 1% Lagrangian radius ($r_{1\%}$, top panel) and of the collisional parameter (Γ, bottom panel) as measured in a a Monte Carlo simulation of GC evolution (see text). Time is normalized to the core collapse time (t_{CC}), while $r_{1\%}$ and Γ are normalized, respectively, to their minimum and maximum values (note that for the simulation shown here $t_{CC} \backsimeq 11.9$ Gyr and the time interval shown in the plots corresponds to about 4.8 Gyr).

rate of collisions during two separate density peaks in the post-core collapse evolution. In order to provide a general illustration of the possible history of the cluster's structural evolution leading to the observed blue-BSS branches, we show in Figure 5.9 the time evolution of the 1% Lagrangian radius (top panel) and of the collisional parameter (bottom panel) as obtained from a Monte Carlo simulation run with the MOCCA code (Giersz, Heggie, and Hurley, 2008). The collisional parameter $\Gamma = \rho_c^2 r_c^3/\sigma_c$ (where ρ_c, r_c, and σ_c are, respectively, the cluster's central density, core radius and central velocity dispersion) is often used to provide a general quantitative measure of the rate of stellar collisions in a GC (see, e.g., Davies, Piotto, and de Angeli 2004). The simulation presented here starts from the initial structural properties discussed in Hong et al. (2017), with 7×10^5 stars, no primordial binaries and an initial half-mass radius equal to 2 pc. We point out that the adopted simulation and initial conditions do not consist in a detailed model of M15, but just illustrate the

general evolution of a cluster reaching a phase of deep core collapse and undergoing core oscillations in the post-core collapse phase.

As shown in Figure 5.9, the initial deep core collapse (clearly distinguishable at $t/t_{CC} = 1$) leads to the largest increase in the value of Γ, and is followed by several distinct re-collapse episodes leading to secondary peaks of different magnitudes in the collisional parameter (all smaller than the initial peak associated to the first collapse). The time interval between the various peaks in Γ is not constant and, for the simulation presented here, typically ranges from approximately a few hundreds million years to approximately a billion years. Although we strongly emphasize that models exploring in detail the actual BSS production in each collapse episode, along with a proper characterization of the collision events and the number of stars involved, are necessary (see e.g. Banerjee, 2016), here we suggest that the BSS populations observed along the two branches of the blue-BSS sequence in M15 might be produced during the initial deep collapse and during one of the subsequent collapse events, one sufficiently deep to trigger a significant number of collisions and BSS production.

Note that a similar argument was used by Simunovic, Puzia, and Sills (2014) to explain the presence of a few bright BSSs located on the blue side of the blue-BSS sequence in NGC 1261. However, this cluster does not show the typical signature of core collapse, and for this reason the authors suggest that it is currently experiencing a bounce state.

5.4.1 Conclusions

We used an exceptional set of high-resolution ACS/HRC images to explore the stellar population in the collapsed core of the GC M15. A high-precision UV-CMD has revealed the existence of two clear-cut sequences of BSSs. In particular, we discovered that the blue sequence, which should be populated by collisional BSSs in the interpretative scenario proposed by Ferraro et al. (2009), consists of two distinct branches nicely reproduced by collisional isochrones of 2 and 5.5 Gyr. We interpret these features as the observational signature of two major collisional episodes suffered by M15, likely connected to the collapse of its core: the first one (possibly tracing the beginning of the core-collapse process) occurred approximately 5.5 Gyr ago, while the most recent one dates back 2 Gyr ago. This result reinforces the evidence of the strong link existing between the observational properties of the BSS population in a cluster and its dynamical history (Ferraro et al., 2009, 2012, 2018b), and it opens a window to gather a deeper understanding of core collapse and post-core collapse evolution, as well as the link between these dynamical phases and a cluster's stellar content.

Chapter 6

Dynamics and Kinematics of NGC 1261

Mainly based on:
Raso et al. (2020), submitted to ApJ

6.1 Introduction

We have already discussed in this Thesis the importance of BSSs as tracers of the dynamical evolution of GCs. In some cases, this information is also complemented by some information on the internal cluster kinematics provided by the measurements of line-of-sight velocities or PMs.

For what regards PMs, recently the *Gaia* mission represented a great improvement in our knowledge of stellar kinematics, also for GCs (see, e.g., Baumgardt et al. 2019). However, in the most central regions of GCs, the quality of *Gaia* data is hampered by crowding. Also, *Gaia* is limited to a G-band magnitude of ~ 21, therefore in GCs it provides information only for brightest stars. If we want to focus on the kinematics of the innermost region of GCs and of stellar populations that are fainter than the TO, the most effective instrument is still the *HST*, given its long life and relative stability. Indeed, various recent studies used *HST* PMs to investigate different aspects of GC internal kinematics and dynamics (see papers from the HSTPROMO Collaboration[1], as Bellini et al. 2014; Watkins et al. 2015a,b; Baldwin et al. 2016; Libralato et al. 2018a; or also Richer et al. 2013; Bellini et al. 2015, 2018; Libralato et al. 2019).

Therefore, we are able to obtain complementary information on cluster internal dynamics from both PMs and BSSs. This Chapter is devoted to compute the structural, kinematical and dynamical properties of the Galactic GC NGC 1261. This is an intermediate-metallicity GC, with very low extinction ([Fe/H]=-1.27 and E($B-V$)=0.01, Harris 1996, 2010 edition). It is a halo GC, with a distance modulus $(m-M)_0 = 15.98$ (Ferraro et al. 1999b), corresponding to a distance from the Sun of 15.7 kpc. It is located farther from the Sun with respect to GCs studied in most of the previous works dealing with internal kinematics from *HST* PMs, which all have distances in the range $5-10$ kpc (Bellini et al. 2014, 2015, 2018; Libralato et al. 2018a, 2019). However, its extremely low extinction and its expected low contamination from field stars (due to its low Galactic latitude, B=$-52.12°$, and its relatively large distance from the Galactic center, D=18.1 kpc, Harris 1996), make it a suitable candidate for PM studies and to test the validity of PM measurements in a less favourable (more distant) case. Simunovic, Puzia, and Sills (2014) proposed the presence of an interesting BSS population, with two separate sequences in the CMD. In addition,

[1] http://www.stsci.edu/~marel/hstpromo.html

TABLE 6.1: List of *HST* images of NGC 1261 used in this work.

Program ID	PI	Epoch (yyyy/mm)	Camera	Filter	Exposures N × t_{exp}
10775	A. Sarajedini	2006/03	ACS/WFC	F606W	1 × 40 s
					6 × 350 s
				F814W	1 × 40 s
					6 × 360 s
13297	G. Piotto	2013/08 - 2014/06	WFC3/UVIS	F275W	2 × 834 s
					4 × 855 s
					2 × 859 s
					2 × 918 s
				F336W	2 × 413 s
					2 × 415 s
					1 × 419 s
				F438W	1 × 164 s
					1 × 165 s
					1 × 167 s
					1 × 168 s
					1 × 170 s
14235	T. Sohn	2017/03	ACS/WFC	F606W	1 × 45 s
					7 × 607 s
					1 × 608 s

NGC 1261 is suspected to have an extra-tidal structure, in the form of an outer envelope (Kuzma, Da Costa, and Mackey 2018; Shipp et al. 2018), and to be associated to the *Gaia*-Enceladus structure (Massari, Koppelman, and Helmi 2019).

6.2 Dataset and Data Reduction

We considered all the images from the UVIS/WFC3 and from the WFC/ACS currently available in the *HST* archive, covering the central regions of the cluster. The details of the observations are listed in Table 6.1.

We performed a photometric reduction of the `_flc` images, following the prescriptions given in Bellini et al. (2017b, 2018). We used `_flc` images because the unresampled pixel data for stellar profile fitting is preserved. These images have also been corrected to remove CTE defects, as described in Anderson and Bedin (2010). In the following, we briefly describe the reduction procedure, which consists of two main steps.

First, we performed a one-pass photometry, a single finding procedure without neighbour subtraction, to identify and measure all bright stars. We made use of spatially-variable PSF models tailored to each image starting from the publicly available library PSFs of the *HST* detectors[2] (e.g., Anderson and King 2006) by using a set of bright, relatively isolated and unsaturated stars in each exposure. These PSFs were used to measure stellar positions and fluxes in each exposure. Stellar positions were corrected for geometric distortion using the solutions provided in Anderson and King (2006), Bellini and Bedin (2009), Bellini, Anderson, and Bedin (2011).

Next, we run a multi-pass photometry using the software `KS2` (see Bellini et al. 2017b for details), which simultaneously performs the finding procedures on all the images and it is able to perform neighbor subtraction. This second step is necessary due to the high level of crowding in the central regions of GCs. `KS2` is able to

[2]Available at `http://www.stsci.edu/~jayander/STDPSFs/`

simultaneously analyze multiple images taken with different filters, combining the results of the one-pass photometry transformed into a common reference frame. As an astrometric reference system, we used the stellar positions in the *Gaia* Data Release 2 (DR2) catalog (Gaia Collaboration et al. 2016, 2018a). We defined a common, pixel-based reference system, based on these Right Ascension (R.A.) and Declination (Dec.) positions, with X and Y increasing toward West and North, respectively, and with a pixel scale of 40 mas pixel^{-1}. We transformed the stellar positions as measured in each exposure onto this common reference frame system by means of six-parameter linear transformations. `KS2` performs the finding procedure through multiple iterations. For each iteration, it finds and subtracts stars that are present in a combination of filters chosen by the user, and then iteratively repeats this procedure for fainter stars that were not subtracted in the previous iteration, together with an improved fit and subtraction of already found stars. In this work, we applied an approach similar to that used in Nardiello et al. (2018): we performed the first four finding iterations on the F606W and F814W exposures, while the fifth, sixth and seventh iterations were performed on the F438W, F336W and F275W images, respectively, to enhance the detection of blue stars that are too faint to be detected in the F606W and F814W exposures. The instrumental magnitudes of each exposure were rescaled to that of the longest available exposure acquired with the same filter.

We calibrated our magnitudes to the `VEGAMAG` photometric system using the stars in common with the public catalog of NGC 1261 from the *HST* UV Globular cluster Survey[3] (Piotto et al. 2015, Nardiello et al. 2018).

We measured PMs using the technique developed by Bellini et al. (2014) and improved in Bellini et al. (2018) and Libralato et al. (2018a). We refer to those papers for a complete description of this procedure, which we briefly summarize in the following. This iterative procedure uses the stellar positions in each single exposure obtained from the multi-pass photometry. We transformed the `KS2`-based positions of each star in each image onto a common reference frame system. We fit these transformed positions as a function of the epoch with a least-square straight line. The slope of the straight line is a direct estimate of the PMs. The transformations to obtain master-frame positions are based on cluster member stars, therefore the PMs thus obtained are *relative* to the cluster bulk motion. For this procedure we used all the catalogs available in our dataset (see Table 6.1), except for those in the F275W filter, which suffer from color-dependent systematic effects (Bellini, Anderson, and Bedin 2011), and therefore are not suitable to measure PMs.

In Figure 6.1, we show an overview of the NGC 1261 catalog obtained in this work. Black/red dots correspond to stars with/without a PM measurement. In the left and central panels we show the optical and UV-blue CMDs of NGC 1261. In the upper right panel we show the FOV covered by our dataset, showing also the core and the half-mass radii (r_c and r_h), obtained in Section 6.3, as white circles. In the lower right panel we show the number of objects (in a log scale) in our PM catalog, as a function of the temporal baseline of the observations used to determine their PMs.

6.3 Structural parameters

In order to derive the structural parameters of NGC 1261, we determined the center of gravity (C_{grav}) and the star density profile.

[3] Available at `http://groups.dfa.unipd.it/ESPG/treasury.php`.

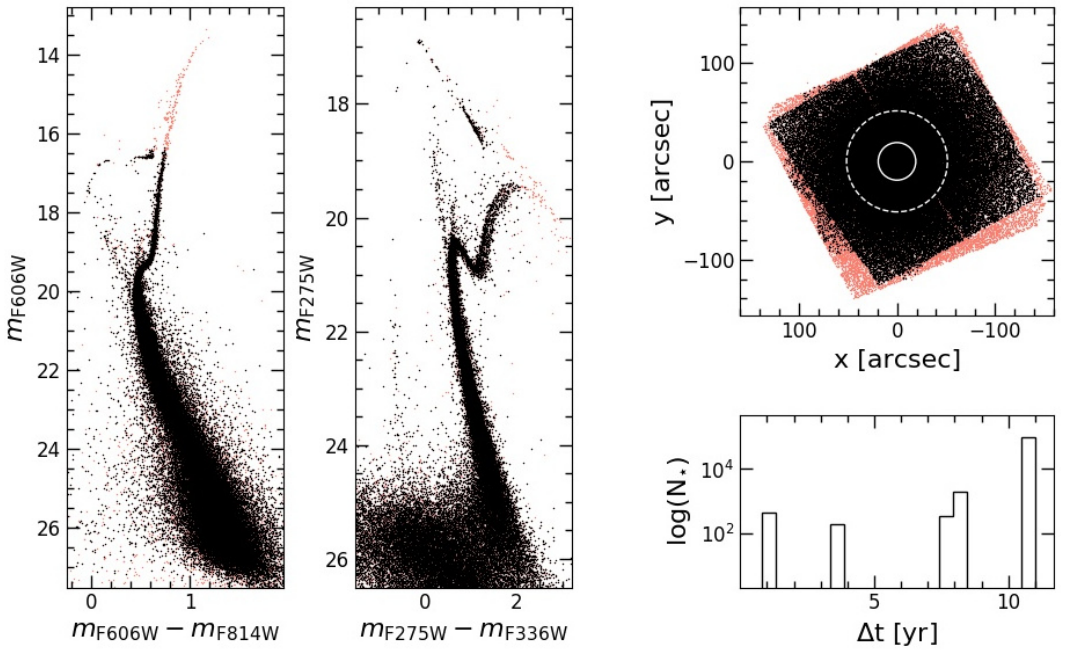

FIGURE 6.1: Overview of the NGC 1261 catalog obtained in this work. In all panels, the red dots refer to the complete photometric catalog, while black dots are stars for which we also have a PM measurement. In the left and central panels we show the optical (m_{F606W} vs. $m_{F606W} - m_{F814W}$) and UV-blue (m_{F275W} vs. $m_{F275W} - m_{F336W}$) CMDs of NGC 1261. In these plots, we show all stars, regardless of their astro-photometric quality. The scattered cloud of points in the bottom left region of the UV-blue CMD is composed of stars that are measured in the F606W and/or F814W bands, but are too faint to be detected in the UV-blue bands. In spite of this, the software forces a fit, which results in an unreliable magnitude estimate that makes the star appear in this region of the CMD. In the upper right panel we show the FOV covered by our dataset, with the center of the cluster (obtained as in Section 6.3) placed in (0,0) and the projected positions of each star with respect to the center plotted along the x- and y-axes. North is up and East is to the left. In this panel we also show r_c and r_h as solid and dashed white circles, respectively, as obtained in Section 6.3. In the lower right panel we show the number of objects (in a logarithmic scale) in our PM catalog, as a function of the temporal baseline of the observations used to measure them.

For the determination of C_{grav}, we followed the iterative procedure described in Montegriffo et al. (1995), and later used in Lanzoni et al. (2010, 2019), Miocchi et al. (2013), and Raso et al. (2017). We measured C_{grav} as the average of the projected x and y positions of stars brighter than a given magnitude and within a given distance from the (first-guess) center. We chose an appropriate limiting magnitude around the TO level, to avoid incompleteness effects while maintaining a sufficient statistics. We assumed as a first-guess center the value of Goldsbury et al. (2010), and iteratively recomputed the center, using each time the center obtained in the previous iteration, until the difference between two consecutive iterations was negligible. The resulting C_{grav} is located at R.A.$= 03^h\ 12^m\ 16.13^s$; Dec. $= -55^\circ\ 12'\ 58.42''$, with uncertainties equal to: $rms_{R.A.} = 0.4''$ and $rms_{Dec.} = 0.2''$. The distance between the Goldsbury et al. (2010) center and the value of C_{grav} estimated in this work is equal to $\sim 0.7''$.

The available *HST* data sample a region of $\sim 200'' \times 200''$ roughly centered on the cluster center. This region is smaller than the tidal radius of NGC 1261 derived from the Harris catalog ($r_t = 304''$, Harris 1996). Therefore, in order to obtain a complete star density profile along the entire extension of the cluster, we combined the

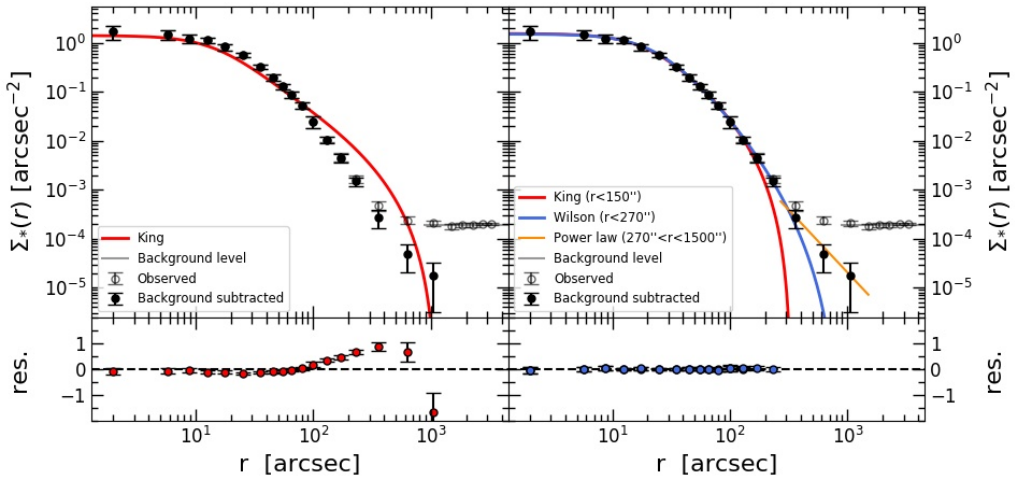

FIGURE 6.2: Top panels: observed (open circles) density profile of NGC 1261. The leftmost 12 points have been obtained from the *HST* data, while the remaining points have been obtained from *Gaia* DR2 data. The assumed level of background, obtained as the average of the five rightmost points, is marked with a solid grey line. The background subtracted profile (filled circles), is obtained as the difference between the observed profile and the background level. In both top panels, the red line is the best fit King model obtained in this work using an MCMC approach (see text for details). In the top left panel, the King model fit has been performed along the entire extension of the background subtracted profile, while in the top right panel we only considered for the fit the points within $r = 150''$. In the top right panel we also show the best fit Wilson profile (blue line), obtained considering only the points within $r = 270''$. The yellow line is a power-law with slope -2.6, which approximately represents the behaviour of the outermost three points, where the profile cannot be fitted with neither the King nor the Wilson models, due to the presence of an outer envelope. Bottom panels: residuals of the best-fit models, in a log scale (i.e., res = $\log \Sigma_{*,\mathrm{mod}} - \log \Sigma_{*,\mathrm{obs}}$). The residuals for the King model fit are shown as red circles, while the residuals for the Wilson model fit are shown in blue.

HST data with *Gaia* DR2 data. We constructed the star density profile as in Miocchi et al. (2013), see also Lanzoni et al. (2010, 2019). We divided the sample into 23 concentric annuli[4], centered on C_{grav}, considering only stars brighter than $m_{\mathrm{F606W}} = 19.5$ (equivalent to $m_{\mathrm{G}} \sim 19.5$ for *Gaia*), to avoid incompleteness effects and to properly combine the density profile obtained from *HST* data with that determined from the *Gaia* observations. Each annulus was divided into four sectors, and the density in each sector was measured as the ratio between the number of stars within the sector and the area of the sector itself. The final density for each annulus corresponds to the mean of the four sector densities, and the density uncertainty is estimated from the variance among the sectors. The final, combined density profile is shown in the upper panels of Figure 6.2. The open circles represent the observed density profile, while the black circles represent the profile after background subtraction (measured as the average of the five rightmost points of the observed profile).

The density profile presented in Figure 6.2 has been obtained using only stars brighter than the TO, i.e., stars with approximately the same mass. For this reason, the cluster structural parameters have been derived by fitting the density profile

[4]12 annuli for the *HST* data, 13 for the *Gaia* DR2 data, with 2 annuli in common between the two datasets. We used this region ($70'' < r < 110''$), where the *Gaia* DR2 data do not suffer yet from incompleteness at the considered magnitude level, to normalize the *Gaia* DR2 and *HST* profiles.

TABLE 6.2: Structural parameters obtained by fitting the observed number density profile with King (column 2) and Wilson (column 3) models, within a cluster centric distance $r = 150''$ and $r = 270''$, respectively.

Parameter	King model	Wilson model
c	$1.19^{+0.07}_{-0.06}$	$1.58^{+0.09}_{-0.07}$
r_c	$(19.2^{+1.5}_{-1.4})''$	$(20.1 \pm 1.3)''$
r_h	$(51.5^{+2.2}_{-2.0})''$	$(51.8^{+1.9}_{-1.8})''$
r_t	$(331.8^{+33.3}_{-27.4})''$	$(890.3^{+131.4}_{-103.7})''$

with single-mass, spherical and isotropic King models (King 1966). We performed the fit using a MCMC approach, using the `emcee` algorithm (Foreman-Mackey et al. 2013). We assumed uniform priors on the parameters of the fit, therefore the posterior PDFs are proportional to the likelihood $\mathcal{L} = \exp(-\chi^2/2)$.

The result of this fit is shown in the left panel of Figure 6.2. While the agreement is satisfactory for $r < 100''$, the outer regions display significant deviations from the model. The disagreement between observations and best-fit model seems to be less severe in Figure E1 of Baumgardt and Hilker (2018). However, this is because their density profile extends to just $\sim 400''$ from the center, while the deviation from the King model distribution increases at large radii. This is consistent with the findings by Kuzma, Da Costa, and Mackey (2018), who detected the possible presence of an extended halo in the outer regions of this cluster.

In order to further explore this topic, we limited the fit of the King models to the innermost region ($r < 150''$) and considered also Wilson models (Wilson 1975; see the right panels of Figure 6.2), which are more radially extended with respect to the King ones. As expected, Wilson models are able to reproduce the observed profile over a more extended radial portion (out to $270''$) with respect to the King family. However, an excess of stars is still observed at $r > 270''$, suggesting the existence of an extended halo, in agreement with what found by Kuzma, Da Costa, and Mackey (2018). In Table 6.2 we list the best fit structural parameters (corresponding to the median of the PDF) and the uncertainties (68% confidence interval) for the King and Wilson models. It is interesting to note that both the core radius and the half-mass radius agree between the two models at better than one arcsecond.

6.4 Internal kinematics

6.4.1 Proper motion selections

We selected stars for the kinematic analysis according to the following criteria: (i) at a given magnitude, they have a `QFIT` parameter (quality of the PSF fit, ranging from 0 to 1; larger values of `QFIT` indicates better quality of the PSF fit) larger than the 95-th percentile; (ii) their o parameter (fraction of neighbour flux within the fitting radius before neighbour subtraction in the multi-pass photometry) is lower than 1; (iii) they were measured in at least 80% of the images; (iv) at any given magnitude, the absolute value of their `RADXS` parameter (residual fractional source flux outside the fitting radius with respect to PSF predictions) is within 3σ from its median value; (v) their reduced χ^2, obtained from the PM fit, is lower than 3; (vi) the fraction of measurements rejected in the PM fit procedure is less than 15%; (vii) they are within $90''$ from the cluster center (i.e. we excluded the edges of the FOV of the PM catalog, which

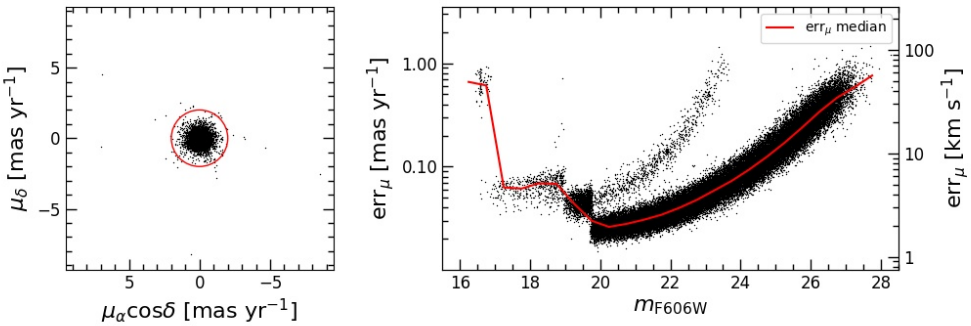

FIGURE 6.3: Left panel: VPD of the stars satisfying criteria (i) to (vii), see text for details. The red circle corresponds to 2 mas yr^{-1}, marking the threshold adopted to reject non cluster members (note, however, the very low level of field contamination). Right panel: 1D PM error as a function of the F606W magnitude for the stars satisfying criteria (i) to (vii). The multiple sequences and discontinuities are due to the different temporal baselines and number of images used to compute the PMs in our project. The red line is the median value of err$_\mu$, measured in magnitude bins 0.5 mag wide.

is slightly smaller than the total FOV - see Figure 6.1); (viii) their PM error is smaller than 50% the local (both in distance and in magnitude) intrinsic PM dispersion.

The VPD (see the left panel of Figure 6.3) shows no prominent sign of field contamination, as expected from the Galactic latitude of this halo cluster (B=−52.12°, Harris 1996). However, we applied a mild cut to exclude likely field stars, rejecting stars with a relative PM larger than 2 mas yr^{-1} (i.e., more than 10 times the observed PM dispersion of the faintest stars detected; see the red circle in the left panel of Figure 6.3).

In the right panel of Figure 6.3 we show the 1D PM error as a function of m_{F606W} for the stars satisfying criteria (i) to (vii). The red line corresponds to the median of the distribution, measured in bins 0.5 mag wide. The different temporal baselines and number of images used to compute the PMs in our project cause the multiple sequences of PM errors clearly visible in the right panel of Figure 6.3.

The observed velocity dispersion obtained from PMs is the combination of the true velocity dispersion of the cluster and the scatter due to PM errors, which must be subtracted in quadrature in order to obtain the true dispersion. Thanks to state-of-the-art reduction techniques, as the ones used in this work and in Bellini et al. (2014, 2015, 2018) and Libralato et al. (2018a, 2019), we are able to keep the PM errors as low as possible. However, for such a distant GC, stellar PMs are small compared to the PM uncertainty and in some cases we were unable to derive meaningful velocity dispersions, even after the subtraction of the PM uncertainty. Hence, for the kinematic analysis presented in Section 6.4.2, we restricted our sample to the magnitude range $19.75 < m_{F606W} < 20.75$. This condition has the double benefit of allowing us to study the kinematics of stars of comparable masses, while using the stars with PM errors as low as possible.

6.4.2 Velocity dispersion profiles

In this Section we present and discuss the velocity dispersion profiles of NGC 1261 over its entire radial extension, derived by combining the kinematical information in

the plane of the sky, obtained from PMs, for the cluster central regions with LOS velocities of individual stars, measured in the external regions from the MIKiS survey (Ferraro et al. 2018a).

The radial and tangential velocity dispersion profiles were measured maximizing the following likelihood in different radial bins:

$$\ln \mathcal{L} = -\frac{1}{2}\sum_n \Big[\frac{v_{\mathrm{rad},n}^2}{\sigma_{\mathrm{rad}}^2+\epsilon_{\mathrm{rad},n}^2} + \ln(\sigma_{\mathrm{rad}}^2+\epsilon_{\mathrm{rad},n}^2) + \frac{v_{\mathrm{tan},n}^2}{\sigma_{\mathrm{tan}}^2+\epsilon_{\mathrm{tan},n}^2} + \ln(\sigma_{\mathrm{tan}}^2+\epsilon_{\mathrm{tan},n}^2)\Big] \tag{6.1}$$

where $v_{\mathrm{rad},n}$ and $v_{\mathrm{tan},n}$ are the radial and tangential components of the velocity of each star in the considered bin, $\epsilon_{\mathrm{rad},n}$ and $\epsilon_{\mathrm{tan},n}$ are the observed errors on the radial and tangential velocity components, and σ_{rad} and σ_{tan} are the radial and tangential velocity dispersions, respectively. We used again a MCMC approach, based on the `emcee` algorithm (Foreman-Mackey et al. 2013), obtaining the posterior PDFs for σ_{rad} and σ_{tan}. The best-fit values correspond to the PDF median, while the resulting uncertainties correspond to the 68% confidence interval.

In order to allow a comparison between the velocity dispersion profiles presented here with previously published profiles, mainly obtained from radial velocities from spectroscopy (therefore measured for a sample of bright stars, with a mass comparable to the TO mass), we must only consider the kinematics of stars of similar mass, because of the effects of energy equipartition. The restriction of our sample to the stars in the m_{F606W} range between 19.75 and 20.75, discussed in the previous Section and made to select only stars with the lowest PM errors, serves also this purpose. We excluded stars brighter than m_{F606W}=19.75 because, as it can be seen in the right panel of Figure 6.3, at brighter magnitudes the PM errors increase significantly, due to the smaller number of images available for the PM computation (the longest exposures are saturated above this magnitude value). We chose m_{F606W}=20.75 as our faint limit to include in our sample only stars with masses comparable to the TO mass. The masses in this magnitude interval, estimated from a PARSEC isochrone (Marigo et al. 2017) with an age of 11.5 Gyr and [Fe/H]=−1.35 (green line in the left panel of Figure 6.4; age and metallicity are taken from Dotter et al. 2010), range from $\sim$0.75 $M_\odot$ to $\sim$0.8 $M_\odot$, while bright stars (e.g., RGB stars) in NGC 1261, according to the same isochrone, have masses up to $\sim$0.82 $M_\odot$. Therefore, even if velocity dispersion decreases when mass increases due to energy equipartition ($\sigma \propto m^{-\eta}$), in such a small mass range the velocity dispersion difference is expected to be negligible. Even in the extreme case of full energy equipartition (η=0.5), which is not expected to be reached (e.g., Bianchini et al. 2016; Trenti and van der Marel 2013), the difference in velocity dispersion for the considered mass range is at most a few tenths of km s^{-1}. We also used a mild color cut ($0.4 < m_{\mathrm{F606W}} - m_{\mathrm{F814W}} < 0.6$) to exclude the most obvious outliers. This mild color cut does not exclude binaries, which have a different kinematics with respect to single stars. However, the binary fraction of NGC 1261 is lower than 5% (Milone et al. 2012), therefore their contribution should be negligible.

Figure 6.4 summarizes our results on the kinematics of MS-TO stars in NGC 1261. In the left panel we show as grey points the CMD of stars in NGC 1261 that have a PM measurement and pass our quality selections (see Section 6.4.1). The MS-TO stars, selected for the kinematical analysis, are shown as black points. In the right

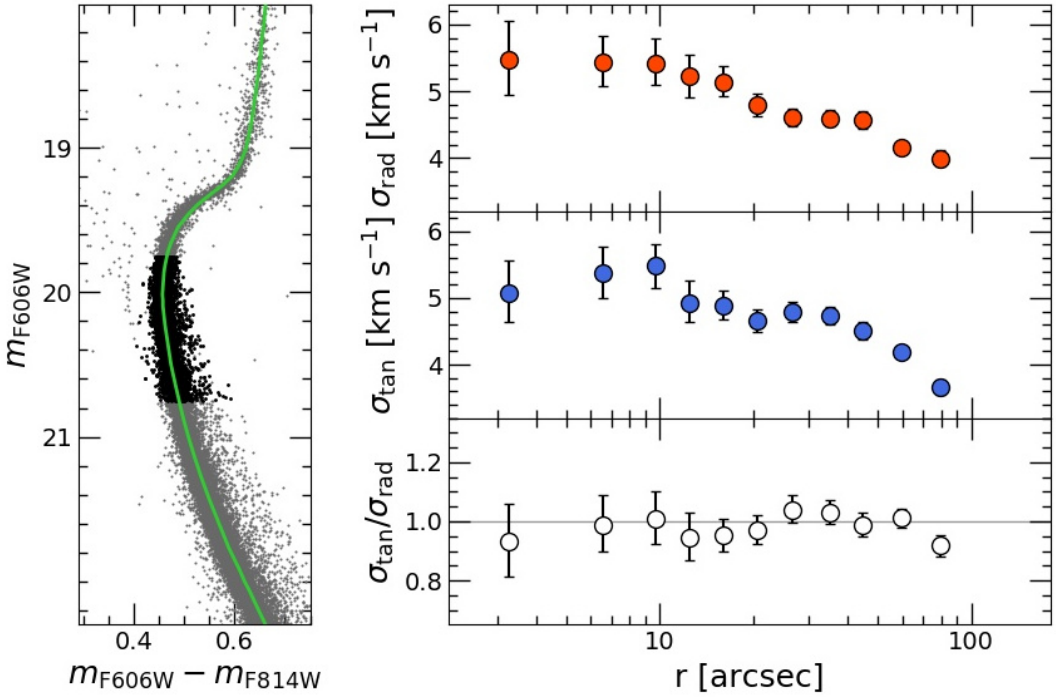

FIGURE 6.4: Left panel: CMD of NGC 1261 (m_{F606W} vs. $m_{F606W} - m_{F814W}$), using the quality-selected PM catalog (grey dots). The black points show the sub-sample of MS-TO stars selected to compute the velocity dispersion profiles. The green line is a PARSEC isochrone (Marigo et al. 2017), with an age of 11.5 Gyr and [Fe/H]=−1.35 (age and metallicity taken from Dotter et al. 2010). Right panels, from top to bottom: radial and tangential velocity dispersion profiles, and anisotropy profile (plotted respectively as red, blue and white circles).

panels of Figure 6.4 we show the velocity dispersion profiles[5] obtained in this work. From top to bottom, we show the radial velocity dispersion profile (σ_{rad}, red circles), the tangential velocity dispersion profile (σ_{tan}, blue circles), and the anisotropy profile ($\sigma_{tan}/\sigma_{rad}$, white circles).

The central region of NGC 1261 appears to be isotropic ($\sigma_{tan}/\sigma_{rad} \sim 1$); the only point in the anisotropy profile that deviates significantly from isotropy is the most external one, at a distance from the center of about 80″, where the cluster appears to be mildly radially anisotropic. Although this trend is consistent with both simulations and observations, which find that some GCs are isotropic in the central regions and radially anisotropic at larger radii (see e.g., Vesperini et al. 2014, Tiongco, Vesperini, and Varri 2016 for simulations and Bellini et al. 2014, 2017a; Watkins et al. 2015a for observational results), this concerns only one point at the edge of the FOV sampled by our observations, corresponding to $\sim 2\, r_h$ from the center. Hence, from now on we make the conservative assumption of an overall isotropy for NGC 1261.

Given the overall isotropy of the sampled region, we determined the global velocity dispersion profile in the plane of the sky (σ_μ), shown in Figure 6.5 (black circles). This has been obtained with the same procedure described above, but imposing $\sigma_\mu = \sigma_{rad} = \sigma_{tan}$ in the likelihood. We combined the global velocity dispersion profile in the plane of the sky with the LOS velocity dispersion profile from Ferraro et al. (2018a). As previously discussed, the two velocity dispersion profiles can be compared because they are obtained from stars that are roughly in the same mass

[5] PMs in mas yr^{-1} have been converted into km s^{-1}, through the equation $\sigma_{km\ s^{-1}} = 4.74\, D_{kpc}\, \sigma_{mas\ yr^{-1}}$ (e.g., van de Ven et al. 2006).

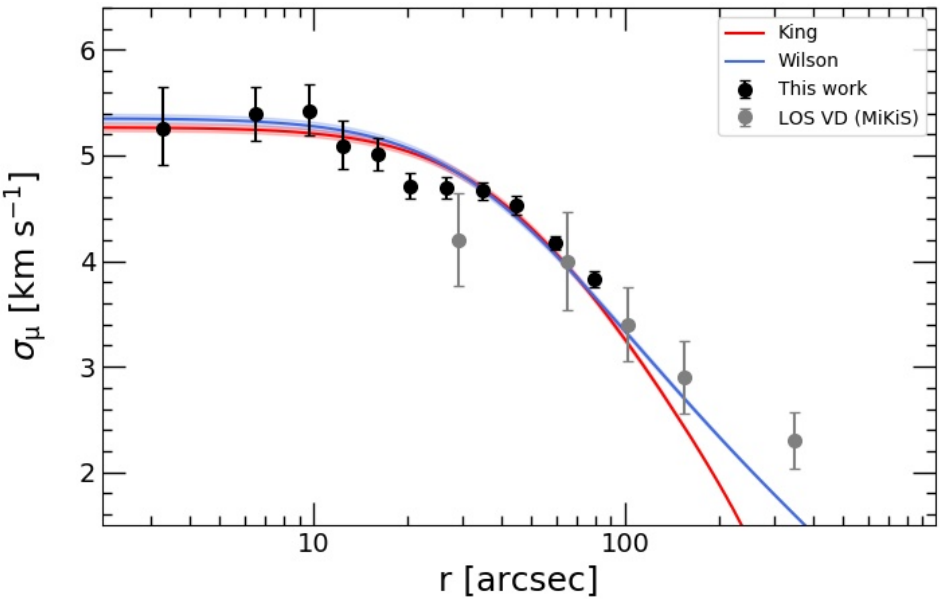

FIGURE 6.5: Global velocity dispersion profile of NGC 1261. The measurements in the plane of the sky, obtained from *HST* PMs are plotted as black circles, while the grey circles correspond to the LOS velocity dispersion profile from Ferraro et al. (2018a). The best-fit King and Wilson profiles are shown as red and blue lines, respectively. The shaded areas around the two best-fit profiles represent the uncertainty on the central velocity dispersion (see text for details on the fitting procedure).

range. As shown in the Figure, the two profiles nicely connect in the radial region in common, with no need for arbitrary vertical shifts.

We then fitted the combined (PMs+LOS) velocity profile with King and Wilson models. We used a MCMC fitting procedure equivalent to the one described previously. We kept the structural parameters obtained in Section 6.3 fixed and we adopted only the central velocity dispersion, σ_0, as a free parameter[6]. For consistency with the density profile fitting procedure (see Section 6.3), we excluded the regions beyond $r = 150''$ and $r = 270''$ for the King and Wilson models, respectively. The observed velocity dispersion profile is reasonably well reproduced by the adopted models (red and blue lines in Figure 6.5), with central dispersion values of $\sigma_{0,K} = 5.27 \pm 0.04$ km s^{-1} and $\sigma_{0,W} = 5.35 \pm 0.04$ km s^{-1}, respectively. These values are comparable to previous estimates based only on radial velocities (thus limited to more external regions of the cluster), e.g., Baumgardt and Hilker (2018) obtain σ_0=5.6 km s^{-1}; Ferraro et al. (2018a) obtain σ_0=5.5$\pm$0.4 km s^{-1}.

The central velocity dispersion measurements can be used to estimate the total mass of NGC 1261, by properly rescaling and integrating the best fit King and Wilson density profiles. We obtained $M = (1.14^{+0.14}_{-0.12}) \times 10^5 M_\odot$ from the King model and $M = (1.13^{+0.12}_{-0.10}) \times 10^5 M_\odot$ from the Wilson model. Although these values formally underestimate the total mass of the system (since they have been derived from the King/Wilson models), the contribution of the stars populating the halo surrounding the cluster is likely negligible. Indeed, the two estimates are very similar (in spite

[6]We want to point out that the fit can be performed also without fixing the structural parameters to the values obtained from the density profile fit. However, the determination of the structural parameters from the velocity dispersion profile is more uncertain than using the density profile, due to the smaller number of points and higher probability of systematics.

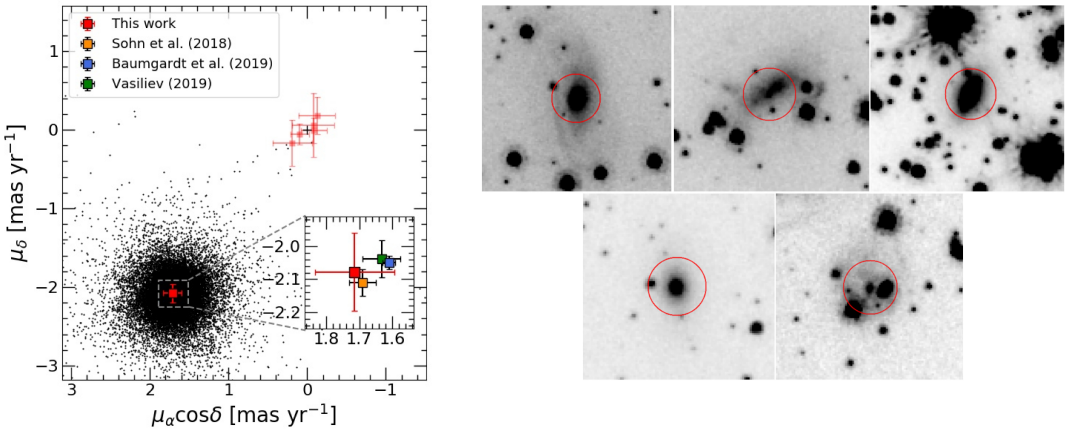

FIGURE 6.6: Left panel: VPD of the absolute proper motions. The light red squares are the PMs of 5 background galaxies found by visually inspecting the images. The cluster absolute proper motion is marked as a dark red square. In the inset we zoom in around the cluster absolute proper motion and we show as yellow, blue and green squares the absolute motion from Sohn et al. (2018), Baumgardt et al. (2019) and Vasiliev (2019), respectively. Right panel: images in the F814W band of the 5 galaxies used to measure the absolute proper motion of NGC 1261.

of a larger extension of the Wilson model, with respect to the King one), and also consistent with the value quoted in Ferraro et al. (2018a, $M = 1.30 \times 10^5 M_\odot$).

6.4.3 Absolute proper motion

As already mentioned, the PMs presented here are *relative* to the bulk motion of the cluster. Its absolute motion is consequently transferred, with the opposite sign, to background objects that, in reality, are essentially not moving with respect to it (e.g., distant galaxies; see, e.g., Massari et al. 2013, Cadelano et al. 2017, Libralato et al. 2018b).

We visually inspected the images in our dataset, looking for background galaxies with sharp nuclei, in order to be able to obtain a meaningful photometry and astrometry with a stellar PSF. We found 5 background galaxies with reliable PMs. Their finding charts are shown in the right panel of Figure 6.6. These galaxies are distributed within the entire FOV, which minimizes the effects of cluster rotation, if present. The absolute PMs of these 5 galaxies are shown in the left panel of Figure 6.6 as light red squares. The absolute proper motion of NGC 1261, shown as a dark red square in Figure 6.6, that we consequently obtain is:

$$(\mu_\alpha \cos\delta, \mu_\delta)_{\rm NGC\ 1261} = (1.71 \pm 0.12, -2.08 \pm 0.12)\ {\rm mas\ yr^{-1}} \tag{6.2}$$

This result is consistent, within the errors, with the results of Sohn et al. (2018), obtained from *HST* data and a data reduction technique specifically designed to well measure the position of galaxies, and Baumgardt et al. (2019) and Vasiliev (2019), obtained from *Gaia* DR2 data. Their results are shown in the inset of Figure 6.6 as yellow, blue and green squares, respectively.

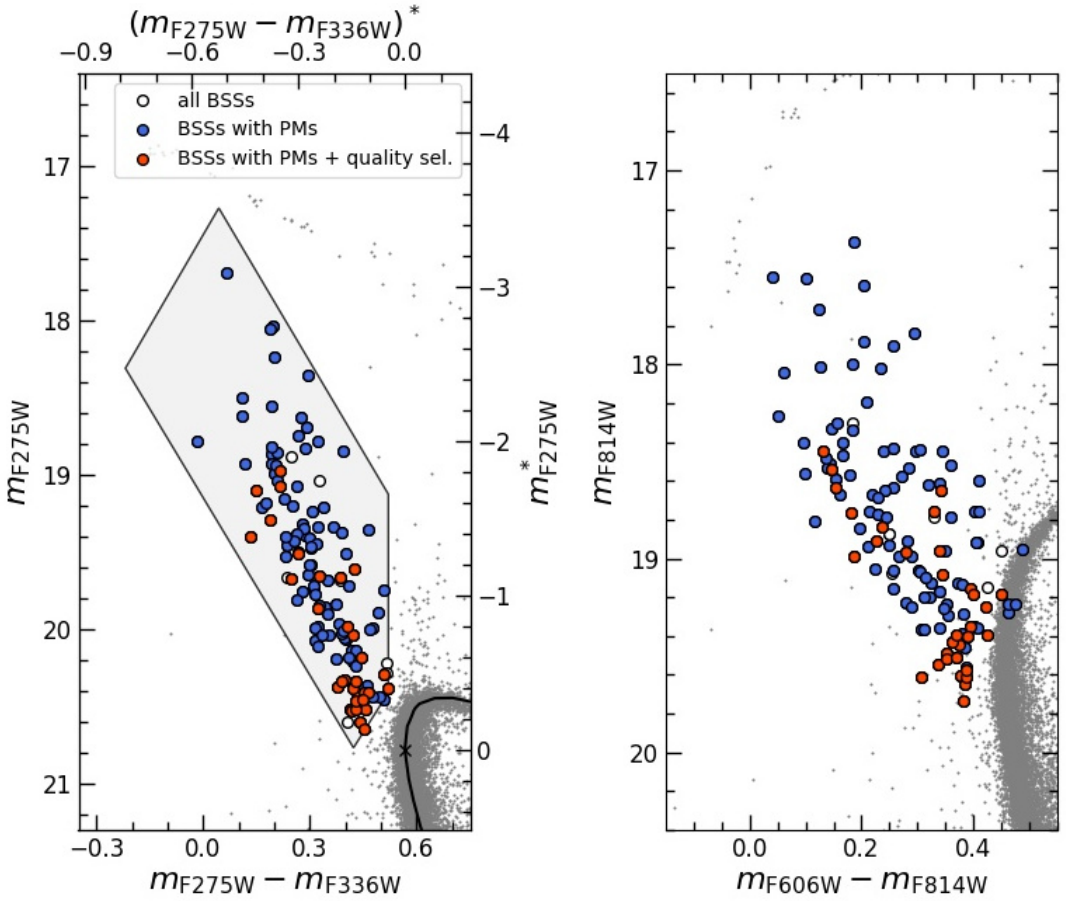

FIGURE 6.7: Left panel: UV CMD of the BSS region of NGC 1261. The shaded box with black contours is the BSS selection box (see text for details). The axis of the n-CMD (i.e., a CMD with color and magnitude rigidly shifted to locate the TO at (0,0)) are reported on the right and top axis. The isochrone and the relative TO point are shown as a black curve and a black cross, respectively. All the stars that fall within the selection box in this CMD are selected as BSSs (black empty circles). We show as blue solid circles all the BSSs that have a measured PM, and in red the BSSs with a measured PM that also pass the selection criteria described in Section 6.4.1. Right panel: optical m_{F814W} vs. $m_{F606W} - m_{F814W}$ CMD, with the UV-selected BSSs shown with the same color code adopted in the left panel.

6.5 Blue Straggler Stars

6.5.1 BSS Selection

As already discussed in Chapter 3, and in Raso et al. (2017) and Ferraro et al. (2018b), a purely UV CMD (e.g., m_{F275W} vs. $m_{F275W} - m_{F336W}$) is the ideal diagram to select BSSs. In this diagram, BSSs define an almost vertical sequence, clearly distinguishable from other evolutionary sequences. Also, at these wavelengths, the cooler stellar populations (e.g., RGB, AGB), which can severely limit our capability of detecting complete samples of BSSs (see Figures 4, 5 and 6 in Raso et al. 2017), are significantly fainter, while BSSs are among the brightest objects.

Therefore, we used the equations reported in Section 3 of Raso et al. (2017) to

define the BSS selection box in the n-CMD[7] of NGC 1261. In the left panel of Figure 6.7 we show the selection box (black thick line and shaded area) and the selected BSSs in the UV CMD (large circles). We also highlight the BSSs that have a measured PM (blue circles) and BSSs with PMs that pass our selection criteria for kinematics, discussed in Section 6.4.1 (red circles). In total, we selected 132 BSSs; 122 BSSs have a PM measurement, 32 of which pass the kinematic selection criteria. In the right panel of the Figure we show the selected BSSs in an optical CMD, with the same color code as in the left panel. As already discussed in Raso et al. (2017), the BSS selection performed in the UV CMD allows us to also safely select very faint BSSs, which in an optical CMD are extremely close to the MS-TO or even overlapping the MS-TO/SGB cluster population.

In the top left panel of Figure 6.8 we show the map of the FOV analyzed in this work, with selected BSSs highlighted with the same color code as in Figure 6.7. As expected, BSSs are found to preferentially populate the central regions of the cluster. In the top right panel of Figure 6.8, we show a zoomed version of the VPD plotted in Figure 6.3. The black circle corresponds to three times the standard deviation of the PM distribution of all stars with magnitude comparable to that of BSSs (roughly, $17 < m_{\rm F814W} < 20$). From this plot, it appears clear that the selected BSSs are members of NGC 1261. In the bottom panel of Figure 6.8 we show the 1D PM error as a function of the F814W magnitude. BSSs are located exactly where the PM errors worsen. This is because the brightest BSSs are saturated in most of the deep optical exposures, and for this reason they have been measured only in a sub-sample of the available images. This reduced the temporal baseline of the PM measurements and the quality of the derived PMs. Only the faintest BSSs have high quality PMs; therefore, when using the BSSs sample selected with the kinematic quality criteria (see Section 6.5.4; red circles in Figure 6.8) we must keep in mind that we are preferentially selecting faint BSSs, i.e., low mass BSSs (see Raso et al. 2019).

6.5.2 BSS radial distribution

As already mentioned, BSSs are a population of heavy stars (with an average mass of $\sim 1.2 M_{\odot}$; see Shara, Saffer, and Livio 1997; Gilliland et al. 1998; Ferraro et al. 2006; Fiorentino et al. 2014; Baldwin et al. 2016; Raso et al. 2019), while the average stellar mass in GCs is significantly smaller, $\langle m \rangle \sim 0.4 M_{\odot}$. Therefore, BSSs are subject to dynamical friction, which progressively makes them sink toward the cluster center. For this reason, the BSS radial distribution is a fundamental tool to measure the dynamical evolution of GCs. In particular, Alessandrini et al. (2016) and Lanzoni et al. (2016) introduced the indicator A^+, able to quantify the level of dynamical evolution of a cluster. This indicator is defined as the area enclosed between the cumulative radial distribution of BSSs and the one of a reference population of lighter stars. The distance from the center is expressed in logarithmic units in order to maximize the sensitivity of the indicator in the central regions, where dynamical friction accumulates most of the BSSs. The value of A^+ depends on the adopted distance from the cluster center. Thus, in order to perform meaningful comparisons among different clusters, Lanzoni et al. (2016) measured this parameter within one half-mass radius ($A^+_{\rm rh}$). Recently, Ferraro et al. (2018b) investigated a sample of 48 Galactic GCs and

[7] The n-CMD is a CMD where the stellar magnitudes and colors have been rigidly shifted so that the MS-TO is at $m^*_{\rm F275W} = 0$ and $(m_{\rm F275W} - m_{\rm F336W})^* = 0$. This is useful when comparing GCs of different metallicity, as in Raso et al. (2017) and Ferraro et al. (2018b), because the BSS sequence is always located in the same region of the n-CMD. For consistency, here we adopt the same procedure, even if we are analyzing a single GC.

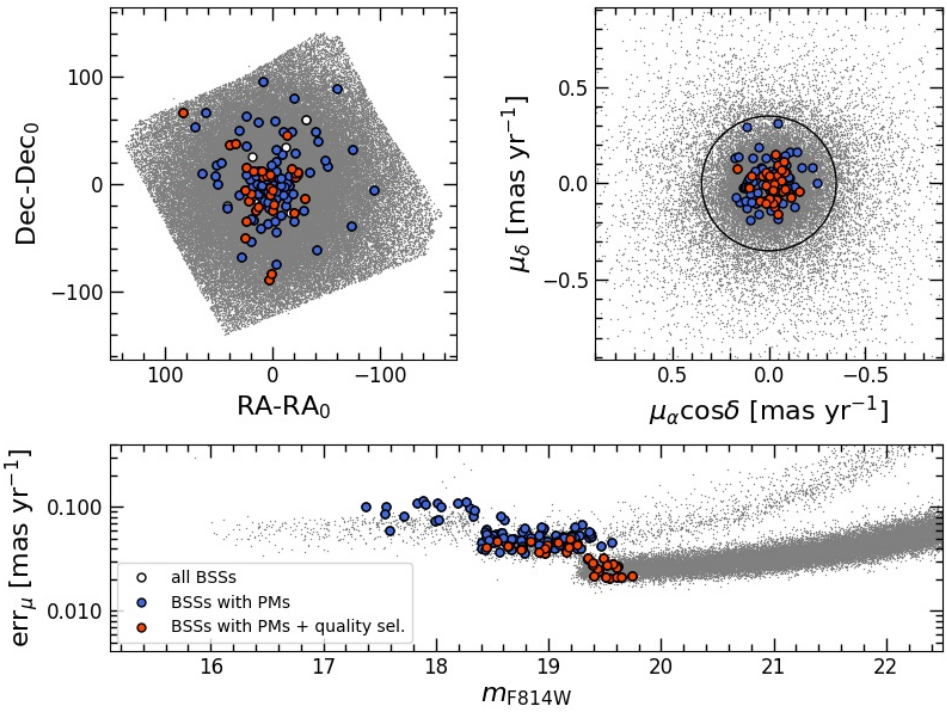

FIGURE 6.8: Top left panel: map of the FOV analyzed in this work. We report in grey all the stars from the photometric catalog, and the selected BSSs as large circles. Here and in the other panels, we use for BSSs the same color code adopted in Figure 6.7, i.e.: empty circles for the complete sample of BSSs, blue circles for BSSs with a PM measurement, red circles for BSS with a PM measurement that pass the kinematic selection criteria described in Section 6.4.1. As expected, BSSs are placed preferentially in the central region of the cluster. Top right panel: a zoomed version of the VPD shown in the left panel of Figure 6.3. We show in grey the stars satisfying criteria (i) to (vii) (see Section 6.4.1). The black circle corresponds to three times the standard deviation of the PM distribution for stars in a magnitude range comparable to BSSs ($17 < m_{F814W} < 20$). Although this value represents a reasonable threshold to separate member BSSs from field contaminants, all BSSs (blue and red circles) fall within this threshold value. Bottom panel: 1D PM error with respect to the F814W magnitude. Clearly, BSS PM errors become larger for increasing stellar luminosity. This is due to the effect of saturation, occurring at different magnitudes for different datasets and thus reducing the total time baseline and/or the number of available exposures that can be used to compute PMs.

found a strong correlation between A^+_{rh} and the number of central relaxation times experienced by the host star cluster. This result confirms the efficiency of A^+ as a tool to measure the dynamical evolution of GCs. Furthermore, Ferraro et al. (2019), explored a sample of 5 old LMC GCs, probing the presence of a correlation between A^+_{rh} and the number of central relaxation times also in stellar systems outside the Milky Way.

NGC 1261 is included in the sample discussed by Ferraro et al. (2018b), who found $A^+_{rh} = 0.10 \pm 0.02$ for this cluster. However, here we re-determine its value using the new center and half-mass radius obtained in this work. Both quantities can have a significant impact on the determination of A^+_{rh}, and, in particular, the half-mass radius adopted by Ferraro et al. (2018b), $r_h = 40.8''$ (taken from Harris

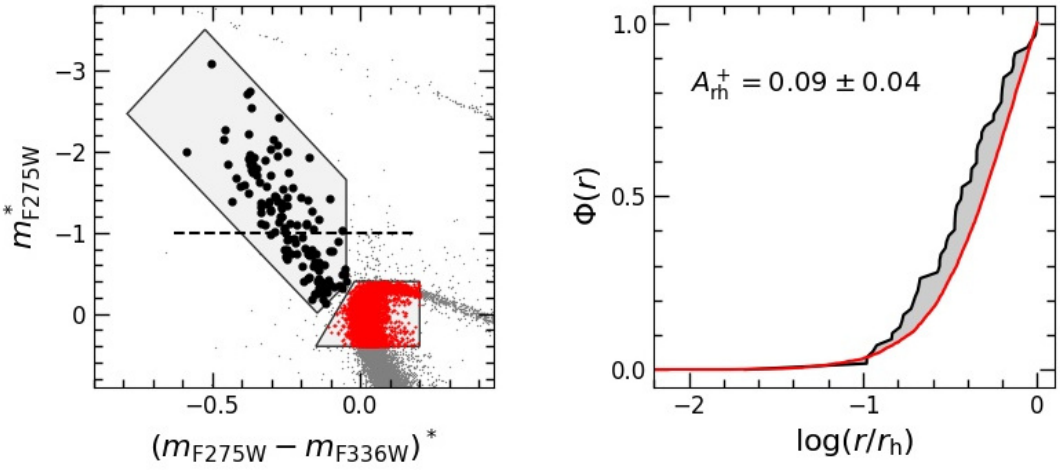

FIGURE 6.9: Left panel: n-CMD of NGC 1261. We show as black circles the selected BSSs. The black dashed line corresponds to the magnitude threshold adopted to measure A^+_{rh} (only BSSs brighter than this magnitude have been used). The red dots are the MS-TO stars used as reference population. Right panel: cumulative radial distribution of BSSs (black line) and MS-TO reference population (red line). The resulting value of A^+_{rh} is labeled within the panel.

1996), is significantly smaller than the value obtained here ($r_h \simeq 52''$, see Table 6.2).

For consistency with previous estimates, to measure A^+_{rh} we used BSSs brighter than $m^*_{F275W} = -1$ in the n-CMD (see the dashed horizontal line in the left panel of Figure 6.9). This way, we select only the heaviest BSSs, for which the effect of dynamical friction is stronger, and we exclude the part of the BSS sequence where there could be a contamination from MS-TO stars or blends. As reference population, we used MS-TO stars, highlighted in red in the left panel of Figure 6.9. In the right panel we show the cumulative radial distributions of BSSs (black line) and MS-TO reference stars (red line). The shaded grey area between the two curves corresponds to the measured value of A^+_{rh}, equal to 0.09 ± 0.04. The errors on A^+_{rh} have been estimated by combining the uncertainties due to small-number statistics, and the uncertainties on the half-mass radius and the position of the center. The former, which turned out to be the primary source of uncertainty, has been estimated with a jackknife bootstraping tecnique (Lupton 1993), as in Ferraro et al. (2018b). The latter has been estimated by repeating the measure of A^+_{rh} 1000 times, each time randomly extracting the values of the center and half-mass radius from a Gaussian distribution with mean and dispersion equal to the estimates obtained in this work.

The derived value of A^+_{rh} is in very good agreement with that quoted by Ferraro et al. (2018b), and indicates that NGC 1261 experienced a moderate level of BSS central sedimentation, thus suggesting a moderate level of dynamical evolution. In particular, by using Eq. (2) in Ferraro et al. (2018b), we obtain $N_{relax} = t_{age}/t_{rc} = 18^{+12}_{-7}$, corresponding to a relatively large central relaxation time: $t_{rc} = 0.65^{+0.41}_{-0.26}$ Gyr. For comparison, the most dynamically evolved clusters in the sample analyzed by Ferraro et al. (2018b), display values of A^+_{rh} as large as 0.4, with $N_{relax} > 300$. These considerations suggest that NGC 1261 is not in an advanced stage of dynamical evolution (see also Dalessandro et al. 2019c).

6.5.3 A double sequence in NGC 1261?

The BSS population of NGC 1261 has been studied by Simunovic, Puzia, and Sills (2014), from the analysis of a subset of the dataset used in this work (the F606W and

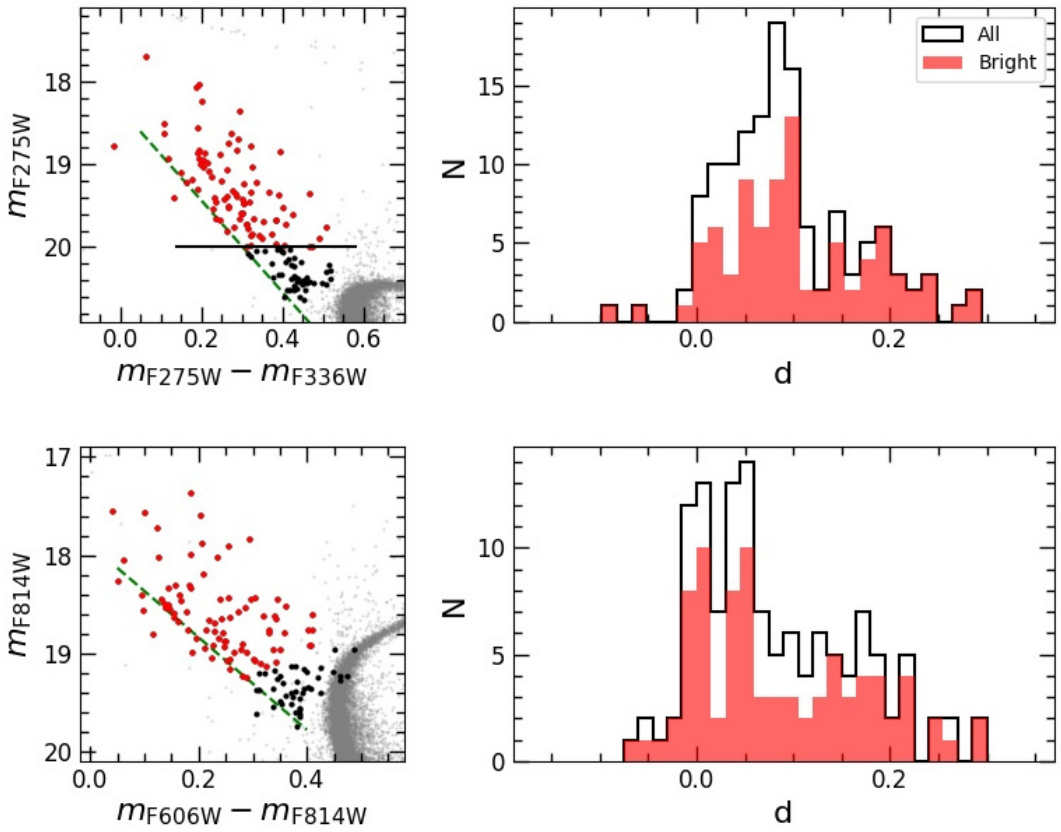

FIGURE 6.10: Top left panel: UV CMD of the BSS region of NGC 1261. The selected BSSs are highlighted as red and black circles. The green dashed line roughly corresponds to the blue edge of the bulk of the BSS sequence, excluding a few scattered, blue objects. We highlight in red the BSS brighter than $m_{F275W} = 20$. Top right panel: histogram of the distances of BSSs from the green dashed line in the top left panel. The black histogram shows the distribution of all the BSSs in our sample, while the red histogram shows the distribution of the BSSs brighter than $m_{F275W} = 20$. Bottom left panel: optical CMD of the BSS region of NGC 1261. The same selections and color code as in the top left panel are adopted. Bottom right panel: as in the top right panel, but for the distances of BSSs from the green line in the optical CMD.

F814W images from GO-10775, and the F336W images from GO-13297 - see Table 6.1 for details). They found that BSSs in this cluster define at least two sequences. As already discussed in Chapter 5, in Galactic GCs this feature has been observed in M30 (Ferraro et al. 2009) and NGC 362 (Dalessandro et al. 2013a; Libralato et al. 2018a), and recently also in M15 (Beccari et al. 2019).

The main characteristic of this feature is the presence of a narrow blue BSS sequence, separated by a clear gap from a broader red BSS sequence. As first suggested by Ferraro et al. (2009), the narrowness of the blue sequence and its impressive agreement with the locus of BSS collisional isochrones (Sills, Karakas, and Lattanzio 2009) point towards a simultaneous and collisional origin of these BSSs, possibly related to the cluster CC, with the possibility of even dating the epoch of such event (see also Portegies Zwart 2019).

We checked our photometry for this feature. In Figure 6.10 we show both the UV CMD used for the BSS selection (top left panel, see Section 6.5.1), and the optical CMD (bottom left panel). The optical CMD is remarkably similar to that published by Simunovic, Puzia, and Sills (2014), and a vague hint of a bimodal distribution can be distinguished by eye, especially if the faintest portion of the BSS sequence

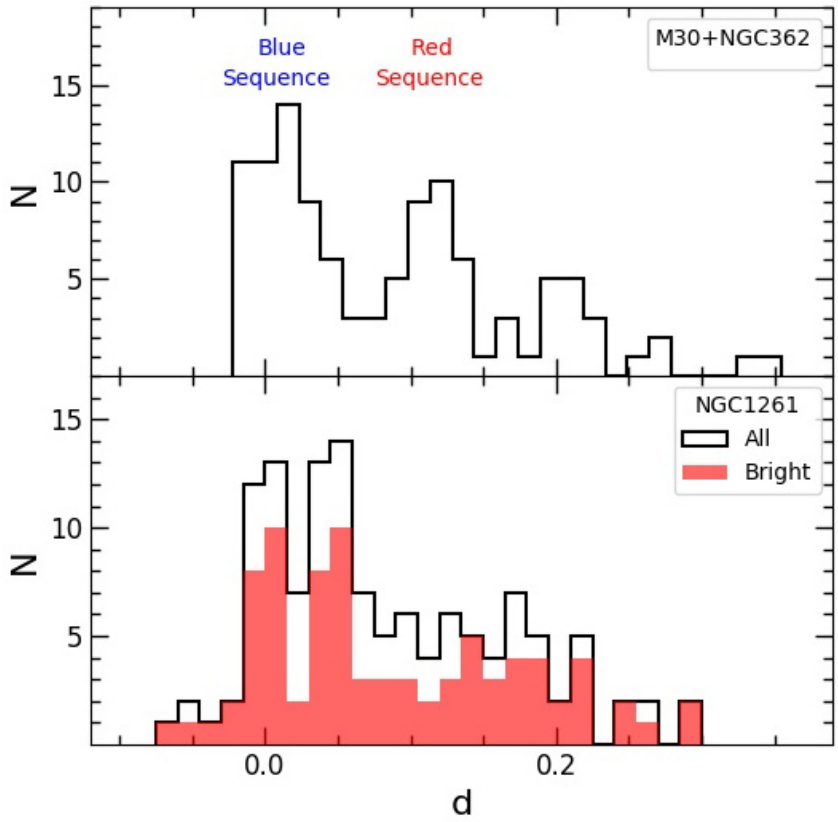

FIGURE 6.11: Histograms of the distances of BSSs in M30+NGC 362 (top panel) and in NGC 1261 (bottom panel). The red histogram in the bottom panel shows the distribution of BSSs brighter than $m_{\mathrm{F275W}} = 20$.

is not considered. In order to quantify this impression, in both diagrams, we draw a straight line roughly corresponding to the blue edge of the BSS sequence (green, dashed lines in Figure 6.10), excluding just a few scattered, blue objects, and we compute the distance of each BSS from those lines. The distributions of the resulting BSS distances is plotted in the right panels of Figure 6.10, both for the complete sample of BSSs (black histogram) and for a selected sample, excluding faint BSSs ($m_{\mathrm{F275W}} < 20$, red histogram). As can be seen, no evidence of bimodal distribution is visible in the distribution of BSS distances computed in the UV CMD. Instead, the optical CMD shows a double peak, very similar to that discussed by Simunovic, Puzia, and Sills (2014).

This is found, however, only if quite narrow bins are adopted, while using wider bins reduces or completely erases the feature. Moreover, the bin width ($\sim$ 0.015 mag) necessary to highlight two distinct peaks in the distribution is comparable to the average photometric error of the BSS population ($\sim$ 0.01 mag). This clearly casts doubts about the real existence of a double BSS sequence in NGC 1261. We also highlight that the distance between the two BSS peaks detected in M30 and NGC 362 ($\sim$ 0.1 mag) is several times larger than in NGC 1261. This is clearly appreciable in Figure 6.11, where the combined distribution of the BSS distances for M30 and NGC 362 (upper panel) is compared to that obtained in NGC 1261 (lower panel). Indeed, the bimodal feature detected in NGC 1261 seems to be morphologically different from those discovered in M30 and NGC 362: the two peaks identified in NGC 1261 are essentially located within the "collisional peak" of the other two clusters. On the other hand, the measure of the BSS sedimentation level, obtained in

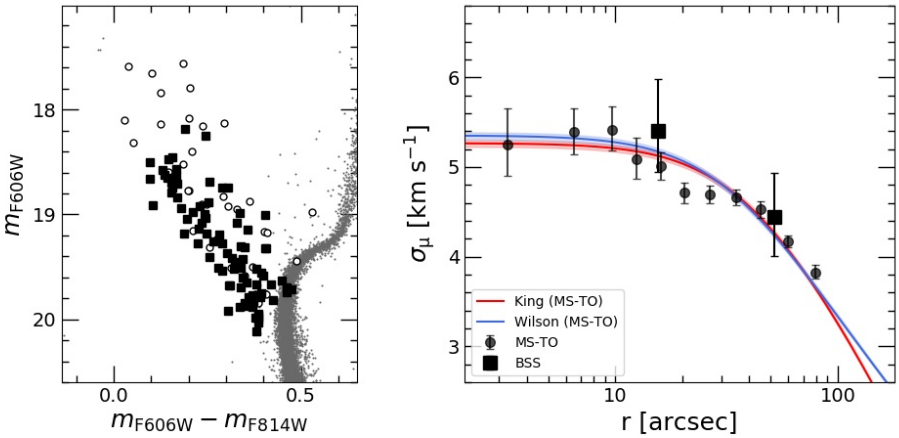

FIGURE 6.12: Left panel: CMD of NGC 1261, zoomed in around the BSS region. We show as black squares the BSSs used for the kinematic analysis, and as empty circles those excluded because of too large PM errors. Right panel: BSS velocity dispersion profile (black squares). For comparison, we report the velocity dispersion profile of MS-TO stars and its best fit King and Wilson models (red and blue lines, respectively), already shown in Figure 6.5).

Section 6.5.2, suggests that NGC 1261 is still far from its CC phase, quite differently from M30 and NGC 362, which are both in very advanced stages of dynamical evolution. This comparison thus poses questions about the similarity of these features: even if confirmed by future observations with higher photometric accuracy, the double BSS sequence in NGC 1261 might have a different origin from that suggested for M30 and NGC 362 (Ferraro et al. 2009; Portegies Zwart 2019).

6.5.4 BSS kinematics

GCs tend to evolve towards a state of energy equipartition, i.e., energy exchanges among stars of different masses redistribute kinetic energy. As a consequence, lighter stars increase their velocity, while heavier stars (like BSSs) tend to slow down. Therefore, it is interesting to compare the velocity dispersion profile of "normal" stars (e.g., MS-TO stars, which have a mass of ~ 0.8 M$_\odot$; see Section 6.4), with the one of BSSs, having larger masses, on average ~ 1.2 M$_\odot$ (Raso et al. 2019).

Using the same technique presented in Section 6.4.2, here we obtain the combined velocity dispersion profile for BSSs in the plane of the sky. As discussed above, most of the analyzed BSSs have PM errors larger than MS-TO stars. Indeed, the PM quality selection described in Section 6.4.1 causes a strong reduction of the BSS sample suitable for a kinematical study (see Figure 6.8). Quantitatively, we are left with only 32 BSSs, i.e., less than 25% of the total sample. Moreover, due to the shape of the PM error distribution, this selection preferentially rejects bright BSSs, which correspond to the most massive ones (Raso et al. 2019). Therefore, applying this selection would imply a study limited only to BSSs with masses (and therefore kinematics) very similar to those of TO stars. With the aim of mitigating this mass selection effect, and to maintain a large enough statistics, we thus dropped the (viii) selection criterion. With this selection, the BSS sample used for the kinematic analysis contains 76 stars, represented as black solid squares in Figure 6.12. In this way, we cover almost the entire magnitude (hence, mass) extension of the BSS sequence, excluding only the brightest 0.5 mag, in which case the PM errors are too large to provide meaningful information about kinematics.

We divided the sample into two equally populated radial bins (38 stars each), and measured the velocity dispersion in each bin with the same method described in Section 6.4.2. The combined BSS velocity dispersion profile is shown in the right panel of Figure 6.12. As apparent, it is consistent with the MS-TO velocity dispersion profile. This is somehow expected from the derived value of $A^+_{\rm rh}$, which suggests a low level of dynamical evolution. Indeed, Baldwin et al. (2016) measured the ratio between the BSS and the MS-TO velocity dispersions ($\alpha = \sigma_{\rm BSS}/\sigma_{\rm MS-TO}$) in 19 GCs and Ferraro et al. (2018b) compared α with the dynamical ages estimated through the A^+ parameter for 14 GCs in common between the two samples. They found an anticorrelation between the two parameters, where clusters with lower values of A^+ (i.e., less dinamically evolved) show larger values of α (see Figure 11 in Ferraro et al. 2018b). By inserting the value of $A^+_{\rm rh}$ determined above for NGC 1261 into Equation 3 of Ferraro et al. (2018b), we expect $\alpha = 0.96 \pm 0.04$, which is fully compatible with what found from the comparison between the BSS and the TO velocity dispersion profiles. This result further confirms that NGC 1261 is poorly dynamically evolved.

6.6 Summary and conclusions

We constructed a high-precision *HST* astro-photometric catalog of the central regions of NGC 1261, a relatively distant ($D_\odot$=15.7 kpc) Galactic GC with intermediate metallicity and low extinction ([Fe/H]=-1.27 and E($B-V$)=0.01, Harris 1996).

We determined the center of gravity and density profile of the system from resolved star counts, also complementing the *HST* catalog with *Gaia* DR2 data to cover the entire radial extension, out to ~ 1 deg. We found that the density profile shows a significant deviation from both a King and a Wilson profile in the outer regions (for $r > 150''$ and $r > 270''$, respectively). This confirms the existence of a diffuse stellar halo around the system, as previously shown by Kuzma, Da Costa, and Mackey (2018).

We measured the *HST* PMs of thousands of individual stars and used them to construct the velocity dispersion and anisotropy profiles in the plane of the sky of NGC 1261. We show that the central regions of the cluster (within r$\approx 80''$) are isotropic. The central velocity dispersion from PMs is consistent with previous determinations from radial velocities. Hence, under the assumption of global orbital isotropy, we combined the PM and LOS measurements and built the most extended velocity dispersion profile of NGC 1261 so far, covering a radial range from the very center, out to $r \sim 800''$. Adopting the structural parameters estimated from the observed density profile and the central velocity dispersion obtained from PMs ($\sigma_0 = 5.3$ kms^{-1}), we find a total mass of $\sim 1.1 \times 10^5$ M$_\odot$ for NGC 1261.

We also found that this GC hosts a quite large BSS population, composed of 132 stars. We measured the dynamical age of the system, by means of the parameter $A^+_{\rm rh}$ (Alessandrini et al. 2016; Lanzoni et al. 2016; Ferraro et al. 2018b), finding comparable results with previous estimates and confirming that it is relatively young from the point of view of dynamical evolution. We also found a hint of a split BSS sequence observed by Simunovic, Puzia, and Sills (2014), although the detectability of the feature is critically dependent on binning. The *HST* PM measurements allowed us to also perform a kinematic study of the BSS population. In spite of large uncertainties due to small statistics, this confirms that NGC 1261 is in a moderate stage of dynamical evolution.

Chapter 7

Summary and Conclusions

The basic concept driving this Thesis is that, being more massive than the average stars in a GC, BSSs significantly suffer from the effects of dynamical friction, which makes them sink toward the cluster center, progressively modifying their radial distribution. This class of exotica is therefore a powerful indicator of the internal dynamical processes of dense stellar systems.

This work consists in a throughout study of BSSs, both as a population and as individual objects, with the aim of properly extracting the dynamical information they bring about their host system. The most relevant results of the Thesis can be summarized as follows.

1. **The first determination of BSS mass along the entire extension of their sequence in the color-magnitude diagram.** This Thesis work demonstrated not only that BSS masses range between $\sim$ 0.8 $M_\odot$ and $\sim$ 1.6 $M_\odot$, with an average value of 1.2 $M_\odot$, but also that standard evolutionary tracks of individual stars can be used for reliable mass estimates of these exotica. These results have been obtained in 47 Tucanae through the analysis of the spectral energy distribution of the largest sample of BSSs ever investigated so far. In addition, demonstrating that standard evolutionary tracks can be safely used for the BSS mass determination opens new perspectives in the study of these stars and their use as dynamical indicators. In fact, the BSS mass can now be easily (but reliably) estimated in any globular cluster, and unexpected correlations with the structural and dynamical parameters of the host system could come to light, thus help understanding the BSS formation mechanisms and the complex interplay between stellar evolution and internal dynamics in dense stellar systems.

   This work is reported in Chapter 2, and it has been presented in Raso et al. (2019).

2. **The quantitative demonstration of the advantages of the UV-guided search for the selection of complete samples of BSSs in the central regions of high-density GCs.** This approach consists in using images acquired at UV wavelengths to construct the master list of detected sources, and then force it to the images acquired in the other filters. The direct comparison between optically-guided and UV-guided catalogs in four GCs (namely NGC 2808, NGC 6388, NGC 6541 and NGC 7078) has shown that a large sample of stars in the innermost region of the systems are lacking when the photometric analysis is performed in the optical bands: the number of missed stars depends on the cluster structure, varying from a few hundreds, up to a few thousands in high density clusters. The vast majority ($>$ 70%) of the missed stars is located within

the innermost $20'' - 30''$ from the cluster center, thus demonstrating the potential risk of using optical-driven catalogs to study the radial distributions and population ratios of BSSs.

This work is reported in Chapter 3, and it has been presented in Raso et al. (2017).

3. **The first dynamical ranking of almost 30% of the Milky Way GCs.** This result has been achieved thanks to the UV-driven selection of complete BSS samples, and the definition of the "A^+ parameter", a powerful dynamical indicator sensitive to the level of BSS central segregation with respect to a lighter population of "normal" cluster stars. Being totally empirical, the A^+ parameter does not suffer from the simplifying assumptions needed for the theoretical estimate of the central relaxation time. Moreover, it is relatively easy to measure and it allows meaningful comparisons among clusters of different properties, provided that the same physical region (e.g., within the half-mass radius) is sampled in all the systems. When A^+ will be known for all the GCs in our Galaxy, possible connections between the cluster dynamical age and other intrinsic properties (as the mass or central density) or external factors (as the level of tidal stripping suffered so far) could be discovered, shedding new light on our understanding of multi-body dynamics.

   This work is reported in Chapter 3, and it has been presented in Ferraro, Lanzoni, Raso, et al. (2018).

4. **The solution to the core-size/age conundrum in the LMC.** The determination of A^+ in an external galaxy (the LMC) is another major achievement of this Thesis work. In fact, the striking agreement between the results obtained in the Milky Way and in the LMC demonstrates that this dynamical indicator can be successfully applied in any galactic environment. Moreover, it allowed us to solve a 30-yr old mystery, showing that the most compact old GCs in this galaxy are more dynamically evolved with respect to those with large core size. This removes the necessity of (unobserved) populations of binary black holes able to (more or less efficiently) expand GC cores, which was previously suggested in the literature for explaining the large spread in core radii observed for old GCs in the LMC. Our work also put into light the real mystery concerning this galaxy: why in the last 3 Gyr, the LMC was able to form only low-mass clusters?

   This work is reported in Chapter 4, and it has been presented in Ferraro, Lanzoni, [...], Raso, et al. (2019).

5. **Dating the core-collapse epoch in post-CC clusters.** This Thesis provided new evidence in support of the hypothesis that double BSS sequences could be connected with the core collapse phase. In fact, we found a double BSS sequence in a post-core collapse cluster (M15), while our findings on NGC 1261 rise doubts about the existence of a double sequence in this cluster, which shows signs of low dynamical evolution (as also confirmed by our kinematical study from *HST* proper motions). In M15 we also found evidence of a split along the bluest sequence, and the comparison with collisional models suggests that these two chains could have been originated by two major collisional events, which can even be dated: the oldest one (occurred approximately 5.5 Gyr ago) corresponds to core collapse, while the most recent one ($\sim$ 2 Gyr ago) could

be a subsequent major re-collapse event, sufficiently intense to trigger the production of a significant number of collisional BSSs.

This work is reported in Chapter 5 and 6, and it has been presented in Beccari, Ferraro, [...], Raso, et al. (2019), and Raso et al. (2020), submitted to ApJ.

The results obtained in this Thesis provide strong evidence supporting the deep connection between the BSS properties and the internal dynamical evolution of collisional stellar systems, also opening new perspectives on the study of extreme phenomena as the CC event and post-CC evolution.

List of Figures

List of Tables

Bibliography

Aarseth, S. J. and D. C. Heggie (1998). "Basic N-body modelling of the evolution of globular clusters - I. Time scaling". In: *Monthly Notices of the Royal Astronomical Society* 297.3, pp. 794–806. DOI: 10.1046/j.1365-8711.1998.01521.x. arXiv: astro-ph/9805344 [astro-ph].

Alessandrini, E. et al. (2014). "Dynamical Friction in Multi-component Evolving Globular Clusters". In: *The Astrophysical Journal* 795.2, p. 169. DOI: 10.1088/0004-637X/795/2/169. arXiv: 1409.4987 [astro-ph.SR].

Alessandrini, E. et al. (2016). "Investigating the Mass Segregation Process in Globular Clusters with Blue Straggler Stars: The Impact of Dark Remnants". In: *The Astrophysical Journal* 833.2, p. 252. DOI: 10.3847/1538-4357/833/2/252. arXiv: 1610.04562 [astro-ph.GA].

Anderson, J. and L. R. Bedin (2010). "An Empirical Pixel-Based Correction for Imperfect CTE. I. *HST*'s Advanced Camera for Surveys". In: *Publications of the Astronomical Society of the Pacific* 122.895, p. 1035. DOI: 10.1086/656399. arXiv: 1007.3987 [astro-ph.IM].

Anderson, J. and I. R. King (2004). *Multi-filter PSFs and Distortion Corrections for the HRC*. Tech. rep., p. 3.

— (2006). *PSFs, Photometry, and Astronomy for the ACS/WFC*. Tech. rep., p. 1.

Anderson, J. et al. (2008). "The Acs Survey of Globular Clusters. V. Generating a Comprehensive Star Catalog for each Cluster". In: *The Astronomical Journal* 135.6, pp. 2055–2073. DOI: 10.1088/0004-6256/135/6/2055. arXiv: 0804.2025 [astro-ph].

Applegate, J. H. (1986). "Dynamical Effects of Stellar Evolution in Globular Clusters". In: *The Astrophysical Journal* 301, p. 132. DOI: 10.1086/163881.

Baldwin, A. T. et al. (2016). "*Hubble Space Telescope* Proper Motion (HSTPROMO) Catalogs of Galactic Globular Clusters. IV. Kinematic Profiles and Average Masses of Blue Straggler Stars". In: *The Astrophysical Journal* 827.1, p. 12. DOI: 10.3847/0004-637X/827/1/12. arXiv: 1606.00836 [astro-ph.SR].

Banerjee, S. (2016). "Blue straggler formation at core collapse". In: *Memorie della Società Astronomica Italiana* 87, p. 497. arXiv: 1606.05213 [astro-ph.GA].

Baumgardt, H. and M. Hilker (2018). "A catalogue of masses, structural parameters, and velocity dispersion profiles of 112 Milky Way globular clusters". In: *Monthly Notices of the Royal Astronomical Society* 478.2, pp. 1520–1557. DOI: 10.1093/mnras/sty1057. arXiv: 1804.08359 [astro-ph.GA].

Baumgardt, H. et al. (2019). "Mean proper motions, space orbits, and velocity dispersion profiles of Galactic globular clusters derived from *Gaia* DR2 data". In: *Monthly Notices of the Royal Astronomical Society* 482.4, pp. 5138–5155. DOI: 10.1093/mnras/sty2997. arXiv: 1811.01507 [astro-ph.GA].

Beccari, G. et al. (2011). "The Non-segregated Population of Blue Straggler Stars in the Remote Globular Cluster Palomar 14". In: *The Astrophysical Journal* 737.1, p. L3. DOI: 10.1088/2041-8205/737/1/L3. arXiv: 1107.0576 [astro-ph.SR].

Beccari, G. et al. (2012). "The Central Blue Straggler Population in Four Outer-halo Globular Clusters". In: *The Astrophysical Journal* 754.2, p. 108. DOI: 10.1088/0004-637X/754/2/108. arXiv: 1205.6293 [astro-ph.SR].

Beccari, G. et al. (2013). "Deep Multi-telescope Photometry of NGC 5466. I. Blue Stragglers and Binary Systems". In: *The Astrophysical Journal* 776.1, p. 60. DOI: 10.1088/0004-637X/776/1/60. arXiv: 1308.5810 [astro-ph.SR].

Beccari, G. et al. (2019). "Discovery of a Double Blue Straggler Sequence in M15: New Insight into the Core-collapse Process". In: *The Astrophysical Journal* 876.1, p. 87. DOI: 10.3847/1538-4357/ab13a4. arXiv: 1903.11113 [astro-ph.SR].

Bedin, L. R. et al. (2003). "*Hubble Space Telescope* Astrometry of M4 and the Galactic Constant V_0/R_0". In: *The Astronomical Journal* 126.1, pp. 247–254. DOI: 10.1086/375646. arXiv: astro-ph/0304071 [astro-ph].

Bekki, K. et al. (2004). "Explaining the Mysterious Age Gap of Globular Clusters in the Large Magellanic Cloud". In: *The Astrophysical Journal Letters* 610.2, pp. L93–L96. DOI: 10.1086/423372. arXiv: astro-ph/0406443 [astro-ph].

Bellini, A., J. Anderson, and L. R. Bedin (2011). "Astrometry and Photometry with *HST* WFC3. II. Improved Geometric-Distortion Corrections for 10 Filters of the UVIS Channel". In: *Publications*

of the Astronomical Society of the Pacific 123.903, p. 622. DOI: 10.1086/659878. arXiv: 1102.5218 [astro-ph.IM].

Bellini, A. and L. R. Bedin (2009). "Astrometry and Photometry with *HST* WFC3. I. Geometric Distortion Corrections of F225W, F275W, F336W Bands of the UVIS Channel". In: *Publications of the Astronomical Society of the Pacific* 121.886, p. 1419. DOI: 10.1086/649061. arXiv: 0910.3250 [astro-ph.IM].

Bellini, A. et al. (2014). "*Hubble Space Telescope* Proper Motion (HSTPROMO) Catalogs of Galactic Globular Clusters. I. Sample Selection, Data Reduction, and NGC 7078 Results". In: *The Astrophysical Journal* 797.2, p. 115. DOI: 10.1088/0004-637X/797/2/115. arXiv: 1410.5820 [astro-ph.SR].

Bellini, A. et al. (2015). "The *Hubble Space Telescope* UV Legacy Survey of Galactic Globular Clusters: The Internal Kinematics of the Multiple Stellar Populations in NGC 2808". In: *The Astrophysical Journal Letters* 810.1, p. L13. DOI: 10.1088/2041-8205/810/1/L13. arXiv: 1508.01804 [astro-ph.GA].

Bellini, A. et al. (2017a). "Hubble Space Telescope Proper Motion (HSTPROMO) Catalogs of Galactic Globular Clusters. V. The Rapid Rotation of 47 Tuc Traced and Modeled in Three Dimensions". In: *The Astrophysical Journal* 844.2, p. 167. DOI: 10.3847/1538-4357/aa7c5f. arXiv: 1706.08974 [astro-ph.GA].

Bellini, A. et al. (2017b). "The State-of-the-art *HST* Astro-photometric Analysis of the Core of ω Centauri. I. The Catalog". In: *The Astrophysical Journal* 842.1, p. 6. DOI: 10.3847/1538-4357/aa7059. arXiv: 1704.07425 [astro-ph.SR].

Bellini, A. et al. (2018). "The *HST* Large Programme on ω Centauri. II. Internal Kinematics". In: *The Astrophysical Journal* 853.1, p. 86. DOI: 10.3847/1538-4357/aaa3ec. arXiv: 1801.01504 [astro-ph.GA].

Benz, W. and J. G. Hills (1987). "Three-dimensional Hydrodynamical Simulations of Stellar Collisions. I. Equal-Mass Main-Sequence Stars". In: *The Astrophysical Journal* 323, p. 614. DOI: 10.1086/165857.

Bettwieser, E. and D. Sugimoto (1984). "Post-collapse evolution and gravothermal oscillation of globular clusters". In: *Monthly Notices of the Royal Astronomical Society* 208, pp. 493–509. DOI: 10.1093/mnras/208.3.493.

Bianchini, P. et al. (2016). "A novel look at energy equipartition in globular clusters". In: *Monthly Notices of the Royal Astronomical Society* 458.4, pp. 3644–3654. DOI: 10.1093/mnras/stw552. arXiv: 1603.00878 [astro-ph.GA].

Binney, J. and S. Tremaine (1987). *Galactic dynamics*.

Bohlin, R. C. (2016). "Perfecting the Photometric Calibration of the ACS CCD Cameras". In: *The Astronomical Journal* 152.3, p. 60. DOI: 10.3847/0004-6256/152/3/60. arXiv: 1606.01838 [astro-ph.IM].

Breen, P. G. and D. C. Heggie (2012). "Gravothermal oscillations in multicomponent models of star clusters". In: *Monthly Notices of the Royal Astronomical Society* 425.4, pp. 2493–2500. DOI: 10.1111/j.1365-2966.2012.21688.x. arXiv: 1207.2672 [astro-ph.GA].

Buonanno, R. et al. (1983). "Automated photographic photometry of stars in globular clusters." In: *Astronomy and Astrophysics* 126, pp. 278–282.

Cadelano, M. et al. (2017). "Proper Motions and Structural Parameters of the Galactic Globular Cluster M71". In: *The Astrophysical Journal* 836.2, p. 170. DOI: 10.3847/1538-4357/aa5ca5. arXiv: 1701.07834 [astro-ph.SR].

Cardelli, J. A., G. C. Clayton, and J. S. Mathis (1989). "The Relationship between Infrared, Optical, and Ultraviolet Extinction". In: *The Astrophysical Journal* 345, p. 245. DOI: 10.1086/167900.

Carretta, E. and R. G. Gratton (1997). "Abundances for globular cluster giants. I. Homogeneous metallicities for 24 clusters". In: *Astronomy and Astrophysics Supplement series* 121, pp. 95–112. DOI: 10.1051/aas:1997116. arXiv: astro-ph/9607078 [astro-ph].

Carretta, E. et al. (2009a). "Na-O anticorrelation and HB. VII. The chemical composition of first and second-generation stars in 15 globular clusters from GIRAFFE spectra". In: *Astronomy and Astrophysics* 505.1, pp. 117–138. DOI: 10.1051/0004-6361/200912096. arXiv: 0909.2938 [astro-ph.GA].

Carretta, E. et al. (2009b). "Na-O anticorrelation and HB. VIII. Proton-capture elements and metallicities in 17 globular clusters from UVES spectra". In: *Astronomy and Astrophysics* 505.1, pp. 139–155. DOI: 10.1051/0004-6361/200912097. arXiv: 0909.2941 [astro-ph.GA].

Chaboyer, B. et al. (1998). "The Age of Globular Clusters in Light of Hipparcos: Resolving the Age Problem?" In: *The Astrophysical Journal* 494.1, pp. 96–110. DOI: 10.1086/305201. arXiv: astro-ph/9706128 [astro-ph].

Chatterjee, S. et al. (2013). "Understanding the dynamical state of globular clusters: core-collapsed versus non-core-collapsed". In: *Monthly Notices of the Royal Astronomical Society* 429.4, pp. 2881–2893. DOI: 10.1093/mnras/sts464. arXiv: 1207.3063 [astro-ph.GA].

Chernoff, D. F. and S. Djorgovski (1989). "An Analysis of the Distribution of Globular Clusters with Postcollapse Cores in the Galaxy". In: *The Astrophysical Journal* 339, p. 904. DOI: 10.1086/167344.

Chernoff, D. F. and S. L. Shapiro (1987). "Globular Cluster Evolution in the Galaxy: A Global View". In: *The Astrophysical Journal* 322, p. 113. DOI: 10.1086/165708.

Chernoff, D. F. and M. D. Weinberg (1990). "Evolution of Globular Clusters in the Galaxy". In: *The Astrophysical Journal* 351, p. 121. DOI: 10.1086/168451.

Chomiuk, L. et al. (2013). "A Radio-selected Black Hole X-Ray Binary Candidate in the Milky Way Globular Cluster M62". In: *The Astrophysical Journal* 777.1, p. 69. DOI: 10.1088/0004-637X/777/1/69. arXiv: 1306.6624 [astro-ph.HE].

Clement, C. M. et al. (2001). "Variable Stars in Galactic Globular Clusters". In: *The Astronomical Journal* 122.5, pp. 2587–2599. DOI: 10.1086/323719. arXiv: astro-ph/0108024 [astro-ph].

Cohn, H., P. Hut, and M. Wise (1989). "Gravothermal Oscillations after Core Collapse in Globular Cluster Evolution". In: *The Astrophysical Journal* 342, p. 814. DOI: 10.1086/167638.

Contreras Ramos, R. et al. (2012). "The Unimodal Distribution of Blue Straggler Stars in M75 (NGC 6864)". In: *The Astrophysical Journal* 748.2, p. 91. DOI: 10.1088/0004-637X/748/2/91. arXiv: 1201.4959 [astro-ph.SR].

Da Costa, G. S. (1991). "The Age-Abundance Relations and Age Distributions for the Star Clusters of the Magellanic Clouds". In: *The Magellanic Clouds*. Ed. by Raymond Haynes and Douglas Milne. Vol. 148. IAU Symposium, p. 183.

Dalessandro, E. et al. (2008). "Another Nonsegregated Blue Straggler Population in a Globular Cluster: the Case of NGC 2419". In: *The Astrophysical Journal* 681.1, pp. 311–319. DOI: 10.1086/588462. arXiv: 0803.2149 [astro-ph].

Dalessandro, E. et al. (2009). "Multiwavelength Photometry in the Globular Cluster M2". In: *The Astrophysical Journal Supplements* 182.2, pp. 509–518. DOI: 10.1088/0067-0049/182/2/509. arXiv: 0903.3527 [astro-ph.GA].

Dalessandro, E. et al. (2013a). "Double Blue Straggler Sequences in Globular Clusters: The Case of NGC 362". In: *The Astrophysical Journal* 778.2, p. 135. DOI: 10.1088/0004-637X/778/2/135. arXiv: 1310.2389 [astro-ph.SR].

Dalessandro, E. et al. (2013b). "Ultraviolet Observations of the Globular Cluster M10 from *HST* and *GALEX*: The BSS Population". In: *The Astrophysical Journal* 770.1, p. 45. DOI: 10.1088/0004-637X/770/1/45. arXiv: 1305.0846 [astro-ph.SR].

Dalessandro, E. et al. (2015). "No Evidence of Mass Segregation in the Low-mass Galactic Globular Cluster NGC 6101". In: *The Astrophysical Journal* 810.1, p. 40. DOI: 10.1088/0004-637X/810/1/40. arXiv: 1507.04776 [astro-ph.GA].

Dalessandro, E. et al. (2018). "The Peculiar Radial Distribution of Multiple Populations in the Massive Globular Cluster M80". In: *The Astrophysical Journal* 859.1, p. 15. DOI: 10.3847/1538-4357/aabb56. arXiv: 1804.03222 [astro-ph.SR].

Dalessandro, E. et al. (2019a). "The double blue-straggler sequence in NGC 2173: an artifact of field contamination". In: *Astronomy and Astrophysics* 621, A45. DOI: 10.1051/0004-6361/201834011. arXiv: 1811.01016 [astro-ph.SR].

Dalessandro, E. et al. (2019b). "The Double Blue Straggler Sequence in NGC 2173: Yes, a Field Contamination Artifact!" In: *Research Notes of the American Astronomical Society* 3.2, p. 38. DOI: 10.3847/2515-5172/ab0829. arXiv: 1903.01525 [astro-ph.SR].

Dalessandro, Emanuele et al. (2019c). "A Family Picture: Tracing the Dynamical Path of the Structural Properties of Multiple Populations in Globular Clusters". In: *The Astrophysical Journal Letters* 884.1, p. L24. DOI: 10.3847/2041-8213/ab45f7. arXiv: 1910.00613 [astro-ph.SR].

Davies, M. B. (2015). "Formation Channels for Blue Straggler Stars". In: *Ecology of Blue Straggler Stars*. Vol. 413, p. 203. DOI: 10.1007/978-3-662-44434-4_9. arXiv: 1406.3477 [astro-ph.SR].

Davies, M. B., G. Piotto, and F. de Angeli (2004). "Blue straggler production in globular clusters". In: *Monthly Notices of the Royal Astronomical Society* 349.1, pp. 129–134. DOI: 10.1111/j.1365-2966.2004.07474.x. arXiv: astro-ph/0401502 [astro-ph].

de Grijs, R. et al. (2002). "Mass segregation in young compact clusters in the Large Magellanic Cloud - III. Implications for the initial mass function". In: *Monthly Notices of the Royal Astronomical Society* 337.2, pp. 597–608. DOI: 10.1046/j.1365-8711.2002.05954.x. arXiv: astro-ph/0208150 [astro-ph].

de Marchi, G., F. Paresce, and F. R. Ferraro (1993). "The Structure of the Core of 47 Tucanae from *Hubble Space Telescope* Observations". In: *The Astrophysical Journal Supplements* 85, p. 293. DOI: 10.1086/191766.

De Marco, O. et al. (2005). "A Spectroscopic Analysis of Blue Stragglers, Horizontal Branch Stars, and Turnoff Stars in Four Globular Clusters". In: *The Astrophysical Journal* 632.2, pp. 894–919. DOI: 10.1086/444372. arXiv: astro-ph/0511497 [astro-ph].

Dieball, A. et al. (2007). "Unveiling the Core of the Globular Cluster M15 in the Ultraviolet". In: *The Astrophysical Journal* 670.1, pp. 379–399. DOI: 10.1086/522103. arXiv: 0709.0114 [astro-ph].

Djorgovski, S. (1993). "Physical Parameters of Galactic Globular Clusters". In: *Structure and Dynamics of Globular Clusters*. Ed. by S. G. Djorgovski and Georges Meylan. Vol. 50. Astronomical Society of the Pacific Conference Series, p. 373.

Djorgovski, S. and I. R. King (1986). "A Preliminary Survey of Collapsed Cores in Globular Clusters". In: *The Astrophysical Journal Letters* 305, p. L61. DOI: 10.1086/184685.

Dotter, A. et al. (2010). "The ACS Survey of Galactic Globular Clusters. IX. Horizontal Branch Morphology and the Second Parameter Phenomenon". In: *The Astrophysical Journal* 708.1, pp. 698–716. DOI: 10.1088/0004-637X/708/1/698. arXiv: 0911.2469 [astro-ph.SR].

Edmonds, P. D. et al. (1996). "Stellar Variability in the Central Populations of 47 Tucanae from WF/PC Observations with the *Hubble Space Telescope*. II. Binary Systems". In: *The Astrophysical Journal* 468, p. 241. DOI: 10.1086/177687.

Elson, R. A. W. (1991). "The Structure and Evolution of Rich Star Clusters in the Large Magellanic Cloud". In: *The Astrophysical Journal Supplements* 76, p. 185. DOI: 10.1086/191568.

— (1992). "Surface brightness profiles for five rich star clusters in the Large Magellanic Cloud." In: *Monthly Notices of the Royal Astronomical Society* 256, pp. 515–518. DOI: 10.1093/mnras/256.3.515.

Elson, R. A. W., K. C. Freeman, and T. R. Lauer (1989). "Core Expansion in Young Clusters in the Large Magellanic Cloud". In: *The Astrophysical Journal Letters* 347, p. L69. DOI: 10.1086/185610.

Ferraro, F. R., F. Fusi Pecci, and M. Bellazzini (1995). "Blue stragglers in Galactic globular clusters: playing with specific quantities." In: *Astronomy and Astrophysics* 294, pp. 80–88. arXiv: astro-ph/9406062 [astro-ph].

Ferraro, F. R., F. Fusi Pecci, and R. Buonanno (1992). "The galactic globular cluster NGC 5897 and its population of blue stragglers." In: *Monthly Notices of the Royal Astronomical Society* 256, pp. 376–390. DOI: 10.1093/mnras/256.3.376.

Ferraro, F. R. et al. (1991). "CCD-photometry of galactic globular clusters - III. NGC 6171." In: *Monthly Notices of the Royal Astronomical Society* 252, p. 357. DOI: 10.1093/mnras/252.3.357.

Ferraro, F. R. et al. (1993). "Blue Stragglers in the Galactic Globular Cluster M3: Evidence for two Populations". In: *The Astronomical Journal* 106, p. 2324. DOI: 10.1086/116804.

Ferraro, F. R. et al. (1997). "*HST* observations of blue Straggler stars in the core of the globular cluster M 3." In: *Astronomy and Astrophysics* 324, pp. 915–928. arXiv: astro-ph/9703026 [astro-ph].

Ferraro, F. R. et al. (1999a). "Blue Straggler Stars: The Spectacular Population in M80". In: *The Astrophysical Journal* 522.2, pp. 983–990. DOI: 10.1086/307700. arXiv: astro-ph/9904196 [astro-ph].

Ferraro, F. R. et al. (1999b). "The Giant, Horizontal, and Asymptotic Branches of Galactic Globular Clusters. I. The Catalog, Photometric Observables, and Features". In: *The Astronomical Journal* 118.4, pp. 1738–1758. DOI: 10.1086/301029. arXiv: astro-ph/9906248 [astro-ph].

Ferraro, F. R. et al. (2001). "Blue Stragglers, Young White Dwarfs, and UV-Excess Stars in the Core of 47 Tucanae". In: *The Astrophysical Journal* 561.1, pp. 337–345. DOI: 10.1086/322773. arXiv: astro-ph/0107056 [astro-ph].

Ferraro, F. R. et al. (2003a). "Blue Straggler Stars: A Direct Comparison of Star Counts and Population Ratios in Six Galactic Globular Clusters". In: *The Astrophysical Journal* 588.1, pp. 464–477. DOI: 10.1086/374042. arXiv: astro-ph/0301261 [astro-ph].

Ferraro, F. R. et al. (2003b). "The Puzzling Dynamical Status of the Core of the Globular Cluster NGC 6752". In: *The Astrophysical Journal* 595.1, pp. 179–186. DOI: 10.1086/377352. arXiv: astro-ph/0306138 [astro-ph].

Ferraro, F. R. et al. (2004). "Discovery of Another Peculiar Radial Distribution of Blue Stragglers in Globular Clusters: The Case of 47 Tucanae". In: *The Astrophysical Journal* 603.1, pp. 127–134. DOI: 10.1086/381229. arXiv: astro-ph/0311317 [astro-ph].

Ferraro, F. R. et al. (2006). "Discovery of Carbon/Oxygen-depleted Blue Straggler Stars in 47 Tucanae: The Chemical Signature of a Mass Transfer Formation Process". In: *The Astrophysical Journal* 647.1, pp. L53–L56. DOI: 10.1086/507327. arXiv: astro-ph/0610081 [astro-ph].

Ferraro, F. R. et al. (2009). "Two distinct sequences of blue straggler stars in the globular cluster M 30". In: *Nature* 462.7276, pp. 1028–1031. DOI: 10.1038/nature08607. arXiv: 1001.1096 [astro-ph.GA].

Ferraro, F. R. et al. (2012). "Dynamical age differences among coeval star clusters as revealed by blue stragglers". In: *Nature* 492.7429, pp. 393–395. DOI: 10.1038/nature11686. arXiv: 1212.5071 [astro-ph.SR].

Ferraro, F. R. et al. (2015). "Blue Straggler Stars in Globular Clusters: A Powerful Tool to Probe the Internal Dynamical Evolution of Stellar Systems". In: *Ecology of Blue Straggler Stars*. Vol. 413, p. 99. DOI: 10.1007/978-3-662-44434-4_5. arXiv: 1406.3471 [astro-ph.SR].

Ferraro, F. R. et al. (2016). "Weighing Stars: The Identification of an Evolved Blue Straggler Star in the Globular Cluster 47 Tucanae". In: *The Astrophysical Journal* 816.2, p. 70. DOI: 10.3847/0004-637X/816/2/70. arXiv: 1512.00649 [astro-ph.SR].

Ferraro, F. R. et al. (2018a). "MIKiS: The Multi-instrument Kinematic Survey of Galactic Globular Clusters. I. Velocity Dispersion Profiles and Rotation Signals of 11 Globular Clusters". In: *The Astrophysical Journal* 860.1, p. 50. DOI: 10.3847/1538-4357/aabe2f. arXiv: 1804.08618 [astro-ph.GA].

Ferraro, F. R. et al. (2018b). "The *Hubble Space Telescope* UV Legacy Survey of Galactic Globular Clusters. XV. The Dynamical Clock: Reading Cluster Dynamical Evolution from the Segregation Level of Blue Straggler Stars". In: *The Astrophysical Journal* 860.1, p. 36. DOI: 10.3847/1538-4357/aac01c. arXiv: 1805.00968 [astro-ph.GA].

Ferraro, F. R. et al. (2019). "Size diversity of old Large Magellanic Cloud clusters as determined by internal dynamical evolution". In: *Nature Astronomy* 3, pp. 1149–1155. DOI: 10.1038/s41550-019-0865-1. arXiv: 1909.02049 [astro-ph.GA].

Fiorentino, G. et al. (2014). "Blue Straggler Masses from Pulsation Properties. I. The Case of NGC 6541". In: *The Astrophysical Journal* 783.1, p. 34. DOI: 10.1088/0004-637X/783/1/34. arXiv: 1312.0388 [astro-ph.SR].

Forbes, D. A. and T. Bridges (2010). "Accreted versus in situ Milky Way globular clusters". In: *Monthly Notices of the Royal Astronomical Society* 404.3, pp. 1203–1214. DOI: 10.1111/j.1365-2966.2010.16373.x. arXiv: 1001.4289 [astro-ph.GA].

Foreman-Mackey, D. et al. (2013). "emcee: The MCMC Hammer". In: *Publications of the Astronomical Society of the Pacific* 125.925, p. 306. DOI: 10.1086/670067. arXiv: 1202.3665 [astro-ph.IM].

Fukushige, T. and D. C. Heggie (1995). "Pre-collapse evolution of galactic globular clusters". In: *Monthly Notices of the Royal Astronomical Society* 276.1, pp. 206–218. DOI: 10.1093/mnras/276.1.206. arXiv: astro-ph/9405058 [astro-ph].

Gaia Collaboration et al. (2016). "*Gaia* Data Release 1. Summary of the astrometric, photometric, and survey properties". In: *Astronomy and Astrophysics* 595, A2. DOI: 10.1051/0004-6361/201629512. arXiv: 1609.04172 [astro-ph.IM].

Gaia Collaboration et al. (2018a). "*Gaia* Data Release 2. Summary of the contents and survey properties". In: *Astronomy and Astrophysics* 616, A1. DOI: 10.1051/0004-6361/201833051. arXiv: 1804.09365 [astro-ph.GA].

Gaia Collaboration et al. (2018b). "*Gaia* Data Release 2. The celestial reference frame (*Gaia*-CRF2)". In: *Astronomy and Astrophysics* 616, A14. DOI: 10.1051/0004-6361/201832916.

Geisler, D. et al. (1997). "A Search for Old Star Clusters in the Large Magellanic Cloud". In: *The Astronomical Journal* 114, p. 1920. DOI: 10.1086/118614. arXiv: astro-ph/9709191 [astro-ph].

Geller, A. M. and R. D. Mathieu (2012). "WIYN Open Cluster Study. XLVIII. The Hard-binary Population of NGC 188". In: *The Astronomical Journal* 144.2, p. 54. DOI: 10.1088/0004-6256/144/2/54. arXiv: 1111.3950 [astro-ph.SR].

Gieles, M., D. C. Heggie, and H. Zhao (2011). "The life cycle of star clusters in a tidal field". In: *Monthly Notices of the Royal Astronomical Society* 413.4, pp. 2509–2524. DOI: 10.1111/j.1365-2966.2011.18320.x. arXiv: 1101.1821 [astro-ph.GA].

Giersz, M. and D. C. Heggie (1994). "Statistics of N-Body Simulations - Part One - Equal Masses Before Core Collapse". In: *Monthly Notices of the Royal Astronomical Society* 268, p. 257. DOI: 10.1093/mnras/268.1.257. arXiv: astro-ph/9305008 [astro-ph].

Giersz, M., D. C. Heggie, and J. R. Hurley (2008). "Monte Carlo simulations of star clusters - IV. Calibration of the Monte Carlo code and comparison with observations for the open cluster M67". In: *Monthly Notices of the Royal Astronomical Society* 388.1, pp. 429–443. DOI: 10.1111/j.1365-2966.2008.13407.x. arXiv: 0801.3968 [astro-ph].

Gilliland, R. L. et al. (1998). "Oscillating Blue Stragglers in the Core of 47 Tucanae". In: *The Astrophysical Journal* 507.2, pp. 818–845. DOI: 10.1086/306363.

Goldsbury, R. et al. (2010). "The ACS Survey of Galactic Globular Clusters. X. New Determinations of Centers for 65 Clusters". In: *The Astronomical Journal* 140.6, pp. 1830–1837. DOI: 10.1088/0004-6256/140/6/1830. arXiv: 1008.2755 [astro-ph.GA].

Grabhorn, R. P. et al. (1992). "Evolving, Dynamical Models for Collapsed-Core Globular Clusters: M15 and NGC 6624". In: *The Astrophysical Journal* 392, p. 86. DOI: 10.1086/171408.

Gratton, R. G., E. Carretta, and A. Bragaglia (2012). "Multiple populations in globular clusters. Lessons learned from the Milky Way globular clusters". In: *The Astronomy and Astrophysics Review* 20, p. 50. DOI: 10.1007/s00159-012-0050-3. arXiv: 1201.6526 [astro-ph.SR].

Gratton, R. G., C. Sneden, and E. Carretta (2004). "Abundance Variations Within Globular Clusters". In: *Annual Review of Astronomy and Astrophysics* 42.1, pp. 385–440. DOI: 10.1146/annurev.astro.42.053102.133945.

Gratton, R. G. et al. (1997). "Ages of Globular Clusters from HIPPARCOS Parallaxes of Local Subdwarfs". In: *The Astrophysical Journal* 491.2, pp. 749–771. DOI: 10.1086/304987. arXiv: astro-ph/9704150 [astro-ph].

Grindlay, J. E. et al. (2001). "High-Resolution X-ray Imaging of a Globular Cluster Core: Compact Binaries in 47Tuc". In: *Science* 292.5525, pp. 2290–2295. DOI: 10.1126/science.1061135. arXiv: astro-ph/0105528 [astro-ph].

Guenther, D. B. et al. (1992). "Standard Solar Model". In: *The Astrophysical Journal* 387, p. 372. DOI: 10.1086/171090.

Guhathakurta, P. et al. (1992). "Globular Cluster Photometry With the *Hubble Space Telescope*. I. Description of the Method and Analysis of the Core of 47 TUC". In: *The Astronomical Journal* 104, p. 1790. DOI: 10.1086/116359.

Harris, W. E. (1996). "A Catalog of Parameters for Globular Clusters in the Milky Way". In: *The Astronomical Journal* 112, p. 1487. DOI: 10.1086/118116.

Hartigan, J. A. and P. M. Hartigan (Mar. 1985). "The Dip Test of Unimodality". In: *Ann. Statist.* 13.1, pp. 70–84. DOI: 10.1214/aos/1176346577. URL: https://doi.org/10.1214/aos/1176346577.

Haurberg, N. C. et al. (2010). "Ultraviolet-bright Stellar Populations and Their Evolutionary Implications in the Collapsed-core Cluster M15". In: *The Astrophysical Journal* 722.1, pp. 158–177. DOI: 10.1088/0004-637X/722/1/158. arXiv: 1009.5694 [astro-ph.SR].

Heggie, D. C. and M. Giersz (2009). "1 Gyr in the life of the globular cluster NGC 6397". In: *Monthly Notices of the Royal Astronomical Society* 397.1, pp. L46–L50. DOI: 10.1111/j.1745-3933.2009.00681.x. arXiv: 0904.4852 [astro-ph.GA].

Heggie, D. C. and P. Hut (2003). *The Gravitational Million-Body Problem: A Multidisciplinary Approach to Star Cluster Dynamics*.

Heggie, D. C. and N. Ramamani (1989). "Evolution of star clusters after core collapse". In: *Monthly Notices of the Royal Astronomical Society* 237, pp. 757–783. DOI: 10.1093/mnras/237.3.757.

Hénon, M. (1961). "Sur l'évolution dynamique des amas globulaires". In: *Annales d'Astrophysique* 24, p. 369.

— (1964). "L'évolution initiale d'un amas sphérique". In: *Annales d'Astrophysique* 27, p. 83.

Hidalgo, S. L. et al. (2018). "The Updated BaSTI Stellar Evolution Models and Isochrones. I. Solar-scaled Calculations". In: *The Astrophysical Journal* 856.2, p. 125. DOI: 10.3847/1538-4357/aab158. arXiv: 1802.07319 [astro-ph.GA].

Hills, J. G. and C. A. Day (1976). "Stellar Collisions in Globular Clusters". In: *Astrophysical Letters* 17, p. 87.

Hong, J. et al. (2017). "Dynamical formation of cataclysmic variables in globular clusters". In: *Monthly Notices of the Royal Astronomical Society* 464.2, pp. 2511–2516. DOI: 10.1093/mnras/stw2595. arXiv: 1611.00779 [astro-ph.GA].

Hypki, A. and M. Giersz (2017). "mocca code for star cluster simulations - VI. Bimodal spatial distribution of blue stragglers". In: *Monthly Notices of the Royal Astronomical Society* 471.3, pp. 2537–2552. DOI: 10.1093/mnras/stx1718. arXiv: 1604.07054 [astro-ph.GA].

Jiang, D. et al. (2017). "Contribution of Primordial Binary Evolution to the Two Blue-straggler Sequences in Globular Cluster M30". In: *The Astrophysical Journal* 849.2, p. 100. DOI: 10.3847/1538-4357/aa8ee1. arXiv: 1709.09643 [astro-ph.SR].

King, I. R. (1966). "The structure of star clusters. III. Some simple dynamical models". In: *The Astronomical Journal* 71, p. 64. DOI: 10.1086/109857.

King, I. R. et al. (1998). "The Luminosity Function of the Globular Cluster NGC 6397 near the Limit of Hydrogen Burning". In: *The Astrophysical Journal Letters* 492.1, pp. L37–L40. DOI: 10.1086/311082. arXiv: astro-ph/9711004 [astro-ph].

Knigge, C., N. W. C. Leigh, and A. Sills (2009). "A binary origin for 'blue stragglers' in globular clusters". In: *Nature* 457.7227, pp. 288–290. DOI: 10.1038/nature07635. arXiv: 0901.2345 [astro-ph.SR].

Knigge, C. et al. (2006). "A Blue Straggler Binary with Three Progenitors in the Core of a Globular Cluster?" In: *The Astrophysical Journal* 641.1, pp. 281–287. DOI: 10.1086/500311. arXiv: astro-ph/0511645 [astro-ph].

Knigge, C. et al. (2008). "Stellar Exotica in 47 Tucanae". In: *The Astrophysical Journal* 683.2, pp. 1006–1030. DOI: 10.1086/589987. arXiv: 0805.0140 [astro-ph].

Kraft, R. P. (1994). "Abundance Differences among Globular Cluster Giants: Primordial vs. Evolutionary Scenarios". In: *Publications of the Astronomical Society of the Pacific* 106, p. 553. DOI: 10.1086/133416.

Kurucz, R. L. (1993). "A New Opacity-Sampling Model Atmosphere Program for Arbitrary Abundances". In: *IAU Colloq. 138: Peculiar versus Normal Phenomena in A-type and Related Stars*. Ed. by M. M. Dworetsky, F. Castelli, and R. Faraggiana. Vol. 44. Astronomical Society of the Pacific Conference Series, p. 87.

— (2005). "ATLAS12, SYNTHE, ATLAS9, WIDTH9, et cetera". In: *Memorie della Societa Astronomica Italiana Supplementi* 8, p. 14.

Kuzma, P. B., G. S. Da Costa, and A. D. Mackey (2018). "The outer envelopes of globular clusters. II. NGC 1851, NGC 5824 and NGC 1261*". In: *Monthly Notices of the Royal Astronomical Society* 473.3, pp. 2881–2898. DOI: 10.1093/mnras/stx2353. arXiv: 1709.02915 [astro-ph.GA].

Lanzoni, B. et al. (2007a). "A Panchromatic Study of the Globular Cluster NGC 1904. I. The Blue Straggler Population". In: *The Astrophysical Journal* 663.2, pp. 1040–1048. DOI: 10.1086/518688. arXiv: 0704.1393 [astro-ph].

Lanzoni, B. et al. (2007b). "The Blue Straggler Population of the Globular Cluster M5". In: *The Astrophysical Journal* 663.1, pp. 267–276. DOI: 10.1086/518592. arXiv: 0704.0139 [astro-ph].

Lanzoni, B. et al. (2007c). "The Surprising External Upturn of the Blue Straggler Radial Distribution in M55". In: *The Astrophysical Journal* 670.2, pp. 1065–1073. DOI: 10.1086/522301. arXiv: 0709.1609 [astro-ph].

Lanzoni, B. et al. (2010). "New Density Profile and Structural Parameters of the Complex Stellar System Terzan 5". In: *The Astrophysical Journal* 717.2, pp. 653–657. DOI: 10.1088/0004-637X/717/2/653. arXiv: 1005.2847 [astro-ph.GA].

Lanzoni, B. et al. (2016). "Refining the Dynamical Clock for Star Clusters". In: *The Astrophysical Journal* 833.2, p. L29. DOI: 10.3847/2041-8213/833/2/L29.

Lanzoni, B. et al. (2019). "Star-density Profiles of Six Old Star Clusters in the Large Magellanic Cloud". In: *The Astrophysical Journal* 887.2, p. 176. DOI: 10.3847/1538-4357/ab54c2. arXiv: 1911.01928 [astro-ph.GA].

Lauer, T. R. et al. (1991). "The Postcollapse Core of M15 Imaged with the *HST* Planetary Camera". In: *The Astrophysical Journal Letters* 369, p. L45. DOI: 10.1086/185955.

Leigh, N. W. C., A. Sills, and C. Knigge (2007). "Where the Blue Stragglers Roam: Searching for a Link between Formation and Environment". In: *The Astrophysical Journal* 661.1, pp. 210–221. DOI: 10.1086/514330. arXiv: astro-ph/0702349 [astro-ph].

— (2011). "Dissecting the colour-magnitude diagram: a homogeneous catalogue of stellar populations in globular clusters". In: *Monthly Notices of the Royal Astronomical Society* 415.4, pp. 3771–3782. DOI: 10.1111/j.1365-2966.2011.18995.x. arXiv: 1105.3192 [astro-ph.SR].

Leigh, N. W. C. et al. (2013). "The origins of blue stragglers and binarity in globular clusters". In: *Monthly Notices of the Royal Astronomical Society* 428.1, pp. 897–905. DOI: 10.1093/mnras/sts085. arXiv: 1210.0542 [astro-ph.SR].

Leigh, N. W. C. et al. (2019). "Constraints on blue straggler formation mechanisms in galactic globular clusters from proper motion velocity distributions". In: *Monthly Notices of the Royal Astronomical Society* 482.1, pp. 231–239. DOI: 10.1093/mnras/sty2707. arXiv: 1810.01895 [astro-ph.SR].

Leonard, P. J. T. and M. Livio (1995). "The Rotational Rates of Blue Stragglers Produced by Physical Stellar Collisions". In: *The Astrophysical Journal Letters* 447, p. L121. DOI: 10.1086/309581.

Li, C. et al. (2018a). "An Unexpected Detection of Bifurcated Blue Straggler Sequences in the Young Globular Cluster NGC 2173". In: *The Astrophysical Journal* 856.1, p. 25. DOI: 10.3847/1538-4357/aaad65. arXiv: 1802.02307 [astro-ph.SR].

— (2018b). "The Double Blue Straggler Sequence in NGC 2173: A Field Contamination Artifact?" In: *Research Notes of the American Astronomical Society* 2.4, p. 215. DOI: 10.3847/2515-5172/aaf290. arXiv: 1812.04807 [astro-ph.SR].

Li, C. et al. (2019). "Blue Straggler Stars beyond the Milky Way. IV. Radial Distributions and Dynamical Implications". In: *The Astrophysical Journal* 871.2, p. 171. DOI: 10.3847/1538-4357/aaf9b3.

Libralato, M. et al. (2018a). "*Hubble Space Telescope* Proper Motion (HSTPROMO) Catalogs of Galactic Globular Cluster. VI. Improved Data Reduction and Internal-kinematic Analysis of NGC 362". In: *The Astrophysical Journal* 861.2, p. 99. DOI: 10.3847/1538-4357/aac6c0. arXiv: 1805.05332 [astro-ph.SR].

Libralato, M. et al. (2018b). "The *HST* Large Programme on ω Centauri. III. Absolute Proper Motion". In: *The Astrophysical Journal* 854.1, p. 45. DOI: 10.3847/1538-4357/aaa59e. arXiv: 1801.01502 [astro-ph.GA].

Libralato, M. et al. (2019). "The *Hubble Space Telescope* UV Legacy Survey of Galactic Globular Clusters. XVIII. Proper-motion Kinematics of Multiple Stellar Populations in the Core Regions of NGC 6352". In: *The Astrophysical Journal* 873.2, p. 109. DOI: 10.3847/1538-4357/ab0551. arXiv: 1902.02787 [astro-ph.SR].

Lombardi, J. C. Jr., F. A. Rasio, and S. L. Shapiro (1995). "On Blue Straggler Formation by Direct Collisions of Main-Sequence Stars". In: *The Astrophysical Journal Letters* 445, p. L117. DOI: 10.1086/187903. arXiv: astro-ph/9502106 [astro-ph].

Lombardi J. C., Jr. et al. (2002). "Stellar Collisions and the Interior Structure of Blue Stragglers". In: *The Astrophysical Journal* 568.2, pp. 939–953. DOI: 10.1086/339060. arXiv: astro-ph/0107388 [astro-ph].

Lovisi, L. et al. (2010). "Fast Rotating Blue Stragglers in the Globular Cluster M4". In: *The Astrophysical Journal Letters* 719.2, pp. L121–L125. DOI: 10.1088/2041-8205/719/2/L121. arXiv: 1007.2343 [astro-ph.GA].

Lovisi, L. et al. (2012). "Chemical and Kinematical Properties of Blue Straggler Stars and Horizontal Branch Stars in NGC 6397". In: *The Astrophysical Journal* 754.2, p. 91. DOI: 10.1088/0004-637X/754/2/91. arXiv: 1205.5561 [astro-ph.SR].

Lugger, P. M., H. N. Cohn, and J. E. Grindlay (1995). "CCD Photometry of Globular Cluster Core Structure. II. U-Band Profiles for 15 Candidate Collapsed-Core Clusters". In: *The Astrophysical Journal* 439, p. 191. DOI: 10.1086/175164.

Lupton, R. (1993). *Statistics in theory and practice*.

Lynden-Bell, D. (1962). "The stability and vibrations of a gas of stars". In: *Monthly Notices of the Royal Astronomical Society* 124, p. 279. DOI: 10.1093/mnras/124.4.279.

— (1967). "Statistical mechanics of violent relaxation in stellar systems". In: *Monthly Notices of the Royal Astronomical Society* 136, p. 101. DOI: 10.1093/mnras/136.1.101.

Lynden-Bell, D. and R. Wood (1968). "The gravo-thermal catastrophe in isothermal spheres and the onset of red-giant structure for stellar systems". In: *Monthly Notices of the Royal Astronomical Society* 138, p. 495. DOI: 10.1093/mnras/138.4.495.

Mackey, A. D. and G. F. Gilmore (2003). "Surface brightness profiles and structural parameters for 53 rich stellar clusters in the Large Magellanic Cloud". In: *Monthly Notices of the Royal Astronomical Society* 338.1, pp. 85–119. DOI: 10.1046/j.1365-8711.2003.06021.x. arXiv: astro-ph/0209031 [astro-ph].

Mackey, A. D. et al. (2008). "Black holes and core expansion in massive star clusters". In: *Monthly Notices of the Royal Astronomical Society* 386.1, pp. 65–95. DOI: 10.1111/j.1365-2966.2008.13052.x. arXiv: 0802.0513 [astro-ph].

Madrid, J. P. et al. (2017). "Mass evaporation rate of globular clusters in a strong tidal field". In: *Monthly Notices of the Royal Astronomical Society* 470.2, pp. 1729–1737. DOI: 10.1093/mnras/stx1350. arXiv: 1706.06635 [astro-ph.GA].

Makino, J. (1996). "Postcollapse Evolution of Globular Clusters". In: *The Astrophysical Journal* 471, p. 796. DOI: 10.1086/178007. arXiv: astro-ph/9608160 [astro-ph].

Mapelli, M. et al. (2004). "The Contribution of Primordial Binaries to the Blue Straggler Population in 47 Tucanae". In: *The Astrophysical Journal* 605.1, pp. L29–L32. DOI: 10.1086/386370. arXiv: astro-ph/0402513 [astro-ph].

Mapelli, M. et al. (2006). "The radial distribution of blue straggler stars and the nature of their progenitors". In: *Monthly Notices of the Royal Astronomical Society* 373.1, pp. 361–368. DOI: 10.1111/j.1365-2966.2006.11038.x. arXiv: astro-ph/0609220 [astro-ph].

Marigo, P. et al. (2017). "A New Generation of PARSEC-COLIBRI Stellar Isochrones Including the TP-AGB Phase". In: *The Astrophysical Journal* 835.1, p. 77. DOI: 10.3847/1538-4357/835/1/77. arXiv: 1701.08510 [astro-ph.SR].

Marín-Franch, A. et al. (2009). "The ACS Survey of Galactic Globular Clusters. VII. Relative Ages". In: *The Astrophysical Journal* 694.2, pp. 1498–1516. DOI: 10.1088/0004-637X/694/2/1498. arXiv: 0812.4541 [astro-ph].

Martocchia, S. et al. (2018). "Age as a major factor in the onset of multiple populations in stellar clusters". In: *Monthly Notices of the Royal Astronomical Society* 473.2, pp. 2688–2700. DOI: 10.1093/mnras/stx2556. arXiv: 1710.00831 [astro-ph.GA].

Massari, D., H. H. Koppelman, and A. Helmi (2019). "Origin of the system of globular clusters in the Milky Way". In: *Astronomy and Astrophysics* 630, p. L4. DOI: 10.1051/0004-6361/201936135. arXiv: 1906.08271 [astro-ph.GA].

Massari, D. et al. (2013). "*Hubble Space Telescope* Absolute Proper Motions Of NGC 6681 (M70) and the Sagittarius Dwarf Spheroidal Galaxy". In: *The Astrophysical Journal* 779.1, p. 81. DOI: 10.1088/0004-637X/779/1/81. arXiv: 1310.2096 [astro-ph.GA].

Massari, D. et al. (2015). "Proper Motions in Terzan 5: Membership of the Multi-iron Subpopulations and First Constraint on the Orbit". In: *The Astrophysical Journal* 810.1, p. 69. DOI: 10.1088/0004-637X/810/1/69. arXiv: 1507.03020 [astro-ph.GA].

McCrea, W. H. (1964). "Extended main-sequence of some stellar clusters". In: *Monthly Notices of the Royal Astronomical Society* 128, p. 147. DOI: 10.1093/mnras/128.2.147.

McLaughlin, D. E. and R. P. van der Marel (2005). "Resolved Massive Star Clusters in the Milky Way and Its Satellites: Brightness Profiles and a Catalog of Fundamental Parameters". In: *The Astrophysical Journal Supplements* 161.2, pp. 304–360. DOI: 10.1086/497429. arXiv: astro-ph/0605132 [astro-ph].

McMillan, S. L. W. and K. A. Engle (1996). "Are Gravothermal Oscillations Gravothermal?" In: *Dynamical Evolution of Star Clusters: Confrontation of Theory and Observations*. Ed. by Piet Hut and Junichiro Makino. Vol. 174. IAU Symposium, p. 379.

Meylan, G. and D. C. Heggie (1997). "Internal dynamics of globular clusters". In: *The Astronomy and Astrophysics Review* 8, pp. 1–143. DOI: 10.1007/s001590050008. arXiv: astro-ph/9610076 [astro-ph].

Milone, A. P. et al. (2012). "The ACS survey of Galactic globular clusters. XII. Photometric binaries along the main sequence". In: *Astronomy and Astrophysics* 540, A16. DOI: 10.1051/0004-6361/201016384. arXiv: 1111.0552 [astro-ph.SR].

Milone, A. P. et al. (2013). "A WFC3/*HST* View of the Three Stellar Populations in the Globular Cluster NGC 6752". In: *The Astrophysical Journal* 767.2, p. 120. DOI: 10.1088/0004-637X/767/2/120. arXiv: 1301.7044 [astro-ph.SR].

Milone, A. P. et al. (2017). "The *Hubble Space Telescope* UV Legacy Survey of Galactic globular clusters - IX. The Atlas of multiple stellar populations". In: *Monthly Notices of the Royal Astronomical Society* 464.3, pp. 3636–3656. DOI: 10.1093/mnras/stw2531. arXiv: 1610.00451 [astro-ph.SR].

Miocchi, P. et al. (2013). "Star Count Density Profiles and Structural Parameters of 26 Galactic Globular Clusters". In: *The Astrophysical Journal* 774.2, p. 151. DOI: 10.1088/0004-637X/774/2/151. arXiv: 1307.6035 [astro-ph.GA].

Miocchi, P. et al. (2015). "Probing the Role of Dynamical Friction in Shaping the BSS Radial Distribution. I. Semi-analytical Models and Preliminary N-body Simulations". In: *The Astrophysical Journal* 799.1, p. 44. DOI: 10.1088/0004-637X/799/1/44. arXiv: 1411.2161 [astro-ph.GA].

Monelli, M. et al. (2015). "The Absolute Age of the Globular Cluster M15 Using Near-infrared Adaptive Optics Images from PISCES/LBT." In: *The Astrophysical Journal* 812.1, p. 25. DOI: 10.1088/0004-637X/812/1/25. arXiv: 1507.08845 [astro-ph.SR].

Montegriffo, P. et al. (1995). "IR-array photometry of Galactic globular clusters - II. JK photometry of 47 TUC". In: *Monthly Notices of the Royal Astronomical Society* 276.3, pp. 739–752. DOI: 10.1093/mnras/276.3.739.

Moretti, A., F. de Angeli, and G. Piotto (2008). "Environmental effects on the globular cluster blue straggler population: a statistical approach". In: *Astronomy and Astrophysics* 483.1, pp. 183–197. DOI: 10.1051/0004-6361:20078416.

Mucciarelli, A. et al. (2008). "The Chemical Composition of Red Giant Stars in Four Intermediate-Age Clusters of the Large Magellanic Cloud". In: *The Astronomical Journal* 136.1, pp. 375–388. DOI: 10.1088/0004-6256/136/1/375. arXiv: 0804.4061 [astro-ph].

Mucciarelli, A. et al. (2014). "No Evidence of Chemical Anomalies in the Bimodal Turnoff Cluster NGC 1806 in the Large Magellanic Cloud". In: *The Astrophysical Journal Letters* 793.1, p. L6. DOI: 10.1088/2041-8205/793/1/L6. arXiv: 1409.0259 [astro-ph.SR].

Muratov, A. L. and O. Y. Gnedin (2010). "Modeling the Metallicity Distribution of Globular Clusters". In: *The Astrophysical Journal* 718.2, pp. 1266–1288. DOI: 10.1088/0004-637X/718/2/1266. arXiv: 1002.1325 [astro-ph.GA].

Murphy, B. W., H. N. Cohn, and P. M. Lugger (2011). "Fokker-Planck Models for M15 Without a Central Black Hole: The Role of the Mass Function". In: *The Astrophysical Journal* 732.2, p. 67. DOI: 10.1088/0004-637X/732/2/67. arXiv: 1205.1049 [astro-ph.GA].

Nardiello, D. et al. (2018). "The *Hubble Space Telescope* UV Legacy Survey of Galactic Globular Clusters - XVII. Public Catalogue Release". In: *Monthly Notices of the Royal Astronomical Society* 481.3, pp. 3382–3393. DOI: 10.1093/mnras/sty2515. arXiv: 1809.04300 [astro-ph.SR].

Parada, J. et al. (2016). "Formation and Evolution of Blue Stragglers in 47 Tucanae". In: *The Astrophysical Journal* 830.2, p. 139. DOI: 10.3847/0004-637X/830/2/139. arXiv: 1609.02115 [astro-ph.SR].

Paresce, F. et al. (1991). "Blue stragglers in the core of the globular cluster 47 Tucanae". In: *Nature* 352.6333, pp. 297–301. DOI: 10.1038/352297a0.

Pietrinferni, A. et al. (2004). "A Large Stellar Evolution Database for Population Synthesis Studies. I. Scaled Solar Models and Isochrones". In: *The Astrophysical Journal* 612.1, pp. 168–190. DOI: 10.1086/422498. arXiv: astro-ph/0405193 [astro-ph].

— (2006). "A Large Stellar Evolution Database for Population Synthesis Studies. II. Stellar Models and Isochrones for an α-enhanced Metal Distribution". In: *The Astrophysical Journal* 642.2, pp. 797–812. DOI: 10.1086/501344. arXiv: astro-ph/0603721 [astro-ph].

Pietrzyński, G. et al. (2013). "An eclipsing-binary distance to the Large Magellanic Cloud accurate to two per cent". In: *Nature* 495.7439, pp. 76–79. DOI: 10.1038/nature11878. arXiv: 1303.2063 [astro-ph.GA].

Piotto, G. et al. (2004). "Relative Frequencies of Blue Stragglers in Galactic Globular Clusters: Constraints for the Formation Mechanisms". In: *The Astrophysical Journal* 604.2, pp. L109–L112. DOI: 10.1086/383617. arXiv: astro-ph/0402592 [astro-ph].

Piotto, G. et al. (2015). "The *Hubble Space Telescope* UV Legacy Survey of Galactic Globular Clusters. I. Overview of the Project and Detection of Multiple Stellar Populations". In: *The Astronomical Journal* 149.3, p. 91. DOI: 10.1088/0004-6256/149/3/91. arXiv: 1410.4564 [astro-ph.SR].

Portegies Zwart, S. F. (2019). "The origin of the two populations of blue stragglers in M30". In: *Astronomy and Astrophysics* 621, p. L10. DOI: 10.1051/0004-6361/201833485. arXiv: 1811.00058 [astro-ph.SR].

Portegies Zwart, S. F. et al. (1998). "On the dissolution of evolving star clusters". In: *Astronomy and Astrophysics* 337, pp. 363–371. arXiv: astro-ph/9803084 [astro-ph].

Raso, S. et al. (2017). "The "UV-route" to Search for Blue Straggler Stars in Globular Clusters: First Results from the *HST* UV Legacy Survey". In: *The Astrophysical Journal* 839.1, p. 64. DOI: 10.3847/1538-4357/aa6891. arXiv: 1704.01453 [astro-ph.SR].

Raso, S. et al. (2019). "Spectral Energy Distribution of Blue Stragglers in the Core of 47 Tucanae". In: *The Astrophysical Journal* 879.1, p. 56. DOI: 10.3847/1538-4357/ab2637. arXiv: 1906.01002 [astro-ph.SR].

Renzini, A. and A. Buzzoni (1986). "Global properties of stellar populations and the spectral evolution of galaxies." In: *Spectral Evolution of Galaxies*. Ed. by Cesare Chiosi and Alvio Renzini. Vol. 122. Astrophysics and Space Science Library, pp. 195–231. DOI: 10.1007/978-94-009-4598-2_19.

Rich, R. M., M. M. Shara, and D. Zurek (2001). "New Photometry for the Intermediate-Age Large Magellanic Cloud Globular Cluster NGC 2121 and the Nature of the LMC Age Gap". In: *The Astronomical Journal* 122.2, pp. 842–848. DOI: 10.1086/321164. arXiv: astro-ph/0105546 [astro-ph].

Richer, H. B. et al. (2013). "A Dynamical Signature of Multiple Stellar Populations in 47 Tucanae". In: *The Astrophysical Journal* 771.1, p. L15. DOI: 10.1088/2041-8205/771/1/L15. arXiv: 1306.1226 [astro-ph.SR].

Sandage, A. R. (1953). "The color-magnitude diagram for the globular cluster M 3." In: *The Astronomical Journal* 58, pp. 61–75. DOI: 10.1086/106822.

Sanna, N. et al. (2012). "The blue straggler star population in NGC 6229". In: *Monthly Notices of the Royal Astronomical Society* 422.2, pp. 1171–1177. DOI: 10.1111/j.1365-2966.2012.20690.x.

Sanna, N. et al. (2014). "The WFPC2 Ultraviolet Survey: The Blue Straggler Population in NGC 5824". In: *The Astrophysical Journal* 780.1, p. 90. DOI: 10.1088/0004-637X/780/1/90.

Sarajedini, A. et al. (2007). "The ACS Survey of Galactic Globular Clusters. I. Overview and Clusters without Previous *Hubble Space Telescope* Photometry". In: *The Astronomical Journal* 133.4, pp. 1658–1672. DOI: 10.1086/511979. arXiv: astro-ph/0612598 [astro-ph].

Sarna, M. J. and J. P. De Greve (1996). "Chemical Evolution of Algols". In: *Quarterly Journal of the Royal Astronomical Society* 37, p. 11.

Sbordone, L. et al. (2004). "ATLAS and SYNTHE under Linux". In: *Memorie della Societa Astronomica Italiana Supplementi* 5, p. 93. arXiv: astro-ph/0406268 [astro-ph].

Shara, M. M., R. A. Saffer, and M. Livio (1997). "The First Direct Measurement of the Mass of a Blue Straggler in the Core of a Globular Cluster: BSS 19 in 47 Tucanae". In: *The Astrophysical Journal* 489.1, pp. L59–L62. DOI: 10.1086/310952.

Shipp, N. et al. (2018). "Stellar Streams Discovered in the Dark Energy Survey". In: *The Astrophysical Journal* 862.2, p. 114. DOI: 10.3847/1538-4357/aacdab. arXiv: 1801.03097 [astro-ph.GA].

Sills, A., T. Adams, and M. B. Davies (2005). "Blue stragglers as stellar collision products: the angular momentum question". In: *Monthly Notices of the Royal Astronomical Society* 358.3, pp. 716–725. DOI: 10.1111/j.1365-2966.2005.08809.x. arXiv: astro-ph/0501142 [astro-ph].

Sills, A., A. Karakas, and J. Lattanzio (2009). "Blue Stragglers After the Main Sequence". In: *The Astrophysical Journal* 692.2, pp. 1411–1420. DOI: 10.1088/0004-637X/692/2/1411. arXiv: 0811.2974 [astro-ph].

Sills, A. et al. (1997). "Evolution of Stellar Collision Products in Globular Clusters. I. Head-on Collisions". In: *The Astrophysical Journal* 487.1, pp. 290–303. DOI: 10.1086/304588. arXiv: astro-ph/9705019 [astro-ph].

Simunovic, M. and T. H. Puzia (2016). "Blue straggler star populations in globular clusters - II. Proper-motion cleaned *HST* catalogues of BSSs in 38 Galactic GCs". In: *Monthly Notices of the Royal Astronomical Society* 462.3, pp. 3401–3418. DOI: 10.1093/mnras/stw1884. arXiv: 1610.09709 [astro-ph.SR].

Simunovic, M., T. H. Puzia, and A. Sills (2014). "The Blue Straggler Star Population in NGC 1261: Evidence for a Post-core-collapse Bounce State". In: *The Astrophysical Journal* 795.1, p. L10. DOI: 10.1088/2041-8205/795/1/L10. arXiv: 1410.0693 [astro-ph.SR].

Sirianni, M. et al. (2005). "The Photometric Performance and Calibration of the *Hubble Space Telescope* Advanced Camera for Surveys". In: *Publications of the Astronomical Society of the Pacific* 117.836, pp. 1049–1112. DOI: 10.1086/444553. arXiv: astro-ph/0507614 [astro-ph].

Sohn, Sangmo Tony et al. (2018). "Absolute Hubble Space Telescope Proper Motion (HSTPROMO) of Distant Milky Way Globular Clusters: Galactocentric Space Velocities and the Milky Way Mass". In: *The Astrophysical Journal* 862.1, p. 52. DOI: 10.3847/1538-4357/aacd0b. arXiv: 1804.01994 [astro-ph.GA].

Sollima, A. and F. R. Ferraro (2019). "Investigating the blue straggler stars radial distribution in globular clusters with Monte Carlo simulations". In: *Monthly Notices of the Royal Astronomical Society* 483.2, pp. 1523–1536. DOI: 10.1093/mnras/sty3237. arXiv: 1811.11174 [astro-ph.GA].

Soto, M. et al. (2017). "The *Hubble Space Telescope* UV Legacy Survey of Galactic Globular Clusters. VIII. Preliminary Public Catalog Release". In: *The Astronomical Journal* 153.1, p. 19. DOI: 10.3847/1538-3881/153/1/19. arXiv: 1612.00714 [astro-ph.GA].

Stetson, P. B. (1987). "DAOPHOT: A Computer Program for Crowded-Field Stellar Photometry". In: *Publications of the Astronomical Society of the Pacific* 99, p. 191. DOI: 10.1086/131977.

— (1994). "The Center of the Core-Cusp Globular Cluster M15: *CFHT* and *HST* Observations, ALLFRAME Reductions". In: *Publications of the Astronomical Society of the Pacific* 106, p. 250. DOI: 10.1086/133378.

Strader, J. et al. (2012). "Two stellar-mass black holes in the globular cluster M22". In: *Nature* 490.7418, pp. 71–73. DOI: 10.1038/nature11490. arXiv: 1210.0901 [astro-ph.HE].

STScI Development Team (Mar. 2013). *pysynphot: Synthetic photometry software package*. Astrophysics Source Code Library. ascl: 1303.023.

Takahashi, K. and S. Inagaki (1991). "Post-Collapse Evolution of Globular Clusters with Stochastic Energy Sources". In: *Publications of the Astronomical Society of Japan* 43, pp. 589–606.

Takahashi, K. and S. F. Portegies Zwart (2000). "The Evolution of Globular Clusters in the Galaxy". In: *The Astrophysical Journal* 535.2, pp. 759–775. DOI: 10.1086/308857. arXiv: astro-ph/9903366 [astro-ph].

Tiongco, M. A., E. Vesperini, and A. L. Varri (2016). "Velocity anisotropy in tidally limited star clusters". In: *Monthly Notices of the Royal Astronomical Society* 455.4, pp. 3693–3701. DOI: 10.1093/mnras/stv2574. arXiv: 1511.02236 [astro-ph.GA].

Trenti, M. and R. P. van der Marel (2013). "No energy equipartition in globular clusters". In: *Monthly Notices of the Royal Astronomical Society* 435.4, pp. 3272–3282. DOI: 10.1093/mnras/stt1521. arXiv: 1302.2152 [astro-ph.GA].

van de Ven, G. et al. (2006). "The dynamical distance and intrinsic structure of the globular cluster ω Centauri". In: *Astronomy and Astrophysics* 445.2, pp. 513–543. DOI: 10.1051/0004-6361:20053061. arXiv: astro-ph/0509228 [astro-ph].

Vasiliev, Eugene (2019). "Proper motions and dynamics of the Milky Way globular cluster system from Gaia DR2". In: *Monthly Notices of the Royal Astronomical Society* 484.2, pp. 2832–2850. DOI: 10.1093/mnras/stz171. arXiv: 1807.09775 [astro-ph.GA].

Vesperini, E. and D. C. Heggie (1997). "On the effects of dynamical evolution on the initial mass function of globular clusters". In: *Monthly Notices of the Royal Astronomical Society* 289.4, pp. 898–920. DOI: 10.1093/mnras/289.4.898. arXiv: astro-ph/9705073 [astro-ph].

Vesperini, E. et al. (2014). "Kinematical fingerprints of star cluster early dynamical evolution." In: *Monthly Notices of the Royal Astronomical Society* 443, pp. L79–L83. DOI: 10.1093/mnrasl/slu088. arXiv: 1406.3634 [astro-ph.GA].

Vilhu, O. (1982). "Detached to contact scenario for the origin of W UMa stars." In: *Astronomy and Astrophysics* 109, pp. 17–22.

Watkins, L. L. et al. (2015a). "*Hubble Space Telescope* Proper Motion (HSTPROMO) Catalogs of Galactic Globular Cluster. II. Kinematic Profiles and Maps". In: *The Astrophysical Journal* 803.1, p. 29. DOI: 10.1088/0004-637X/803/1/29. arXiv: 1502.00005 [astro-ph.GA].

— (2015b). "*Hubble Space Telescope* Proper Motion (HSTPROMO) Catalogs of Galactic Globular Clusters. III. Dynamical Distances and Mass-to-Light Ratios". In: *The Astrophysical Journal* 812.2, p. 149. DOI: 10.1088/0004-637X/812/2/149. arXiv: 1509.00513 [astro-ph.GA].

Wilkinson, M. I. et al. (2003). "Core radius evolution of star clusters". In: *Monthly Notices of the Royal Astronomical Society* 343.3, pp. 1025–1037. DOI: 10.1046/j.1365-8711.2003.06749.x. arXiv: astro-ph/0304522 [astro-ph].

Wilson, C. P. (1975). "Dynamical models of elliptical galaxies." In: *The Astronomical Journal* 80, pp. 175–187. DOI: 10.1086/111729.

Xin, Y. et al. (2015). "The Binary Mass Transfer Origin of the Red Blue Straggler Sequence in M30". In: *The Astrophysical Journal* 801.1, p. 67. DOI: 10.1088/0004-637X/801/1/67. arXiv: 1501.01358 [astro-ph.SR].